Simulations and associated data analysis for realistic LISA configuration

Quang Nam Dam

École doctorale 560:
Sciences de la Terre et de l'Environnement et Physique de l'Univers

THÈSE DE DOCTORAT DE PHYSIQUE

Univesité Paris Cité
Laboratoire AstroParticules et Cosmologie (APC)

Simulations and associated Data Analysis for realistic LISA configuration

présentée par

ĐÀM Quang Nam

Sous la direction de

Dr. Chiara Caprini
et **Dr. Antoine Petiteau**

Soutenue publiquement le 13 décembre 2022 devant le jury composé de:

Président: **Eric Chassande-Mottin** (DR, Université Paris Cité, APC, France)
Rapporteur: **Marc Besancon** (DR, Université Paris-Saclay, CEA/IRFU/DPhP, France)
Rapporteur: **Jonathan Gair** (Professeur, Université de Potsdam, AEI/MPI, Allemange)
Examinatrice: **Isabelle Petitbon** (Ingénieur, CNES, France)
Examinateur: **Hubert Halloin** (MCF-HDR, Université Paris Cité, APC, France)
Directrice de thèse: **Chiara Caprini** (DR, CERN (en détachement du CNRS), Suisse)
Membre invité: **Antoine Petiteau** (Chercheur, DPhP/IRFU/CEA-Saclay & APC, France)

Acknowledgments

To my father.

I'm grateful to Dr. Chiara Caprini and Dr. Antoine Petiteau for the opportunity to work on gravitational wave physics and the LISA mission during my internship and Ph.D. Thanks to your patience and encouragement, I have endured many difficult times during my research and writing manuscript. Chiara has taught me a lot about the stochastic gravitational wave background and its detection with LISA. Antoine is a massive library of LISA and its science. I appreciate your kindness and support during my living in Paris. I'm also grateful to Dr. Henri Inchauspé for co-supervising my thesis. You helped me countless times while researching LISA Dynamics and its implementation in the simulator.

I also want to thank Dr. Stanislav Babak and Dr. Eric Chassande-Mottin for being examiners of my comité de thèse during my Ph.D. Your supervision and encouragement accelerated my progress in writing the manuscript in the last few months. Thanks to Stas for many lessons about gravitational waves and data analysis during my internship and Ph.D. I'm very impressed by your enthusiasm and insights.

Working within international LISA collaboration is a great experience for me to meet and discuss with many colleagues in different countries. I want to thank all members of the LISA Simulation, Performance Model, and Data Analysis groups, especially those with whom I have had the pleasure of discussing and collaborating on my thesis projects.
Special thanks to Dr. Jean-Baptiste Bayle and Dr. Olaf Hartwig for many pedagogical lectures in several workshops about the LISA simulator and instrument model. Jean-Baptiste was also a dedicated senior during my internship and an impressive programmer.

I want to thank Dr. Yves Lemière, Dr. Joseph Martino and Martin Staab for their collaboration in conducting the noise propagation study.
I'm equally grateful to Dr. Germano Nardini and Dr. Mauro Pieroni for many discussions about the SGWB project. Thank you very much, Germano, for your kind hosting during my visit to the University of Stavanger.

I want to thank all the members of the APC laboratory, particularly the Gravitation and LISA-APC groups, for my experiences in both academy and social life during my time there. I'm especially grateful to Dr. Guillaume Patanchon, Dr. Yannick Giraud-Héraud, Dr. Danièle Steer for your support during my Master 2 and Ph.D. at APC.
Many thanks to my close friends and colleagues in my office, Léon and Mikel, for various discussions in science, languages, politics, music, food and life. We have a lot of good times together in our Ph.D.

My family is always supporting me. I sincerely thank my mother, my sister, my brother-in-law and all of my relatives in my hometown. I love you all. I also thank my friends in France (Viet, Hoa, a Minh, a Nhan, a Khanh, a Trung, c Tram, c Quyen, c Suong) and Vietnam (Tien, Duy, Hau, Vu, Quang, Bac, Tuan, Ti, Teo) had been encouraged and helped me a lot to reach this point.

I gratefully acknowledge support from Centre National de la Recherche Scientifique (CNRS) during my Ph.D., funding from European Cooperation in Science and Technology (COST) for the opportunity to exchange at the University of Stavanger, and support from COSPAR Grants program for my attendance in COSPAR scientific assembly 2022 at Athen.

Abstract

Title: Simulations and associated data analysis for realistic LISA configuration

Gravitational Wave (GW) astronomy has provided a new window to investigate our Universe. In the effort to broaden the frequency band of GW observations, the Laser Interferometer Space Antenna (LISA) will be the first-ever space-based GW detector, aiming at detecting the GW signals from various astrophysical and cosmological sources in the band from 0.02 mHz to 1 Hz. LISA was chosen to be one of the large missions of the European Space Agency and it is one of the most complex space missions ever. It will consist of three spacecraft, separated by about 2.5 million kilometers, using laser interferometry to monitor the variation of the spacetime due to the passing GWs. For the success of the mission, we need to develop a simulator, associated data processing pipelines and robust data analysis methods to study the performance of the LISA instrument and the feasibility of extracting the information from various GW sources from the measured data.

The first goal of this thesis is to improve the current LISA simulator, namely `LISANode`, for simulating more realistic instrumental configurations. In particular, we have implemented new features in the simulator, related to instrumental noises contributing to the interferometric measurements with some options for correlation and non-stationarity.

Another contribution to `LISANode` concerns the dynamics of the instrument. The reference points for measuring the proper distance in spacetime, which contains the information of passing GWs, are the test-masses. The Drag-Free Attitude Control System (DFACS) will allow the test-masses to follow their geodesics along the sensitive axis of the interferometric measurement, while maintaining the positions and attitudes of the test-masses (in other directions) and spacecraft to keep them rigid to each other. The implementation and related study made during this thesis are on the realistic motion of the Moving Optical Sub-Assembly (MOSA), which hosts the test-mass in the spacecraft.

A study has been conducted about noise propagation through the instrument and the Time Delay Interferometry (TDI), which is the main algorithm used to suppress the dominant noise sources. We derived the analytical models for the propagation of different noises, in the

transfer functions for the power and cross-power spectral densities. These models have been validated with data generated with `LISANode`. The study of the noise propagation through TDI is also applied on experimental LISA-like data, such as LISA-On-Table.

The second goal of the thesis is to examine the data analysis method searching for GW signals. In particular, we focus on the Stochastic Gravitational Wave Backgrounds (SGWBs) that could be detected by LISA, either of cosmological origin or of astrophysical origin. The signal reconstruction from experimental data is challenging because of the possible confusion between the SGWBs and the instrumental noise. In this work, we use the `SGWBinner` code to study the simultaneous reconstruction of a Stochastic Gravitational Wave Background (SGWB) signal and the instrumental noise. Using the adapted instrumental noise model which we infer from the study of the LISA instrument and from the noise propagation through TDI, we improve the signal reconstruction for realistic data generated either with `LISANode` or with a data generation tool dedicated for SGWBs, `SGWB_data`.

Associated keywords: gravitational wave, LISA, TDI, simulation, LISANode, noise propagation, LISA Dynamics, SGWB

Résumé

Titre: Simulations et analyse des données associées pour une configuration réaliste de LISA

L'astronomie des ondes gravitationnelles (OG) a ouvert une fenêtre réaliste et prometteuse pour étudier notre Univers. Afin d'élargir la bande des fréquences d'observation des ondes gravitationnelles, l'antenne spatiale à interféromètre laser (LISA) a été conçue pour être le tout premier détecteur spatial d'ondes gravitationnelles, visant à détecter les signaux d'ondes gravitationnelles provenant de diverses sources astrophysiques et cosmologiques dans la bande allant de 0,02 mHz à 1 Hz. LISA sera composé de trois vaisseaux spatiaux, séparés par environ 2,5 millions de kilomètres, qui utiliseront l'interférométrie laser pour surveiller la variation de l'espace-temps due au passage des ondes gravitationnelles. Le développement du simulateur LISA, du pipeline de traitement de données associé et du pipeline d'analyse des données est essentiel pour étudier les performances de l'instrument LISA et la faisabilité de l'extraction de différentes sources d'OG à partir des données de mesure.

Le premier objectif de cette thèse est de développer le simulateur LISA actuel, à savoir LISANode, pour une configuration instrumentale plus réaliste. En particulier, nous avons implémenté de nouvelles fonctionnalités dans le simulateur liées aux bruits instrumentaux contribuant aux mesures interférométriques avec quelques options pour la corrélation et la non-stationnarité.

En outre, une étude sur la propagation du bruit à travers la conception de l'instrument et l'interférométrie à retardement (TDI), qui est le principal algorithme pour supprimer le bruit de fréquence laser dominant, a été menée pour vérifier les performances de la simulation instrumentale. Il s'avère que les modèles analytiques pour la propagation TDI de différents bruits sont validés avec les densités spectrales de puissance calculées à partir des données simulées par LISANode. L'étude de la propagation du bruit est également utile pour tester les performances de certaines données expérimentales de type LISA, telles que LISA-On-Table.

L'une des technologies clés pour le succès de la mission LISA est le système de contrôle d'attitude sans traînée (DFACS). Il permettra aux test-masses, qui jouent le rôle de point de

référence pour la mesure de la distance propre dans l'espace-temps, de suivre leurs géodésiques le long de l'axe sensible à la mesure interférométrique tout en maintenant les positions et les attitudes des test-masses (dans d'autres directions) et du vaisseau spatial pour qu'ils restent rigides les uns par rapport aux autres. Une partie de cette thèse contribue à l'implémentation de la dynamique de LISA dans LISANode, en particulier pour le mouvement plus réaliste du Moving Optical Sub-Assembly (MOSA), qui contient la masse test, dans le vaisseau spatial. Nous montrons que l'impact du mouvement du MOSA peut avoir des effets sur la performance du DFACS.

Le deuxième objectif de la thèse est d'examiner la méthode d'analyse des données pour la recherche des signaux OG. En particulier, nous nous concentrons sur les fonds stochastiques d'ondes gravitationnelles (SGWBs) qui pourraient être détectés par LISA, qu'il s'agisse de sources cosmologiques ou astrophysiques. La reconstruction du signal des fonds stochastiques d'ondes gravitationnelles à partir de données expérimentales est difficile en raison des diverses composantes qui peuvent contribuer au signal, et des bruits instrumentaux, qui peuvent être confondus avec le signal même. Dans notre travail, nous utilisons l'outil SGWBinner pour étudier la reconstruction simultanée du signal SGWB et du bruit instrumental. Avec le modèle de bruit instrumental adapté que nous avons developpé avec de l'étude de l'instrument LISA et de la propagation du bruit à travers TDI, nous pouvons obtenir une meilleure reconstruction du signal en utilisant les données simulées plus réalistes de LISANode et d'un autre outil de génération de données, SGWB_data.

Mot-clef associés: onde gravitationnelle, LISA, interférométrie, retardée (TDI), simulation, LISANode, propagation du bruit, dynamique de LISA, fond stochastique d'ondes gravitationnelles (SGWB)

Résumé substantiel

Titre: Simulations et analyse des données associées pour une configuration réaliste de LISA

L'astronomie des ondes gravitationnelles a ouvert une fenêtre réaliste et prometteuse pour étudier notre Univers. Afin d'élargir la bande de fréquence d'observation des ondes gravitationnelles, l'antenne spatiale à interféromètre laser (LISA) a été conçue pour être le tout premier détecteur spatial d'ondes gravitationnelles, visant à détecter les signaux d'ondes gravitationnelles provenant de diverses sources astrophysiques et cosmologiques dans la bande allant de 0,02 mHz à 1 Hz. LISA a été sélectionné comme l'une des principales missions de l'Agence spatiale européenne, et le début de son exploitation est prévu pour le milieu des années 2030. LISA est l'une des missions spatiales les plus complexes jamais entreprises. Elle consistera en trois engins spatiaux, séparés par environ 2,5 millions de kilomètres, qui utiliseront l'interférométrie laser pour mesurer les variations de l'espace-temps due au passage des ondes gravitationnelles. Le développement du simulateur LISA et des chaînes de traitement et d'analyse des données est essentiel pour étudier les performances de l'instrument LISA et la faisabilité de l'extraction de différentes sources d'onde gravitationnelle à partir des mesures. Une simulation aussi réaliste que possible est nécessaire pour tester le design de LISA et la validation de ses performances et pour développer des méthodes d'analyse des données appropriées.

Le premier objectif de cette thèse est de contribuer au développement du simulateur actuel de LISA, à savoir LISANode, pour une configuration instrumentale plus réaliste. En particulier, nous avons implémenté de nouvelles fonctionnalités liées aux bruits instrumentaux dans les mesures interférométriques avec des options pour la corrélation et la non-stationnarité. L'impact de ces caractéristiques réalistes dans la propagation du bruit et l'analyse des données a pu être examiné avec ces données simulées.

En outre, une étude sur la propagation du bruit à travers l'instrument et l'interférométrie retardée (TDI), qui est le principal algorithme pour supprimer le bruit de fréquence laser dominant, a été menée. Les modèles analytiques pour la propagation TDI de différents bruits sont validés avec les densités spectrales de puissance calculées à partir des données simulées par LISANode. L'étude de la propagation du bruit est également utile pour tester les performances

de certaines données expérimentales de type LISA, telles que les données de l'expérience LISA-On-Table.

L'une des technologies clés pour le succès de la mission LISA est le système de contrôle d'attitude et de maintien de la chute libre (DFACS). Il permettra aux test-masses, qui jouent le rôle de point de référence pour la mesure de la distance propre dans l'espace-temps, de suivre leurs géodésiques le long de l'axe sensible à la mesure interférométrique tout en maintenant les positions et les attitudes des test-masses (dans d'autres directions) et du vaisseau spatial pour qu'ils restent rigides les uns par rapport aux autres. Une partie de cette thèse contribue à l'implémentation de la dynamique de LISA dans LISANode, en particulier pour le mouvement plus réaliste du sous-ensemble optique mobile (MOSA), qui contient la masse test, dans le vaisseau spatial. Nous montrons que l'impact du mouvement du MOSA peut avoir des effets sur la performance du DFACS.

Le deuxième objectif de la thèse est d'examiner la méthode d'analyse des données pour la recherche des signaux d'ondes gravitationnelles. En particulier, nous nous concentrons sur les fonds stochastiques d'ondes gravitationnelles (SGWBs) qui pourraient être détectés par LISA, qu'il s'agisse de sources cosmologiques ou astrophysiques. La reconstruction du signal des fonds stochastiques d'ondes gravitationnelles à partir de données expérimentales est difficile en raison des diverses composantes qui peuvent contribuer au signal, et des bruits instrumentaux, qui peuvent être confondus avec le signal même. Dans notre travail, nous utilisons l'outil SGWBinner pour étudier la reconstruction simultanée du signal SGWB et du bruit instrumental. Avec le modèle de bruit instrumental adapté que nous avons développé par l'étude de l'instrument LISA et de la propagation des bruits dans TDI, nous pouvons obtenir une reconstruction du signal. Cette reconstruction a été utilisée sur des données simulées réalistes de LISANode et sur celles généré par un autre outil de génération de données, SGWB_data.

Cette thèse est organisée en sept chapitres. Le premier chapitre donne une introduction aux ondes gravitationnelles. Nous revisitons le cadre théorique des ondes gravitationnelles dans la théorie de la relativité générale, ainsi que leurs propriétés. Nous abordons ensuite l'idée de détecter les ondes gravitationnelles et passons en revue certains détecteurs actuels et futurs ainsi que leurs techniques de détection. Dans la dernière partie de ce chapitre, nous présentons plusieurs sources de rayonnement gravitationnel et leur détectabilité par les détecteurs actuels et futurs, notamment la mission LISA. Les fonds stochastiques d'ondes gravitationnelles sont discutés plus en détail car nous nous concentrons principalement sur ce type de source dans notre étude au chapitre 6.

Le chapitre 2 présente l'architecture de LISA, notamment la configuration actuelle de la constellation, son concept de mesure et un aperçu de sa charge utile. Nous passons également

en revue le système de mesure et d'interférométrie DFACS, qui est essentiel pour notre étude dans les chapitres suivants, avant de passer en revue les bruits instrumentaux dans LISA. Ce chapitre présente également un modèle instrumental de la configuration actuelle de LISA. Ce modèle est implémenté dans un simulateur LISANode. Dans la philosophie de LISANode, une simulation peut être représentée comme un graphe, qui est construit en connectant plusieurs nœuds ou sous-graphes. De cette façon, un graphe complexe peut être construit pour s'adapter au développement instrumental de la mission LISA. Dans la dernière section du chapitre 3, nous présentons l'architecture logicielle de LISANode et notre contribution à son développement avec l'implémentation de bruits corrélés et non-stationnaires.

Le chapitre 3 se concentre sur TDI. Tout d'abord, nous présentons une version du pipeline initial de réduction du bruit, qui est une chaîne de traitement des données visant à réduire les sources de bruit les plus dominantes dans les données brutes de LISA afin de fournir des données utilisables à des fins scientifiques. TDI est une étape crucial de ce pipeline. Nous discutons ensuite du principe de TDI pour éliminer le bruit de fréquence laser et donnons la formulation de TDI. La dernière section de ce chapitre présente une étude de la réduction du bruit avec TDI dans des données expérimentales avec le simulateur LISA-On-Table. Nous présentons brièvement LISA-On-Table, un simulateur électro-optique de LISA, puis nous examinons les performances de l'algorithme dans la réduction du bruit de fréquence laser sur des données générées par ce simulateur dans différentes configurations.

Le chapitre 4 présente le résultat principal de l'étude de la propagation du bruit à travers TDI. Nous introduisons d'abord une méthodologie de calcul des spectres de puissance à partir des variables TDI, qui peut être appliquée de manière générale à la propagation de tout bruit secondaire LISA. Quelques exemples de calculs de fonctions de transfert TDI sont discutés avant de résumer les résultats de propagation pour la plupart des bruits secondaires LISA. En outre, nous examinons les caractéristiques réalistes de la configuration LISA dans la propagation du bruit, y compris les impacts du schéma de verrouillage du laser et des corrélations du bruit. Nous validons ensuite le modèle analytique de bruit en comparant sa formulation avec les spectres de puissance estimés à partir des données simulées avec le simulateur LISANode.

Le chapitre 5 traite du travail sur l'implémentation de LISA Dynamics dans le simulateur LISANode. Nous donnons d'abord un aperçu des cadres de référence et des équations qui décrivent la dynamique des cibles LISA (c'est-à-dire la masse d'essai, le MOSA, le vaisseau spatial). Ces équations sont cruciales pour l'implémentation de la dynamique de LISA dans LISANode, qui est discutée dans la section suivante du chapitre. Pour simplifier l'implémentation, nous linéarisons les équations du mouvement et les exprimons dans la représentation de l'espace d'état. Nous examinons ensuite la version de LISANode pour le cas d'une configuration fixe de MOSAs avant de modifier le code pour l'adapter à un cas simplifié de MOSAs en rotation. Enfin, nous montrons les résultats de cette implémentation dans

LISANode.

Une étude de la recherche de SGWBs est décrite dans le chapitre 6. Nous présentons deux pipelines de génération possibles pour les données simulées en utilisant différents outils de simulation, à savoir SGWB_data et LISANode. Ce dernier pipeline avec le simulateur LISANode est plus intéressant pour nous car il fournit les données en séries temporelles avec des caractéristiques réalistes telles que le bruit corrélé et/ou non stationnaire. Comme la connaissance du bruit instrumental est essentielle pour cette étude, nous discutons en détail le modèle de bruit utilisé dans le pipeline de génération et d'analyse des données. Le modèle de bruit de base habituel pour l'analyse des données LISA provient du LISA Science Requirement Document. Cependant, un terme supplémentaire doit être ajouté dans le modèle de bruit pour tenir compte de la propagation précise du bruit TDI dans le système de métrologie optique, selon notre étude présentée au chapitre 4. Nous utiliserons ce modèle de bruit modifié pour générer les données de l'étude. Nous discutons également de certains modèles de SGWBs et d'un modèle pour l'avant-plan galactique. Ensuite, nous passons en revue une méthodologie d'analyse de nos données, utilisant la reconstruction dans de multiples intervalles de fréquence par les codes SGWBinner, pour extraire un SGWB arbitraire étant donné un modèle de bruit. Cette analyse est basée sur une méthode bayésienne. Comme ces variables sont quasi-orthogonales, les données utilisées dans l'analyse sont les spectres de puissance des variables TDI AET des simulateurs LISA pour éviter la corrélation croisée. Les données du canal TT sont utilisées pour redéfinir les apriori de bruit avant de les appliquer dans l'analyse SGWB pour les canaux AA et EE, qui sont plus sensibles aux ondes gravitationnelles. Enfin, nous présentons les résultats de plusieurs analyses en exécutant SGWBinner sur des données simulées, y compris le cas de l'utilisation de différents modèles de bruit dans la génération des données et dans l'analyse des données.

Le dernier chapitre donne les conclusions et les études futures sur les sujets traités dans cette thèse.

Mot-clef associés: onde gravitationnelle, LISA, interférométrie, retardée (TDI), simulation, LISANode, propagation du bruit, dynamique de LISA, fond stochastique d'ondes gravitationnelles (SGWB)

Contents

List of Figures

List of Tables

Chapter 1

Gravitational wave astronomy

In this chapter, we give an overview of gravitational waves (GWs) from the point of view of both theory and experiment. The first section addresses the theoretical framework of the GWs, including their derivation from General Relativity theory and their effect on matter. In the second section, we introduce the principle of GW detection and review some current and future detectors contributing to the GW astronomy. The last section gives brief descriptions for some GW radiation sources, mainly those that are detectable by the future space-based detector Laser Interferometer Space Antenna (LISA). In the scope of this thesis, we will focus on the stochastic gravitational wave backgrounds.

1.1 Gravitational waves

This section briefly presents the fundamental physics behind the GWs and their properties. The material presented in this chapter is based on the references [109, 133, 56]. In those references, ones can find detailed explanations and proofs for the mathematical treatment presented in this section.

1.1.1 Limitations of Newtonian theory of gravity

Although the gravitational force in Newton's Law of Universal Gravitation can explain the physics of various phenomena with great precision, it cannot explain some astronomical observations, for example, the precession of the perihelion of Mercury.

In addition, the causality of the gravitational interaction has been questioned for a long time, even by Newton himself. Newton's equation indicates that the gravitational force instantaneously affects two massive objects at any distance without mediation. Newton was also puzzled, as he wrote [116]: "It is inconceivable that inanimate brute matter should, without the mediation of something else which is not material, operate upon and affect other matter

without mutual contact... That one body may act upon another at a distance through a vacuum without the mediation of anything else, by and through which their action and force may be conveyed from one another, is to me so great an absurdity that, I believe, no man who has in philosophic matters a competent faculty of thinking could ever fall into it."

Furthermore, Newton put the origin of gravitation aside by his famous dictum "hypotheses non fingo". The relevant passage in [117], English translation of 1729 by Francis Motte, was: "I have not been able to discover the cause of those properties of gravity from phenomena, and I frame no hypotheses; for whatever is not deduced from the phenomena is to be called a hypothesis, and hypotheses, whether metaphysical or physical, whether of occult qualities or mechanical, have no place in experimental philosophy."

Several theories were proposed to explain the origin of gravitation. In some theories, the gravitational interaction is propagated via some form of mediation, such as the *aether*. However, none was proven to be the correct one. The experiments built by Michelson et al. to measure the velocity of the aether relative to the Earth's rotation proved that there was no such mediation [137].

Interestingly, those experiments also indicated that the speed of light is constant relative to any inertial reference frame, which is one of two postulates of the Special Relativity theory proposed by A.Einstein [64]. Following the development of Special Relativity, Einstein found General Relative theory [62], which applies not only to inertial frames but also to non-inertial ones, e.g. accelerated frames. In the context of General Relativity, gravitation is interpreted as the curvature of spacetime, which depends on the mass and energy of the matter content.

1.1.2 General Relativity

In General Relativity theory, the 3 space dimensions and the time are treated equally and combined into a 4-dimensional set called spacetime. An individual point in spacetime is called an *event*, expressed in (t, x, y, z). In flat spacetime, the interval or proper distance between any two events is defined by

$$ds^2 = -cdt^2 + dx^2 + dy^2 + dz^2, \tag{1.1}$$

where c is the speed of light. In the general case, we can use the definition of the metric tensor and the geometrized units, in which $c = 1$, to rewrite this equation as

$$ds^2 = g_{\mu\nu} dx^\mu dx^\nu, \tag{1.2}$$

where x^μ indicates t, x, y, z for μ running from 0 to 3, $g_{\mu\nu} = \eta_{\mu\nu} = \mathrm{diag}(-1, 1, 1, 1)$ is Minkowski metric in the case of flat spacetime. The formula uses the Einstein summation convention, i.e. duplicated indices in superscripts and subscripts are sum over.

In the presence of a massive object or energy, spacetime is no longer flat, and the interval cannot be defined by the Minkowski metric. Instead, we need to compute the metric tensor $g_{\mu\nu}$ from the curvature of spacetime. That curvature drives the motion of a test particle around the object. Any test particle will follow a free-falling trajectory in the curved spacetime in the shortest distance path, called *geodesic*. This geodesic is not a straight line in the curved spacetime. With this toolset, we can interpret the motion of a test particle around a massive object by classical gravitational force as its geodesics in the curved spacetime. The gravitational interaction is given by the curvature of spacetime locally. Therefore, it is no longer considered an instantaneous interaction. General Relativity also predicts that the speed of the propagation of the interaction is identical to the speed of light, as we will derive later. The means of the propagation of the gravitation interaction, i.e. gravitational waves, is an analogy of electromagnetic waves in the electromagnetic interaction [63]. To summarise this correlation between spacetime and gravitation, we use the paraphrase of John Wheeler's quote: "The matter defines the curvature of spacetime, and spacetime tells the matter how to move."

Using this theory, one can explain and compute the precession of the perihelion of Mercury with the highest precision. The theory has also been tested by several astronomical observations, such as the bending of light from a far-away star when it travels nearby the Sun. Furthermore, the gravity theory's causality problem is also solved since the speed of gravitational interaction is now limited, equal to the speed of light, as we will see later. The gravitational waves were also predicted but not observed at that time. About 100 years later, this prediction of Einstein's theory of gravity was confirmed by direct detection. Nevertheless, we are looking for more tests to challenge the correctness of General Relativity and many modified theories of gravity, which have been developed to explain more phenomena such as the accelerated expansion of the Universe.

To express the curvature of spacetime mathematically, we first define Christoffel's symbols from the covariant derivative ∇_μ of a vector field V^ν, given as:

$$\nabla_\mu V^\nu = \partial_\mu V^\nu + \Gamma^\nu_{\mu\sigma} V^\sigma \tag{1.3}$$

$$\Gamma^\lambda_{\mu\nu} = \frac{1}{2} g^{\lambda\sigma} \left(\partial_\mu g_{\nu\sigma} + \partial_\nu g_{\sigma\mu} - \partial_\sigma g_{\mu\nu} \right). \tag{1.4}$$

The covariant derivative is a generalization of the total derivative in the 4-dimensional spacetime, which gives the connection relating vectors in the tangent spaces of nearby points [56]. Conventional General Relativity uses the Christoffel connection or Levi-Civita connection. The derivation of this symbols uses the two specific properties: torsion-free $\Gamma^\lambda_{\mu\nu} = \Gamma^\lambda_{\nu\mu}$ and metric compatibility $\nabla_\rho g_{\mu\nu} = 0$.
Then, we compute the Riemann tensor from the Christoffel symbols as

$$R^\alpha_{\beta\mu\nu} := \partial_\mu \Gamma^\alpha_{\beta\nu} - \partial_\nu \Gamma^\alpha_{\beta\mu} + \Gamma^\alpha_{\sigma\mu} \Gamma^\sigma_{\beta\nu} - \Gamma^\alpha_{\sigma\nu} \Gamma^\sigma_{\beta\mu}. \tag{1.5}$$

Riemann tensor of a flat spacetime is null, $R^{\alpha}_{\beta\mu\nu} = 0$. In the study of the curvature of spacetime, we also use Riemann tensor contraction, called Ricci tensor, defined as:

$$R_{\alpha\beta} := R^{\lambda}_{\alpha\lambda\beta}, \tag{1.6}$$

and similarly Ricci scalar reads:

$$R := g^{\mu\nu} R_{\mu\nu}. \tag{1.7}$$

With these mathematical objects, we can write down the field equations for General Relativity, called Einstein's field equations,

$$R^{\alpha\beta} - \frac{1}{2} R g^{\alpha\beta} + \Lambda g^{\alpha\beta} = \kappa T^{\alpha\beta}. \tag{1.8}$$

There are 10 coupled differential equations extracted from Eq.(1.9), instead of 16 because $R^{\alpha\beta}, g^{\alpha\beta}, T^{\alpha\beta}$ are symmetric. We can solve these equations to get metric tensor $g_{\mu\nu}$ for a given matter content encoded in the stress-energy tensor $T^{\mu\nu}$. Constant κ can be determined by matching Einstein's field equations with Newtonian's gravitational field equations so that General Relativity can capture the physics of classical gravity theory. The constant Λ remains arbitrary. Historically, this constant was introduced in the first version of Einstein's field equations to ensure a solution for a static Universe. It was then removed due to the observation of expanding Universe discovered by Hubble. Finally, it was reinstated to explain the accelerated expansion of the Universe. Here, we neglect the constant Λ and use the geometrized units, $c = G = 1$, to get the form of Einstein's field equations as follows:

$$R^{\alpha\beta} - \frac{1}{2} R g^{\alpha\beta} = 8\pi T^{\alpha\beta}. \tag{1.9}$$

Since the $g_{\mu\nu}$ are the components of the metric tensor in some coordinate system, 4 degrees of freedom among 10 $g_{\mu\nu}$ can be fixed by the choice of the reference frame as the equations (1.9) are coordinate-invariant. Therefore, there are only 6 dependent differential equations to be solved to characterize spacetime geometry independently on the coordinates.

1.1.3 Solution of Einstein's field equations in weak-field regime: Gravitational Waves

Einstein's field equations are non-linear: the Ricci tensor and scalar include the second derivatives of the metric tensor. Therefore, solving these equations is challenging. In fact, very few cases provide the exact analytical solutions, for example the Schwarzschild metric describing a non-rotating spherical black hole and the Friedmann–Lemaître–Robertson–Walker metric to describe a homogenous isotropic and expanding Universe. Even in the case in vacuum, to describe the gravitational waves propagating on spacetime far away from the source, which is indicated by $T^{\mu\nu} = 0$, the solutions are not easily worked out.

The absence of matter leads to a flat spacetime. A weak gravitational fields curves spacetime to be *nearly* flat. Therefore, we can use perturbation approach to solve the Einstein's field equations in the weak gravitational field regime. In particular, one can find coordinates for which the metric tensor is given by:

$$g_{\mu\nu} = \eta_{\mu\nu} + h_{\mu\nu}, \tag{1.10}$$

where $|h_{\mu\nu}| \ll 1$ is the pertubation of the flat Minkowski metric $\eta_{\mu\nu} = \text{diag}(-1, 1, 1, 1)$.

Expanding equation (1.9) at first order in $h_{\mu\nu}$, and using the trace-reversed perturbation

$$\bar{h}^{\alpha\beta} := h^{\alpha\beta} - \frac{1}{2}\eta^{\alpha\beta}h_{\mu\nu}g^{\mu\nu}, \tag{1.11}$$

we could obtain:

$$\Box\bar{h}_{\mu\nu} + \eta_{\mu\nu}\partial^\rho\partial^\sigma\bar{h}_{\rho\sigma} - \partial^\rho\partial_\nu\bar{h}_{\mu\rho} - \partial^\rho\partial^\mu\bar{h}_{\nu\rho} = -16\pi T_{\mu\nu}. \tag{1.12}$$

where $\Box$ is the D'Alambertian or wave operator,

$$\Box f = \eta^{\mu\nu}\partial_\mu\partial_\nu f = \left(-\frac{\partial^2}{\partial t^2} + \nabla^2\right) f = \left(-\frac{\partial^2}{\partial t^2} + \frac{\partial^2}{\partial x^2} + \frac{\partial^2}{\partial y^2} + \frac{\partial^2}{\partial z^2}\right) f. \tag{1.13}$$

We can further simplify equation (1.12) by choosing *Lorenz gauge*[56] for the coordinate frame, in which

$$\partial^\nu\bar{h}_{\mu\nu} = 0, \tag{1.14}$$

and then the Einstein's field equations take the *linearized theory* form

$$\Box\bar{h}_{\mu\nu} = -16\pi T_{\mu\nu}. \tag{1.15}$$

The equation describing gravitational waves far away from the source is the homogeneous equation deduced from (1.15) by choosing $T^{\mu\nu} = 0$:

$$\left(-\frac{\partial^2}{\partial t^2} + \nabla^2\right)\bar{h}_{\mu\nu} = 0. \tag{1.16}$$

This equation is a wave equation with speed of propagation equal to the speed of light, $c = 1$ in our conventions. The solution of (1.16) is the superposition of monochromatic plane waves of the form

$$\bar{h}^{\alpha\beta} = A^{\alpha\beta}\exp(ik_\mu x^\mu), \tag{1.17}$$

where $A^{\alpha\beta}$ is the wave amplitude, and k_μ is the wave vector. One can show that k_μ is a null four-vector, $k_\mu k^\mu = 0$, tangent to the photon worldline.

Within the Lorentz class of gauges (1.14), we can further use the gauge freedom to restrict the degrees of freedom of $A^{\alpha\beta}$ as

$$A^\mu{}_\mu = g_{\mu\nu}A^{\mu\nu} = 0 \quad \text{and} \quad A^{\mu\nu}k_\nu = 0. \tag{1.18}$$

These constraints together are called the *transverse-traceless* (TT) gauge conditions. The first equation in (1.18) implies $\bar{h}^{TT}_{\mu\nu} = h^{TT}_{\mu\nu}$ so that we can omit the bar notation on trace-reversed perturbation from now on. From these conditions, we can translate to the constraints on the perturbation $h^{\alpha\beta}$ in TT-gauge as follows:

$$h^i{}_i = 0, \qquad \partial_i h^{ij} = 0, \qquad h^{0\mu} = 0 \tag{1.19}$$

Hence, we have only 2 independent components remaining for $A^{\alpha\beta}$, which represent the physical degrees of freedom of GWs and later we will see that they are associated with the polarization of GWs. One should notice that the TT-gauge choice is a consequence of the gauge invariance of the Einstein's field equations (1.9). In the other word, the physics does not change in another reference frame, and the TT-frame is used just because it is convenient in order to extract the physical information of the gravitational waves, e.g. their polarization[1]. We can choose coordinates so that a GW propagates along the z direction $k^\mu = (\omega, 0, 0, \omega)$, where ω is the angular frequency of the GW. Then the solution of the gravitational wave equations (1.16) in transverse-traceless frame is given by

$$h^{TT}_{\mu\nu}(t, z) = \begin{pmatrix} 0 & 0 & 0 & 0 \\ 0 & h_+ & h_\times & 0 \\ 0 & h_\times & -h_+ & 0 \\ 0 & 0 & 0 & 0 \end{pmatrix} \cos\left[\omega(t - z)\right] \tag{1.20}$$

where $h_+, h_\times$ are the polarization states of the GW with the basis formed by unit vectors $(\hat{\mathbf{u}}, \hat{\mathbf{v}})$ living in the plane perpendicular to the wave propagation direction, i.e. the z-axis. The tensor basis for $A_{\mu\nu}$ is:

$$e^+_{ij} = \hat{\mathbf{u}}_i\hat{\mathbf{u}}_j - \hat{\mathbf{v}}_i\hat{\mathbf{v}}_j = \begin{pmatrix} 1 & 0 & 0 \\ 0 & -1 & 0 \\ 0 & 0 & 0 \end{pmatrix} \quad ; \quad e^\times_{ij} = \hat{\mathbf{u}}_i\hat{\mathbf{v}}_j + \hat{\mathbf{u}}_j\hat{\mathbf{v}}_i = \begin{pmatrix} 0 & 1 & 0 \\ 1 & 0 & 0 \\ 0 & 0 & 0 \end{pmatrix}. \tag{1.21}$$

1.1.4 Effect of gravitational waves

Here, we examine the effect of GW on matter. Consider a free particle initially at rest in TT-gauge, it obeys the geodesic equation [133]:

$$\frac{d}{d\tau}U^\alpha + \Gamma^\alpha{}_{\mu\nu}U^\mu U^\nu = 0, \tag{1.22}$$

where $U^\alpha = \frac{dx^\alpha}{d\tau}$ is four-vector velocity, τ is the proper time. Since the particle is initially at rest $U^i_{\tau=0} = 0$, its initial acceleration is

$$\left.\frac{dU^i}{d\tau}\right|_{\tau=0} = -\left[\Gamma^i_{00}\frac{dt}{d\tau}\frac{dt}{d\tau}\right]_{\tau=0}. \tag{1.23}$$

[1]The TT-gauge cannot be chosen in the vicinity of the source, but we still have two polarization states for the GW in general [68].

In TT-gauge reference frame, (1.19), we have

$$\Gamma^i_{00} = \frac{1}{2} h^{i\mu} \left(2\partial_0 h_{0\mu} - \partial_\mu h_{00}\right) = 0. \tag{1.24}$$

This result indicates that the particle initially at rest will remain at rest forever regardless of the passing gravitational waves. This is an artifact of the TT-gauge: the coordinates are chosen so that they wiggle in spacetime as the GW is passing, and the initially at rest particle remains attached to the same point in the coordinates. However, to access the physical information, we need to look into some coordinate-invariant quantities, for instance the proper distance (1.2) between the two particles. In the setting leading to equation (1.20), the proper distance reads

$$\begin{aligned} ds^2 &= g_{\mu\nu} dx^\mu dx^\nu = \left(\eta_{\mu\nu} + h^{TT}_{\mu\nu}\right) dx^\mu dx^\nu \\ &= -dt^2 + dz^2 + \left\{1 + h_+ \cos\left[\omega(t-z)\right]\right\} dx^2 \\ &\qquad + \left\{1 - h_+ \cos\left[\omega(t-z)\right]\right\} dy^2 + 2h_\times \cos\left[\omega(t-z)\right] dxdy. \end{aligned} \tag{1.25}$$

From the above expression, we see that the effect of the h_+ polarization state is on the x, y directions of the plane perpendicular to the gravitational wave propagation vector, and GW will stretch and contract spacetime in both directions in returns. On the other hand, $h_\times$ changes spacetime in the cross term of the two directions x, y. This effect is similar to the h_+ one, if we rotate the coordinates of x, y by an angle of $\pi/4$. That justifies our initial notations for the two polarization states of GW. The illustration of the two polarization states of GW is shown in figure 1.1.

Let's consider that one particle is initially at rest at the origin of the coordinate system, and a similar one is at the location $(\epsilon, 0, 0)$ nearby the first one. The coordinate distance between the two particles is constant, $\triangle x = \epsilon$, in the TT-frame even with a passing GW. Assuming that the coordinate distance ϵ between the two particles is very small, one can obtain (see for example section 9.1 in [133] for a detailed derivation):

$$\Delta s \equiv \int |ds^2|^{1/2} \approx \epsilon \sqrt{1 + h_+ \cos(\omega t)} \approx \epsilon \left(1 + \frac{1}{2} h_+ \cos(\omega t)\right), \tag{1.26}$$

where the final equality is the Taylor expansion with $h_+ \ll 1$. It appears that the proper distance varies with time as the GW passes. Therefore, one can measure the proper distance between two test particles following their geodesics in spacetime to detect GWs. This is the theoretical idea behind the experimental measurement of GW experimentally that we introduce in the next section. The equation (1.26) also indicates that the effect of GW on the proper distance is proportional to the initial separation between the test particles. The bigger the initial distance is, the bigger proper distance changes due to the passage of GWs.

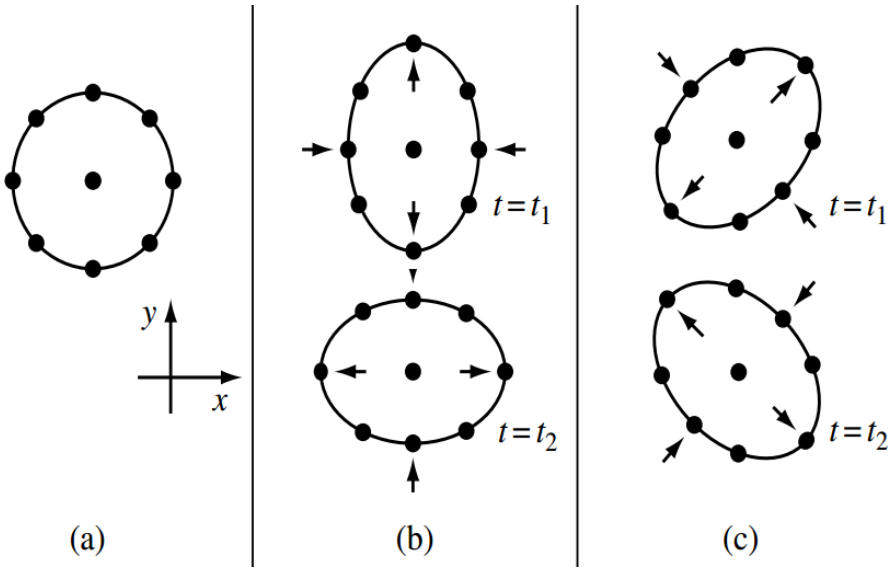

Figure 1.1: Illustration for the effect of a GW on a circle of test particles, taken from [133]. (a) The initial circle of test particles before the GW traveling along z-axis reaches it. (b) The distortion of the circle by the effect of the h_+-polarization state of the GW, in two pictures for different times corresponding to two phases of the GW separated by 180^o. (c) Similar as (b) for the $h_\times$-polarization of the GW.

Therefore, GW detectors are huge devices, in order to maximize the effect of GW[2]. Last but not least, the effect is extremely small because of the tiny perturbation of spacetime due to GWs. The typical GW amplitude observed by detectors on Earth is of the order of $h_{+/\times} < 10^{-20}$. Therefore, one needs extremely sensitive detectors in order to search for the GWs, and to deal with potential noises which can blur such tiny amplitude signals.

1.2 Gravitational wave detection

1.2.1 General overview

Although many achievements have been obtained in astronomy with electromagnetic waves, as the observable spectrum band broadened with decades, there are some events in the Universe which cannot be observed with electromagnetic detectors.

Gravitational waves can open a new window for astronomy, since a large fraction of astrophysical and cosmological events/objects can emit these signals. According to the current astronomical observations, only 4% of the mass-energy of the Universe is in charged particles that can emit or absorb electromagnetic waves, and the remaining 96% cannot radiate electro-

[2]Note that, in our derivation of (1.26), we assume that the initial separation between the two particles is small enough for the metric tensor not to change significantly. Hence, this equation is not always valid to characterize precisely the measurements in GW detectors.

magnetic signals. However, all these objects are coupled by gravity, and some of them could radiate GWs. With the observation of GWs, we can enrich our knowledge of the Universe, either finding unknown and unexpected events/objects, or investigating already known ones, or testing the theory of gravity, Etc. Moreover, gravitational waves can carry information that the electromagnetic ones cannot, since GWs are hardly influenced by matter during their propagation. Consequently, GWs can give us the chance to look deeper into the history of the Universe in the early times before the recombination epoch, which is not observable with electromagnetic waves.

In order to directly detect the tiny effect of GWs, two types of detectors have been developed: bars and interferometers. The bar detectors are based on the resonance effect on solid masses that are influenced by the incoming GW. However, the interferometric detectors have better sensitivity so that we will not discuss bar detectors in detail in this thesis. On the other hand, we will briefly introduce pulsar timing, which is searching GWs at very low frequency band. In the following, we will present the principles of GW detectors, and some of their representatives.

1.2.2 Measuring distances with light

As we have discussed in section 1.1, the effect of a passing GW is the variation of the proper distance between particles in spacetime. We can use this effect to detect GWs. In particular, we can use light to measure the distance between two free-falling test particles, which are following their own geodesics in spacetime. By measuring the time of arrival of electromagnetic signals, e.g. laser beam, from one particle to the second one, one can monitor the effect of the passage of GWs on the variation of the light time of arrivals.

The detailed derivation of the variation of the time of arrival due to the passage of GW can be found, for example, in chapter 9.2 of [133]. We examine a laser beam sent from a test particle at the origin of a TT-gauge reference frame to another one separated from the first by a distance L, and returning back to the origin, during the passage of a gravitational wave. Considering only the h_+ polarization, as in equation (1.26), the differential (the rate of change) of the time of arrival w.r.t. the time of emission reads:

$$\frac{dt_{\text{return}}}{dt_{\text{start}}} = 1 + \frac{1}{2}\left[h_+(t_{\text{start}} + 2L) - h_+(t_{\text{start}})\right], \tag{1.27}$$

where t_{start} is the time of the laser beam emission at the origin, and t_{return} is the time we receive it after propagating in the round trip[3]. The relation between the rate of change of the

[3] t_{start} is the time when the first crest of the electromagnetic wave of laser beam is emitted, and t_{return} is the time when crest returns back after the round trip.

time of arrival of the laser beam and its frequency, $\frac{dt_{\text{return}}}{dt_{\text{start}}} = \frac{\nu_{\text{return}}}{\nu_{\text{start}}}$, leads to the equation

$$\frac{\nu_{\text{return}} - \nu_{\text{start}}}{\nu_{\text{start}}} = \frac{h_+(t_{\text{start}} + 2L) - h_+(t_{\text{start}})}{2}, \tag{1.28}$$

where ν_{return}, ν_{start} are the frequencies of the laser beam at the reception and emission times, respectively. Therefore, we can detect the effect of GWs by measuring the change in frequency of a laser exchanging between the two test particles when they are following their own geodesics. This the detection principle is applied for most of the modern GW detectors.

The equation (1.28) can be expressed in a more general setting as shown in chapter 3.2.6 of [40]. In particular, one can consider a laser beam sent from one test particle to another one separated by a distance L, but the two particles are located in a generic coordinates. The sender point is $\vec{\mathbf{x}}_0(t_0)$ and the receiver one is $\vec{\mathbf{x}}_1(t_1)$, where t_0, t_1 are respectively the sending and receiving times. The unit vector linking the two particles is $\hat{\mathbf{n}}(t_1) = ||\vec{\mathbf{x}}_0(t_0) - \vec{\mathbf{x}}_1(t_1)||$. The relative fluctuation frequency attributed to the variation of the time of arrival due to the passage of a GW propagating along the unit vector $\hat{\mathbf{k}}$ is given by

$$\frac{\nu_{\text{return}}(t_1) - \nu_{\text{start}}(t_0)}{\nu_{\text{start}}(t_0)} \approx \frac{1}{2\left(\hat{\mathbf{k}} \cdot \hat{\mathbf{n}}(t_1)\right)} \left\{ H\left[t_1 - L - \hat{\mathbf{k}} \cdot \vec{\mathbf{x}}_0(t_0)\right] - H\left[t_1 - \hat{\mathbf{k}} \cdot \vec{\mathbf{x}}_1(t_1)\right] \right\}, \tag{1.29}$$

where $H(t)$ is the deformation of spacetime along the laser link induced by the passage of GW, given as

$$\begin{aligned} H(t) = &\left[h_+(t)\cos(2\psi(t)) - h_\times(t)\sin(2\psi(t))\right] \xi_+(\hat{\mathbf{u}}, \hat{\mathbf{v}}, \hat{\mathbf{n}}(t)) \\ &+ \left[h_+(t)\sin(2\psi(t)) + h_\times(t)\cos(2\psi(t))\right] \xi_\times(\hat{\mathbf{u}}, \hat{\mathbf{v}}, \hat{\mathbf{n}}(t)), \end{aligned} \tag{1.30}$$

where ψ is the polarization angle, and the antenna pattern functions $\xi_+, \xi_\times$ are defined within a right-handed system $(\hat{\mathbf{u}}, \hat{\mathbf{v}}, \hat{\mathbf{n}})$ as[4]

$$\xi_+(\hat{\mathbf{u}}, \hat{\mathbf{v}}, \hat{\mathbf{n}}) = (\hat{\mathbf{u}} \cdot \hat{\mathbf{n}})^2 - (\hat{\mathbf{v}} \cdot \hat{\mathbf{n}})^2, \tag{1.31}$$

$$\xi_\times(\hat{\mathbf{u}}, \hat{\mathbf{v}}, \hat{\mathbf{n}}) = 2\,(\hat{\mathbf{u}} \cdot \hat{\mathbf{n}})\,(\hat{\mathbf{v}} \cdot \hat{\mathbf{n}}). \tag{1.32}$$

1.2.3 Interferometer detectors

One possibility to detect GWs using the measurement principle presented previously is via spacecraft tracking [67]. The interplanetary spacecraft responds as the transponder to the radio signals sent from Earth. The signals received by the spacecraft are amplified and sent back to the ground tracking station on Earth. The measurement of the return time provides the distance between the spacecraft and the ground tracking station. Therefore, one can detect

[4] Remind that $\hat{\mathbf{n}}$ is the unit vector linking between the two test particles.

GWs by measuring the variation of the return time, as shown in Eq.(1.27). However, even assuming that one can solve practical issues in spacecraft tracking, such as discriminating the effects of GWs from the ones of light refraction in plasma and ionosphere, the clock stability can limit the accuracy of the measurement. In particular, the current best clock has stability of the level of 10^{-19}, while the amplitude of GWs, which we would like to detect on Earth, is of 10^{-20} or below.

In order to solve the problem of clock stability, one can use a Michelson interferometer, illustrated in figure 3.2. It is composed of a stable laser beam passing through a beam splitter which sends two half-power beams in two perpendicular arms. The two beams then have correlated phases. They travel along their arms and are reflected off mirrors at the end of the arms, then are brought back into the interferometer. The interference allows to measure the difference between the two armlengths so one can detect GWs that stretch and contract the distances, as shown in Eq.(1.26) for the h_+ polarization. In the interferometer detector, one of the two beams effectively plays the role of clock reference to perform the measurement of the light arrival time, so the limitation of the clock stability can be solved. On the other hand, the laser frequency fluctuations lead to a noise, called laser frequency noise, in the interferometric measurement. If the two arms of the interferometer have the same or almost equal lengths, the laser frequency noise is significantly suppressed in the interferometer. We will discuss this noise and its reduction further in section 3.2.1.

1.2.4 Inteferometric observatories

Interferometric detectors are currently the most sensitive instruments in operation to search for GWs. Ground-based interferemeters are the Laser Interferemeter Gravitational Wave Observatory (LIGO), Virgo (Virgo), and Kamioka Gravitational Wave Detector (KAGRA). LIGO has two observatories located at Hanford and Livingston, in the United States. They both use the Michelson interferometer, with Fabry-Perot cavities to increase the effective arm-lengths for the laser beams before the interference. The physical length of each arm is about 4 km. The Virgo detector, located in Cascina, Italy. It has the same design of LIGO but with smaller physical arm-length, about 3 km similar to KAGRA, located underground at the Kamioka observatory, in Japan. The first direct GW detection was announced by the LIGO/Virgo collaboration after enormous efforts to enhance the sensitivity of the detectors during several years. On the 14th of September 2015, they detected the signal named GW150914 with the coincidence in both LIGO observatories. The signal is compatible with the GWs generated from the merger of a binary system of two black holes, with masses of about 36 and 29 solar masses. The final black hole after merger has mass of about 62 solar masses. About 3 solar masses of energy from this merger were radiated as GWs. This extraordinary discovery was awarded the Nobel prize in Physics in 2017. In the following years, the LIGO/Virgo collaboration contin-

ued announcing GW detections of many events, including black hole binaries mergers, neutron star-black hole binaries mergers and neutron star binaries mergers. Currently, LIGO/Virgo finished their third operation run and will be ready for the fourth operation run together with KAGRA in December 2022.

In the coming decades, the Indian Initiative in Gravitational-wave Observations (INDIGO) will join the ground-based GW observatories network. We also expect to develop a third generation of GW observatories, with projects such as the Einstein Telescope in Europe and the Cosmic Explorer in United States. With an increasing number of detectors in different locations, one expects to constrain better the location of the GW radiating source by triangulation. Moreover, multiple detectors can allow to discriminate instrumental glitches from GW signals if they are not detected coincidentally by other detectors. With different orientations of multiple detectors, one can also better determine the polarization of the passing GWs, which is not feasible with a single Michelson interferometer.

The ground-based observatories have some limitations. First of all, the seismic noises and other gravitational disturbances from the environment (for example human activities, atmospheric variations, ...) are dominant at low frequency, so the GW signals with $f < 10Hz$ cannot be detected. The interferometer detectors use staged suspension and pendulums to isolate the mirrors from the ground vibrations. The mirrors play the role of the free-falling particles so they are the references to measure the proper distance as described in section 1.1. These mechanical systems act as a low-pass filter, but they are limited in suppressing significantly the seismic noise at low frequency. At high frequency, above 200 Hz, the shot noise dominates. This noise is due to the quantum effect of counting the photons reaching the photodiode. The random fluctuations of the incident power due to counting the photons could lead to misleading GW signals in the interferometric measurements. Increasing the laser power reduces the shot noise but it raises another noise, related to the thermo-mechanical coupling between laser beams and the optical devices.

Some of above limitations of the ground-based detectors can be removed by placing the instrument into space. Hence, the earth-based effects such as seismic noise. Moreover, the armlengths of the interferometer can be longer in space, so the sensitivity of the detector is shifted into a lower frequency band compared to the ground-based detectors. For example, an armlength of about a million km gives the most sensitive observational frequency band around mHz. There are many potential GW sources generating signals in this band, as we will introduce in section 1.3. Therefore, the space-based GW observatories are complementary to the ones on ground, so one can broaden the GW observational spectrum. One of the future space-based detectors is the Laser Interferometer Space Antenna (LISA). Due to technological challenges and the time it takes to build an instrument of such a high precision, it is expected to be in operation in the middle of the 2030s. This thesis is oriented to the LISA detector,

so we will describe it in more detail in chapter 2. Other proposed space-based detectors are TianQin [105], TaiJi [85], and the DECi-hertz Interferometer Gravitational wave Observatory (DECIGO) [93]. The TianQin and TaiJi missions probe the GWs in the same frequency band as LISA, while DECIGO operates in the frequency band from 0.1 to 10 Hz, to fill the gap in frequency between other space-based GW detectors and the ground-based ones.

1.2.5 Pulsar timing

Another way to detect GW at low frequency, about 10^{-9} Hz, is to use the signal from pulsars [140]. A pulsar is a highly magnetized rotating neutron star, which emits electromagnetic waves in radio frequency from its magnetic poles. Each time the magnetized jet points toward the Earth, the radiated electromagnetic signal is observed as a pulse. The pulses are extremely regular due to ultra-stable rotation rate of the pulsar, so that we can use them as a reference clock. Using an array of calibrated pulsars, it is possible to detect GWs passing through spacetime between these pulsars and the Earth by looking for correlated irregularities in the times of arrival of the pulses from multiple pulsars observed by on-ground radio telescopes. Currently, there are three main pulsar timing array (PTA) collaborations (European Pulsar Timing Array, NANOGrav and Parkes Pulsar Timing Array) joint into the International Pulsar Timing Array (IPTA). They collect the data of several radio telescopes around the world to search for GWs. At the time of writing this thesis, no GW signal has been detected by PTAs with sufficient confidence, but there are upper bounds on the amplitude of the GW signals in the PTAs frequency band, and most importantly, the evidence for a common red signal [57, 33, 17]. In the coming years, accumulating data, using better calibrated pulsars, improving of the PTAs sensitivity, and developing new data analysis methods will allow to detect GWs in such a low frequency band. We will present some sources which emit GWs in that frequency band in the next section.

1.3 Gravitational wave sources

1.3.1 Principles of GW generation

To derive the GW generation by a source, one solves for the linearized Einstein's field equations (1.15) with non-vanishing mass-energy tensor $T_{\mu\nu}$. The detailed derivation can be found in [56], [133].

For simplicity, we assume here that the source is isolated, far away for the observer's location, and slowly moving. For example an isolated binary system, rotating with a slowly-varying angular frequency Ω. The center of mass of the binary system is at spatial distance L in the chosen coordinate frame, which has the origin at the observer's location. R characterizes the size of the binary source. If the binary system assumed rotates in a circular orbit, R is the

radius of this orbit. The slow-motion approximation implies that the typical velocity inside the source region, which is the source angular frequency multiplied with the size of source $\Omega \cdot R$, is small.

At the observer's location, which is far away from the source at a distance of L so we can use TT-gauge coordinates, and have $\bar{h}_{ij}^{TT} = h_{ij}^{TT}$, the metric perturbation tensor is given by [56]:

$$h_{ij}(t, \vec{\mathbf{x}}) = \frac{2}{L} \frac{d^2 I_{ij}}{dt^2}(t - L), \tag{1.33}$$

where we define the quadrupole moment tensor as

$$I_{ij}(t) = \int T^{00}(t, \vec{\mathbf{x}}) x_i x_j dV. \tag{1.34}$$

Some remarks are in order following equation (1.33). First of all, the metric perturbation tensor does vanish if quadrupole moment tensor is null. In particular, the source with spherically symmetric mass distribution, which has zero-quadrupole moment, cannot emit any GW. Moreover, since the metric perturbation tensor does not depend on terms of order less than the quadrupole, there is no dipole GW emission from a GW source in contrast to the case of electromagnetic radiation. Within the theory of linearized gravity, the conservation of the linear and angular momenta justify this conclusion. The amplitude of the GWs generated by a source is decreasing as the inverse of the distance L from the observer to the source. This amplitude is proportional to Newton's gravitational constant, which is assumed to be the universal constant, $G = 6.674 \times 10^{-11} \mathrm{m}^3.\mathrm{kg}^{-1}.\mathrm{m}^{-2}$. At the beginning of this section we set $G = 1$ so it does not appear in (1.33). Last but not least, equation (1.33) gives the dominant component of radiation of GWs, i.e. the quadrupole approximation. The higher order moment tensors, e.g. octupole, can contribute to the GW generation.

Let us consider a binary system of point particles, with the same mass M, rotating in a circular orbit of radius R with almost constant angular frequency Ω. The orbital plane of the system is in the plane Oxy such that at the beginning, the two particles are aligned along the x-axis. The corresponding energy density is given by

$$T^{00}(t, \vec{\mathbf{x}}) = M\delta(z) \left[\delta\left(x - R\cos(\Omega t)\right) \delta\left(y - R\sin(\Omega t)\right) + \delta\left(x + R\cos(\Omega t)\right) \delta\left(y + R\sin(\Omega t)\right)\right], \tag{1.35}$$

where δ is Dirac delta function, such that $\int_{-\infty}^{\infty} \delta(x) f(x) dx = f(0)$ for an arbitrary function $f(x)$. Substituting equation (1.35) into the quadrupole moment tensor (1.34) and then into equation (1.33), we obtain the following result for the two polarization states of GWs generated by that binary system (see for example section 7.5 in [56]):

$$h_+(t, \vec{\mathbf{x}}) = -\frac{8M}{L}\Omega^2 R^2 \cos\left[2\Omega(t - L)\right] \quad \text{and} \quad h_\times(t, \vec{\mathbf{x}}) = -\frac{8M}{L}\Omega^2 R^2 \sin\left[2\Omega(t - L)\right]. \tag{1.36}$$

From the above equations, we note that the GWs generated by a binary system source, with the orbital frequency $f_{\text{orbital}} = \frac{\Omega}{2\pi}$, have frequency $f_{\text{grav}} = 2f_{\text{orbital}}$.

In the non-relativistic case, when the binary system consists of two objects with masses of m_1 and m_2, one can apply the Newtonian approach to derive the angular frequency:

$$\Omega = 2\pi f_{\text{orbital}} = \left(\frac{M_{\text{tot}}}{4R^3}\right)^{1/2}, \tag{1.37}$$

where $M_{\text{tot}} = m_1 + m_2$ and we assume the binary system is rotating in a circular orbit of radius of R. Therefore, the monochromatic GW signal generated by a non-relativistic binary system has the frequency

$$f_{\text{grav}} = \left(\frac{GM_{\text{tot}}}{4\pi^2 R^3}\right)^{1/2}, \tag{1.38}$$

where we restored the explicit factor of G to facilitate the comparison with the value from the experiments.

In the following subsections, we will review some GW radiation sources both in cosmology and in astrophysics, the typical GW frequencies emitted by these sources, as well as the detectors which could detect these signals. The figure 1.2 gives an overview of the GWs spectrum, the main sources and the detection systems. The material in the following sections is mostly extracted from the LISA mission proposal [16], literature books [133, 56], and the lecture notes [129].

1.3.2 Galactic binaries

From the astronomical observations, we know there are many compact galactic binary systems. In particular, we expect that a few tens of millions of Galactic Binaries (GBs) in our Galaxy, the Milky Way, are emitting GWs. There are various types of GBs, composed of mostly white dwarfs, but also of neutron stars and SOBHs. The masses of these objects are less than a thousand solar masses. During the inspiral phase, the gravitational radiation signals are continuous and quasi-monochromatic in the source frame [115].

These GW signals are mostly in the LISA and LIGO/Virgo frequency bands, from about few mHz to hundred Hz, depending on the masses of the objects in the system and on how far they are separated (as expressed in equation (1.38)). The GW signals from GBs far from merger are weak and so their Signal-to-Noise Ratio (SNR) are low. Therefore, we cannot be detected individually all of GBs, and their GW signals attribute to a confusion background or stochastic gravitational wave foreground (see Figure 1.3). Some louder (higher SNR) signals, from heavy GBs and/or close to merger phase, can be better characterized. Some GBs also emit electromagnetic (EM) radiations, for example if they include pulsars. Hence, they are also detectable by EM wave detectors such as Gaia and Large Synoptic Survey Telescope

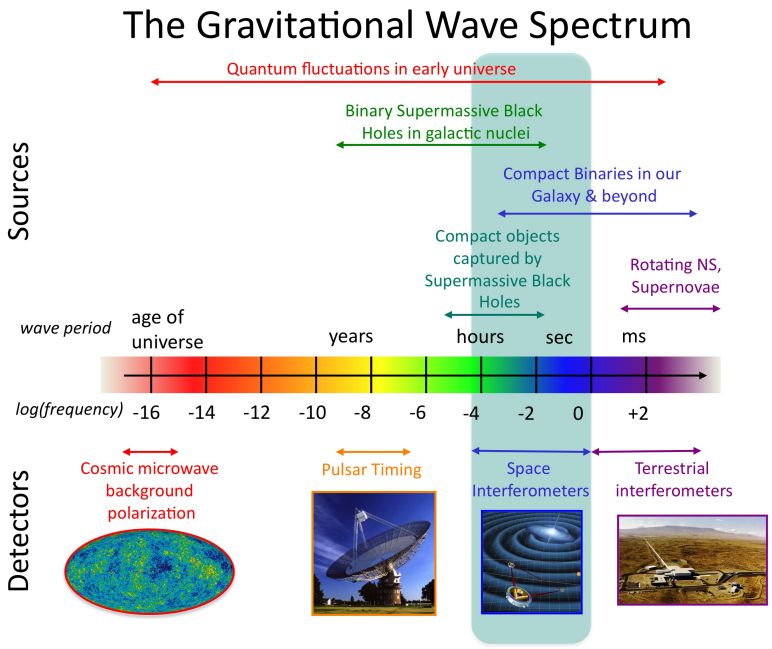

Figure 1.2: The gravitational wave spectrum with possible sources and detectors. Image from NASA Goddard Space Flight Center website, https://science.gsfc.nasa.gov/663/research/index.html.

(LSST) [95, 97]. Along then, there are known GBs, which are called verification binaries. Since these verification binaries emit GW signals in the LISA frequency band, one can use them to check the performance of the instrument.

As presented in section 1.3.1, the detected GWs from a binary system could provide information on its intrinsic properties such as the mass, orbital frequency, size, Etc. In addition, we can constraint the external parameters such as the distance of the source to our observatory and the sky location of the source. In the case of LISA, we expect to detect and resolve about 25 000 individual GBs. With sufficiently long observations, LISA can constraint the sky localization of these GW sources and provide information on the distribution of GBs in the Galaxy. These information turn out the formation and the evolution of GBs. Moreover, the joint observation of gravitational and electromagnetic waves can be useful for studying the physics of the compact binary systems, such as the tidal forces that brings the bodies of the system closer over time in the inspiral phase before the merger.

1.3.3 Stellar-origin black hole binaries

Stellar Origin Black Hole (SOBH) binaries emit the GWs in several frequency bands, either around the mHz with quasi-monochromatic signals detectable by LISA or at higher frequency,

with transient signals during the late inspiral and merger phases, which are observed by ground-based observatories. In their inspiral phase, the SOBH binaries of about tens to hundreds solar masses can emit GWs in the LISA band for years. We expect to detect and resolve these signals during the LISA operating duration, which will allow to constrain their parameters, especially the sky localization, eccentricity, and even the time of coalescence with a good precision [16]. For a subset of events, it might be possible for the triggering of alerts to the ground-based GW detectors by few months or weeks before the merger for observing the higher frequency GWs emitted during the merger phase. In addition, the EM wave detectors can also be re-pointed at the coalescence to probe the potential EM counterparts. Although the latter are not expected for the SOBH binary mergers, in contrary to the neutron star binary mergers, for example GW170817 [2]. The joint observations of GWs in either multi-band or multi-messenger astronomy will be a great opportunity to study the environment close to SOBH binaries and disentangle their alternative formation channels, as well as to test General Relativity and other theories of gravity, and possibly to constrain cosmological parameters [6].

1.3.4 Supermassive black hole binaries

Supermassive black holes are characterized by the masses of millions to billions solar masses. According to astronomical observation, we expect that almost every large galaxy has a supermassive black hole at its center. Several EM observations [132, 7], indicate that there is a supermassive black hole (SMBH), named Sagittarius A*, at the center of the Milky Way. Recently, the Event Horizon Telescope was able to capture the image of that black hole [11] after the first image of the SMBH at the center of the M87 galaxy in 2019 [10].

The origin of SMBHs is still not well-known. Although, there are models on how they grow in size, for instance by accretion of matter in active galactic nuclei, or by the merger with other black holes [151, 96, 119]. The merger of two massive black holes could follow the collision of galaxies in galaxy clusters. The transient GW signals emitted during the late inspiral and merger phases of SMBH binaries have high SNR and can be observed in the LISA frequency band, lasting from months to days down to hours (see figure 1.3). Few tens events per year are expected [94]. In addition, GWs radiated by SMBH binaries with even higher masses, of the order of 10^9 solar masses, can be detected by pulsar timing arrays [140].

Thanks to their high SNR, the luminosity distance and the localization of the events can be extracted from the GW data with high accuracy, possibly identifying the galaxy where the event has occurred. Then, we can estimate the redshift of the source if the EM radiation of the galaxy is also detected. The redshift and the luminosity distance from multiple events are the inputs to estimate the Hubble constant and other cosmological parameters. In addition, the detailed motion of objects in a SMBH binary merger can be very interesting for testing

the theory of gravity in the strong-field regime.

With the detection of GWs from SMBH binaries at high redshift, we expect to trace their growth in the cosmic history, especially the formation and the merger history which helps to elucidate the cosmic matter structure [16].

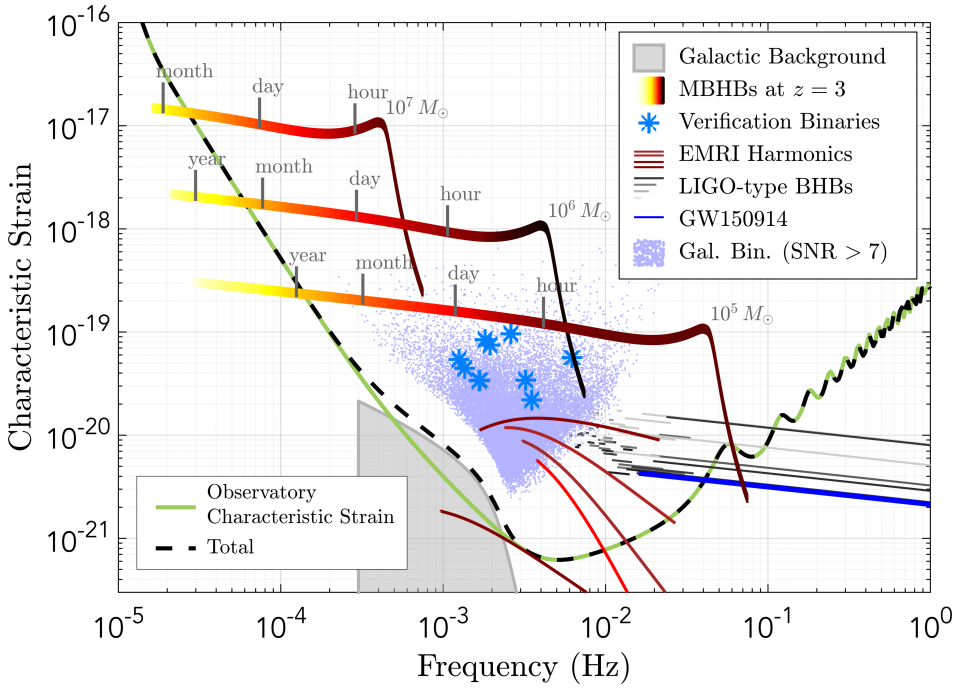

Figure 1.3: The LISA expected sensitivity with the signal of detectable GW sources in the unit of dimensionless characteristic strain. The total sensitivity indicated in the dashed black line includes the instrumental sensitivity noise curve, in green line, and the confusion foreground from the unresolved galactic binaries, in the grey shape. This figure is taken from [16].

1.3.5 Extreme mass-ratio Inspirals

Another interesting sources emitting GWs in the LISA frequency band are extreme mass-ratio inspiral (EMRIs). They correspond to a small object (typically a black-hole or a neutron star) of a few to hundreds solar masses, orbiting around a massive black hole with a mass of the order of, for example, a few millions solar masses. The orbit of the small object is very complex and hard to compute. The event rate of EMRIs is highly uncertain, from few to few thousands events per year [34]. These sources are very interesting, in particular to understand the dynamics of dense nuclear clusters and to test General Relativity since the small object is mapping spacetime around the massive black hole.

1.3.6 Stochastic Gravitational Wave Backgrounds (SGWBs)

1.3.6.1 SGWBs of astrophysical origin

One of the sources of SGWBs is the superposition of GW signals which are weak and/or too numerous to be resolved individually. Detailed discussions about the astrophysical origin and the cosmological origin of SGWB can be found in [106]. We already mentioned one of the possible SGWB detectable by space-based GW detectors coming from the large number of unresolved compact galactic binaries, c.f. section 1.3.2.

In the LIGO/Virgo frequency band, the low SNR gravitational radiation from binary systems consisting of small mass objects or SOBHs and/or neutron stars, from distant mergers, will hardly be resolved individually. From the first LIGO/Virgo run, the estimated total rate of mergers for the SOBH binaries is about 1 event per minute or few events per hour [1] and the rate for the neutron star binary merger is predicted to be roughly one event per 15 seconds [5]. The duration of the SOBH merger signals is of a few seconds, which is much smaller than the average duration between successive mergers. Hence, the GW signals from these events are separated by periods of silence. On the other hand, the duration of neutron star merger signals is about 100 s, so that these signals overlap in time. Therefore, in LIGO/Virgo detector we expect to observe the SGWB from SOBH binary mergers as the *popcorn* noise, while the SGWB from neutron star binary mergers is the continuous background [3].

The GW background from SOBH and neutron star binaries in their inspiral phase could also be detected in the LISA frequency band. In this band we also expect to observe the GW background generated by compact white-dwarf binaries in the Milky Way [92]. This is one of the guaranteed GW signals for the LISA mission [16]. In fact, this confusion signal is expected to be stronger than the instrumental noise, as illustrated in figure 1.3, so that we call it galactic foreground and treat it as an additional noise source when extracting louder sources in the LISA frequency band.

The inspiral and merger phases of SMBH binaries are generating the GWs at very low frequencies, from 10^{-9} to 10^{-6} Hz [136]. We expect to detect these signals as an overall stochastic background and maybe resolve some individual systems with high SNR, by pulsar timing arrays in the near future.

1.3.6.2 SGWBs of cosmological origin

In addition to the astrophysical sources presented above, there are theoretical predictions of SGWBs of cosmological origin in the early Universe. Since the GWs interact weakly to the matter they pass through, information about the events occurring in very early Universe, which are inaccessible through EM signals, could be imprinted in SGWBs. Therefore, SGWBs

can offer the opportunity to look deeper in the Universe history to understand better how it was evolving in its earliest ages.

One possible source of cosmological SGWB is Inflation, a phase of rapid expansion of the Universe. The theory of Inflation has been proposed to solve the problems of horizon and flatness of the hot Big Bang model (see chapter 12 of [133] for more detail). During that period, the quantum fluctuations in the geometry of spacetime, expanded to the macroscopic scales, could lead to a stationary SGWB [106]. This relic gravitational wave background could influence to the B-mode polarization of the Cosmic Microwave Background (CMB) radiation [135]. Besides the effort to search for this signal with CMB observatories, this type of signal could be detected by GW detectors in different frequency regions since the relic gravitational radiation predicted from the standard Inflation theory spreads over many frequencies (see figure 2 in [52]).

Another possible sources of SGWB are first order phase transitions in the Early Universe. The phase transitions in cosmology are the transition of regions of the Universe from a state to another, which is more energetically favorable. In quantum field theory, the phase transitions is performed, for example, by a scalar field $\phi(t)$, like the Higgs field, or a set of them. The effective potential, deduced from the Lagrangian of this scalar field by ignoring the dynamical terms, can have several local minima depending on the temperature of the Universe at that moment. The global minimum of the effective potential corresponds to the vacuum expectation value (VEV) of the scalar field. At the critical temperature T_c, other local minima become degenerate with the global one. At $T < T_c$, the phase transition occurs: from the vacuum state which is energically favorable at temperature $T > T_c$, to another one more favorable at lower temperature $T < T_c$. We usually call the latter the "true" vacuum state and the former the "false" vacuum state.

The phase transition manifests a spontaneous symmetry breaking, a feature of the gauge theory. An example of spontaneous symmetry breaking is the Goldstone-Higgs mechanism, which breaks the electroweak symmetry to provide the masses of gauge bosons and fermion particles [58]. If a potential barrier separates the two minima, the scalar field at the false vacuum state can transit to the true vacuum state by quantum tunneling or thermal fluctuations. This phase transition occurs out of the thermal equilibrium, and is classified it as a first-order phase transition.

A first-order phase transition proceeds through the nucleation of bubbles in the thermal plasma (cosmic fluid) at a temperature below the critical value. Inside the bubbles, the scalar field is in the true vacuum state. The bubbles then expand due to the different pressure between the interior and exterior of the bubble walls. Eventually, they collide with each other if the speed of bubble expansion exceeds the expansion rate of the Universe and the whole

Universe transits to the true ground state after the phase transition completes.

The spherically symmetric bubble expansion cannot generate gravitational waves (a spherically symmetric mass distribution cannot emit GWs, as mentioned in section 1.3.1). However, the collision of the bubbles and their interaction with the thermal plasma can produce GWs via several processes [55, 52, 53]:

1. collisions of bubble walls and shocks (if any) in the plasma. The gradient energy of the bubble collisions is partially released into the gravitational waves. The GW spectrum from bubble collisions can be worked out, for example, with numerical simulations using the envelope approximation [86].

2. sound waves in the bulk fluid (plasma). The percolation induces bulk motion in the plasma, in the form of sound waves. The bulk flow is due to the coupling of the scalar field to the plasma particles, considered as the friction. With sufficient large friction, the bubble wall reaches a terminal velocity and the latent heat driving the bubble expansion is also converted into kinetic energy of the bulk motion. When they collide, the sound wave fronts create a non-zero anisotropic stress-energy tensor that generates GWs. The GW contribution of this process to the global GW power spectrum can be worked out with numerical simulations [83, 84].

3. magnetohydrodynamic turbulence in the plasma after the collisions of bubble walls. Besides the sound waves, the bulk motion due to the percolation can be chaotic and vortical if the Reynolds number of the plasma is extremely high (indeed, it is of the order of 10^13 at 100 GeV [51]. Therefore, we expect magnetohydrodynamic turbulence in the plasma to occur. This can lead to another GW source during the phase transition. Some studies of the GW contribution of magnetohydrodynamic turbulence, such as [51, 49], provide the expected GW spectrum for this process.

The expected spectral shape for these SGWBs is usually broken power laws with a maximum depending on the energy scale of the phase transition. For many models, this peak is in the LISA frequency band, see figure 1.4. There can be several phase transitions in the early Universe, such as the electroweak phase transition and the quantum chromodynamics phase transition. The typical energy scale for the electroweak phase transition is of the order of 100 GeV [55, 52]. The quantum chromodynamics phase transition takes place at about 200 MeV [52]. Other Beyond Standard Model (BSM)-motivated phase transitions with an energy scale of up to thousands TeV could also be detectable by LISA [16].

Another possible source of SGWBs is associated to a network of cosmic strings, which are topological defects moving in the Universe [52]. This signal also has a broad frequency range

and could be peaked at any specific frequency depending on the parameters of the cosmic string network.

1.3.6.3 SWGB properties

The stochastic backgrounds of gravitational radiation have several properties that can be used to infer the source generating them.

1. The first property for characterizing the SGWB is the angular distribution of the GW power over the sky. For example, cosmological SGWBs, generated during phase transitions or Inflation, are theoretically predicted to be statistically isotropic, similarly to the CMB. We will present the arguments leading to this property when characterizing the SGWB later on. The GW sources generating cosmological backgrounds are anisotropic, following their spatial distribution in the early phases of the Universe, but the average GW power for different realizations of the source is isotropic. On the other hand, some astrophysical SGWBs are not isotropic, even statistically. For example, the confusion background generated by galactic white-dwarf binaries, which is one of the important sources of SGWBs for LISA, has a preferred direction on the sky. The GW power of this background is concentrated in the direction of the Milky Way, with the main emission coming from the Galactic bulge.

2. The stochastic backgrounds could also differ from one another in the temporal distribution and the amplitude of the signals. For instance, the confusion background from white-dwarf binaries ,which would be detected by LISA, has the modulated amplitude with a 6-month period due to the cartwheeling motion of the whole constellation around the Sun, so that the antenna pattern of LISA will point toward the center of our Galaxy twice a year.

3. Finally, the spectral shape could be used to distinguish the SGWBs of different sources. As illustrated in figure 1.4, the SGWBs from first order phase transition in the early Universe have a particular shape linked to some fundamental properties of the Universe.

For the mathematical description of the SGWB, we remind that the individual signals contributing to the background are either too weak, and/or too numerous, and/or with too small correlation scale, so that we cannot characterize them individually. Hence, the combined signals leading to the SGWB should be treated as a set of random variables. Then, one describes the SGWB statistically, using the ensemble average over different realizations of the background. Since we have only one observable Universe, we use the *ergodic* hypothesis of cosmology: the different realizations of the background correspond either to the different signals at different spatial locations averaged over a large enough region on the sky or to the

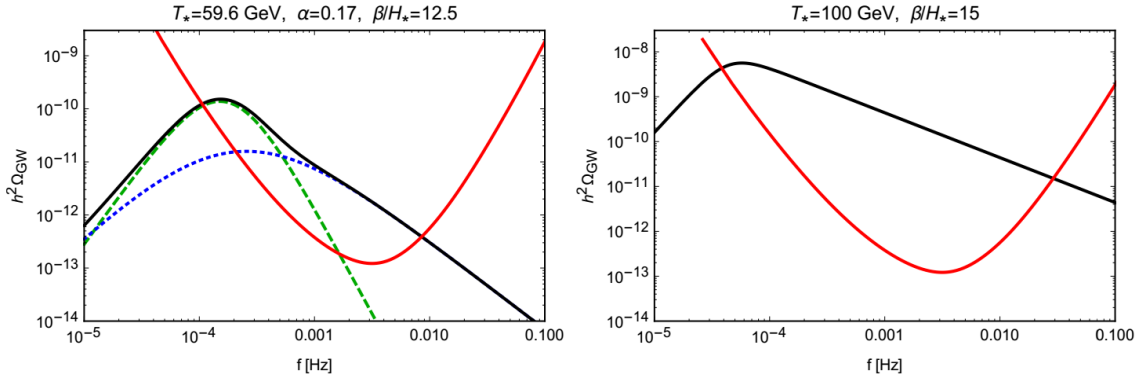

Figure 1.4: Power spectra of SGWB in two different scenarios of first order phase transition compared to the estimated sensitivity curve of LISA, for the red line in both subfigures. The left-hand plot is for the Higgs portal scenario [55]. The green dash line represents the GW signal from sound waves while the blue dotted curve is the GW signal from magnetohydrodynamics turbulence. The right-hand plot shows the case of a phase transition connected to the radion stabilization of Randall-Sundrum model [55]. Image from [52], see there for a more detailed description.

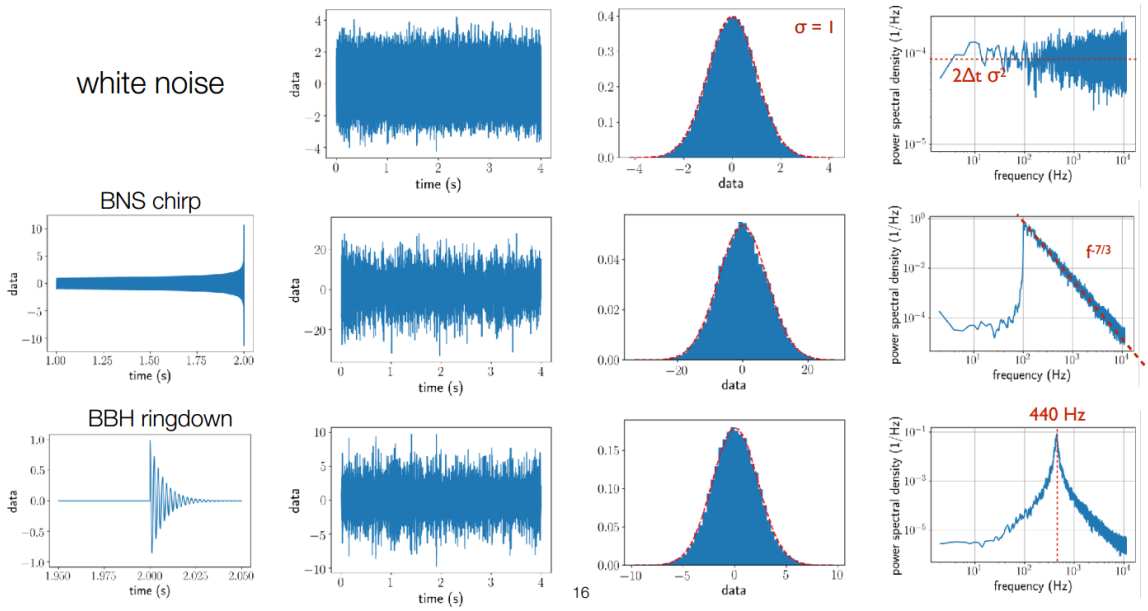

Figure 1.5: Simulated time-series data for different GW stochastic signals from astrophysical sources, comparing with the white noise signal. Image from [130]. The authors of [130] used the overlapped GW signals for a sufficiently large number of individual events, either neutron star binary mergers or SOBH ringdown for producing the SGWBs, as shown in the second column. The distribution of the amplitude of the signal is Gaussian, as shown in the third column. The power spectra computed from the combined time-series signals are different for each type of source, and can be distinguished from the power spectrum of a white noise signal.

different signals in the same sky location but observed for a long enough time. This hypothesis requires two conditions: the almost homogeneous and isotropic Universe, and the causality of the GW sources. The first condition is frequently used in cosmology from the observations in the large scale Universe. The second one indicates that the typical size of the region of causal contact at the time of action of GW source generating SGWBs was much smaller than the causal horizon today[5] [52].

Therefore, the SGWB of sources operating in the early Universe is generally considered to be statistically homogeneous and isotropic, unpolarized and Gaussian. We can write the combined signals from sources contributing to the SGWB in the TT frame in the following form [129]

$$h_{ab}(t,\vec{\mathbf{x}}) = \int_{-\infty}^{\infty} df \int d^2\Omega_k \sum_{A=+,\times} h_A(f,\hat{\mathbf{k}}) e^A_{ab}(\hat{\mathbf{k}}) e^{i2\pi f\left(t-\frac{\hat{\mathbf{k}}\vec{\mathbf{x}}}{c}\right)}, \tag{1.39}$$

where $h_A(f,\hat{\mathbf{k}})$ are the Fourier coefficients of the plane wave expansion, $\hat{\mathbf{k}}$ is the unit vector along the direction of the propagation of the plane wave, $A = +,\times$ indicates the polarization, $e^A_{ab}(\hat{\mathbf{k}})$ are the polarization tensors defined from two orthogonal unit vectors $(\hat{\mathbf{l}},\hat{\mathbf{m}})$ in the plane orthogonal to $\hat{\mathbf{k}}$, as shown in figure 1.6.

With the assumption of statistically homogeneous and isotropic, and unpolarized background, the ensemble average of the second-order moments of the Fourier coefficients reads:

$$\langle h_A(f,\hat{\mathbf{k}}) h^*_{A'}(f',\hat{\mathbf{k}}')\rangle = \frac{1}{4}\mathcal{P}(f,\hat{\mathbf{k}})\delta(f-f')\delta_{AA'}\delta^2(\hat{\mathbf{k}},\hat{\mathbf{k}}'), \tag{1.40}$$

where $\mathcal{P}(f,\hat{\mathbf{k}})$ is the strain power spectral density per unit solid angle $\Omega_{\hat{\mathbf{k}}}$, so that the strain power spectral density of the SGWB is given by

$$S_h(f) = \int d^2\Omega_{\hat{\mathbf{k}}}\mathcal{P}(f,\hat{\mathbf{k}}). \tag{1.41}$$

With the further assumption that the background is Gaussian, all cubic or higher order moments are either identical to zero or presented in terms of the second-order moment. Then, the quadratic expectation values of the Fourier coefficients is sufficient to fully characterize statistically the SGWB.

For convenience, we typically express the strain power spectral density of a SGWB as [52]:

$$S_h(f) = \frac{3H_0^2}{4\pi^2}\frac{\Omega_{\rm gw}}{f^3}, \tag{1.42}$$

where $H_0 = 100\ h$ km s^{-1}Mpc^{-1} is the Hubble constant, and h encodes the experimental uncertainty of the Hubble constant at the time of observation. $\Omega_{\rm gw}(f)$ is the normalized GW

[5] The second condition is not fulfilled during the inflationary period, when the Universe is predicted to expand exponentially. However, the gravitational radiation produced in this period is still intrinsically stochastic [52].

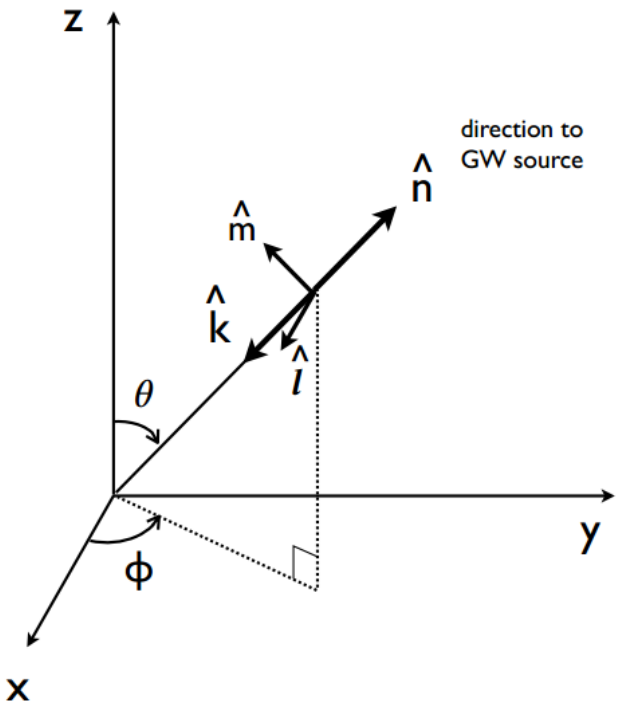

Figure 1.6: Coordinates and unit vectors for the description of a GW source. Image from [129].

energy density spectrum defined as

$$\Omega_{\rm gw}(f) = \frac{1}{\rho_c}\frac{d\rho_{\rm gw}}{d\log f}, \tag{1.43}$$

where $\rho_{\rm gw}$ is the total energy density in GWs, $\rho_c = \frac{3H_o^2}{8\pi G}$ is the critical energy density today. The GW energy density spectrum depends on the type of GW source contributing to the background, and in simple cases, it can be formulated as a power law. For example, the energy density spectrum of the SGWB generated by the inspiral phase of binary systems is $\Omega_{\rm gw}(f) \propto f^{2/3}$, see section 3.4 in [129] for a detailed derivation. The strain power spectral density for this type of SGWB from (1.42) is then $S_h(f) \propto f^{-7/3}$, as illustrated in figure 1.5.

We will discuss more possible shapes for the SGWB energy density spectrum, and hence its strain power spectral density for the case of the LISA detector, in chapter 6.

Due to their stochastic nature, the SGWBs are similar to an effective source of noise in the detector. This leads to an important challenge in the detection of stochastic backgrounds, i.e. to distinguish the signal behaving as noise from the actual instrumental noise. Some possibilities to extract the SGWB from the measurement data have been investigated such as

1. The first way is to have good enough characterization of the instrumental noise, including

its amplitude and spectral shape, so that any excess noise in the data can be interpreted as the SGWB. This is how Penzias and Wilson detected the CMB as an excess of noise in their radio antenna, not related to any known noise source. However, it is extremely challenging to know the noise amplitude and spectral shape precise enough, especially since the SGWB can be weaker than the noise. Furthermore, in the case of LISA, we generally do not know the spectral shape of all noise sources. However, it might be possible to use the GW null channels, i.e. ome specific Time Delay Interferometry (TDI) combinations [126, 112], to reduce the contribution of the signal and better characterize the noise before extracting the GW signals from other channels. In the chapter 6, we will demonstrate how the noise characterization can affect to the data analysis of SGWBs with LISA simulated data.

2. Another possible way is to use the data from multiple detectors if they have uncorrelated noises. In this case, one looks for to the common disturbances of due to the same SGWB in multiple data streams. The signal in the data is modulated by the physical separation and relative orientation of the different detectors. Effectively, the random output of one detector is used as the template for the data analysis of the other one to search for the common signal. This is the best option for the network of ground-based GW detectors to search for SGWBs. Interestingly, the SNR of the signal extracted from the cross-correlation is proportional to the square root of the number of data samples, or of the observation time. In other words, even though the SGWB is weak compared to the instrumental noise, one could still access it if the cross-correlation measurement is performed for a long enough time.

Chapter 2

LISA introduction and instrumental model for simulation

This chapter briefly introduces the space-based gravitational wave detector, Laser Interferometer Space Antenna (LISA). In particular, we present the current configuration of LISA to detect GW, as well as the noises that could influence the measurements during the mission. Then, we discuss the LISA instrumental model, which helps understand the propagation of noises and GW signal in the LISA instrument and the interferometric measurements. Finally, we introduce a LISA simulator, `LISANode`, used to generate simulated data for most projects in this thesis. In addition, we present some works that contribute to developing the `LISANode` simulator in the noise implementation, such as correlation and non-stationarity, which are interesting in the realistic LISA configuration.

2.1 LISA constellation and orbit

LISA will consist of 3 spacecraft forming an equilateral triangle with armlengths of about 2.5 million kilometers. The orbital set-up is optimized so that the rate of change of the distance between spacecraft is less than ± 8 m/s for the whole mission duration (about 4 to 10 years). In addition, the opening angle of the constellation triangle varies around its mean value 60^o by less than $\pm 1^o$ with the maximum rate of 1.2×10^{-2} deg/day [72]. This constellation will be trailing behind the Earth between 50 and 65 million kilometers in heliocentric orbit. The constellation is rotating in a cartwheel motion with a one-year cyclic period (see figure 2.1).

In the current design, all spacecraft are launched by a single Ariane 6.4 launcher, and they will be positioned to their final orbits after about 15 months. After that, the test-masses inside each spacecraft are released into their free-falling state. The spacecraft will be in a drag-free state with its position and attitude controlled using the measurements of the position and

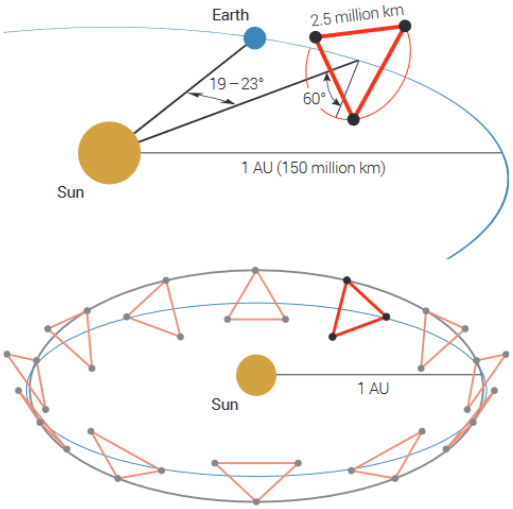

Figure 2.1: LISA constellation and its orbits, from [31]. The constellation trails the Earth by about $19 - 23^o$, corresponding to about $50 - 65$ million kilometers from the Earth. The constellation plane tilts by about 60^o w.r.t. the Earth's ecliptic plane. Each spacecraft moves around the Sun with different orbits, so the whole constellation is in a heliocentric orbit with cartwheel rotation.

the attitude of test-masses, the wavefront sensor measurements for the incoming laser beam, and the sun sensors. These test-masses are the reference points for measuring the spacecraft distances, which is used to monitor the variation of spacetime due to GWs. The next section discusses the measurement concept in detail for that purpose.

2.2 Concept of measurement

Each spacecraft of the LISA constellation contains two test-masses. They are the reference points for monitoring the tidal deformation of the whole constellation due to gravitational waves passing through. For that, we measure the light travel time between test-masses along the same arm by measuring the optical phase variation in each spacecraft via laser interferometry. Inevitably, this measurement is limited by the noise in the optical measurements and any disturbances on the test-masses themselves. Therefore, the spacecraft are used as shields for the test-masses, which follow their geodesics, so-called *free-falling* motion. It is important to notice that this free-falling motion of the test-masses is only left along the sensitive interferometry axes, which are parallel to constellation triangle sides and change over time. Then, the spacecraft follows the test-masses in those sensitive axes, so call *drag-free* motion, by μN thrusters. Meanwhile, the test-masses are kept in the center of their housing by applying suitable forces and torques with a control loop system. This control system, called Drag-Free

Attitude Control System (DFACS), is one of the key technologies for the LISA mission, and it has been demonstrated fruitfully by LISA Pathfinder (LPF) mission [32]. We will discuss a bit detail about DFACS in subsection 2.4.

In order to mitigate the jitter noise of the spacecraft motion w.r.t the test-masses, the distance changes between test-masses are measured by *split interferometry*. In principle, the total distance between the two test-masses on the arm spacecraft 2 - spacecraft 3 is split into three parts:

- distance from test mass, *often proof mass* (TM) 2 to the optical bench in spacecraft 2,
- distance from the optical bench in spacecraft 2 to the one in spacecraft 3,
- and distance from the optical bench in spacecraft 3 to the TM 3.

These optical pathlength measurements use heterodyne laser interferometers to extract the differences in frequency of the interference beams, called *beatnote*. Due to the significant distance between spacecraft, the incoming beam in one spacecraft has low power when it reaches the receiving spacecraft. Consequently, it cannot be reflected to perform the return path. In the mission proposal [16], the OBs in the spacecraft will act like a transponder, which is transmitting a new fresh high-power laser beam phase-locked to the incoming one with a fixed offset frequency. Eventually, one laser in the whole constellation is used as the primary laser, and the others are phase-locked to it with some offset frequencies. In order to ensure the beatnotes within the readout frequency ranges of the photodiodes, the offset frequencies are changed after a certain period following a predefined frequency planning [79].

By combining these measurements along six constellation links in the on-ground data post-processing, we can suppress the spacecraft motion jitter noise. Further post-processing algorithms such as TDI will be applied to remove the other dominating laser frequency noise. A common time frame for all data will also be established in post-processing, called the clock calibration process. Since TDI is one of the critical features for the LISA mission, and our works in this thesis are highly based on it, we will describe it carefully in chapter 3.

2.3 Payload overview

This section gives a brief overview of the instrumental architecture of LISA. This design has been studied and presented in European Space Agency (ESA) technical note [72] for the start of Phase A of the mission, i.e. the preliminary design phase. We note that it is not the final design but the preliminary baseline as the current best understanding of the LISA instrument.

Overall, all three spacecraft of the LISA constellation are identical. Each carries two MOSAs and the other necessary support and interface structure. Each MOSA points to one of the other two distant spacecraft. It is movable to track the variation of the vertex angles of the constellation triangle, $60^o \pm 1^o$, due to the orbital motion as described in section 2.1.

Each MOSA is the assembly of a telescope, an Optical Bench (OB), a Gravitational Reference Sensor (GRS) and a support structure.

- The OB hosts all the necessary optical devices for the interferometric measurements. The design of the OB is based on the experience gained in the LPF mission. We adapt it for the LISA interferometric measurement system, presented in section 2.5.

- Due to the large distances between spacecraft, the transmitting beams among spacecraft will diverge, and the power per unit area decreases proportionally to the square of travel distance. We use a telescope to convert the small diameter beam (2.24 mm) on the OB into the large diameter of the telescope (300 mm) for transmitting the beam to the distance spacecraft and vice versa for also receiving the beam from that one. That will help limit the transmit beam's divergence and increase the reception area for catching the received one.

- The GRS carries the TM within an electrode housing surrounded by mechanical and electrical equipment. One of its functions is to monitor the position and attitude of the TM, to provide the forces and torques for sufficient compensation of the translational and angular motion of the TM in non-sensitive interferometric measurement axes. In addition, the GRS can shield the TM from the stray forces to keep it in the free-falling motion along the sensitive axis. These functions are critical for the DFACS, as described in section 2.4.

- The supporting structure helps to maintain these above objects mounted in correct alignment in the MOSA, in the order from inside the spacecraft to out the space: GRS, OB and telescope.

2.4 Drag-free attitude control systems

One of the critical technologies for the LISA mission is maintaining the test-masses in free-falling motion in their interferometric sensitive axes. In addition, we need to control the positions and attitudes of the test-masses and the spacecraft to ensure the spacecraft follows the test-mass in the sensitive axis and the test-mass is rigidly attached to the spacecraft in other degrees of freedom. This problem is worked out by Drag-Free Attitude Control System (DFACS), which was demonstrated partly in the LPF mission [32], [31].

There are sensors around the test-masses within the electrode housing of the GRS to monitor its position and attitudes. The DFACS uses the measurements from these sensors in a closed-loop control system to command μN thrusters and steer the spacecraft in the test-mass free-falling trajectory. On the other hand, this system also applies the necessary forces and torques on the TM in non-sensitive interferometric axes to keep the TM at the center of the housing of the GRS. These forces and torques are controlled by an onboard computer and driven by electrostatic actuators. Thanks to its local measurements, the DFACS suppresses spurious forces contributing to the armlength variations while preserving the gravitational wave effect.

The key technologies associated with the DFACS and GRS have been successfully demonstrated on the LPF mission [18, 20, 22, 25, 26, 27, 28, 31, 32]. In LPF, the DFACS has multiple working modes:

- suspension/differential mode to control the electrostatic forces applied on the TM to compensate for the differential acceleration between two TMs;
- common/drag-free mode to keep the spacecraft in drag-free motion with commanded forces/torques applied via the micro-thrusters;
- attitude mode to support the controller of the spacecraft attitudes w.r.t. inertial Galilean frame with the information of the star trackers.

These DFACS modes will be adapted for LISA. The main significant difference are the following.

- The suspension mode along the sensitive axis is not necessary in LISA since two TMs of the long-arm measurement are in free-falling mode and their perspective spacecraft are drag-free in this direction.
- The spacecraft attitude for the LPF mission is controlled by the information of the star trackers; in the LISA we will use the differential wavefront sensing of the incoming laser beams as the reference
- About the coupling of the TM to the spacecraft motion due to the force gradients at their nominal positions, in LPF the TMs are coupled to the same spacecraft but in LISA each TM is coupled to its own spacecraft.

The LPF demonstrated the LISA top-level test-mass acceleration noise requirements and the other functional requirements of GRS. However, some aspects still need to be studied to understand and ensure the performance of the DFACS, such as sensing and actuation noises,

more realistic configuration of LISA (orbits, jittering MOSAs w.r.t. two more distant spacecraft) including the non-stationary effects such as tilt-to-lengths, glitches (spurious transients), thermal instability and gas leaking (for Brownian motion), Etc. Therefore, it is essential to study the performance of the DFACS and to simulate them. In this thesis, we investigate the moving MOSAs impacts on the DFACS, as described in chapter 5.

2.5 Interferometry measurement system

2.5.1 LISA interferometric measurements

To monitor the changes in the distance among spacecraft due to the GWs, we use the exchanged laser beams to measure distances between TMs by split interferometry, which is mentioned in section 2.2. In addition, we need some interferometric measurements to reduce the dominating noises in the post-processing steps. In the current LISA data architecture, there are three main optical interferometric measurements and two other auxiliary ones in each MOSAs:

- The Inter-Spacecraft Interferometer (ISI) measurement is the interference between the distance laser beam and the local one.
- The Test Mass Interferometer (TMI) measurement is the interference between the laser beam in the adjacent MOSA and the local one in the same spacecraft (S/C). Before interfering, the adjacent laser beam will be redirected to bounce off the TM in the local MOSA.
- The Reference Interferometer (RFI) measurement is the same interference as the TMI, but the adjacent laser beam does not bounce off the local TM.
- Two auxiliary measurements are the sideband ISI and sideband RFI. These data are necessary for the clock noise reduction algorithm, but it is out of the scope of this thesis.

All those measurements will be performed in the OB of the MOSA. The construction techniques for the optical bench with sufficient alignment accuracy and pathlength stability requirements for the LISA mission have been demonstrated in LPF [32]. However, in the LISA case, we have two identical OBs for each spacecraft, so we need to adapt the experience gained from LPF to study the mechanisation of the series production in that OBs.

Each OB has a laser source at 1064 nm with excellent frequency stability. The laser is distributed on the OB via several beam splitters and optical devices to provide the beams for several interferometric measurements, as described above. Part of the laser beam of each OB is exchanged to the adjacent one to do the TMI and RFI measurements. This exchange is performed by the bi-directional backlink using an optical fibre. The OBs interacts with

the telescope and the TM contained in the GRS via some optical interfaces. The design of these interfaces is optimized to minimize the backscattered light from the transmitting beam to the received one and to have high stability of the optical path length w.r.t the temperature fluctuations [16].

All the interferometric measurements are performed in photodiodes, which are quadrant devices with integrated pre-amplifiers implemented on OB. Then the generated heterodyne beatnotes are read by the phasemeter. It is essential to extract the optical path length variation between two interfering beams and the angle between their wavefronts since the latter will be helpful for the alignment procedures and integration in the optical metrology system. These angular measurements are performed using the differential wavefront sensing (DWS) technique. By comparing the average phase over four areas of the Quadrant photodiode (QPD), we can reconstruct the misalignment between the wavefronts of two incoming beams at the photodiode since there is a phase shift between the signals recorded in the different areas [80]. The DWS information will also be used as the input for the DFACS for controlling the TM and spacecraft attitude, as well as the on-ground calibrations for reducing Tilt-To-Length (TTL) couplings effect [120].

2.5.2 Frequency planning

The beatnotes of the different interferometers need to be within photodiode-phasemeter bandwidth, which is approximate from 5 to 25 Mhz. However, these beatnotes vary due to the Doppler shifts in the distant long-arm beam. To handle this problem and maintain the beatnotes in the detection range, all the lasers of the constellation are phase-locked to one chosen primary laser using control loops with a fixed offset frequency.

According to the current design, each spacecraft contains two laser sources and receives beams from distant spacecraft. Therefore, each local laser can be locked by either the adjacent laser beam using the RFI or the distant beam. This distant beam can be either the one arriving on the same OB as the laser source to be locked (locking via ISI) or the one arriving on the adjacent OB (locking via ISI and RFI). The last possibility is the so-called *frequency-swap* laser locking scheme. We have several laser locking schemes depending on the chosen primary laser and the topology of the locking strategy. The set of offset frequencies for locking all locked lasers and their evolution over the mission duration is called the frequency plan.

The computation for the frequency plan is complex because we need to find 5 offsets for 5 locked lasers to control the values of different beatnote frequencies. These offsets depend on the LISA orbit because the laser beams accumulate the Doppler shifts during the propagation. Therefore, the frequency planning will update the set of offset frequencies after a certain period (every few weeks) during the mission to ensure that all beatnotes are within the detection

bandwidth. This problem is discussed in detail in [79]. We will apply one of the laser locking schemes to the study of noise propagation in chapter 4.

2.5.3 Onboard processing

Phasemeter

All the beatnotes are processed by the phasemeter. They are converted from the analog signal provided by the photodiode to the digital one, using an Analog-to-Digital Converter (ADC). The core of the phasemeter, digital phase locked loop (DPLL), reads the phase and frequency of the beatnote.

The principle of DPLL is to generate a digital replica of the input signal of which phase and frequency can be accessible. It is sketched in figure 2.2. A numerically controlled oscillator (NCO) inside DPLL generates a sine or cosine wave signal, which is then mixed with the input signal in a multiplier. The combined signal goes through a low-pass filter to remove the harmonic part of the signal frequency (2f). After that, the input signal mixer with the sine wave is used as the error signal for the servo, a proportional-integral (PI) controller, to extract the instantaneous signal frequency. This result is stored in PIR. Following that, the PA integrates the instantaneous frequency to get the total phase as well as the fractional part to feed the sine/cosine LUT for generating the replicated signal. When the loop is closed and locked, the input and NCO sine signal have the same frequency and 90^o shifted in their total phases so that the error signal in the PI controller has a zero on average.

The main outputs of the DPLL are the frequency and the phase (total and fractional), which are in digital form as the values stored in PIR and PA, respectively. On the other hand, the error signal and the signal amplitude are also available from the DPLL. The signal amplitude comes from the mixer of the input signal with cosine wave generated by NCO.

ADC jitter noise correction

As mentioned in previous part, the interferometric heterodyne beatnotes are digitized by ADC. For the time reference, each spacecraft hosts a single ultra-stable oscillator (USO) to trigger all ADCs. Any imperfection in the ADC triggering by the USO will corrupt the following digitized signal and be inherited in other processing steps, including the digital blocks that exist in DPLL. This distortion leads an additional noise, considered as the ADC jitter noise [36], which violates the LISA requirement [103].

Unfortunately, it cannot be removed by any known on-ground post-processing algorithm. Hence, we correct it onboard by generating a reference signal with the USO, called the *pilot tone*, which is sampled together with the beatnotes by the ADC. The phase of this pilot tone is tracked by a DPLL. Since the pilot tone has a stable constant frequency, its phase

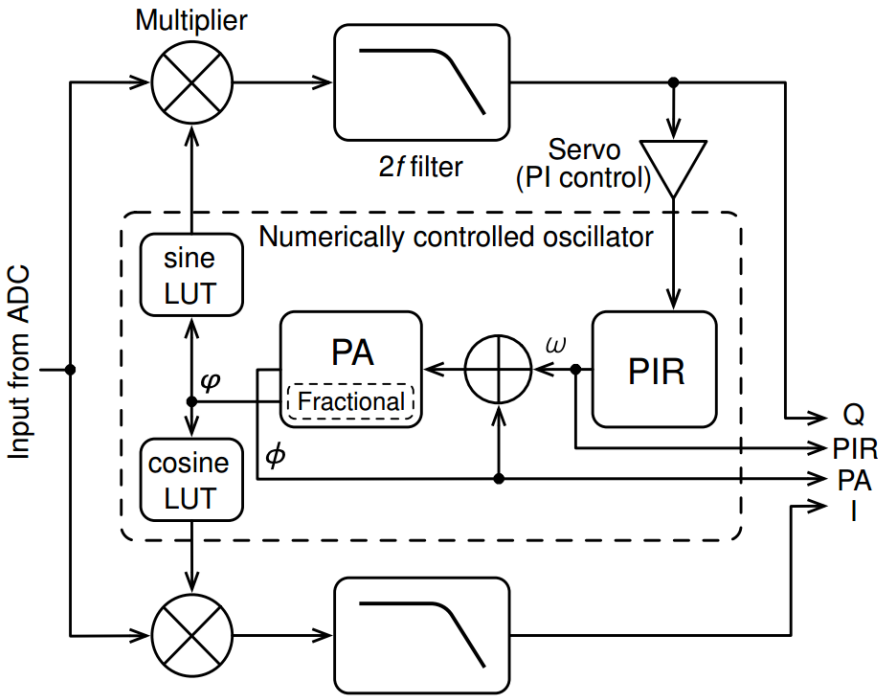

Figure 2.2: Schematic for DPLL, from [80]. The input analog signal from the ADC mixed to the sine/cosine wave signal generated by NCO, providing the quadrature signal $Q(t)$ and in-phase signal $I(t)$. In both, the harmonic part of 2f-frequency is suppressed by low-pass filters. The quadrature signal Q is then used to feed the PI controller to extract the instantaneous signal frequency, stored in PIR, which is converted to phase by the PA. The fractional of the integrated phase is then used by LUT to generate the sine/cosine wave signal for the mixers. The outputs of the DPLL are the quadrature $Q(t)$, the in-phase signal $I(t)$, the phase and frequency of the input signal stored in PIR and PA, respectively. $Q(t)$ is the error signal of the control loop, while $I(t)$ contains the input signal amplitude information.

evolution could be used as the reference to correct the distortion in the digitized signals in other DPLLs due to the ADC jitter. As illustrated in figure 2.3, the input signal, e.g. beatnote, is digitized by a jittering ADC at non-equidistant intervals even with the assumed perfect USO. Consequently, the replica digital signal, output of ADC, has shifts in the phase record, which could be misinterpreted as contributions from gravitational wave signals. A pilot tone, e.g. well-known sinusoidal signal, is generated and digitized by ADC in parallel with the signal. It is used as the reference signal to correct the time jitter in the phase record by comparing the replica signal of the pilot tone with its well-known shape. Hence, we can reconstruct the input signal in digital format.

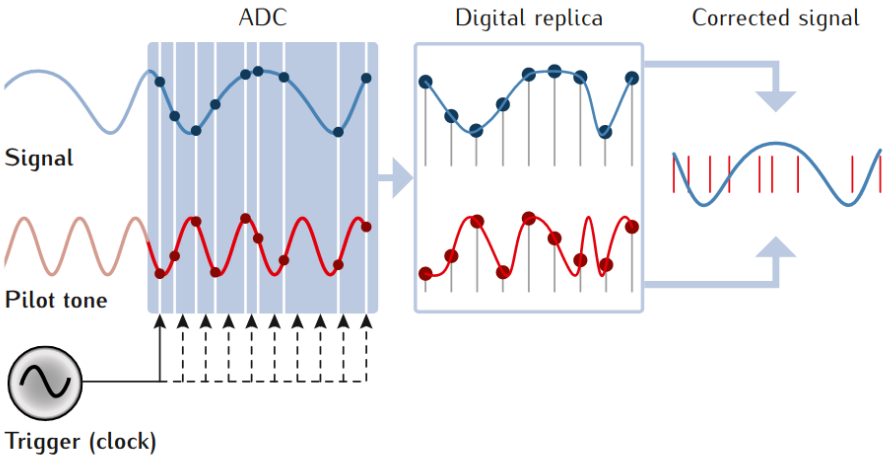

Figure 2.3: Schematic for the ADC jitter noise correction using pilot tone, taken from [37].

Clock jitter noise

On the other hand, the USO also has its own jitter, usually known as clock jitter noise. This noise will degrade the data points triggered by the ADC since it uses USO as the time reference. Furthermore, the USO in each spacecraft has a drift, making it difficult to synchronize all the LISA measurements. In other words, the data recorded in each spacecraft could have different time stamps with differential clock noise.

The solution for this problem is to use sidebands on the exchanging laser beam among spacecraft, which are modulated with the amplified clock noise imprinted by the Electro-Optical Modulator (EOM). Then, we can measure the differential phase noise between USOs of all spacecraft and use it for correct clock noise. The detail of this technical solution is described in [40, 76].

Ranging estimation

The dominant noise in the LISA measurement is laser frequency noise. The baseline algorithm for suppressing this noise is Time Delay Interferometry (TDI). We will discuss more detail about the laser frequency noise and TDI algorithm in chapter 3. Accordingly, TDI needs additional information about the absolute distances between spacecraft. One way to get this information is to imprint a unique pseudo-random noise (PRN) code in the beams exchanged among spacecraft, see section 3.6.4 in [76] for a detailed description. Some algorithms can be applied in post-processing to improve the distance estimation up to a few centimeters, such as Time Delay Interferometry Ranging (TDIR) [144].

Frequency distribution

For an overview picture of all processing discussed previously, we show in diagram 2.4 the links of all the processing blocks with their associated signals and sampling frequencies in one OB. This diagram is based on the original one from [76], and one can find a more detailed description in [37]. The values of the frequency placed in some blocks might be changed as the time the LISA mission evolves.

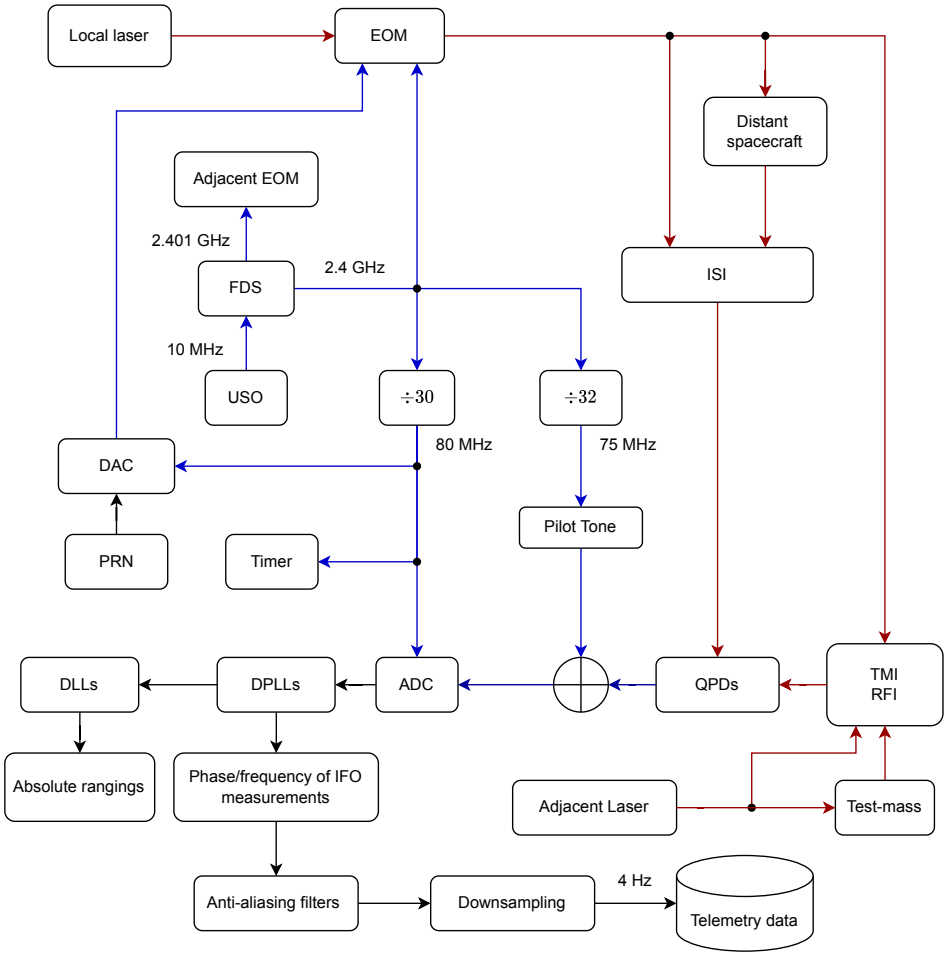

Figure 2.4: Diagram of main onboard processing with frequency distribution in one OB. The signal links represented in red, blue and black lines are associated with laser (optical), analog (electrical) and digital signals, respectively.

Accordingly, the timing signal produced by a single USO assumed at 10 MHz is fed to a Frequency Distribution System (FDS) to generate two electronic signals at 2.401 and 2.4 GHz. These signals are used to drive the EOM of two OBs in the spacecraft. EOMs convert them into the phase modulation of the local laser beam to generate sideband beatnotes.

The 2.4 GHz signal is also used as the time reference for other signal processing steps. In

particular, the ADC will trigger data at 80 MHz, a divider of 30 from the 2.4 GHz timing signal. This 80 MHz sampling frequency is applied for most onboard processing of the phasemeter, i.e. DPLLs and delay-locked loop (DLL)s. In addition, it is used by a Digital-to-Analog Converter (DAC) to convert PRN code from digital to analog signal and a timer to provide the time stamps for all phasemeter measurements. On the other hand, a 75 MHz signal, a divider of 32 from the 2.4 GHz timing signal, is used as a time reference to generate a pilot tone. This pilot tone is combined with the beatnotes measured by QPDs before being converted from analog signal to digital one by ADC.

The output of DPLLs could be the phase or frequency of the interferometric measurements with the ADC jitter correction by using pilot tone, as discussed previously.

Since 80 MHz data is enormous to be delivered to the Earth, we need to downsample them onboard before the telemetry. The onboard computer will apply an antialiasing filter to the data before downsampling them to avoid the effect of aliasing when decimating data [40, 43]. Eventually, the data are sampled at 4 Hz and sent to the Earth for on-ground data post-processing with a daily communication schedule [16].

2.6 Noises

Concerning the complexity of the LISA mission, we expect that many noise sources could critically influence the GW detection. This section will review the dominating noises, their (potential) shape and level. Most of the content of this section is referenced by [82] and [38]. We classify the considered noises into two big groups:

- The suppressed noises, which are the most dominant noise sources, should be reduced by some post-processing algorithms. They are laser frequency, clock jitter, spacecraft jitter, and tilt-to-length effect noises.

- The non-suppressed noises are secondary noises, so it is unnecessary to suppress them in data post-processing. However, studying these noises is still crucial since they contribute significantly to the LISA sensitivity after the dominating noises are suppressed. In particular, there are test-mass acceleration noise, optical path-length noise, readout noise, ranging noise, backlink noise, Etc.

2.6.1 Laser frequency noise

The first noise source is related to the instability of laser frequency. As described in 2.3, the laser source in the spacecraft generates a 1064 nm wavelength laser beam, so its frequency is about 282 THz. However, this frequency fluctuates by several MHz due to the quantized

mechanism of the laser. The shape of this frequency fluctuation is complex, based on the study for spacecraft-qualified laser source [141]. The laser is pre-stabilized using a stable cavity to reduce the frequency fluctuations. According to the requirements of the LISA mission, the laser frequency noise is considered as white noise with the absolute frequency stability in amplitude spectral density (ASD) of [82]:

$$\sqrt{S_p} = 30\frac{\text{Hz}}{\sqrt{\text{Hz}}}\sqrt{1+\left(\frac{2\times10^{-3}\text{Hz}}{f}\right)^4}, \tag{2.1}$$

where the factor $u_{\text{OMS}}(f) = \sqrt{1+\left(\frac{2\times10^{-3}\text{Hz}}{f}\right)^4}$ is the common factor for noises in the optical metrology system in order to allow a relaxation of the performance model at low frequency [82]. In `LISANode` simulator, which we will described in section 2.8, the laser frequency noise is implemented according to this model, with approximated absolute frequency stability at 28.8 $\frac{\text{Hz}}{\sqrt{\text{Hz}}}$ [38].

2.6.2 Clock jitter noise

As discussed in section 2.5.3, the USOs are used to generate the time reference signal for all onboard processing. The instability and drifts of the USOs in all the spacecraft affect the data triggering by ADC, which contributes a noise in the LISA measurements. This noise is called clock jitter noise, or clock noise for short.

In `LISANode` simulator, we model the clock noise as [38]:

$$\dot{q}_i(\tau) = \dot{N}_i^q(\tau) + y_{0,i} + y_{1,i}\tau + y_{2,i}\tau^2, \tag{2.2}$$

where

- q_i is the clock timing jitter of the USO in spacecraft i.
- τ is the spacecraft proper time;
- $N_i^q(\tau)$ is the random jitter noise for the USO in spacecraft i, generated as a flicker noise with following PSD, in fractional frequency derivative unit,

$$S_{\dot{N}_i^q}(f) = \left(6.32\times10^{-14}\right)^2\frac{1}{\text{Hz}}f^{-1}. \tag{2.3}$$

- $y_{0,i}$ is a constant deterministic frequency offset for the USO in spacecraft i. The three default values used in simulation for the 3 spacecraft are $5\times10^{-8}, 6.25\times10^{-7}, -3.75\times10^{-7}$.
- $y_{1,i}$ is a constant deterministic frequency linear drift for the USO in spacecraft i. The three default values used in simulation for the 3 spacecraft are $8\times10^{-16}\text{s}^{-1}, 1\times10^{-14}\text{s}^{-1}, -6\times10^{-15}\text{s}^{-1}$.

- $y_{2,i}$ is a constant deterministic frequency quadratic drift for the USO in spacecraft i. The three default values used in simulation for the 3 spacecraft are $3 \times 10^{-24}\mathrm{s}^{-2}, 2.25 \times 10^{-23}\mathrm{s}^{-2}, -3.75 \times 10^{-23}\mathrm{s}^{-2}$.

2.6.3 Spacecraft jitter noise

The spacecraft jitter noise is the residual motion of the spacecraft w.r.t inertial space in the LISA frequency band. It appears in multiple measurements (ISI and TMI), and is largely reduced by intermediary steps in the TDI algorithm (see chapter 3).

2.6.4 Tilt-to-length

The Tilt-To-Length (TTL) noise is related to the misalignment of the laser beam in OMS, both in the ISI and in the TMI. In the ISI, this is about the tilt of the normal vector of the wavefront of the incoming beam with the drag-free axis of the test-mass inside MOSA. While in the case of TMI, it is due to the disagreement of the normal vector of the bouncing beam from the adjacent MOSA and the drag-free axis of the test-mass [120]. The model for this noise is complex and out of the scope of this thesis.

2.6.5 Test-mass acceleration noise

Due to several spurious forces/disturbances, the test-mass is not perfectly free-falling in its sensitive axis as we proposed for the reference points for GW detection. We can list some of them as follows:

- The local gravitational gradients due to the imbalance of the spacecraft and MOSA mass distribution at the test-mass location could carry out a spurious force on the test-mass. This imbalance of mass distribution has many contributors. One is the gravitational fluctuation due to the thermal-elastic deformation of the spacecraft and test-mass, which depends eventually on temperature and pressure fluctuations.

- The elastic force gradients or "stiffness" coupling the test-mass to the motion of the surrounding objects such as GRS, OB, MOSA and spacecraft [82].

- The residual molecules in the vacuum chamber, containing the test-mass, create Brownian noise to the test-mass. This noise is strongly dependent on the temperature and pressure in the chamber, and its level decreases over time by the residual gas damping in the spacecraft. This effect is the motivation for a study of non-stationary noise, which is described in sections 2.8.2 and 4.2.4.

- The cosmic rays could charge the test-masses. Hence, it is sensitive to the average stray electrostatic field in electrode housing by, for example, the stray forces from GRS actuators. This effect leads to electrostatic fluctuations of the test-mass. However, this noise could be mitigated by a discharging system to neutral the test-mass charge [25].
- As we described in section 2.4, the actuators provides some forces and torques to control the position and attitude of the test-mass inside GRS w.r.t. the spacecraft in non-sensitive axes. The imperfection or any noise in the actuators could lead to the disturbance on the test-mass.
- Radiation pressure noise from the laser beam bouncing on the test-mass. The exchange momentum of test-mass and the EM field of the laser can lead to the spurious force on the test-mass.

The experimental shape for the test-mass acceleration noise of the LISA mission is still under investigation. However, we could use the experience gained from the LPF about the test-mass acceleration noise. From the LPF data, we construct the possible test-mass acceleration noise in PSD as [82, 103]:

$$S_\delta(f) = \left(2.4 \times 10^{-15}\right)^2 \frac{\mathrm{m}^2}{\mathrm{s}^4\mathrm{Hz}} \left[1 + \left(\frac{0.4 \times 10^{-3}\mathrm{Hz}}{f}\right)\right] \left[1 + \left(\frac{f}{8 \times 10^{-3}\mathrm{Hz}}\right)^4\right]. \tag{2.4}$$

We can neglect the last factor, which contributes mostly at the high frequency, to simplify the implementation. Therefore, the test-mass acceleration noise that we adopt to implement in `LISANode` is given by

$$S_\delta(f) = \left(2.4 \times 10^{-15}\right)^2 \frac{\mathrm{m}^2}{\mathrm{s}^4\mathrm{Hz}} \left[1 + \left(\frac{0.4 \times 10^{-3}\mathrm{Hz}}{f}\right)\right]. \tag{2.5}$$

2.6.6 Optical path-length noise

This noise category accounts for all contributions to the optical path-length variation in the MOSAs, either inside the OB or in the telescope. Most of them are due to temperature fluctuation. Hence, the optical path-length noise is sometimes called thermo-mechanical noise. This noise occurs in many parts of MOSA such as point-ahead angle mechanism (PAAM) piston, OB baseplate, interferometer waveplates, OB mirror, test-mass, GRS window, Etc. [82].

These noises are white noise with the relaxation factor, given in ASD as

$$\sqrt{S_{N^{\mathrm{op}}}} = A\sqrt{1 + \left(\frac{2 \times 10^{-3}\mathrm{Hz}}{f}\right)^4}, \tag{2.6}$$

where the noise level depends on the laser beam to which they contribute. For the telescope optical path-length noise, we set:

- in the incoming laser beams at the telescope received by the spacecraft: $A = 10^{-15} \frac{\mathrm{m}}{\sqrt{\mathrm{Hz}}}$,
- in the outgoing laser beams at the telescope sent by the spacecraft: $A = 2 \times 10^{-15} \frac{\mathrm{m}}{\sqrt{\mathrm{Hz}}}$,
- we also give an common mode noise in both incoming and outgoing laser beams to account for the fully-correlated noise in two beams: $A = 1.5 \times 10^{-15} \frac{\mathrm{m}}{\sqrt{\mathrm{Hz}}}$. Some correlation scenarios of telescope optical path length noise are addressed in section 2.7.6 and used for the study of noise propagation in chapter 4.

For the overall optical path-length noise in the OB, we set:

- for the local beams in the TMI, $A = 4.24 \times 10^{-12} \frac{\mathrm{m}}{\sqrt{\mathrm{Hz}}}$,
- for the local beams in the RFI, $A = 2 \times 10^{-12} \frac{\mathrm{m}}{\sqrt{\mathrm{Hz}}}$,
- for the other beams, $A = 10^{-15} \frac{\mathrm{m}}{\sqrt{\mathrm{Hz}}}$,

These values are partially provided by LISA Performance Model [82], and some unknown ones has been chosen insignificant (about femtometers) in the simulation to avoid the overall shape. They will be updating based on LISA instrument design and testings in the next phase of the LISA mission.

The TTL is also an optical path noise, and implemented in the current version of `LISANode`. However, it is excluded in the simulation used in this thesis.

2.6.7 Readout noise

This terminology covers all noise terms related to the readout process in the OMS, including readout noise (photoreceiver and phasemeter noises), optical noises (shot noise, stray light, Relative Intensity Noise (RIN)...) and thermal noises.

The main expected contributors to the readout noise are listed below.

- The noise from the front-end electronics of the photoreceiver.
- The shot noise is due to the quantum statistical property of the weak power interference beams. The number of photons received by the photodiodes is infinitesimally varying with the Poisson distribution. This fluctuation is proportional to the reciprocal of the square root of the number of photons, which eventually depends on the power of the laser beams. Shot noise is one of the dominant noise sources in the overall readout noise of the ISI since the power of the received beam is low, about hundreds of pW (300 pW in the current performance model [82]).

- The stray light from the scattering of laser beams in the optical bench or the telescope could end up a phase noise in the interferometric measurements.
- The RIN corresponds to the instability of the laser beam power. This noise comes from the laser cavity vibration, fluctuations in laser gain medium, Etc. RIN typically peaks at the relaxation oscillation frequency of the laser, i.e. the heterodyne frequency, and then falls off in the higher frequency band.

In `LISANode` simulator, we have implemented the overall readout noise in ASD as the white noise, given by ASD [38]

$$\sqrt{S_{N^{\mathrm{ro}}}} = A\sqrt{1+\left(\frac{2\times 10^{-3}\mathrm{Hz}}{f}\right)^4}, \tag{2.7}$$

where noise level A depends on the interferometric measurements,

- inter-satellite interferometer: $A = 6.35\times 10^{-12}\frac{\mathrm{m}}{\sqrt{\mathrm{Hz}}}$,
- sideband inter-satellite interferometer: $A = 1.25\times 10^{-11}\frac{\mathrm{m}}{\sqrt{\mathrm{Hz}}}$,
- test-mass interferometer: $A = 1.42\times 10^{-12}\frac{\mathrm{m}}{\sqrt{\mathrm{Hz}}}$,
- reference interferometer: $A = 3.32\times 10^{-12}\frac{\mathrm{m}}{\sqrt{\mathrm{Hz}}}$,
- sideband reference interferometer: $A = 7.9\times 10^{-12}\frac{\mathrm{m}}{\sqrt{\mathrm{Hz}}}$,

and $u_{\mathrm{OMS}}(f) = \sqrt{1+\left(\frac{2\times 10^{-3}\mathrm{Hz}}{f}\right)^4}$ is the relaxation factor for the noises in the optical metrology system.

2.6.8 Backlink noise

As mentioned in 2.5.1, two OBs are connected by a bi-directional backlink to exchange the local laser beams. In the current LISA instrumental baseline, an optical fibre is used so the MOSA can freely rotate w.r.t. each other. However, the differential path of the two direction links in the fibre could add up noises to the TMI and RFI measurements, which is known as non-reciprocity of the backlink. It eventually carries out a residual path-length noise in the measurements.

In `LISANode` simulator, we implemented the non-reciprocal backlink noise in ASD as follow:

$$\sqrt{S_{N^{\mathrm{bl}}}} = 3\times 10^{-12}\frac{\mathrm{m}}{\sqrt{\mathrm{Hz}}}\sqrt{1+\left(\frac{2\times 10^{-3}\mathrm{Hz}}{f}\right)^4}. \tag{2.8}$$

Note that we used the same noise level for backlink noise for both RFI and TMI but in fact it will be slightly different. Moreover, two backlink noises in optical measurements in different

MOSAs in the spacecraft are certainly correlated. We will examine some correlation scenarios for the backlink noise in chapter 4.

2.6.9 Ranging noise

The absolute distances among spacecraft are the input for the TDI algorithm, described in chapter 3. We use PRN codes imprinted in the exchanged laser beam in the LISA constellation for the ranging estimation, as mentioned in section 2.5.3. Consequently, the error in this estimation contributes to the data processing as ranging noise. Currently, we use an ad-hoc model for studying the ranging noise and for `LISANode` implementation. This model takes account for a systematic bias $N^{\mathrm{R},o}$, for example, by cable transmission delays, and for a stochastic Gaussian white noise $N^{\mathrm{R},\epsilon}$, as follows

$$N^{\mathrm{R}}(t) = N^{\mathrm{R},o} + N^{\mathrm{R},\epsilon}(t), \tag{2.9}$$

where the bias could be a few nanoseconds (default value in `LISANode` is $N^{\mathrm{R},o} = 0$ s), and the amplitude spectral density of the stochastic ranging noise is

$$\sqrt{S_{N^{\mathrm{R},\epsilon}}} = 3 \times 10^{-9} \frac{\mathrm{s}}{\sqrt{\mathrm{Hz}}}. \tag{2.10}$$

2.6.10 Noise unit conversion

As we can see, the noises are usually expressed in different units. In order to use them (comparison, linear or quadratic sum for the noise budget, simulation, Etc.), we need to convert them into the same unit. The relation between the PSD of the noise in acceleration unit of $\mathrm{m}^2.\mathrm{s}^{-4}.\mathrm{Hz}^{-1}$, and the one in displacement (length unit) of $\mathrm{m}^2.\mathrm{Hz}^{-1}$ is

$$S_{acc,\mathrm{m}}(f) \quad = \quad S_{acc,\mathrm{m.s}^{-2}}(f) \times \left(\frac{1}{2\pi f}\right)^4 \mathrm{m}^2.\mathrm{Hz}^{-1}. \tag{2.11}$$

The conversion for the PSD in displacement and in relative frequency units of Hz^{-1} is

$$S_{\frac{\delta\nu}{\nu}}(f) \quad = \quad S_m(f) \times \left(\frac{2\pi f}{c}\right)^2 \mathrm{Hz}^{-1}. \tag{2.12}$$

2.7 Instrumental model

In this section, we will give a detailed model for the propagation of the laser beams in the LISA constellation and the onboard processing in spacecraft.

2.7.1 Laser model

First, we start with the model for the electromagnetic (EM) field of the laser beam. In classical principle, an EM is represented by two three-dimensional vectors for the electric and magnetic

fields. For simplicity, we use the plane wave approximation to consider only the amplitude of the EM field. Any effect of the imperfect wavefront of the EM vector field in the interferometer will be considered by equivalent longitudinal path-length variations. Furthermore, since the electric and the magnetic fields have a close correlation, i.e. one can determine the amplitude of the magnetic field from the electric one (see for example [70]), we can use only the electric field for modelling the laser beam. Hence, in our simplified model, the laser beam is represented by an electric field given by

$$E(t) = E_0(t) \exp\left[j\Phi(t)\right] = E_0(t) \exp\left[j\left(2\pi\nu_0 t + \phi(t)\right)\right], \tag{2.13}$$

where the reference time is the spacecraft proper time. $\Phi(t)$ is the instantaneous total phase of the laser beam, in radian unit, which includes the nominal phase $2\pi\nu_0 t = \omega_0 t$ and the phase deviation $\phi(t)$. We can deduce the instantaneous frequency from $\Phi(t)$ via the relation:

$$\nu(t) = \frac{1}{2\pi}\frac{d\Phi(t)}{dt} = \nu_0 + \frac{1}{2\pi}\frac{d\phi(t)}{dt}, \tag{2.14}$$

where ν_0 is the central or nominal laser frequency, a constant at 281.6 THz.

The information of the laser beam can be represented as its total phase or, equivalently, its instantaneous frequency. In the `LISANode` simulator, we use the frequency to express the laser beam since the phase is increasing quickly in time and hence more complicated to be implemented. In addition, the evolution of the instantaneous frequency is driven by the frequency planning and Doppler effects when exchanging beams between relative moving spacecraft. Consequently, the instantaneous frequency has a large frequency offset of about MHz, by the sideband modulation of about 2.4 GHz, and by interested GW signal imprinted in the frequency shift of a few hundreds of nHz. Furthermore, the instrumental noises and their residuals after post-processing algorithms also contribute to the total instantaneous frequency, in order of hundreds nHz. In order to avoid the limitations of the numerical precision in the simulation, we express the total instantaneous laser frequency variable in two time-dependent components representation, the large frequency offsets $\nu^o(t)$ and the small frequency fluctuation $\nu^\epsilon(t)$, by the following relation [38]:

$$\nu(t) = \nu_0 + \nu^o(t) + \nu^\epsilon(t). \tag{2.15}$$

Hence, the amplitude of an electric field reads

$$E(t) = E_0(t) \exp\left(j2\pi \int_{t_0}^{t} \nu(\tau) d\tau\right). \tag{2.16}$$

In the case of stable laser frequency, it is convenient to use the timing jitter $x(t)$ in second or fractional frequency deviations $y(t)$ to express the information contained in the laser beam,

as defined by

$$x(t) = \frac{\phi(t)}{2\pi\nu_0} \tag{2.17}$$

$$y(t) = \frac{\nu(t)-\nu_0}{\nu_0} = \frac{\dot{\phi}(t)}{2\pi\nu_0} = \dot{x}(t), \tag{2.18}$$

so that

$$\Phi(t) = 2\pi\nu_0(t+x(t)) \tag{2.19}$$

$$\nu(t) = \nu_0(1+y(t)). \tag{2.20}$$

2.7.2 Laser beam propagation

Let us consider a laser beam propagating from one spacecraft to another. Assuming the propagation in the perfect pointing from spacecraft A to spacecraft B, the received beam at spacecraft B as a phase (for details, see sections 3.4.3 of [40] and 5.5.1 of [76]):

$$\Phi_B(\tau_B) = \Phi_A(\tau_B - \tau_{AB}(\tau_B)), \tag{2.21}$$

where τ_B is the proper time of the co-moving reference frame with spacecraft B, and τ_{AB} is the light travel time between both spacecraft (proper pseudo-range). In fractional frequency deviation, we can show [76] that

$$\nu_B(\tau_B) \approx \nu_A(\tau_B - \tau_{AB}(\tau_B))(1-\dot{\tau}_{AB}(\tau_B)). \tag{2.22}$$

Then since $\dot{\tau}_{AB} \ll 1$, we can simplify it to

$$\nu_B(\tau_B) \approx \nu_A(\tau_B - \tau_{AB}(\tau_B)). \tag{2.23}$$

For convenience, we will use the notation of delay operator acting on a time-series signal as

$$\mathbf{D}_{AB}\nu_B(\tau_B) = \nu_B\left(\tau_B - \tau_{AB}(\tau_B)\right). \tag{2.24}$$

In the study of this thesis, we assume that the independent spacecraft proper times have already been converted to the global one such as Barycentric Coordinate Time (TCB), as we will discuss further in section 3.1. Hence, the standard notation t is used for the time reference. The following subsections focus on how we construct the beams that participate in the IFO measurement. Most of the materials in these parts are extracted from our to-be-published article [127].

2.7.3 Notation and convention

We follow the convention for the LISA constellation proposed by LISA Consortium [102]. The indexing is summarized on figure 2.5. Spacecraft are indexed 1, 2, 3 clockwise when looking down at their solar panels. Each of them hosts two MOSA which include the test-mass and its housing, the optical bench and the telescope. A laser source is associated with each MOSA. MOSAs on each spacecraft are indexed with two numbers ij:

- The first number i is the index of the S/C the MOSA is mounted on, i.e. the local S/C.
- The second number j is the index of the S/C the MOSA points to.

All subsystems of the MOSA, such as OB, the associated laser and the optical measurements, are indexed according to this MOSA. There are 3 main IFO measurements in each MOSA: ISI, TMI and RFI, which are respectively denoted as isi, tmi, rfi.[1]

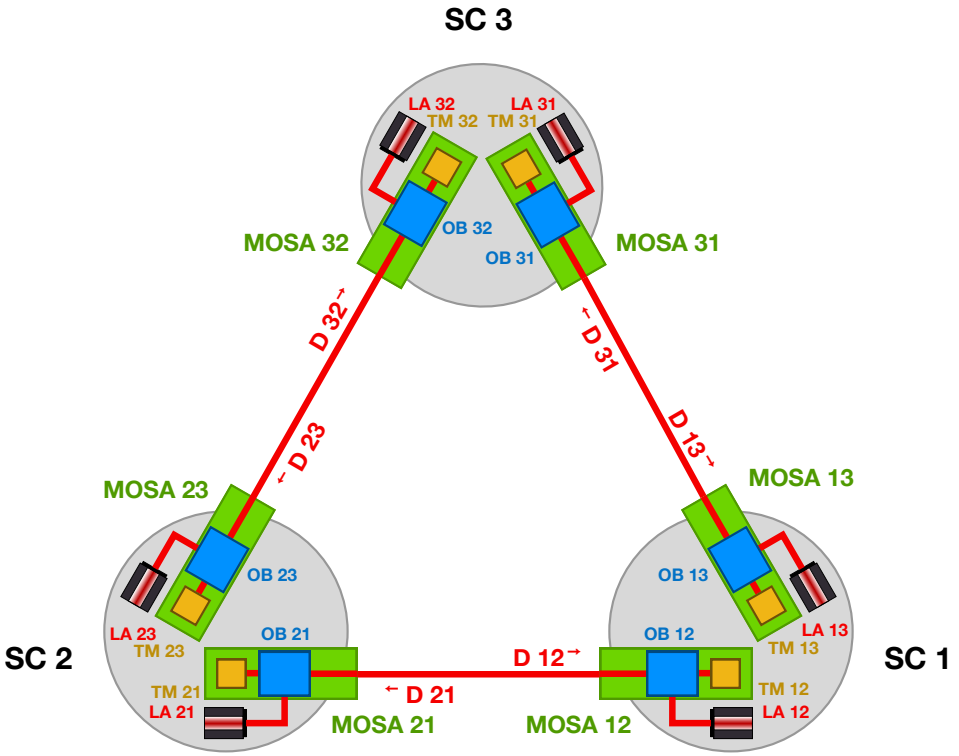

Figure 2.5: LISA constellation convention. The MOSA hosted on SC1 pointing at SC2 is labeled MOSA_{12}. Each element hosted on this MOSA and the associated laser source will share the same indexes. For example the noise due to the laser associated to the MOSA_{12} will be labeled p_{12}.

[1] To feed the clock noise reduction algorithm, we also need the sideband measurements in the ISI and the RFI [77].

We define $L_{ij}(t)$ as the light travel time from S/C j to S/C i, in seconds. Here, the time reference t is the time when the beam arrives at the spacecraft i. For the propagation of light, we denote the propagation delay operator[2] by $\mathbf{D}_{ij}$, so that $\mathbf{D}_{ij}u(t) = u(t - L_{ij}(t))$ for any time-series $u(t)$. We also use the TDI delay operator $\mathcal{D}_{ij}$, such that $\mathcal{D}_{ij}u(t) = x(t - \hat{L}_{ij}(t))$, where $\hat{L}_{ij}(t)$ is the estimate of the light travel time $L_{ij}(t)$. For nested delay operators, we use the short hand notation $d_{i_1 i_2 \ldots i_n} \equiv d_{i_1 i_2} d_{i_2 i_3} \ldots d_{i_{n-1} i_n}$, where d could be $\mathbf{D}$ or $\mathcal{D}$. In general, those delay operators are not commutative since light travel times evolve with time. If we use the commutator notation of $[A, B] = AB - BA$ then $[\mathbf{D}_{ij}, \mathbf{D}_{mn}]u(t) \neq 0$ when $(i, j) \neq (m, n)$. But if delay times or armlengths are assumed to be constant, delay operators become commutative. We will use this approximation to simplify the computation process later on.

Another process we indicate using an operator is the action of the anti-aliasing filters, which are used to prevent power folding in the band of interest during decimation. Its operator is denoted as $\mathcal{F}$, such as $\mathcal{F}u(t) = (f * u)(t)$, where the asterisk stands for the convolution of time-series $u(t)$ with the filter kernel $f(t)$.

The GW signal measured in the ISI_{ij}, caused by the accumulated delay of the beam received on S/C i from S/C j due to a GW, is labelled H_{ij}.

The wavelength of laser associated to MOSA_{ij} is λ_{ij} and its frequency is denoted as $\nu_{ij} = c/\lambda_{ij}$. We also define the frequency of the laser beam received by MOSA_{ij} from MOSA_{ji} as $\nu_{i \leftarrow j}$. Due to the Doppler shift along the link L_{ji}, $\nu_{i \leftarrow j} \neq \nu_{ji}$. The laser frequency ν is the sum of nominal frequency (carrier or sideband – THz), an offset frequency (Doppler and laser locking – MHz) and small fluctuations (noises and GWs – nHz to Hz), following equation (2.15) as discussed in section 2.7.1.

The interferometric signals in LISA are the heterodyne beatnote frequencies, i.e., the frequency differences between the frequencies of associated beams (offsets and small fluctuations). Their signs are (beatnote polarities) θ^{isi} and θ^{rfi} for isi and tmi / rfi signals, respectively.

$$\begin{cases} \theta^{\text{isi}}_{ij} &= \text{sign}(\omega_{i \leftarrow j} - \omega_{ij}), \\ \theta^{\text{tmi}}_{ij} = \theta^{\text{rfi}}_{ij} &= \text{sign}(\omega_{ik} - \omega_{ij}), \end{cases} \tag{2.25}$$

where $\omega = 2\pi\nu$, (i, j, k) matches every permutation of $(1, 2, 3)$. In general, $\theta^{isi}_{ij} \neq -\theta^{\text{isi}}_{ji}$ but $\theta^{\text{rfi}}_{ij} = -\theta^{\text{rfi}}_{ik}$.

For the noise notation using in the beams, The laser frequency noise is the dominant noise source in LISA, and suppressed by TDI post-processing algorithm (see section 3.2.2). Other noises that are not suppressed by TDI or other post-processing algorithms are classified

[2]Technically, since the measurements will be expressed in relative frequency fluctuation units, $\mathbf{D}_{ij}$ is a Doppler-delay operator $\mathbf{D}_{ij}u(t) = (1 - \dot{L}_{ij}(t))u(t - L_{ij}(t))$ (see section 7.2 of [76]).

unsuppressed noises. Unsuppressed noises are subdominant (for example with respect to laser frequency noise or clock noise) but once these dominant noises have been suppressed, they contribute to the LISA noise budget. It is therefore necessary to study their propagation through TDI.

The measurements will be either in phase or frequency, or a mixture of both. The final choice is not yet made. Since the noises we are interested are expressed as small fluctuations (phase or frequency), we will assume that the measurements are in relative frequency fluctuations. It is also the unit used for most of the GW analyses.

We will denote the LISA instrumental noises as follows:

- p_{ij}: laser frequency noise (free-running or locked, see 2.7.7) of the laser on MOSA ij;
- $\delta_{ij} = \vec{\delta}_{ij}.\hat{\mathbf{n}}_{ji}/c$: projection of test-mass ij jitter noise vector $\vec{\delta}_{ij}$ onto the sensitive axis. $\hat{\mathbf{n}}_{ji}$ is the reference axis for the MOSA ij, i.e., from test-mass to OB (see figures 2.5 and 2.6). We assume that all measurements are in fractional frequency units. The test-mass jitter noise is expressed in velocity (m/s), so we need the factor $1/c$ (see [40] for the detailed derivation);
- $\Delta_{ij} = \vec{\Delta}_{ij}.\hat{\mathbf{n}}_{ji}/c$: projection of MOSA ij jitter noise vector $\vec{\Delta}_{ij}$ onto the sensitive axis (longitudinal axis);
- $N^{\text{op}}_{\alpha,ij}$: generic optical path (OP) noise term due to optical path fluctuations on OB ij. α refers to:
  - TX/isi: OP noise on the beam transmited to the distant S/C induced by the sending S/C;
  - RX/isi: OP noise on the beam received from the distant S/C induced by the receiving S/C;
  - tmi: OP noise on adjacent beam in the TMI measurement;
  - rfi: OP noise on adjacent beam in the RFI measurement;
  - loc/isi: OP noise on local beam in the ISI measurement;
  - loc/tmi: OP noise on local beam in the TMI measurement;
  - loc/rfi: OP noise on local beam in the RFI measurement.
- $N^{ro}_{x,ij}$: readout noise for the x measurement of OB ij, $x \in \{\text{isi}, \text{tmi}, \text{rfi}\}$;
- $\mu^{x}_{ij\to ik}$: backlink noise for measurement x, $x \in \{\text{tmi}, \text{rfi}\}$. This noise is dominated by straylight in the optical fibre connecting two MOSAs of the same S/C (from OB ij to OB ik, (i, j, k) is the every combination of $(1, 2, 3)$). In general, this noise is non-reciprocal, i.e. $\mu^{x}_{ik\to ij} \neq \mu^{x}_{ij\to ik}$.

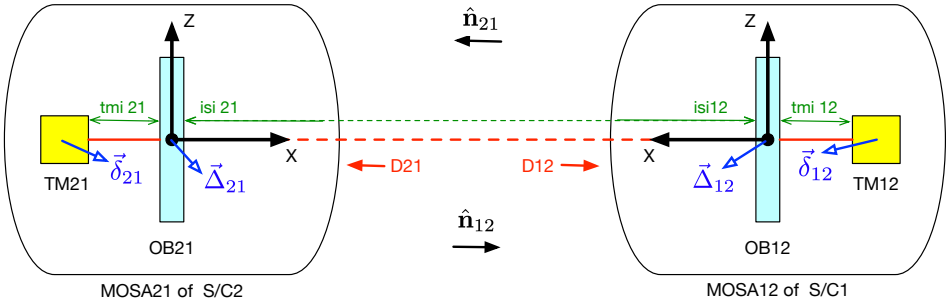

Figure 2.6: Conventions for direction of beams and motions for MOSA 12 and MOSA 21. Note that the unit vector along x-axis of local reference frame for MOSA 12 is $\hat{\mathbf{n}}_{21}$, inverse the two indices w.r.t MOSA convention.

2.7.4 Beam modeling

In order to model the interference measurement, we start by modeling the beams that interfere in terms of combination of noises. The main six beams of the three interferometers in the MOSA 12 are described as

$$b_{\text{isi},21\to12} = \mathbf{D}_{12}\left[p_{21} + N^{\text{op}}_{TX/\text{isi},21} - \frac{1}{c}\hat{\mathbf{n}}_{12}.\vec{\Delta}_{21}\right] + H_{12} - \frac{1}{c}\hat{\mathbf{n}}_{21}.\vec{\Delta}_{12} + N^{\text{op}}_{RX/\text{isi},12} \tag{2.26a}$$

$$b_{\text{tmi},13\to12} = p_{13} + \mu^{\text{tmi}}_{13\to12} + N^{\text{op}}_{\text{tmi},12} \tag{2.26b}$$

$$b_{\text{rfi},13\to12} = p_{13} + \mu^{\text{rfi}}_{13\to12} + N^{\text{op}}_{\text{rfi},12} \tag{2.26c}$$

$$b_{\text{isi},12\to12} = p_{12} + N^{\text{op}}_{loc/\text{isi},12} \tag{2.26d}$$

$$b_{\text{tmi},12\to12} = p_{12} + \frac{2}{c}\hat{\mathbf{n}}_{21}.(\vec{\Delta}_{12} - \vec{\delta}_{12}) + N^{\text{op}}_{loc/\text{tmi},12} \tag{2.26e}$$

$$b_{\text{rfi},12\to12} = p_{12} + N^{\text{op}}_{loc/\text{rfi},12}, \tag{2.26f}$$

where

- $b_{\text{isi},21\to12}$ is the beam from MOSA 21 received by MOSA 12,
- $b_{\text{rfi},13\to12}$ and $b_{\text{tmi},13\to12}$ are the beams propagating from MOSA 13 to MOSA 12 through the backlink, which respectively contribute to RFI and TMI measurements.
- $b_{x,12\to12}$ are the local beams of the MOSA 12 with $x \in \{\text{isi}, \text{tmi}, \text{rfi}\}$.

In the current design, the local beam of the tmi, $b_{\text{tmi},12\to12}$, is bouncing on the test-mass. The sign convention is such that if the test-mass moves towards the OB, i.e. $\vec{\delta}_{12}$ points in the positive direction which is $\hat{\mathbf{n}}_{21}$, the optical path on the beam $b_{\text{tmi},12\to12}$ decreases. If the OB

moves away from the test-mass, i.e., $\vec{\Delta}_{12}$ points in the positive direction, the optical path on the beam $b_{\text{tmi},12\to12}$ increases while it decreases on $b_{\text{isi},21\to12}$.

The beams in MOSA 13 are constructed in the same way. One can easily write them from the formulae of MOSA 12 by replacing index 2 by 3 everywhere. The beams in other the MOSAs can be deduced by circular permutation of indices ($1 \to 2 \to 3 \to 1$).

2.7.5 Interferometer measurement

Using those beams, we can construct the 3 main IFO measurements, for example in the MOSA 12, as follows

$$\begin{cases} \text{isi}_{12} &= \mathcal{F}\left[\theta_{12}^{\text{isi}}\left(b_{\text{isi},21\to12} - b_{\text{isi},12\to12}\right) + N^{ro}_{\text{isi},12}\right] \\ \text{tmi}_{12} &= \mathcal{F}\left[\theta_{12}^{\text{rfi}}\left(b_{\text{tmi},13\to12} - b_{\text{tmi},12\to12}\right) + N^{ro}_{\text{tmi},12}\right] \\ \text{rfi}_{12} &= \mathcal{F}\left[\theta_{12}^{\text{rfi}}\left(b_{\text{rfi},13\to12} - b_{\text{rfi},12\to12}\right) + N^{ro}_{\text{rfi},12}\right]. \end{cases} \tag{2.27}$$

As indicated before, the measurements are expressed in relative frequency fluctuation units. In phase units, these equations are similar, with additional conversion factors.

2.7.6 Correlations

Even though, the impact of correlations has been discussed in early TDI studies [139]. In most studies, as for example [128, 100, 16, 103], the LISA Instrument noise performance are assessed as uncorrelated single link contribution from optical measurement system and test-mass acceleration. This assumption simplifies the calculation of noise propagation but may induce non-negligible errors in the estimation of LISA performances. To quantitatively estimate the deviation from the ideal case, we will consider some generic scenarios of correlation in this study. Furthermore, we can split the noises into two parts, the correlated and uncorrelated terms, and derive their transfer functions separately.

One obvious correlation scenario is related to the thermo-mechanical OP noises in the telescope[3]. Since the same telescope is used for both sending and receiving beams, it will imprint an identical noise at the ISI beam, located at both end of a link. The optical path noise on the emitted beam $N^{OP}_{TX/\text{isi},ij}$ and the received beam $N^{OP}_{RX/\text{isi},ij}$ in the telescope of MOSA ij are fully correlated:

$$N^{OP}_{TX/\text{isi},ij} = N^{OP}_{RX/\text{isi},ij}. \tag{2.28}$$

Another correlation scenario is related to test-mass acceleration noise. The two test-masses share the same S/C and thus will likely have correlated source of noises like temperature

[3]While the optical path noise enters in the ISI measurements in the same way as the MOSA jitter noise, it is not canceled in the TDI algorithm, which is described later in chapter 3, because it does not appear in the TMI measurement.

driven noises (stiffness, symetric outgassing), cross-talk of S/C jitter, coupling with local and interplanetary magnetic fields or local gravity field fluctuation. We express it by the following correlation relation

$$\vec{\delta}_{ij}.\hat{\mathbf{n}}_{ji} = \gamma\, \vec{\delta}_{ik}.\hat{\mathbf{n}}_{ki}, \tag{2.29}$$

where γ is the correlation factor and (i, j, k) can be any permutation of $(1, 2, 3)$. γ is 1 in the case of fully-correlated noise, or -1 in case of anti-correlation. We will derive the propagation of the fully-correlated acceleration noise in section 4.2.4. In addition, we also give the result of transfer function for other correlation scenarios such as anti-correlated acceleration noise, fully correlated and anti-correlated adjacent (same S/C) interferometer noise, and fully-correlated optical path noise at the same telescope.

2.7.7 Frequency planning - laser locking scheme

The inter-satellite separation distance varies in time due to orbital dynamics. As a consequence, the laser beam coming from the distant S/C is frequency-shifted by about 10 MHz according to the Doppler effect. The laser frequencies used for the interferometric measurement are slightly offset. There is a time evolution of the beatnote between the two beams used to measure phase shift via heterodyne interferometry.

The optical measurement system tracks the beatnote frequencies in the range of 5 to 25 MHz, which is not compatible with free running lasers and Doppler-shifted beams. To accomodate this constraint, we lock the lasers by controlling the frequency of a laser (therefore the beatnote frequencies) such that they remain equal to a pre-programmed reference value [79]. We use the RFI measurement to phase-lock a laser with its adjacent laser in the same S/C (local locking), and the ISI signal to lock the local laser to the distant laser (distant locking). In the end, 5 of 6 lasers will be locked on the primary laser. In this study, we assume that laser frequency control works perfectly so the locking beatnote offset, laser frequency offset plus the Doppler shift if it is distant locking, is exactly equal to the desired value. We also do not consider the beatnote offset in the IFO measurement, as discussed in subsection 2.7.5. The constraint equation of the beatnote fluctuation is used without filter since the laser locking control loop operates at high frequency before measurements are filtered and downsampled [76].

In this study, the configuration N4-32 (cfg_N2c in [79]) has been used[4]. A schematic of this phase-locking is shown on figure 2.7. The constraints on the beatnote fluctuations (without anti-aliasing filter, denoted by $\not{\mathcal{F}}$, since the locking is done by a closed-loop before the IFO

[4]We used N4-32 because it was the preferred configuration when this study started. Currently the preferred configuration is N1-12 but this does not change the final results which are independent of the locking configuration.

measurements are read by phasemeter and then processed in the anti-aliasing filter) are

$$\cancel{\text{isi}}_{21} = 0, \tag{2.30a}$$
$$\cancel{\text{rfi}}_{31} = 0, \tag{2.30b}$$
$$\cancel{\text{isi}}_{13} = 0, \tag{2.30c}$$
$$\cancel{\text{rfi}}_{12} = 0, \tag{2.30d}$$
$$\cancel{\text{isi}}_{23} = 0, \tag{2.30e}$$

which yields the following formulation for the 5 locked laser frequency fluctuations:

$$p_{23} = \theta_{23}^{\text{isi}} N_{\text{isi},23}^{ro} + b_{\text{isi},32\to23} - N_{loc/\text{isi},23}^{op}, \tag{2.31a}$$
$$p_{31} = \theta_{31}^{\text{rfi}} N_{\text{rfi},31}^{ro} + b_{\text{rfi},32\to31} - N_{loc/\text{rfi},31}^{op}, \tag{2.31b}$$
$$p_{13} = \theta_{13}^{\text{isi}} N_{\text{isi},13}^{ro} + b_{\text{isi},31\to13} - N_{loc/\text{isi},13}^{op}, \tag{2.31c}$$
$$p_{12} = \theta_{12}^{\text{rfi}} N_{\text{rfi},12}^{ro} + b_{\text{rfi},13\to12} - N_{loc/\text{rfi},12}^{op}, \tag{2.31d}$$
$$p_{21} = \theta_{21}^{\text{isi}} N_{\text{isi},21}^{ro} + b_{\text{isi},12\to21} - N_{loc/\text{isi},23}^{op}. \tag{2.31e}$$

2.8 `LISANode` simulator

Since LISA is planned to be launched in the next decades, to study the feasibility of its instrument and the performance of the related data analysis methods, some simulators have been developed to generate data as realistic as possible. We can list some of them such as `SyntheticLISA` by M.Vallisneri et al. [148], `LISASimulator` by N.Cornish et al. [131], `LISACode` by A.Petiteau et al. [125], `LISANode` by J-B.Bayle et al. [45], `LISA Instrument` by J-B.Bayle, M.Staab et al. [42], Etc. Currently, the LISA simulation is mostly using `LISANode`. This software, written in Python and C++, generates time-series data of interferometric measurement data (L0 data). It has been used with collaborative development tools such as GitLab, Wikis, and Continuous Integration. Therefore, it is user-friendly for adjusting the configuration, adapting new features, and testing some units of the full implementation. In this section, we will briefly introduce `LISANode`, its architecture and the implementation philosophy. Then, we present some new features we contributed to the `LISANode` simulator during this PhD.

2.8.1 Software Architecture

According to the initial functional requirements of the LISA simulation, a simulator should:

- have optional arguments at the beginning of the simulation, such as time duration, switch on or off for each noise component, noise level, Etc.;

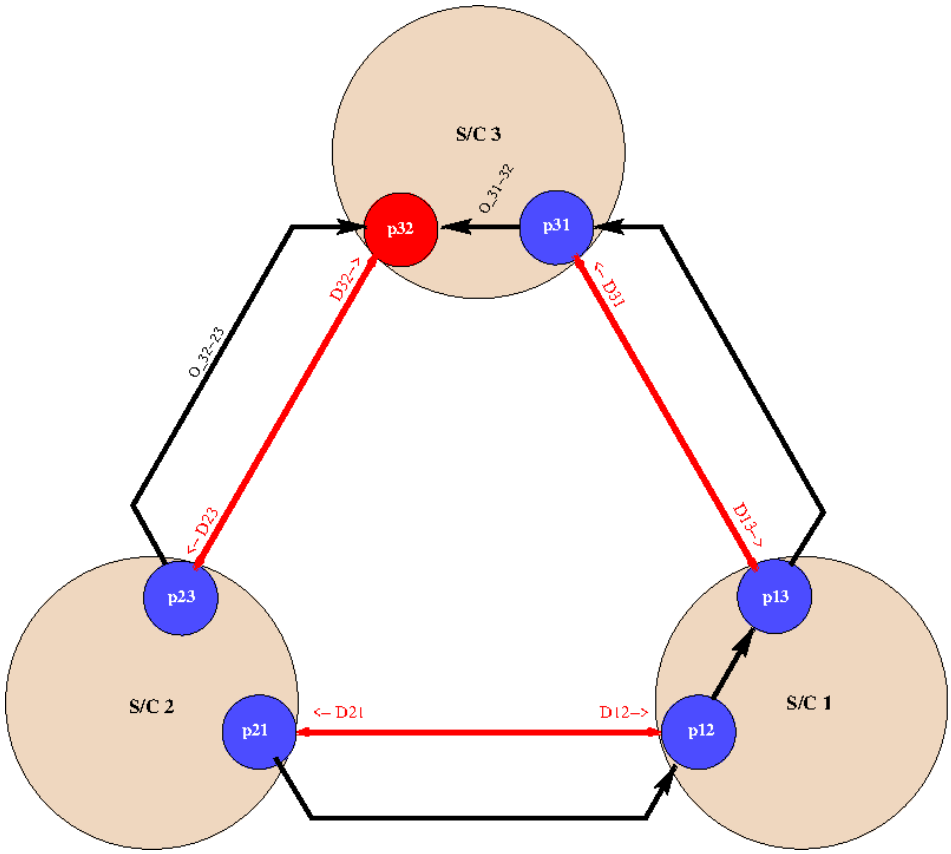

Figure 2.7: Frequency planning configuration N4-32 (cfg_N2c in [79]). The primary laser is 32 with frequency fluctuations p_{32}. The other lasers are locked via RFI measurements (31 and 12) or via ISI measurements (13, 21 and 23).

- be able to set up a complete configuration for the whole mission simulation duration, including the different sampling frequencies for each subsystem which is described in 2.5;
- be able to implement complex artifacts such as non-linearity, non-stationary, Etc.;
- be able to take the input data from files for such as the pre-calculated orbit, glitches, gravitational waves, Etc. and also to give outputs in open format files, such as binary or text;
- be open-source software which can be run with different operating systems.

In order to fulfill these requirements, `LISANode` has been generating LISA raw data in the time domain, with the time-series output for different pre-defined sampling rates. The data stream, or signal, goes through the simulation via smaller blocks called nodes, which support generating or transforming the signal. Each node has some parameters, inputs and outputs. These nodes then could be connected by propagating the outputs (whole or partial)

of one node to one or many of the inputs of the others. Therefore, each simulation could be represented as a graph and visualized by LISANode itself.

A node is built based on a physical process to generate the outputs from the inputs, with some defined parameters. The model for the physical process could be simple like mathematical operations or more complex like random number generator, filters, node to delay time-series data, Etc. They are called atomic nodes, which are implemented in C++ within subclass *Node*.

By connecting some atomic nodes, we can build a complicated graph for a subsystem in LISA, such as a telescope or optical bench or for functionality like a noise generator with a specific shape. As the same as the subclass *Node*, the subclass *Graph* has its own parameters, inputs and outputs. In addition, a graph could be connected to nodes and other graphs to make more complex ones. This nested architecture is robust to adapt the instrumental development of LISA mission and create different abstraction levels of the simulation system. In particular, we can start with a simple physical model as a graph/node for implementing a system and then split it into smaller nodes/sub-graphs to adapt to a more advanced model. The node and graph connections are programmed in Python.

Each node/sub-graph in a simulation graph has a different name, even though some of them could be built for the same atomic node or sub-graph. Hence, the inputs and outputs of the node/sub-graph will be well-defined and extracted.

When LISANode runs for a simulation graph, first, it unwraps the graph into compound nodes, which are only atomic ones. Then, it checks the graph consistency, schedules the execution of each atomic block, and compiles it into an executable in C++. Finally, we run the executable to produce the output data with the optional argument via command lines.

The top-level graph simulation of LISANode is $\boxed{LISA}$, which gives the outputs of interferometric measurements (beatnotes) and other auxiliary measurements such as Measured Pseudo-Range (MPR), DWS angles, and timer deviations. $\boxed{LISA}$ is constructed by connecting 3 sub-graphs $\boxed{Spacecraft}$, in each of which we simulate the onboard physical processes. The positions of all spacecraft are either read from a prepared file, generated by the outsources for a realistic model, or generated by LISANode itself for a simple model of orbits such as the ones with polynomials armlength variation. All the beams are exchanged among spacecraft by $\boxed{LaserLinks}$ graph. This graph delays the sent laser beams by the light travel time along the associated link to simulate the laser propagation in space. It connects the delayed laser beams to the spacecraft as the receiving signals.

Each $\boxed{Spacecraft}$ graph is constructed by several smaller sub-graphs, including two $\boxed{OpticalBench}$, two $\boxed{Telescope}$, one $\boxed{OnboardTimer}$, one $\boxed{Phasemeter}$, one $\boxed{ADC}$, one $\boxed{OnboardComputer}$, and other auxiliary sub-graphs.

The *OpticalBench* graph is the central block for simulating the beatnote measurements, and generating the instrumental noises like test-mass acceleration noise, backlink noise, optical path-length noises in OB, DWS and readout noise. The laser beam generated within this OB simulated graph could be locked according to the laser locking scheme defined in the configuration. The telescope optical path-length noise is added to the incoming and outgoing beams of the OB in the *Telescope* sub-graph.

The *OnboardTimer* graph gives the information of the onboard clock times, including clock noise. On the other hand, the laser beam phases and the beatnote measurements are time-stamped at the spacecraft proper time, which is different from the onboard clock time by time-stamping error implemented as a white noise. All of these times can be expressed as the functions of the Barycentric Coordinate Time (TCB), which is the reference frame of the simulator.

An auxiliary graph *PseudoRangingMeasurement* will use the output of onboard clock times and the time deviations from the associated spacecraft proper time to measure the distances among spacecraft. This graph adds a generic measurement error as the ranging noise.

In the *Phasemeter*, we simulate the readout process by the phasemeter with the time stamps from the USO. In the current simulation model, we rescale the beatnote frequency offset by the accumulated clock offsets and add the clock jitter noise to the beatnote frequency fluctuation. Then, the *ADC* graph re-samples the *Phasemeter* outputs from the spacecraft proper time to the onboard clock time since the ADC is sampling the data at the time triggered by the USO, or onboard timer.

Finally, the signals are propagated through an anti-aliasing filter and then decimated in the *OnboardComputer* graph. The implemented anti-aliasing filter is a Kaiser filter [46], and its coefficients are computed at the beginning of the simulation. The effects of this filter on the data processing have been studied in [43, 40]. According to the frequency distribution system illustrated in figure 2.4, the analog signals are sampled by the phasemeter at the high frequency of 80 Mhz. Then, they are downsampled at 4 Hz before sending to the Earth. In the simulator, we use the sampling rate of the signals in the physical and most of the onboard processing at the DFACS sampling rate, which is 16 Hz, to optimize the memory of data productions. After the decimation, the data is downsampled to 4 Hz as the requirement.

The detailed description for `LISANode` architecture and its instrumental model could be found in [40, 38]. The instrumental model and the implementation in `LISANode` presented in this thesis could be different in the near future since this simulator is a living project.

In the next subsections, we will demonstrate how the `LISANode` works, by examining some specific implementations.

2.8.2 Correlated noise

In this part, we first introduce the implementation of the backlink noises in the LISANode and then describe how they can be correlated according to different scenarios.

All of the noises implemented in LISANode are generated by a pseudo-random generator based on Mersenne Twister algorithm [108]. It can generate a very long period sequence of random numbers concerning the method `rand()` in the C++ standard library. Like any pseudo-random generator, it needs a seed as a random number to be initiated. In general, we can take a random number of the device when we start the simulation, such as the local time in the computer. In LISANode, we can indicate the seed number of the noise generator. If two seeds of generators for two separated noise blocks are identical, these noises will be fully-correlated.

The pseudo-random number generator provides a noise realization in time series as a stationary Gaussian signal for a given amplitude spectral density $\sqrt{S_n(f)}$ and the sampling frequency f_s. Each data point of the series is drawn from a normal independent and identical distribution.

$$n(t) = N(0, \sigma), \tag{2.32}$$

where the standard deviation is computed from the amplitude spectral density. For example in the case of white noise, the power spectral density is frequency independent $S_n(f) = S_n$, then $\sigma = \sqrt{S_n}\sqrt{\frac{f_s}{2}}$.

For different noise shapes, we can start to generate the white noise time-series signal and then propagate it through one or some filters to have the colored noise. This approach is the principle for implementing backlink noise, which is modelled as equation (2.8). As illustrated in figure 2.8, the time-series backlink noise is generated by two independent noise chains, one is based on the first term of the ASD in equation (2.8), proportional to f, and the other is for the second term in equation (2.8), proportional to $1/f$.

The first chain starts with $\boxed{WhiteNoise}$ node to generate the white noise signal. Then, the signal is propagated through $\boxed{CenteredDerivative}$, which is a filter to generate a time-series signal with f-proportional ASD (for unit conversion from displacement to relative frequency fluctuations, see section 2.6.10).

Similarly, the second noise generation chain generates a white noise signal then the signal is filtered by $\boxed{Integrator}$ node to convert into $1/f$-proportional noise. After that, the output is connected to a $\boxed{Gain}$ node to account for the relaxation frequency factor 2 mHz.

After that, two signals of these noise production chains are summed up in $\boxed{Addition}$ node and go through a $\boxed{Gain}$ node to multiply with the overall noise level. Finally, we have another $\boxed{Gain}$ node to indicate which type of correlation to simulate. For example, if the same seed

parameter feeds two backlink noise generators, they are fully correlated as the default. If we set up the input parameters in correlation $\boxed{Gain}$ nodes as 1 and -1 for each noise generator, respectively, the two noises are anti-correlated.

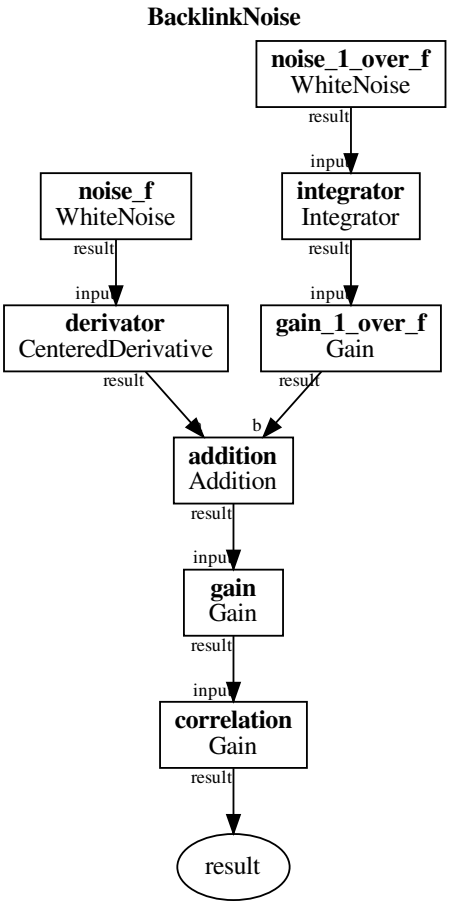

Figure 2.8: Visualization of backlink noise graph by `LISANode`.

We will use this implementation method to study the propagation of correlated noises, presented in chapter 4. In particular, we generate the LISA data with some correlation scenarios of some specific noises, such as test-mass acceleration noise, optical path noise in the telescope, and backlink noise. Then, we validate our analytical formulation for the noise propagation in LISA data processing with the simulation.

2.8.3 Non-stationary noise

In the final part of this chapter, we consider non-stationary effect in the test-mass acceleration noise. Its associated implementation will be given shortly based on that study.

As mentioned in section 2.6.5, we recognized the decreasing of Brownian noise level due to the gas depletion in the vacuum chamber of the GRS as well as the whole spacecraft. The Brownian motion depends on the pressure, which is eventually proportional to the number of molecules in the chamber. In figure 2.9, the average ASD of the differential test-mass acceleration, Δg, measured during LPF mission decreases over time. This differential acceleration corresponds to the acceleration noise of one test-mass divided by $\sqrt{2}$. Since the test-mass acceleration noise is dominant at low frequency, we will use the result of the average ASD of Δg in the frequency band of $3-8$ mHz for setting the parameters of the non-stationary noise model.

We model the above non-stationary behavior of the test-mass acceleration noise by evolving the noise level of the amplitude spectral density of test-mass acceleration noise in equation (2.5) as a function in time. In particular, we express the gain of the time-varying noise level $A_\delta(t)$ w.r.t. $A_\delta^{\text{stationary}} = 2.4 \times 10^{-15} \frac{\text{m}}{\text{s}^2\sqrt{\text{Hz}}}$ by

$$\text{Gain}(t) = A_0 e^{-\alpha t}, \tag{2.33}$$

where $A_0 = \frac{A_\delta(t=0)}{A_\delta^{\text{stationary}}}$ and α are the coefficients to account for the decreasing Brownian noise. They are both computed from the average amplitude spectral density trend of the test-mass acceleration noise measured in LPF mission, shown in figure 2.9, in the frequency band of $3-8$ mHz. The calculated values are $A_0 = 0.9999999966666666$ and $\alpha = 7.995087128451548 \times 10^{-7}$.[5]

To implement this effect in LISANode, we assume that the noise produced by the pseudo-random generator is still valid for time-varying variance. The normal distribution in the generator is no longer identical since the variance is computed from varying amplitude spectral density:

$$\sigma(t) = \sqrt{S_\delta(t)}\sqrt{\frac{f_s}{2}}, \tag{2.34}$$

where $\sqrt{S_\delta(t)} = \text{Gain}(t) \times A_\delta^{stationary}$ is the amplitude spectral density of the test-mass acceleration noise at the time t, f_s is the sampling frequency of the generated noise data.

We start with the implementation of stationary test-mass acceleration noise, illustrated in figure 2.10. In the LISANode, the test-mass acceleration noise formulated in equation (2.5) has two components, after unit conversion (see section 2.6.10): one proportional to f and

[5] Practically, there is no significant difference by using the approximate values $A_0 = 1, \alpha = 8 \times 10^{-7}$. We introduce the the high precision number here to be consistent with the values we set in the simulator.

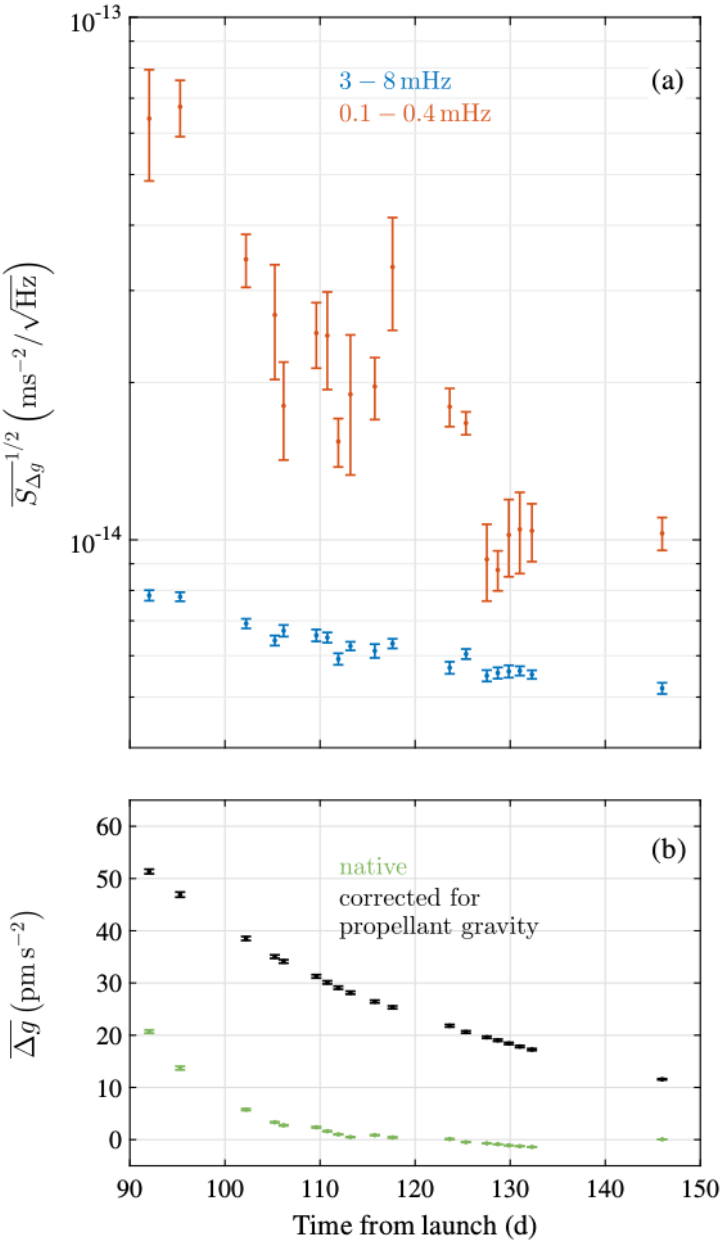

Figure 2.9: Result of differential test-mass acceleration measured by LISA Pathfinder (LPF), taken from [32]. Figure (a) shows the square root of the average amplitude spectral density of Δg in the $3-8$ mHz and $0.1-0.4$ mHz frequency bands evolving in mission duration. The average spectral density is calculated in a specific frequency band by $\bar{S} = \frac{1}{f_2-f_1}\int_{f_1}^{f_2} S_{\Delta g}(f)df$. Figure (b) gives the quasistatic value of $\overline{\Delta g}$ as a function of time. We will use the result of the average spectral density of Δg in the frequency band of $3-8$ mHz to deduce the parameter for non-stationary test-mass acceleration noise implemented by `LISANode`.

the second to f^2. Hence, two associated noise production chains are built for these two components. Both chains start with a noise generator in $\boxed{WhiteNoise}$ node. Each generated signal goes through delicate filters to have either f- or f^2-proportional shape. Then, we sum up both components and multiply the resultant with a correlation gain similarly to the backlink noise implementation described in section 2.8.2.

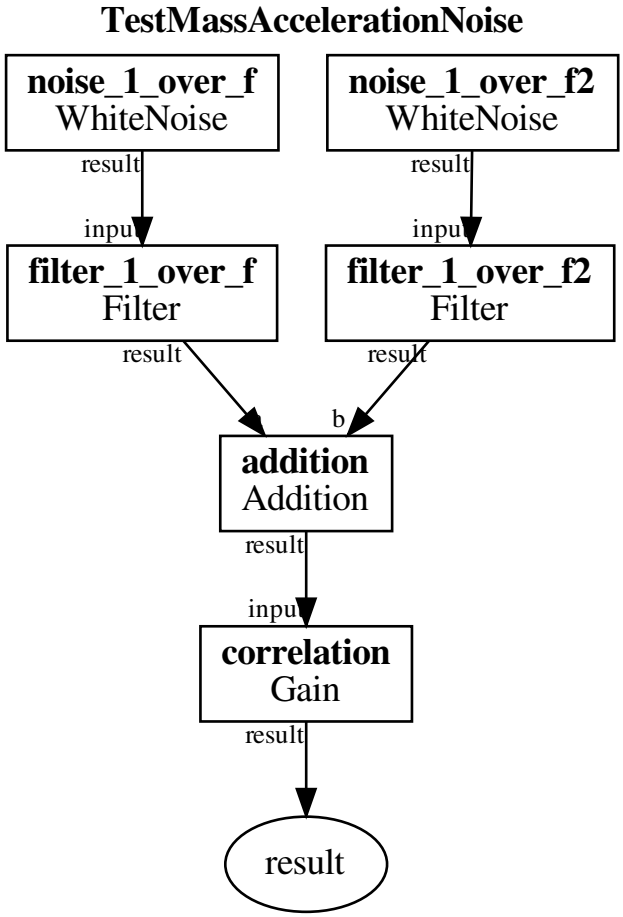

Figure 2.10: Visualization of test-mass acceleration noise graph by LISANode in the stationary scenario.

For the non-stationary scenario, the amplitude spectral density decreases over time, as discussed at the beginning of this subsection. We still have two separate noise production chains, but now the noises generated by $\boxed{NonStationaryWhiteNoise}$ node to have the time-varying variance, as illustrated in figure 2.11. The initial noise level gain and exponential coefficient

are fed to the *Expression* node to construct the varying gain modelled in equation (2.33). Then it is connected to each *NonStationaryWhiteNoise* to generate non-stationary noises. After the node *Expression*, the graph is the same as the one of the stationary case, except for the correlation gain before providing the final result noise signal.

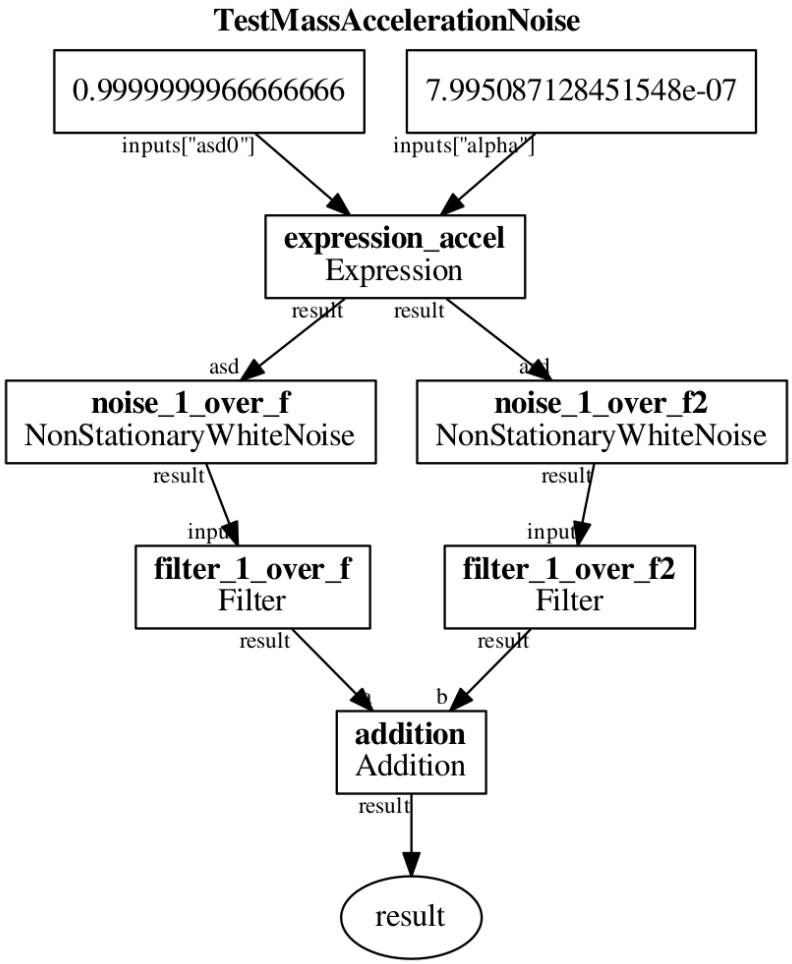

Figure 2.11: Visualization of test-mass acceleration noise graph by `LISANode` in the non-stationary scenario. This graph is produced by a specific branch of `LISANode` in an old version, so that there are some nodes/classes removed.

For verifying our implementation, we simulate the *TestMassAccelerationNoise* graph for 30×10^4 seconds and split the output into 30 data segments. We compute the spectral density of each data segment and take the average in the frequency band of $3 - 8$ mHz. After that, we compare it to the analytic curve of time-varying amplitude spectral density of the test-mass acceleration noise, $\sqrt{S_\delta} = \text{Gain}(t) \times A_\delta^{stationary}$, with the gain expressed in equation (2.33). The result shown in figure 2.12 indicates a good matching. In the future, we want to test the data analysis methods to extract the GW information with the impact from

such as this non-stationary effect.

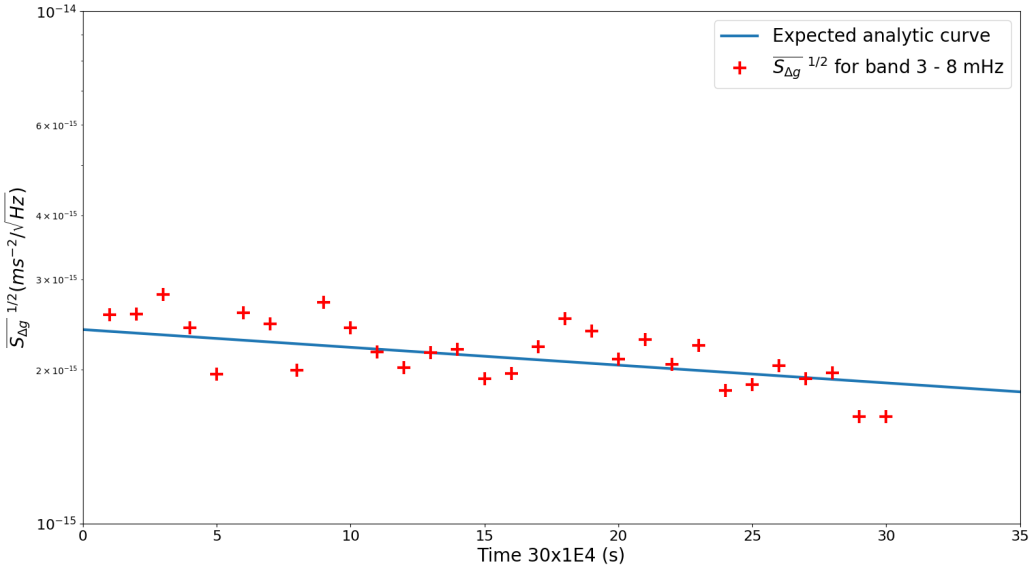

Figure 2.12: Result of non-stationary test-mass acceleration noise implementation in LISANode. The data are generated for 3e5 seconds and split into 30 smaller chunks. Then, we compute the average spectral density within the frequency band of $3-8$ mHz for each chunk i. The red cross points in the plot are the average spectra for each data chunk. We compare those with the analytic non-stationary test-mass acceleration noise model, indicated in the blue curve. This analytic model is constructed by equation (2.5) and equation (2.33).

Chapter 3

Time-Delay Interferometry

This chapter reviews the pipeline used in LISA data processing of the raw data (L0) to L1 data in the pipeline. The pipeline includes some data processing algorithms to reduce the dominant noises in the L0 data. In particular, we focus on the Time Delay Interferometry (TDI) algorithm used to suppress the laser frequency noise, which is presented in the second section of this chapter. In the final section, we examine the performance of TDI on experimental data generated by LISA-On-Table electronic simulator.

3.1 Initial noise reduction pipeline

The LISA raw measurements cannot be used to extract the GW information since the data are contaminated by many noise sources, as described in section 2.6. One of the dominant noises is the laser frequency noise, which is several orders of magnitude higher than the detection level of GW in the LISA frequency bandwidth. Therefore, this requires some dedicated post-processing algorithms to mitigate the noise in the data, such as the TDI algorithm to suppress the laser frequency noise and, additionally, the spacecraft jitter noise. We will introduce TDI in the next section. Moreover, the data are sampled in all spacecraft on their own reference times, called the spacecraft proper time. Hence, we need to transform the data to the global reference frame, such as the Barycentric Coordinate Time (TCB), to accurately reduce the noises, extract the source parameters and allow for the multi-messenger observation. This process sometimes is called *clock synchronization*.

All these processing steps are packed in the pipeline, named Initial Noise-Reduction Pipeline (INREP). This pipeline transforms the raw data, measured and telemetered by the LISA spacecraft, to the data which we can directly analyze for searching GW signals. The first data set is called level 0 (L0) data, and the latter is level 1 (L1) data. The full INREP is still under development, so some post-processing blocks, as described in this thesis, could be changed

or even reformulated in future. Some possible pipelines for INREP are illustrated in figure 3.1 [78]. In the following, we give one of the possible INREP pipelines, which has been studied recently. This pipeline suppresses two important noise sources such as laser frequency noise and clock noise [77, 43]. It has been tested and validated on simulated data from `LISANode` and/or `LISA Instrument`. In addition, the pipeline is expected to reduce the longitudinal spacecraft jitter noise and TTL effects, as well as synchronize the data in TCB.

According to the instrumental model introduced in section 2.7, the raw data measured in LISA spacecraft will be given in either total phase or total frequency. However, the data would be expressed in some formats that are optimized to telemeter to Earth. Hence they need to be converted to physical units before any further processing step. The format for the raw telemetry data is still not yet decided, so we assume that this conversion has been done before the data go through the INREP. Accordingly, we get the data in a physical unit, and assume the data expressed in the total frequency as we simulate in `LISANode`. In addition, we postulate the values of all variables are given as double precision floating point type. The impacts of the physical units and the precision numerical programming type have been studied recently [41] and need further investigation.

The first block of our considered INREP is the ranging noise reduction since the TDI algorithm needs as input the spacecraft distances. The Measured Pseudo-Range (MPR) mentioned in section 2.5 will be used. To reduce the ranging measurement noise, the technique called Time Delay Interferometry Ranging (TDIR) would be applied [144]. Moreover, the pseudo-ranging measurements could suffer from a constant systematic bias, as modelled in section 2.6.9. We expect to identify and suppress this bias by estimating the optimal delays using the TDI algorithm itself with TDIR technique [144].

Then, we can combine the ISI measurements with the RFI and TMI measurements to establish the measurement of the virtual link between two test-masses along with the laser link connecting two spacecraft. This is the split interferometry we introduced in section 2.2. The advantage of this method is to remove the spacecraft jitter motion w.r.t. the inside test-mass. The number of free-running lasers of the LISA constellation is reduced by half using the RFI measurements (see section 3.2.2. These steps are carried out as the intermediary steps in the TDI algorithm.

The next step is to suppress the dominant laser frequency noise, which is the core step in the TDI algorithm. We combine the raw measurements in a specific way to construct virtual equal photon path interferometer measurements, so the laser frequency fluctuations are suppressed to be below the requirements. There are several possible TDI combinations with different levels to adapt better to some LISA configurations, for example, second generation of Michelson combination for the breathing armlengths given by realistic orbits, presented in

the section 3.2.2.

Then, the clock noise and the TTL effects are reduced by some algorithms. The clock noise reduction algorithm has been studied and applied successfully to the simulated data [77], while the TTL subtraction strategy is still under investigation [120]. These algorithms are probably carried out after the TDI block, but the order of chain is unclear when this thesis is writing. The main challenge of TTL subtraction in post-processing is to define the coupling coefficients of the beam tilt into the phase readout, which is imprinted in the raw measurement data. That would be complicated since the impact of TTL coupling is tiny compared to the laser frequency noise in the raw onboard measurement data. As a consequence, the calibration to determine the TTL coupling has to work with the TDI variables, which is in the complex combination of delayed raw measurements.

Finally, we convert the reference frame of the outputs from the three independent spacecraft proper time reference to the global one like the TCB. There are several ongoing studies on this conversion. In some current studies, this kind of calibration could be worked out by combining the onboard measurements with the on-ground observation in a Kalman-like optimal filter [152].

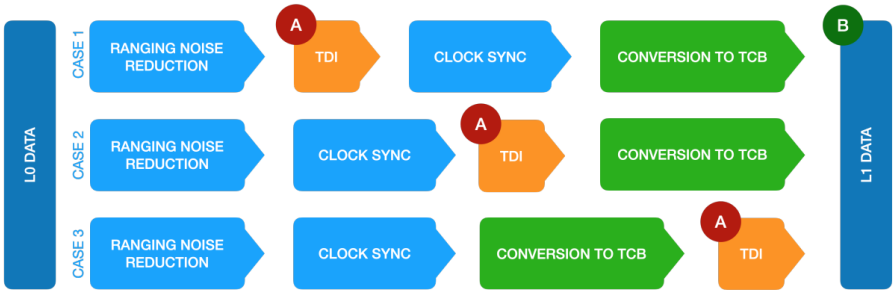

Figure 3.1: Schematic of possible INREP pipelines. Credits: Jean-Baptiste Bayle and Olaf Hartwig.

3.2 Time-Delay Interferometry

3.2.1 Principle of Time Delay Interferometry (TDI)

As described in section 2.5, the laser beams are exchanged among spacecraft to interfere with the local laser. The ISI measurement imprinted the effect of GWs is, in fact, a one-way IFO measurement, which is the interference between a local laser beam and a distant one. We can assume each one-way IFO measurement as a Michelson interferometer with different armlengths, as illustrated in figure 3.2. The heterodyne beatnote of the Michelson

interferometer is given by, considering only laser frequency fluctuation of the sources $p(t)$,

$$\begin{aligned} y(t) &= p\left(t - \frac{L_1}{c}\right) - p\left(t - \frac{L_2}{c}\right) \\ &\approx \Delta L p\left(t - \frac{L_1}{c}\right), \end{aligned} \tag{3.1}$$

where in the second step, we use the Taylor expansion for $\Delta L = (L_1 - L_2)/c$, assuming that it is small, so the highest frequency of the signal we want to measure is $f_{max} \ll 1/\Delta L$. It is obvious that unless the two armlengths in the Michelson interferometer are equal, the laser frequency fluctuation does not cancel out. Let us see how big it is in the case of one-way IFO measurement for a single laser link in LISA. The armlength mismatch is approximately equal to the nominal armlength of the triangle of LISA constellation, i.e. 2.5 million kilometers. The amplitude spectral density of the beatnote in fractional frequency units is then

$$\sqrt{S_y(f)} \equiv \frac{1}{\nu_0}\langle y^*(t)y(t)\rangle = \frac{\Delta L}{\nu_0}\sqrt{S_p(f)}, \tag{3.2}$$

where $\nu_0 = 282$ THz is the nominal frequency of the laser sources using in LISA. The stability of the laser in LISA design is required $\sqrt{S_p(f)} \approx 30\frac{\text{Hz}}{\sqrt{\text{Hz}}}$, c.f. (2.1) without relaxation factor. Therefore, the order of amplitude spectral density of the laser frequency fluctuation, what we call *laser frequency noise* from now on, is about 10^{-13} in strain sensitivity, about 8 orders of magnitude higher than the typical GW signal expected to be detectable by LISA, about 10^{-21}.

In the full configuration of LISA, the laser frequency noises in the two interference beams are generally different.[1] Considering only laser frequency noise, the one-way measurements for ISI signals are read from the general expression (2.27) as

$$\begin{cases} \text{isi}_{12} = \mathbf{D}_{12}p_{21} - p_{12} \quad ; \quad \text{isi}_{13} = \mathbf{D}_{13}p_{31} - p_{13}; \\ \text{isi}_{23} = \mathbf{D}_{23}p_{32} - p_{23} \quad ; \quad \text{isi}_{21} = \mathbf{D}_{21}p_{12} - p_{21}; \\ \text{isi}_{31} = \mathbf{D}_{31}p_{13} - p_{31} \quad ; \quad \text{isi}_{32} = \mathbf{D}_{32}p_{23} - p_{32}. \end{cases} \tag{3.3}$$

An idea to suppress the laser frequency noise is to have a linear combination of these measurements with some applied delay operators so that all the noise terms will be cancelled out. The general combination M is written as

$$M = \sum_{\substack{i,j=\{1,2,3\} \\ i\neq j}} \mathfrak{F}_{ij}\left(\mathbf{D}_{12}, \mathbf{D}_{23}, \mathbf{D}_{31}, \mathbf{D}_{13}, \mathbf{D}_{32}, \mathbf{D}_{13}\right) \text{isi}_{ij}, \tag{3.4}$$

[1] According to the LISA design, six laser beams in the constellation will be in a locking scheme, presented in section 2.5, so that only one laser frequency noise of the master laser source remains in all IFO measurements, assuming the locking is perfect.

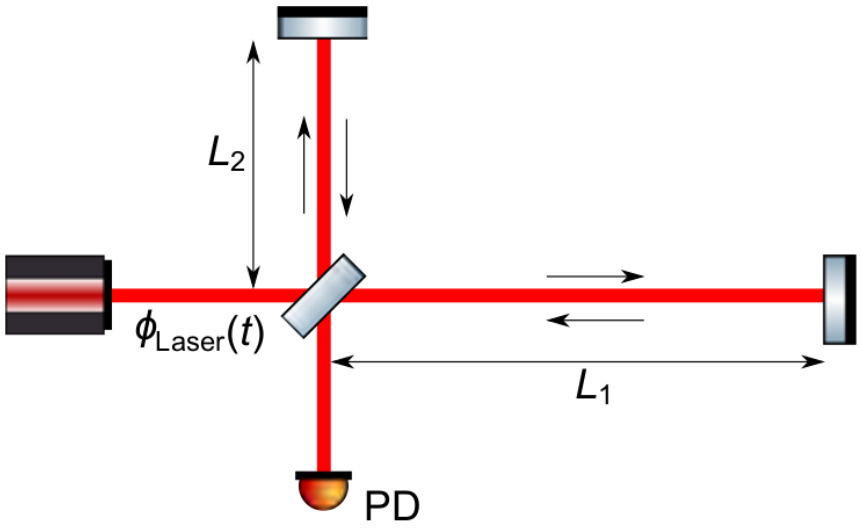

Figure 3.2: Schematic of a Michelson interferometer. A laser beam from the source is split at the beam splitter to have two different arms, traveling along L_1 and L_2, respectively and then returning back to interfere altogether at photo-diode (PD). Image from the thesis of Markus Otto [118]

where $\mathfrak{F}_{ij}\left(\mathbf{D}_{12}, \mathbf{D}_{23}, \mathbf{D}_{31}, \mathbf{D}_{13}, \mathbf{D}_{32}, \mathbf{D}_{13}\right)$ are the polynomial functions of delay operators. These functions could be solved algebraically with the constraint $M = 0$ (see section 3.2.1 in [118] for detailed derivation and relevant references of this problem).

Several possible combinations fulfill the requirement of $M = 0$ with some specific conditions. For example, with the non-flexing (or fixed) armlength of LISA so that L_{ij} are constant, a possible combination is

$$X = (1 - \mathbf{D}_{121})\,\text{isi}_{13} - (1 - \mathbf{D}_{131})\,\text{isi}_{12} - (1 - \mathbf{D}_{131})\,\mathbf{D}_{12}\text{isi}_{21} + (1 - \mathbf{D}_{121})\,\mathbf{D}_{13}\text{isi}_{31}, \tag{3.5}$$

where we used the notation for a nested delay operator $\mathbf{D}_{ijk} = \mathbf{D}_{ij}\mathbf{D}_{jk}$, i.e. multiple delay operators applied to one signal in a specific order, which was introduced in section 2.7.3. The expansion of X_1 (the index of 1 will be explained later) via one-way ISI measurements (3.3) is then

$$X_1 = \mathbf{D}_{12131}p_{13} - \mathbf{D}_{13121}p_{12} = \mathbf{D}_{12}\mathbf{D}_{21}\mathbf{D}_{13}\mathbf{D}_{31}p_{13} - \mathbf{D}_{13}\mathbf{D}_{31}\mathbf{D}_{12}\mathbf{D}_{21}p_{12}. \tag{3.6}$$

We will see later that the frequency noises of lasers in different MOSA but in the same spacecraft can be reduced to one single noise term by using the RFI measurements. With $p_{12} = p_{13} = p$, we can see from equation (3.6) that $X_1 = 0$ if all armlength L_{ij} are constant. Indeed, as we mentioned in section 2.7.3, the delay operators are commutative with constant armlengths, so that the previous result is obvious.

From a geometrical point of view, the result shown by equation (3.6) can be illustrated in figure 3.3a. Therefore, the combination of suitable nested delay operators applied on IFO measurements, which gives the same photon path length for two laser frequency noises in the same spacecraft, can significantly suppress the laser frequency noise. One can check that this combination does not annihilate the GW imprinted in IFO measurements (see, for example, section 3.2.2 of [118]). This is the basic idea of the Time Delay Interferometry (TDI) algorithm, which is currently the baseline technique to suppress laser frequency noise down to the requirement of the LISA mission.

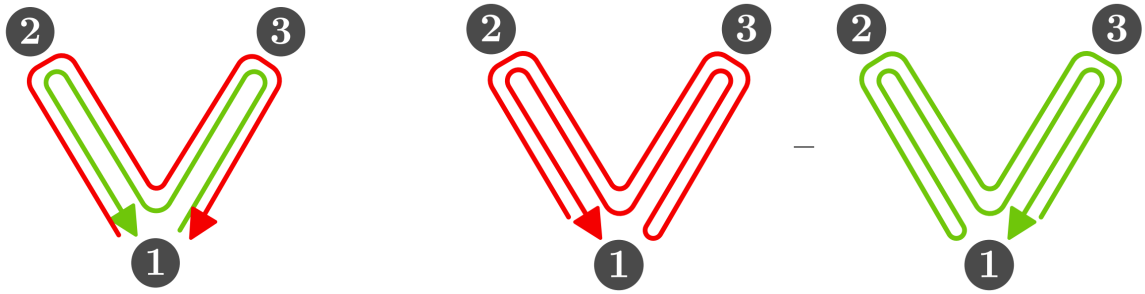

(a) X_1 (b) X_2

Figure 3.3: Illustration for combining two virtual photon paths to suppress laser frequency noise, in TDI Michelson X combination. Sub-figure (a) is for the first generation of Michelson combination, while sub-figure (b) is for the second generation one. In subfigure (a), the laser frequency noise p_{12} imprinted in the laser beam from MOSA 12, travel in the virtual photon path from spacecraft $1 \to 2 \to 1 \to 3 \to 1$. The noise p_{13} travel in a similar photon path but with a reversed direction. The photon path in subfigure (b) could be interpreted similarly as (a). Credit: Jean-Baptiste Bayle, in [40].

The combination (3.5), called Michelson combination, is one of possible TDI combinations. Since there are three spacecraft in LISA constellation, there are three Michelson combinations X, Y, Z. The Y_1, Z_1 combination could be deduced from the expression (3.5), by index permutation. We will discuss more TDI combinations which could be applied on LISA in the next section 3.2.2.

On the other hand, the Michelson combination in (3.5) cannot suppress the laser frequency noise in the case of flexing armlengths which is the realistic configuration in the LISA mission. In this case, the delay operators are not commutative so we need a new combination for laser frequency noise reduction. The TDI combination applied for the case of fixed armlengths is classified as the first generation of TDI, so we have used the subscription index of 1. For the case of flexing armlengths, we introduce the second generation of TDI. As the same idea for the first generation construction, we tailor the ISI measurements with suitable nested delay

operators so that the next generation of TDI Michelson combination (3.5) is given by

$$\begin{aligned} X_2 &= (1-\mathcal{D}_{12131})\left[(\mathrm{isi}_{13}+\mathcal{D}_{13}\mathrm{isi}_{31})+\mathcal{D}_{131}\left(\mathrm{isi}_{12}+\mathcal{D}_{12}\mathrm{isi}_{21}\right)\right] \\ &\quad -(1-\mathcal{D}_{13121})\left[(\mathrm{isi}_{12}+\mathcal{D}_{12}\mathrm{isi}_{21})+\mathcal{D}_{121}\left(\mathrm{isi}_{13}+\mathcal{D}_{13}\mathrm{isi}_{31}\right)\right]. \end{aligned} \tag{3.7}$$

The expansion with one-way ISI measurements, (3.3), reads

$$X_2 = \mathbf{D}_{131212131}p_{13} - \mathbf{D}_{121313121}p_{12}. \tag{3.8}$$

The illustration for the virtual photon path of this equation is shown in figure 3.3b. This second generation of the TDI combination can reduce the laser frequency noise up to the first order of armlength derivative $\dot{L}_{ij}(t)$ [43]. This is the generation of TDI we will focus on in this thesis.

Moreover, the construction of the TDI combination we discussed above is only a step in the Time Delay Interferometry (TDI) algorithm, a part of the INREP pipeline presented in section 3.1. In fact, the goal of this algorithm is not only to suppress the laser frequency noise but also to reduce the number of free-running lasers and the spacecraft jitter noise. In the next subsection, we will present the full TDI algorithm and its detailed formulation.

3.2.2 Formulation

The TDI formulation involves several steps, which give yield the TDI variables. The first step is to suppress the spacecraft motion (also dubbed optical bench displacement, so called MOSA jitter) noise Δ_{ij}.

$$\begin{aligned} \xi_{12} &= \mathrm{isi}_{12} - \theta_{12}^{\mathrm{isi}}\theta_{12}^{\mathrm{rfi}}\frac{\lambda_{12}}{\lambda_{21}}\frac{\mathrm{tmi}_{12}(t)-\mathrm{rfi}_{12}(t)}{2} \\ &\quad -\theta_{12}^{\mathrm{isi}}\theta_{21}^{\mathrm{rfi}}\frac{\mathcal{D}_{12}\left[\mathrm{tmi}_{21}(t)-\mathrm{rfi}_{21}(t)\right]}{2}, \end{aligned} \tag{3.9}$$

$$\begin{aligned} \xi_{13} &= \mathrm{isi}_{13} - \theta_{13}^{\mathrm{isi}}\theta_{13}^{\mathrm{rfi}}\frac{\lambda_{13}}{\lambda_{31}}\frac{\mathrm{tmi}_{13}(t)-\mathrm{rfi}_{13}(t)}{2} \\ &\quad -\theta_{13}^{\mathrm{isi}}\theta_{31}^{\mathrm{rfi}}\frac{\mathcal{D}_{13}\left[\mathrm{tmi}_{31}(t)-\mathrm{rfi}_{31}(t)\right]}{2}. \end{aligned} \tag{3.10}$$

The logic behind this step is to extract the motion of the spacecraft and the test-mass by combining TMI and RFI, then subtract it from the ISI so that only the spacecraft motion disappears. Then, we can build the second set of intermediary variables to reduce the number of laser noises by half using the RFI measurements, as

$$\eta_{12}(t) = \theta_{12}^{\mathrm{isi}}\xi_{12}(t) + \frac{\mathcal{D}_{12}\left[\theta_{21}^{\mathrm{rfi}}\mathrm{rfi}_{21}(t)-\theta_{23}^{\mathrm{rfi}}\mathrm{rfi}_{23}(t)\right]}{2}, \tag{3.11}$$

$$\eta_{13}(t) = \theta_{13}^{\mathrm{isi}}\xi_{13}(t) - \frac{\theta_{13}^{\mathrm{rfi}}\mathrm{rfi}_{13}(t)-\theta_{12}^{\mathrm{rfi}}\mathrm{rfi}_{12}(t)}{2}. \tag{3.12}$$

From the intermediary variables η_{ij}, we can build the TDI combination that reduce laser noise. Several TDI combinations exist [76, 111, 113, 147].

In this thesis, we focus on the second generation Michelson variables X_2, Y_2, Z_2, where each of the two virtual beams of the TDI Michelson [147], visits both distant spacecraft twice. We compute X_2 as

$$\begin{aligned} X_2 \;=\; & (1-\mathcal{D}_{12131})\left[(\eta_{13}+\mathcal{D}_{13}\eta_{31})+\mathcal{D}_{131}\left(\eta_{12}+\mathcal{D}_{12}\eta_{21}\right)\right] \\ & -(1-\mathcal{D}_{13121})\left[(\eta_{12}+\mathcal{D}_{12}\eta_{21})+\mathcal{D}_{121}\left(\eta_{13}+\mathcal{D}_{13}\eta_{31}\right)\right]. \end{aligned} \tag{3.13}$$

The other two Michelson combinations Y_2 and Z_2 are derived from this equation by circularly permuting all indices.

Another interesting TDI combination is the quasi-orthogonal AET [126], which is the optimal combination constructed from Michelson combinations. The advantage of this combination is that we can minimize the effect of the correlation of secondary instrumental noises in the final TDI variables. In mathematical words, the covariance matrix of this TDI combination is diagonal, so we say these variables are orthogonal. However, this is valid only for the case of ideal configuration: all armlengths are equal and same type noises in different MOSAs have the same statistical characterization. If these assumptions do not hold, the covariance matrix is almost diagonal, with small off-diagonal elements. Hence, we have called AET the quasi-orthogonal combinations. The formulation of the second generation AET combination is given by

$$\begin{cases} A_2 = \dfrac{1}{\sqrt{2}}(Z_2 - X_2) \\ E_2 = \dfrac{1}{\sqrt{6}}(X_2 - 2Y_2 + Z_2) \\ T_2 = \dfrac{1}{\sqrt{3}}(X_2 + Y_2 + Z_2) \end{cases} . \tag{3.14}$$

3.3 TDI testing on experimental data

In this section, we demonstrate TDI algorithm to suppress the laser frequency noise on experimental data generated by LISA-On-Table (LOT). LOT is an apparatus, which includes an electro-optical bench in a simplified LISA configuration to generate LISA-like data. We use LOT to generate the interferometric measurements, which are considered as the L0 data in the LISA data pipeline. Then, we apply the TDI algorithm using `PyTDI` software [138] to get the laser frequency noise-suppressed data. This work has been carried out in collaboration with L.Vidal.

LOT has been developed for several years by a collaborative group at APC laboratory, in particular led by H.Halloin, P.Grunning, M.Laporte [99] and L.Vidal [150]. It is an electro-optical simulator of LISA with the goal of testing the noise reduction method, i.e. TDI, on experimental data, as well as the LISA-like instrument for the data acquisition chain, such as phasemeter, filters, EOM, USO, Etc.

The instrumental model for the interferometric measurements in LOT is simplified from the LISA configuration. Only Inter-Spacecraft Interferometer (ISI) measurements in one spacecraft are carried out in LOT. We assume the laser locking is done perfectly, and there is no transponder mode for the laser beam sent from the distant spacecraft. Instead, we assume the laser beams sent from the local spacecraft are reflected by ideal mirrors, return back and interfere with the local laser beams to build the ISI measurements, as illustrated in figure 3.4. There are no test-mass or its related simulation in LOT since we assume all test-masses are following their geodesics and are attached rigidly to the spacecraft. The laser frequency fluctuations of the lasers in two MOSAs in the local spacecraft are identical as the result of the perfect laser locking.

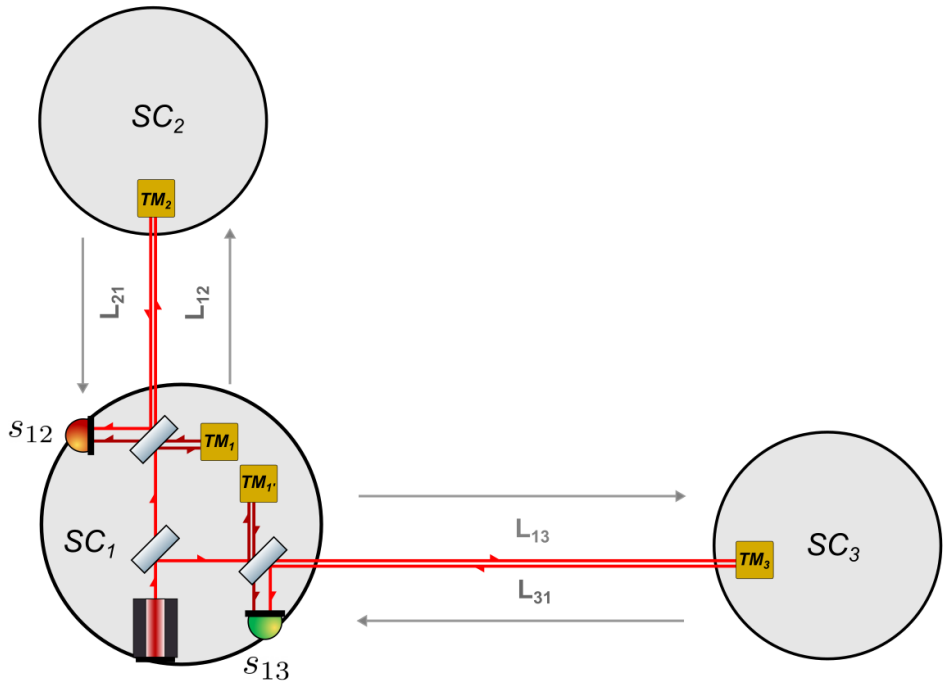

Figure 3.4: Schematic of LOT interferometric measurement, with detailed description in section 3.3 Credits: Léon Vidal [150]

.

LOT includes 4 subsystems: control/command, electronic interferometer, optical interferometer, and phasemeter. The control/command part provides the radio frequency (RF) signals driven by Direct Digital Synthesizer (DDS)s with a mathematical model. Based on

signal model and input parameters given for the simulation, a computer provides the demands to DDSs to synthesize analog signals. We can add the laser frequency noise using a specific mathematical model for the frequency of the signal. In particular, LOT uses a sinusoidal function for the signal model:

$$s(t) = A(t)sin\left[2\pi f(t)t + \phi(t)\right], \tag{3.15}$$

where $A(t)$ and $\phi(t)$ are set to be fixed for simplicity, $f(t) = f_0 + N(t)$ with a fixed offset f_0, and $N(t)$ is a white noise representing for the laser frequency noise. The laser frequency noises in the signals for the distant beams are delayed according to virtual photon paths from the local spacecraft to the distant one and returning back to the local. In the LOT, the $N(t-\tau)$ is obtained from interpolation of origin $N(t)$, where the delay time τ associated with the virtual photon path. Then the RF signals for three laser beams (local, delayed along pathway $1 \to 2 \to 1$ and delayed along pathway $1 \to 3 \to 1$) alternately go through the electronic and optical interference parts. In the optical part, the RF signals are used to modulate the beams generated by laser sources by acousto-optic modulator (AOM)s before constructing the measurements. In the electronic part, the signals are combined in the mixer to generate the interferometric measurements. In both two interference ways, we have the pilot tone to correct the jittering of ADC when it triggers the interferometric data and the DPLLs to track the phase of the signal with the same design as in LISA, shown in figure 2.4. The final subsystem includes the phasemeter to sample the data with the time reference from the USO providing the timing signal at 10 MHz. In addition, there are Cascaded Integrator–Comb (CIC) filters to avoid the aliasing when we downsample the data from 40 MHz to about 38 Hz, by 20 times 2-divided decimation. The design of the filter-decimation used by LOT is written in [73]. The data saved in the computer will be the input for the data analysis process.

In the current version of LOT, we removed the optical part and use only the electronic one, as illustrated in figure 3.5, because the electronic interferometers are easier to work with and more precise than the optical counterparts. Although we cannot test the interferometer data from the optical systems, it is important to verify the alternative data from the electronic part in LOT, and therefore in the LISA case, since they are using a similar baseline of the electronic system in the data acquisition chain. We also emphasize that in the LOT simulator, the gravitational wave effect is not considered at the moment. Hence, the electronic interferometers give the same output as the optical ones, and we can test the noise reduction algorithm on either of the two data production chains.

The LOT outputs are the time-series of interferometric measurements in the phase unit as the output of the phasemeter, as well as the delay information, or called ranging data, from the noise generation parameters and which are necessary for TDI algorithm. In principle, the required ranging data is generated by the Measured Pseudo-Range (MPR) process in LISA.

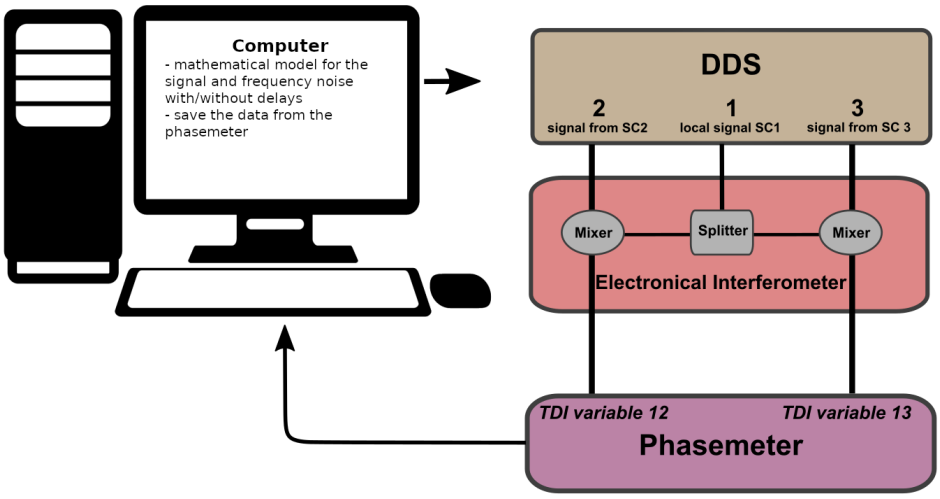

Figure 3.5: Schematic for LOT experimental setup. The detailed description is presented in 3.3. Credits: Léon Vidal.

However, in our simplified study case, the information on the delays are imprinted in other signals generated by the DDS and are read by the phasemeter. Then the measurements and ranging data are transformed into frequency fluctuation data by detrending the frequency offset in the total phase. The data file is converted into a LISANode-like data format to be used by `PyTDI`. Then, we compute the TDI variables from the raw L0 data and their spectral densities. In the following subsections, we present the preliminary results of testing the TDI algorithm on the LOT data with different configurations.

3.3.1 Static equal armlengths

For the first test, we use the simple LISA configuration with the equal and fixed armlengths. With this configuration, the first generation of TDI is sufficient to suppress the laser frequency noise to be below the requirements for the LISA mission. For the noise generation, we use the following input parameters:

- The level of the signal as the laser frequency noise is $\sqrt{S_\nu} = 100\sqrt{2}\frac{\text{Hz}}{\sqrt{\text{Hz}}}$. We choose this value so that this noise is about 8 orders of magnitude higher than the intrinsic noise of the LOT. This is similar to the case of LISA where the laser frequency noise is about 8 orders of magnitude higher than the requirement. In other words, in this study, we require that the TDI should reduce the laser frequency noise to the LOT intrinsic noise. The formula of LOT intrinsic noise is interpolated from the LOT data.

$$S_{\text{LOT-instrinsic-noise}}(f) = 32\sin^2(\omega L_0)\sin^2(2\omega L_0)(2.69\times 10^{-6} f^{-0.551})^2 \frac{\text{Hz}^2}{\text{Hz}} \tag{3.16}$$

- The time delays for the laser links 12, 21, 13, 31 are fixed and all equal at $L_{12} = L_{21} = L_{13} = L_{31} = L_0 = 2.5 \times 10^9/c$ seconds, with c the speed of light. Nevertheless, we save this information together with the measurement data in a file, and there is a small numerical error of about 10 ns from the true value we set up to generate the delayed signals. This is shown in figure 3.6. Consequently, this error is a systematic error for the ranging estimation in the LISA case although we did not use any method to estimate it in the LOT case. We expect that it is the numerical error of saving data points in the file. The origin of that error will be investigated in the future.

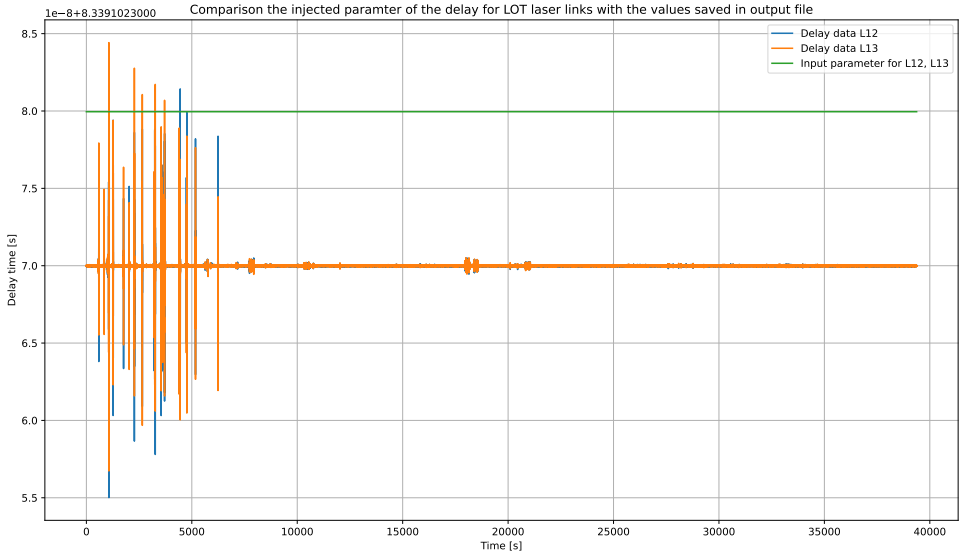

Figure 3.6: Difference between the injected values and the saved ones for the delay applied on the signals in LOT experiment for the configuration of equal and fixed armlengths. The difference are stable at 10 ns for a while after the start of experiment.

Then we check the propagation of the signal, i.e. the laser frequency noise, in the LOT configuration. The analytical PSD of ISI measurement s_{12} is given by:

$$\mathrm{PSD}[s_{12}] = 4\sin^2(\omega L_0) S_\nu, \tag{3.17}$$

The PSD of the ISI measurement computed by the Welch method [153, 59] with Nuttall-type window is compared with the above analytic formula, shown in figure 3.7.

Finally, we check the TDI algorithm applied to the LOT data by using `PyTDI` to compute the first generation Michelson variables X_1, Y_1, Z_1 from the measurement data. From the result shown in figure 3.8, we can see that the TDI 1.0 generation is sufficient to suppress the

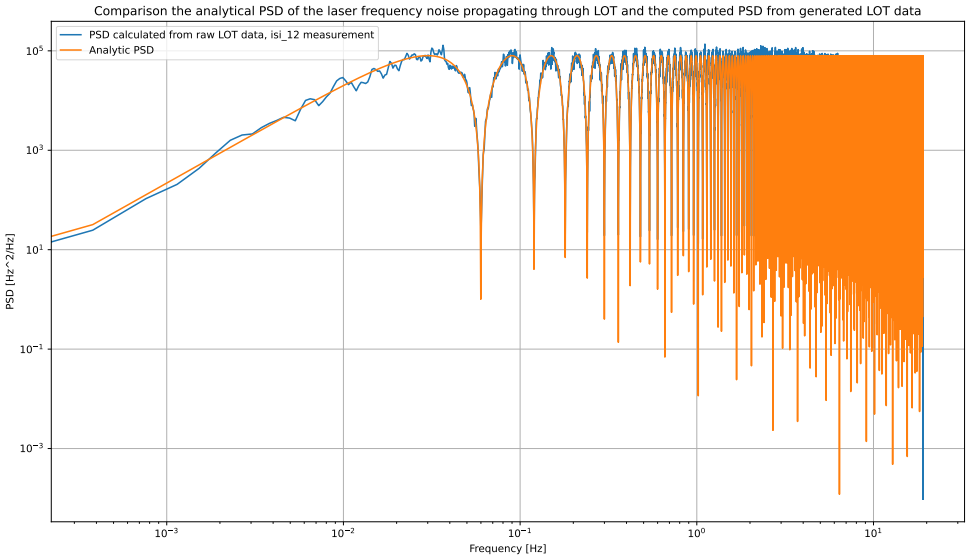

Figure 3.7: The propagation of the signal through LOT via the ISI measurement. The PSD computed from the s_{12} data from the LOT output is compared with the analytic curve.

dominant laser frequency noise injected in the beam signals to be about the level of the LOT intrinsic noise, in the configuration of equal and fixed armlengths. We meet the requirement of the noise reduction, which is 8 orders of magnitude reduction, and the residual signal at the intrinsic noise level. At higher frequencies, there is a mismatch between the residual signal curve and the intrinsic one. We expect that the systematic error of the delay values saved in the LOT output file could explain that discrepancy. Unfortunately, the PSD of this ranging bias coupling to the laser frequency noise (the formulation of the TDI propagation of this noise can be found in INREP technical notes) shown in the red dash line in the plot cannot explain this difference well.

3.3.2 Static unequal armlengths

We move to a more advanced case: the configuration with unequal armlengths, but still time-independent. With this configuration, we still expect the first generation of TDI can suppress the laser frequency noise to the LOT intrinsic level.

For the noise generation, we use the following input parameters:

- The level of the signal as the laser frequency noise is $\sqrt{S_\nu} = 100\sqrt{2}\frac{\text{Hz}}{\sqrt{\text{Hz}}}$, the same as in the equal armlength case.

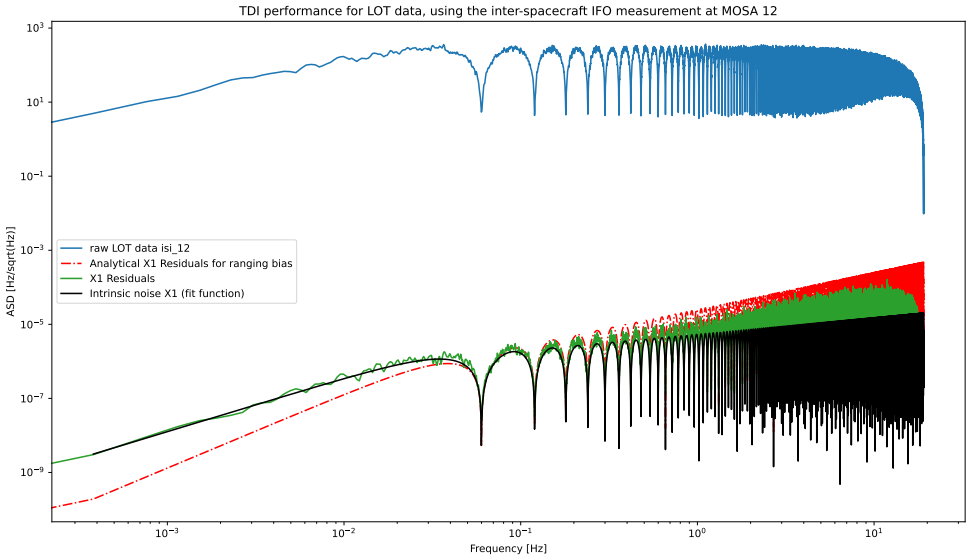

Figure 3.8: TDI performance on experimental data produced by LOT in static equal arm-length. The PSD computed from the TDI Michelson variable X, the green curve, is compared to the PSD of the ISI measurement s_{12} as the blue curve, as well as the intrinsic noise in black. The ISI measurements are generated by LOT, before being processed by `PyTDI` to get the TDI Michelson variables. The intrinsic noise is extracted from LOT data without laser frequency noise in the signal, given by the equation (3.16).

- We test two types of delay time for the distances between spacecraft, which is the delay time to be applied on distant beams. The first one corresponds to integer delay, which means the delay time is an integer number times the inverse of LOT sampling frequency.The second one corresponds to non-integer delay. The first type of delay time has no error in the interpolation for the delay operator in TDI, while the second type has to deal with that. The integer delays are $636/(2 * fs)$ and $644/(2 * fs)$ seconds for distances L_{12}, L_{13}, respectively, where $fs = \frac{40\text{MHz}}{2\times10^{20}}$ is the sampling rate of LOT data. The non-integer delays are $L_{12} = 16.6/2$ and $L_{13} = 16.76/2$ seconds.

The process of computing the TDI variables and their spectral densities is the same as in the previous case. The results are shown in figure 3.9 for integer delay and figure 3.10 for non-integer delay. We verify that the TDI algorithm works well for laser frequency noise suppression in both cases. The residual signal is compatible with the LOT intrinsic noise for most of the frequency band. At high frequencies, in the non-integer case, there are some bumps related to the interpolation error. The analytical model for this effect has not been studied yet for the LOT, which is interesting for future tasks. We also add the reference curve for the

LISA standard noise model to compare with the residual noise signal. This reference curve is from the LISA Science Requirement Document [103] and consists of the most dominant secondary noises, such as test-mass acceleration and readout noise. We note that the noise level of laser frequency noise of LOT and LISA are different: the LOT noise level above about 1 order of magnitude higher, $100\sqrt{2}$ (in LOT) vs 30 Hz (in LISA). We can conclude that the performance to suppress the laser frequency noise on LOT is good because the residual noise is below the other possible secondary noise sources and the noise reduction is about 8 orders of magnitude.

3.3.3 LOT data with linear varying armlength

In the last part, we examine the more realistic configuration for the LOT, which accounts for the varying armlengths. Nevertheless, the model for the armlength is simple as a linear function on time. The inputs for the signal generation are given as follows:

- The level of the signal as the laser frequency noise is $\sqrt{S_\nu} = 100\sqrt{2}\frac{\text{Hz}}{\sqrt{\text{Hz}}}$, the same as in the equal armlength case.

- The delays for the distances among spacecraft are given in the formula:

$$L_{12}(t) = L_{21}(t) = L_{12}^0 + \dot{L}_{12} \times t, \tag{3.18}$$

$$L_{13}(t) = L_{31}(t) = L_{13}^0 + \dot{L}_{13} \times t, \tag{3.19}$$

  where the L_{12}^0, L_{13}^0 are the initial delays of the virtual laser links, extracted from the first LOT data point of the delays. The delay derivatives are parameterized by $\dot{L}_{12} = \frac{5\text{m/s}}{c}$ and $\dot{L}_{13} = \frac{10\text{m/s}}{c}$.

The PSDs of TDI variables computed from the LOT data in this configuration are shown in figure 3.11. In this case, we do not have perfect suppression in the TDI Michelson variables even for the second generation of TDI, which is expected to suppress the laser frequency noise to below the secondary noise level. At very high frequencies, the bumps could be explained by the error in the interpolation of the delay operators. While at middle and low frequencies, the residual laser frequency noise is above the intrinsic noise level, as well as the LISA SciRD [103]. We first guessed the coupling of the CIC filter and the delay operator with the varying delays in the TDI algorithm could explain the discrepancy. However, we rejected this hypothesis after some tests with simple signal processing via LOT and single-delay operators. A very recent study from Léon Vidal turns out that the effect of CIC filters and the decimation steps in the phasemeter have a significant contribution to the TDI residual noise and could explain this result. All details of this work are presented in his PhD thesis [150].

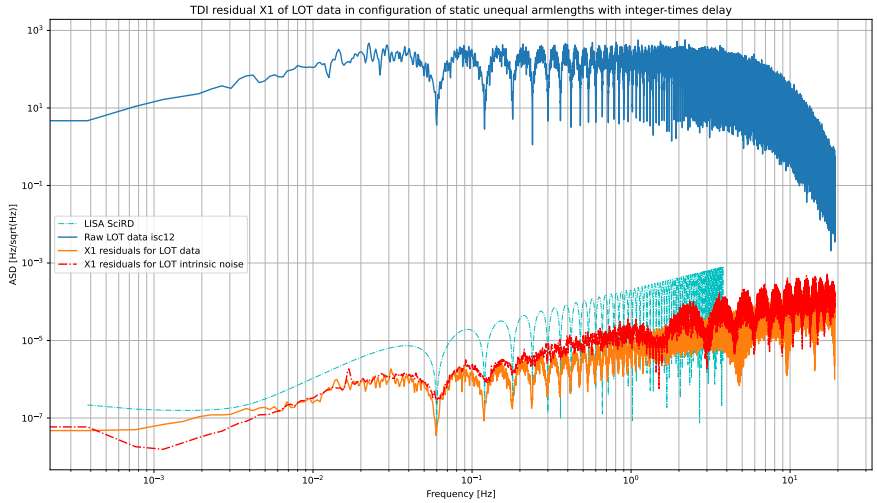

(a) 1st generation of TDI X

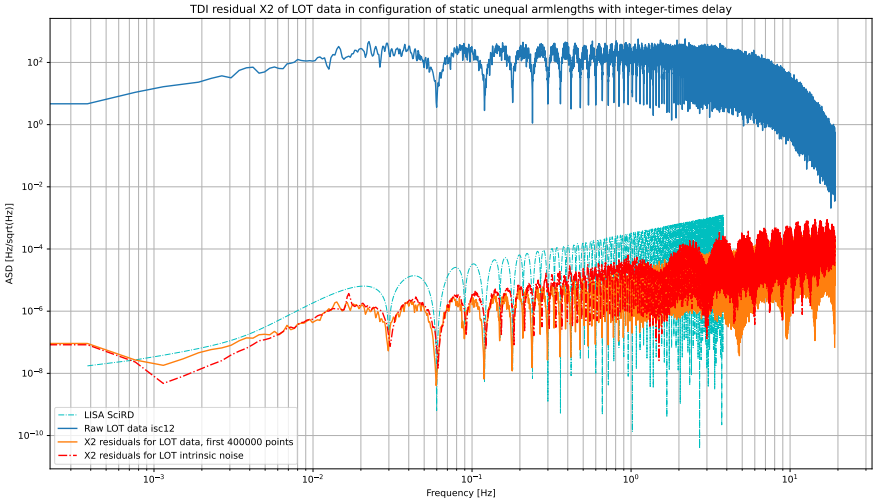

(b) 2nd generation of TDI X

Figure 3.9: TDI performance on experimental data produced by LOT in static unequal arm-length with integer (times inverse of LOT sampling frequency) delay. The first generation of TDI shown in sub-figure (a), while in sub-figure (b) is TDI second generation. The PSD computed from the TDI Michelson variable X, the orange curve, is compared to the PSD of the ISI measurement s_{12} as the blue curve, as well as the intrinsic noise in red dash line. We also indicate the LISA standard noise model from LISA SciRD [103] as a reference to compare the TDI residual signal of LOT with the secondary noise exist in the LISA case.

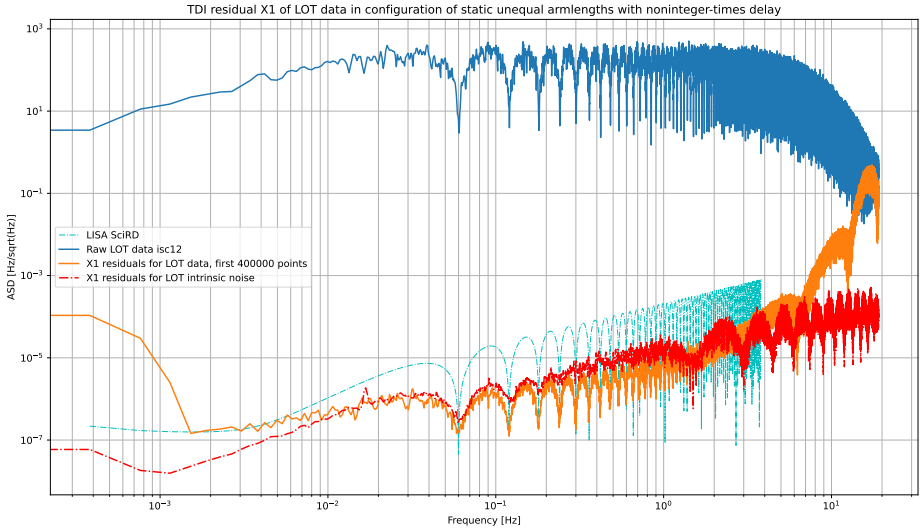

(a) 1st generation of TDI X

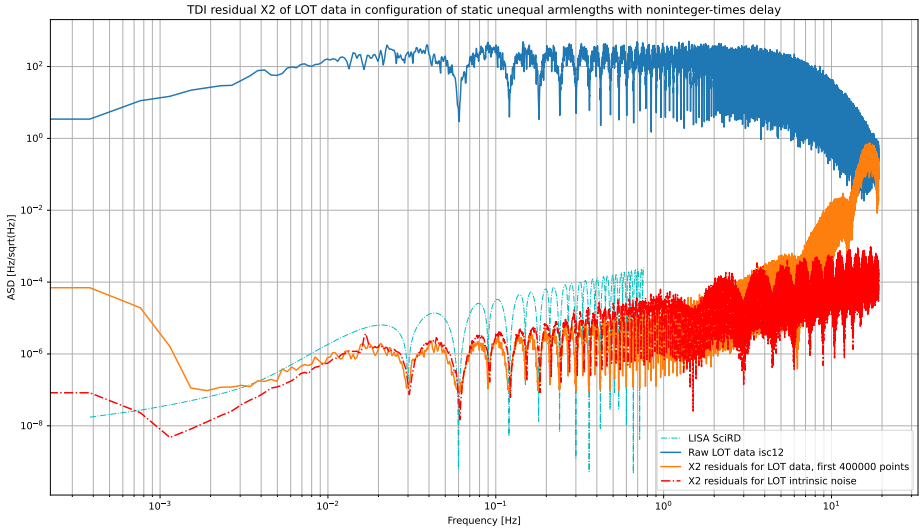

(b) 2nd generation of TDI X

Figure 3.10: TDI performance on experimental data produced by LOT in static unequal arm-length with noninteger (times inverse of LOT sampling frequency) delay. The first generation of TDI shown in sub-figure (a), while in sub-figure (b) is TDI second generation. The legend for the curves is the same as figure 3.9.

In the subsequent studies, we want to examine LOT data with the impact of changing CIC filter and the decimation plan in LISA design. The effect of electronic devices in data processing in both LOT and LISA will help us to improve LISA instrument design. On the other hand, the clock jitter noise could be added in the LOT data generation to test the performance of clock noise reduction.

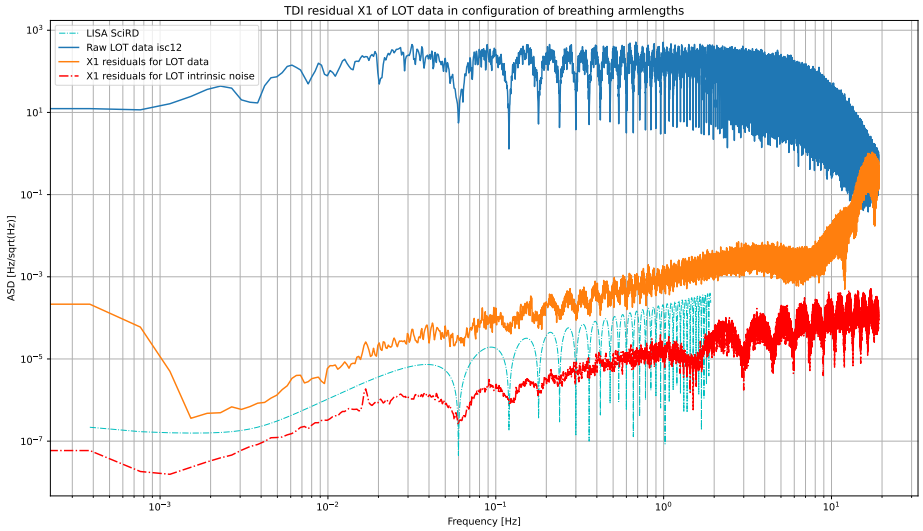

(a) 1st generation of TDI X

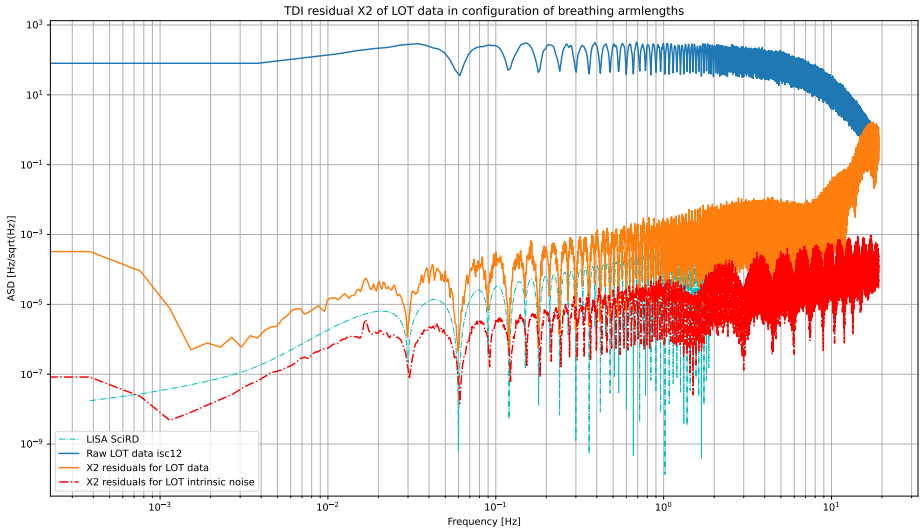

(b) 2nd generation of TDI X

Figure 3.11: TDI performance on experimental data produced by LOT in linear varying arm-length configuration. The first generation of TDI shown in sub-figure (a), while in sub-figure (b) is TDI second generation. The legend for the curves is the same as figure 3.9.

Chapter 4

Noise propagation through TDI

Due to the TDI algorithm introduced in the previous chapter, the noises in the instrument or any other sources will evolve in the spectral shape from the raw measurements to the TDI variables. This chapter considers the TDI impact on LISA noises (mostly secondary ones) by computing their transfer function through the TDI algorithm with the current instrumental model. We also examine some scenarios for noise correlation in this study.

This chapter is mainly the work in the to-be-published article [127]. First, we will give an overview of the TDI transfer function computation methodology. The beam model and IFO measurements constructed in section 2.7 and the TDI formulation in section 3.2.2 are applied to conduct the analytical transfer function of noises propagating through TDI. An example of test-mass acceleration noise propagating through TDI will be presented, including the case of laser locking and some noise correlation scenarios. Then, we summarize all the analytical results and compare the derived analytical noise propagation model with the numerical power spectral density of the data simulated by `LISANode`, presented in section 2.8.

4.1 Methodology

In this section, we introduce our method to compute the TDI transfer function of the noise propagation, using as an example test-mass acceleration noise. Approximations for the simplified result are then justified. Finally, we validate the analytical transfer functions of several noises using the `LISANode` simulator.

4.1.1 PSD/CSD computation

We will briefly introduce a method for calculating the spectral density, which follows the procedure used in the software [39]. The CSD of two signals $u(t)$ and $v(t)$ can be defined as

$$S_{uv}(f) = CSD[u,v] = \lim_{T\to\infty} \frac{1}{T}\tilde{u}_T^*(f)\tilde{v}_T(f) \equiv \langle \tilde{u}^*(f)\tilde{v}(f)\rangle. \tag{4.1}$$

where $\tilde{u}(f)$ is the Fourier transform of $u(t)$ at the frequency f. $u_T(t)$ is $u(t)$ restricted to a time window of duration T. $\tilde{u}_T(f)$ is the Fourier transform of $u_T(t)$. It is obvious to show that $S_{vu}(f)$ is just the complex conjugate of $S_{uv}(f)$. The PSD of some stationary signal $u(t)$ is S_{uu}. It describes the energy contained in the signal $u(t)$ around the frequency f.

To compute the Fourier transform of TDI variables, we should consider the atomic block in TDI formulation: the nested delay operator. We model the light travel times as constants, i.e. $L_{ij}(t) = L_{ij}$. For a nested delay operator applied to a time-series signal,

$$v(t) = \mathcal{D}_{i_1 i_2 \ldots i_n} u(t) = u\left(t - \sum_{k=1}^{n-1} L_{i_k i_{k+1}}\right) \tag{4.2}$$

, its Fourier transform is

$$\tilde{v}(\omega) = \exp\left(-j\omega \sum_{k=1}^{n-1} L_{i_k i_{k+1}}\right)\tilde{u}(\omega). \tag{4.3}$$

The PSD of the usual TDI generator (X, Y and Z) are usually compositions of a limited set of patterns. For each term, we use (4.3) to form the Fourier transform and then compute the PSD.

We will use the short-hand notation

$$\bar{L}_{ij} = \frac{L_{ij} + L_{ji}}{2} \quad \text{and} \quad \bar{L}_{ijik} = \frac{L_{ij} + L_{ji} + L_{ik} + L_{ki}}{4}. \tag{4.4}$$

$$\tag{4.5}$$

Here, the PSD computation is done for the simple nested delay operator $\pm\left(1 - \mathcal{D}_{ii'}\right) u(t)$. The list of all useful patterns is provided in table 4.1.

$$\begin{aligned} PSD\left[\pm\left(1-\mathcal{D}_{iji}\right)u(t)\right](\omega) &= \left\langle \left[\left(1-\widetilde{\mathcal{D}_{iji}}\right)u(t)\right](\omega) \times \left[\left(1-\widetilde{\mathcal{D}_{iji}}\right)u(t)\right]^*(\omega)\right\rangle \\ &= \left\langle \left(1-e^{-j\omega(L_{ij}+L_{ji})}\right)\left(1-e^{j\omega(L_{ij}+L_{ji})}\right)\widetilde{u}(\omega)\widetilde{u}^*(\omega)\right\rangle \\ &= 4\sin^2\left(\omega\bar{L}_{ij}\right) S_u. \end{aligned} \tag{4.6}$$

The CSD computation have some common patterns. Note that we need to respect the order of the terms in the calculation.

Nested delay operator	PSD
$\pm\left(1-\mathcal{D}_{iji}\right)u(t)$	$4\sin^2\left(\omega\bar{L}_{ij}\right)S_u$
$\pm\left(1+\mathcal{D}_{iji}\right)u(t)$	$4\cos^2\left(\omega\bar{L}_{ij}\right)S_u$
$\pm\left(1-\mathcal{D}_{iji}\right)\mathcal{D}_{i_1i_2\ldots i_n}u(t)$	$4\sin^2\left(\omega\bar{L}_{ij}\right)S_u$
$\pm\left(1+\mathcal{D}_{iji}\right)\mathcal{D}_{i_1i_2\ldots i_n}u(t)$	$4\cos^2\left(\omega\bar{L}_{ij}\right)S_u$
$\pm\mathcal{D}_{i_1i_2\ldots i_n}\left(1-\mathcal{D}_{iji}\right)u(t)$	$4\sin^2\left(\omega\bar{L}_{ij}\right)S_u$
$\pm\mathcal{D}_{i_1i_2\ldots i_n}\left(1+\mathcal{D}_{iji}\right)u(t)$	$4\cos^2\left(\omega\bar{L}_{ij}\right)S_u$
$\pm\left(1+\mathcal{D}_{iji}\right)\left(1-\mathcal{D}_{klk}\right)u(t)$	$16\cos^2\left(\omega\bar{L}_{il}\right)\sin^2\left(\omega\bar{L}_{kl}\right)S_u$
$\pm\left(1-\mathcal{D}_{iji}\right)\left(1+\mathcal{D}_{klk}\right)u(t)$	$16\sin^2\left(\omega\bar{L}_{ij}\right)\cos^2\left(\omega\bar{L}_{kl}\right)S_u$
$\pm\left(1+\mathcal{D}_{iji}\right)\left(1+\mathcal{D}_{klk}\right)u(t)$	$16\cos^2\left(\omega\bar{L}_{ij}\right)\cos^2\left(\omega\bar{L}_{kl}\right)S_u$
$\pm\left(1-\mathcal{D}_{iji}\right)\left(1-\mathcal{D}_{klk'}\right)u(t)$	$16\sin^2\left(\omega\bar{L}_{ij}\right)\sin^2\left(\omega\bar{L}_{kl}\right)S_u$
$\pm\left(1-\mathcal{D}_{iji}-\mathcal{D}_{ijiki}+\mathcal{D}_{ikijiji}\right)u(t)$	$16\sin^2\left(\omega\bar{L}_{ij}\right)\sin^2\left(2\omega\bar{L}_{ijk}\right)S_u$
$(a\pm b\mathcal{D}_{iji})x(t)$	$\left[a^2+b^2\pm 2ab\cos\left(\omega\bar{L}_{ij}\right)\right]S_u$

Table 4.1: Table of PSD for the usual patterns present in TDI time domain formulations.

1. $X=\pm(1\pm\mathcal{D}_{iji})x(t)$ and $Y=\pm\left(1\pm\mathcal{D}_{klk}\right)u(t)$. We choose one case of specific set of signs in front of the nested delay operators, the others are easily worked out in the same way.

$$\begin{aligned}
CSD\left[XY\right] &= CSD\left[(1-\mathcal{D}_{iji})u(t),\left(1+\mathcal{D}_{klk}\right)u(t)\right] \\
&= \left\langle\widetilde{\left[(1-\mathcal{D}_{iji}\right)u(t)](\omega)}\times\widetilde{\left[(1+\mathcal{D}_{klk}\right)u(t)]}^{*}(\omega)\right\rangle \\
&= \left\langle\left(1-e^{-2j\omega\bar{L}_{ij}}\right)\left(1+e^{2j\omega\bar{L}_{kl}}\right)\times\widetilde{u}(\omega)\widetilde{u}^{*}(\omega)\right\rangle \\
&= e^{j\omega(-\bar{L}_{ij}+\bar{L}_{kl})}\left(e^{j\omega\bar{L}_{ij}}-e^{-j\omega\bar{L}_{ij}}\right) \\
&\quad\times\left(e^{-j\omega\bar{L}_{kl}}+e^{j\omega\bar{L}_{kl}}\right)\langle\widetilde{u}(\omega)\widetilde{u}^{*}(\omega)\rangle \\
&= e^{j\omega(-\bar{L}_{ij}+\bar{L}_{kl})}2j\sin(\omega\bar{L}_{ij})2j\cos(\omega\bar{L}_{kl})S_u \\
&= -4\sin(\omega\bar{L}_{ij})\cos(\omega\bar{L}_{kl})e^{j\omega(-\bar{L}_{ij}+\bar{L}_{kl})}S_u
\end{aligned}\tag{4.7}$$

2. $X=\pm(a\pm b\mathcal{D}_{iji})x(t)$ and
$Y=\pm\left(1\pm\mathcal{D}_{klk}\right)\mathcal{D}_{i_1i_2\ldots i_n}u(t)$. We choose one case of specific set of signs in front of the

nested delay operators, the others are easily worked out in the same way.

$$\begin{aligned} CSD\left[XY\right] &= CSD\left[(a+b\mathcal{D}_{iji})u(t) * (1-\mathcal{D}_{klk})\,\mathcal{D}_{i_1 i_2 \ldots i_n} u(t)\right] \\ &= \Big\langle [(a+\widetilde{b\mathcal{D}_{iji}})\,u(t)](\omega) \\ &\quad \times [(1-\mathcal{D}_{klk})\,\widetilde{\mathcal{D}_{i_1 i_2 \ldots i_n}} u(t)]^{*}(\omega) \Big\rangle \\ &= \Big\langle \left(a+be^{-j\omega(L_{ij}+L_{ji})}\right)\left(1-e^{j\omega(L_{kl}+L_{lk})}\right) \\ &\quad \times e^{j\omega(L_{i_1}+L_{i_2}+\ldots+L_{i_n})}\widetilde{u}(\omega)\widetilde{u}^{*}(\omega) \Big\rangle \\ &= e^{j\omega(L_{i_1}+L_{i_2}+\ldots+L_{i_n}-\bar{L}_{ij}+\bar{L}_{kl})}\left(e^{-j\omega\bar{L}_{kl}}-e^{j\omega\bar{L}_{kl}}\right) \\ &\quad \times \left(ae^{j\omega\bar{L}_{ij}}+be^{-j\omega\bar{L}_{ij}}\right)\langle\widetilde{u}(\omega)\widetilde{u}^{*}(\omega)\rangle \\ &= -2j\sin(\omega\bar{L}_{kl})e^{j\omega(L_{i_1}+L_{i_2}+\ldots+L_{i_n}-\bar{L}_{ij}+\bar{L}_{kl})} \\ &\quad \times \left(ae^{j\omega\bar{L}_{ij}}+be^{-j\omega\bar{L}_{ij}}\right)S_u. \end{aligned} \tag{4.8}$$

4.1.2 Approximation justification

In the previous subsections, some assumptions and approximations are made to reduce the complexity of the calculation. There are collected and justified here.

1. We assume that clock noise has been suppressed totally by the clock noise reduction algorithm [77]. Therefore, we do not need to consider the sideband beams in our beam model since they are only used for clock noise reduction [77, 76]. Since the residual clock noise is expected below secondary noises, this assumption is acceptable in our study case.

2. All measurements are perfectly synchronized in the Barycentric Coordinate Time (TCB). Hence, there are no errors in time stamping the onboard measurements. This assumption simplifies the complexity of the computation.

3. All IFO measurements are expressed as fractional frequency fluctuations around the nominal laser frequency. We assume this nominal laser frequency is constant and equal for all laser source, and it is equal to the nominal laser frequency, $c/1064$ nm $= 282$ THz.

4. The DFACS is ignored in this study, which means the S/C and test-masses are treated as independent bodies. We also neglect the tilt-to-length coupling noise in the beam model.

5. We are assuming that S/C hardware from the noise performance perspective are statistically identical. Hence, 6 test-mass acceleration noises have the same PSD, or a

correlation noise appearing between two adjacent test-masses will occur similarly on all S/C.

6. All armlengths of the LISA constellation are constant, and so delay operators are commutative. We use this approximation frequently with unsuppressed noises because the armlength variation is a second-order effect for these noises. Therefore, this approximation is justified in the study of unsuppressed noises.

$$L_{ij}(t) = L_{ij} \qquad \forall i, j \in \{1, 2, 3\} \tag{4.9}$$

7. Mostly in the case of unsuppressed noises, we neglect ranging and interpolation errors so the propagation delay operators and the TDI delay operators can be treated similarly, $\mathbf{D} \approx \mathcal{D}$. The effect of ranging and interpolation errors will contribute more significantly in the case of suppressed noises but this is out of the scope of the article as well as this thesis.

8. To simplify the final transfer functions, we use the approximation of equal armlengths, which could be consider as the average armlength for long duration of the mission operation. Due to the almost equilateral configuration of the LISA constellation, we expect the average of each armlength should be not too different.

In the simulation validation studies (see section 4.4), the first five approximations (no clock jitter noise, synchronized measurements, constant nominal laser frequency, no DFACS and noises of the same kind statistically similar) are made. The validity of these approximations will not be tested here, whereas it will be for approximations 6 to 8.

4.1.3 Procedure for spectral density computation

We will now detail the calculation of the transfer functions for unsuppressed noises, using as example test-mass acceleration noise. The propagation of other unsuppressed noises are worked out in a similar way.

The calculation are performed in several steps:

1. If we consider laser frequency planning, laser noises from the locking scheme should be substituted into the beam model, as shown in section 2.7.4[1].

[1] An alternative approach is shown in section 12.2 of [76]. In principle, TDI algorithm makes sure all the p_{ij} terms are strongly suppressed, so any secondary noise terms in p_{ij} due to laser locking are suppressed alongside the laser noise. Therefore, we expect the secondary noise levels to remain identical regardless of the locking scheme, as verified by the explicit computation.

2. Since most of the time, we assume that noises of different types are uncorrelated, we can ignore all noises in the beams except for the one of interest. The LISA total noise transfer function is then simply the sum of all individual noise transfer functions. If a noise correlation scenario is considered, we need to apply the correlation relations and keep only one of the correlated noises in the beam model.

3. After deriving all the IFO measurements expressed in section 2.7.5, the next step is the computation of TDI variables, presented in subsection 3.2.2. First are the intermediary variables, then the TDI combinations. We write the result in terms of the product of nested delay operator applied to each noise, to ease the identification of patterns in the next step.

4. Hence, we can use the patterns PSD/CSD presented in subsection 4.1.1 for quick computation of the spectral density of individual noise terms. The noise terms are considered uncorrelated. The correlations are treated by introducing the same noise term in multiple measurements.

5. We use the approximation of constant armlengths (4.9) to simplify the computation (allowing to commute delay operators). Most of the time, the PSD XX and the CSD XY are enough because we can use index permutation to deduce the other spectral densities. This apply if the beams are symmetric, so it does not for the cases with frequency planning.

6. Finally, we sum up all components and simplify the result using some approximations presented in the end of subsection 4.1.2.

4.2 A few examples

4.2.1 Uncorrelated test-mass acceleration noise without laser locking

In this section, we only consider test-mass acceleration noise. For simplicity, we omit the time dependency in the noise notation δ, but still remember that it is a time varying signal. We only consider the projection of test-mass displacement noise on the sensitive axis, δ_{ij}, since it is what enters the measurements.

Without frequency planning and correlation, the formulation of the measurements in S/C 1 are:

$$\begin{cases} \mathrm{isi}_{12} &= 0 \\ \mathrm{rfi}_{12} &= 0 \\ \mathrm{tmi}_{12} &= 2\,\mathcal{F}\,\theta^{\mathrm{rfi}}_{12}\,\delta_{12} \end{cases} \qquad \begin{cases} \mathrm{isi}_{13} &= 0 \\ \mathrm{rfi}_{13} &= 0 \\ \mathrm{tmi}_{13} &= 2\,\mathcal{F}\,\theta^{\mathrm{rfi}}_{13}\,\delta_{13} \end{cases} \tag{4.10}$$

We then compute the TDI intermediary variables. We neglect the ranging and interpolation errors such that the two types of delay operators are equivalent, $\mathbf{D} \approx \mathcal{D}$. Moreover, the nominal laser wavelength for every laser source is constant and equal, i.e., $\lambda_{ij} = \lambda$. Applying these approximation to equations (3.9), (3.10), (3.11) and (3.12), we get

$$\xi_{12} = -\theta_{12}^{\text{isi}}\, \mathcal{F}\left(\mathcal{D}_{12}\delta_{21} + \delta_{12}\right), \tag{4.11}$$

$$\xi_{13} = -\theta_{13}^{\text{isi}}\, \mathcal{F}\left(\mathcal{D}_{13}\delta_{31} + \delta_{13}\right), \tag{4.12}$$

and then

$$\eta_{12} = -\mathcal{F}\left(\mathcal{D}_{12}\delta_{21} + \delta_{12}\right), \tag{4.13}$$

$$\eta_{13} = -\mathcal{F}\left(\mathcal{D}_{13}\delta_{31} + \delta_{13}\right). \tag{4.14}$$

The Michelson combination is computed as follows, using the constant armlength approximation (4.9) (we can commute the delay operators with themselves and with antialiasing filter operator[2]).

$$\begin{aligned}
X_2 &= \left(1 - \mathcal{D}_{12131}\right)\left[\left(\eta_{13} + \mathcal{D}_{13}\eta_{31}\right)\right. \\
&\quad \left.+\mathcal{D}_{131}\left(\eta_{12} + \mathcal{D}_{12}\eta_{21}\right)\right] - \left(1 - \mathcal{D}_{13121}\right) \\
&\quad \times\left[\left(\eta_{12} + \mathcal{D}_{12}\eta_{21}\right) + \mathcal{D}_{121}\left(\eta_{13} + \mathcal{D}_{13}\eta_{31}\right)\right] \\
&\approx \left(1 - \mathcal{D}_{12131}\right)\left[\left(1 - \mathcal{D}_{121}\right)\left(\eta_{13} + \mathcal{D}_{13}\eta_{31}\right)\right. \\
&\qquad \left.- \left(1 - \mathcal{D}_{131}\right)\left(\eta_{12} + \mathcal{D}_{12}\eta_{21}\right)\right] \\
&= \mathcal{F}\Big\{ - \left(1 - \mathcal{D}_{12131}\right)\left(1 - \mathcal{D}_{121}\right)\left(1 + \mathcal{D}_{131}\right)\delta_{13} \\
&\qquad -2\left(1 - \mathcal{D}_{12131}\right)\left(1 - \mathcal{D}_{121}\right)\mathcal{D}_{13}\delta_{31} \\
&\qquad + \left(1 - \mathcal{D}_{12131}\right)\left(1 - \mathcal{D}_{131}\right)\left(1 + \mathcal{D}_{121}\right)\delta_{12} \\
&\qquad +2\left(1 - \mathcal{D}_{12131}\right)\left(1 - \mathcal{D}_{131}\right)\mathcal{D}_{12}\delta_{21}\Big\}
\end{aligned} \tag{4.15}$$

The Y-channel is just the index permutation of X-channel.

$$\begin{aligned}
Y_2 &= \mathcal{F}\Big\{ - \left(1 - \mathcal{D}_{23212}\right)\left(1 - \mathcal{D}_{232}\right)\left(1 + \mathcal{D}_{212}\right)\delta_{21} \\
&\qquad -2\left(1 - \mathcal{D}_{23212}\right)\left(1 - \mathcal{D}_{232}\right)\mathcal{D}_{21}\delta_{12} \\
&\qquad + \left(1 - \mathcal{D}_{23212}\right)\left(1 - \mathcal{D}_{212}\right)\left(1 + \mathcal{D}_{232}\right)\delta_{23} \\
&\qquad +2\left(1 - \mathcal{D}_{23212}\right)\left(1 - \mathcal{D}_{212}\right)\mathcal{D}_{23}\delta_{32}\Big\}
\end{aligned} \tag{4.16}$$

The PSD of these Michelson variables can be worked out by collecting the Fourier transforms of the auto-correlation functions of each noise in each MOSA. Assuming uncorrelated

[2] This is not true in the case of suppressed noises like laser frequency noise. In such cases, we need to take into account the non-commutation of delay operators with themselves and with filter operators [43].

noises, the cross-terms between two different noises, such as $\langle \widetilde{\delta_{12}}^*(f)\widetilde{\delta_{13}}(f)\rangle$, are vanishing. We can also use results from section 4.1.1 for fast deduction. For example, the contribution to the PSD of X-channel $S_{XX}(f)$ of acceleration noise in MOSA 13 reads:

$$\begin{aligned}
&\mathrm{PSD}\left[-\mathcal{F}\left(1-\mathcal{D}_{12131}\right)\left(1-\mathcal{D}_{121}\right)\left(1+\mathcal{D}_{131}\right)\delta_{13}\right](\omega)\\
&= 64 S_{\mathcal{F}}(\omega) S_{\delta_{13}}(\omega)\sin^2\left[\omega(\bar{L}_{12}+\bar{L}_{31})\right]\\
&\quad\times\sin^2(\omega\bar{L}_{12})\cos^2(\omega\bar{L}_{31}),
\end{aligned} \tag{4.17}$$

where $S_{\mathcal{F}}(\omega)=\langle|\tilde{\mathcal{F}}(f)|^2\rangle$ and $S_{\delta_{13}}(\omega)=\langle|\widetilde{\delta_{13}}(f)|^2\rangle$. Then, one can check that the PSD of the X-channel for the uncorrelated test-mass acceleration noise is:

$$\begin{aligned}
\mathrm{S}_{\mathrm{XX}}^{\text{uncorr acc tm}}(\omega) &= 64 S_{\mathcal{F}}(\omega)\sin^2\left[\omega(\bar{L}_{12}+\bar{L}_{31})\right]\\
&\quad\times\Big\{\sin^2(\omega\bar{L}_{12})\left[\cos^2(\omega\bar{L}_{31})S_{\delta_{13}}(\omega)\right.\\
&\quad\left.+S_{\delta_{31}}(\omega)\right]+\sin^2(\omega\bar{L}_{31})\\
&\quad\times\left[\cos^2(\omega\bar{L}_{12})S_{\delta_{12}}(\omega)+S_{\delta_{21}}(\omega)\right]\Big\}
\end{aligned} \tag{4.18}$$

The PSD of Y-channel, $\mathrm{S}_{\mathrm{YY}}^{\text{uncorr acc tm}}$, has the same form with permuted indices $\{1\to 2, 2\to 3, 3\to 1\}$. We can use the equal armlength approximations $L_{ij}=L$ and that all test-mass acceleration noises share the same PSD, $S_{\delta_{ij}}=S_{\delta}$, to get:

$$\begin{aligned}
\mathrm{S}_{\mathrm{XX}}^{\text{uncorr acc tm}}(\omega) &= \mathrm{S}_{\mathrm{YY}}^{\text{uncorr acc tm}}(\omega)\\
&= 64\sin^2(2\omega L)\sin^2(\omega L)\left[3+\cos(2\omega L)\right]\\
&\quad\times S_{\mathcal{F}}(\omega)S_{\delta}(\omega)
\end{aligned} \tag{4.19}$$

To compute the CSD between X and Y, we use the same procedure and collect the non-zero terms that have the same noise index. Note that $CSD[YX]=CSD[XY]^*$, so we only need to compute the CSD of XY. We can also use the CSD result from section 4.1.1. For example, the contribution of acceleration noise in MOSA 12 to the CSD S_{XY} reads:

$$\begin{aligned}
&\mathrm{CSD}\Big[\mathcal{F}\left(1-\mathcal{D}_{12131}\right)\left(1-\mathcal{D}_{131}\right)\left(1+\mathcal{D}_{121}\right)\delta_{12}\\
&\qquad *(-2)\left(1-\mathcal{D}_{23212}\right)\left(1-\mathcal{D}_{232}\right)\mathcal{D}_{21}\delta_{12}\Big](\omega)\\
&= -64 S_{\mathcal{F}}(\omega)S_{\delta_{12}}(\omega)\sin\left[\omega(\bar{L}_{12}+\bar{L}_{31})\right]\\
&\quad\times\sin\left[\omega(\bar{L}_{12}+\bar{L}_{23})\right]\sin(\omega\bar{L}_{13})\sin(\omega\bar{L}_{23})\cos(\omega\bar{L}_{12})\\
&\quad\times\exp\left[-j\omega\left(2\bar{L}_{13}-2\bar{L}_{23}+\bar{L}_{12}-L_{21}\right)\right]
\end{aligned} \tag{4.20}$$

One can find the CSD of XY is given by

$$\begin{aligned}\mathrm{S}_{\mathrm{XY}}^{\text{uncorr acc tm}}(\omega) &= -64 S_{\mathcal{F}}(\omega)\sin\left[\omega(\bar{L}_{12}+\bar{L}_{31})\right] \\ &\quad\times\sin\left[\omega(\bar{L}_{12}+\bar{L}_{23})\right]\sin(\omega\bar{L}_{13}) \\ &\quad\times\sin(\omega\bar{L}_{23})\cos(\omega\bar{L}_{12})e^{-j\omega\frac{L_{12}-L_{21}}{2}} \\ &\quad\times e^{-2j\omega\left(\bar{L}_{13}-\bar{L}_{23}\right)}\left[S_{\delta_{12}}(\omega)+S_{\delta_{21}}(\omega)\right]\end{aligned} \tag{4.21}$$

Assuming equal armlengths and the same test-mass acceleration noise level in all MOSAs, we obtain

$$\mathrm{S}_{\mathrm{XY}}^{\text{uncorr acc tm}}(\omega) = -64 S_{\mathcal{F}}(\omega)\sin^3(2\omega L)\sin(\omega L)\, S_{\delta}(\omega) \tag{4.22}$$

4.2.2 Uncorrelated test-mass acceleration noise with laser locking

To account for frequency planning, we need to derive the locked laser frequency fluctuations as functions of the primary laser, p_{32}, before substituting them in the beam model and IFO measurements. We use the group of equations (2.31) and we only keep track of the test-mass acceleration and primary laser noises,

$$p_{23} = \mathbf{D}_{12}\, p_{32} \tag{4.23a}$$
$$p_{31} = p_{32} \tag{4.23b}$$
$$p_{13} = \mathbf{D}_{21}\, p_{32} \tag{4.23c}$$
$$p_{12} = \mathbf{D}_{21}\, p_{32} \tag{4.23d}$$
$$p_{21} = \mathbf{D}_{321}\, p_{32}. \tag{4.23e}$$

Due to laser locking, the beams and IFO measurements are no longer symmetric for the different S/C. We therefore give the IFO signals for the whole LISA constellation

- On S/C 1:

$$\begin{cases} \mathrm{isi}_{12} &= \theta_{12}^{\mathrm{isi}}\mathcal{F}\left(\mathbf{D}_{121}-1\right)\mathbf{D}_{13}p_{32} \\ \mathrm{rfi}_{12} &= 0 \\ \mathrm{tmi}_{12} &= 2\,\mathcal{F}\,\theta_{12}^{\mathrm{rfi}}\,\delta_{12} \end{cases} \tag{4.24}$$

$$\begin{cases} \mathrm{isi}_{13} &= 0 \\ \mathrm{rfi}_{13} &= 0 \\ \mathrm{tmi}_{13} &= 2\,\mathcal{F}\,\theta_{13}^{\mathrm{rfi}}\,\delta_{13} \end{cases} \tag{4.25}$$

- On S/C 2:

$$\begin{cases} \mathrm{isi}_{23} &= 0 \\ \mathrm{rfi}_{23} &= \theta^{\mathrm{rfi}}_{23}\mathcal{F}\left(\mathbf{D}_{213}-\mathbf{D}_{23}\right)p_{32} \\ \mathrm{tmi}_{23} &= \theta^{\mathrm{rfi}}_{23}\mathcal{F}\left[\left(\mathbf{D}_{213}-\mathbf{D}_{23}\right)p_{32}+2\delta_{23}\right] \end{cases} \tag{4.26}$$

$$\begin{cases} \mathrm{isi}_{21} &= 0 \\ \mathrm{rfi}_{21} &= \theta^{\mathrm{rfi}}_{21}\left(\mathbf{D}_{23}-\mathbf{D}_{213}\right)p_{32} \\ \mathrm{tmi}_{21} &= \theta^{\mathrm{rfi}}_{21}\mathcal{F}\left[\left(\mathbf{D}_{23}-\mathbf{D}_{213}\right)p_{32}+2\delta_{21}\right] \end{cases} \tag{4.27}$$

- On S/C 3:

$$\begin{cases} \mathrm{isi}_{31} &= \theta^{\mathrm{isi}}_{31}\left(\mathbf{D}_{313}-1\right)p_{32} \\ \mathrm{rfi}_{31} &= 0 \\ \mathrm{tmi}_{31} &= 2\mathcal{F}\theta^{\mathrm{rfi}}_{31}\delta_{31} \end{cases} \tag{4.28}$$

$$\begin{cases} \mathrm{isi}_{32} &= \theta^{\mathrm{isi}}_{32}\left(\mathbf{D}_{323}-1\right)p_{32} \\ \mathrm{rfi}_{32} &= 0 \\ \mathrm{tmi}_{32} &= 2\mathcal{F}\theta^{\mathrm{rfi}}_{32}\delta_{32} \end{cases} \tag{4.29}$$

The next step is to compute the TDI intermediary variables ξ, η. Assuming $\mathbf{D} = \mathcal{D}$, one can verify that

$$\eta_{12} = \mathcal{F}(\mathcal{D}_{123}-\mathcal{D}_{13})p_{32} - \mathcal{F}\left(\mathcal{D}_{12}\delta_{21}+\delta_{12}\right) \tag{4.30}$$

$$\eta_{13} = -\mathcal{F}\left(\mathcal{D}_{13}\delta_{31}+\delta_{13}\right) \tag{4.31}$$

$$\eta_{23} = -\mathcal{F}\left(\mathcal{D}_{23}\delta_{32}+\delta_{23}\right) \tag{4.32}$$

$$\eta_{21} = \mathcal{F}(\mathcal{D}_{213}-\mathcal{D}_{23})p_{32} - \mathcal{F}\left(\mathcal{D}_{21}\delta_{12}+\delta_{21}\right) \tag{4.33}$$

$$\eta_{31} = \mathcal{F}(\mathcal{D}_{313}-1)p_{32} - \mathcal{F}\left(\mathcal{D}_{31}\delta_{13}+\delta_{31}\right) \tag{4.34}$$

$$\eta_{32} = \mathcal{F}(\mathcal{D}_{323}-1)p_{32} - \mathcal{F}\left(\mathcal{D}_{32}\delta_{23}+\delta_{32}\right) \tag{4.35}$$

We note that, except for the terms with laser frequency noise p_{32}, all terms in η are identical to the case without laser locking. That is expected because the locking constraints (2.31) do not contain test-mass acceleration noise in any term. The X-channel for laser noise only is

$$\begin{aligned} X_2^{\text{p-only}} = \mathcal{F}\big[&(1-\mathcal{D}_{13121})(1-\mathcal{D}_{12131}) \\ &-(1-\mathcal{D}_{12131})(1-\mathcal{D}_{13121})\big]p_{32}, \end{aligned} \tag{4.36}$$

which is cancelled out when we commute the TDI delay, i.e. constant delays assumption. In the end, the TDI combinations X, Y and Z in the case of laser locking for the test-mass acceleration noise are exactly the same as in the case without locking, (4.19) and (4.22).

4.2.3 Uncorrelated readout and optical path noises with laser locking

The locking constraints (2.31) contain readout noises, $N^{ro}_{x,ij}$, and optical path noises, $N^{op}_{loc/x,ij}$. Therefore, the situation is different from acceleration noise. Expanding η_{12} without laser locking, we get:

$$\begin{aligned}\eta_{12} &= \theta^{\rm isi}_{21}\mathcal{F}N^{ro}_{s,12} - \theta^{\rm rfi}_{21}\mathcal{F}\mathcal{D}_{12}\frac{N^{ro}_{\epsilon,21} - N^{ro}_{\rm rfi,21}}{2} \\ &\quad -\theta^{\rm rfi}_{12}\mathcal{F}\frac{N^{ro}_{\epsilon,12} - N^{ro}_{\rm rfi,12}}{2} + \theta^{\rm rfi}_{21}\mathcal{D}_{12}\mathcal{F}\frac{N^{ro}_{\rm rfi,21} + N^{ro}_{\rm rfi,23}}{2},\end{aligned} \tag{4.37}$$

while we get with laser locking:

$$\begin{aligned}\eta_{12} &= \theta^{\rm isi}_{12}\mathcal{F}N^{ro}_{s,12} - \theta^{\rm rfi}_{21}\mathcal{D}_{12}\mathcal{F}\frac{N^{ro}_{\epsilon,21} - N^{ro}_{\rm rfi,21}}{2} \\ &\quad -\theta^{\rm rfi}_{12}\mathcal{F}\frac{N^{ro}_{\epsilon,12} - N^{ro}_{\rm rfi,12}}{2} + \theta^{\rm rfi}_{21}\mathcal{D}_{12}\mathcal{F}\frac{N^{ro}_{\rm rfi,21} + N^{ro}_{\rm rfi,23}}{2} \\ &\quad -\theta^{\rm isi}_{13}\mathcal{F}N^{ro}_{s,13} + \theta^{\rm isi}_{23}\mathcal{F}\mathcal{D}_{12}N^{ro}_{s,23} \\ &\quad -\theta^{\rm rfi}_{31}\mathcal{F}\mathcal{D}_{13}N^{ro}_{\rm rfi,31} - \theta^{\rm rfi}_{12}\mathcal{F}N^{ro}_{\rm rfi,12}\end{aligned} \tag{4.38}$$

We observe that laser locking introduces additional terms. These terms actually vanish at the next TDI step, when forming the variable η. Considering, for example, solely $N^{ro}_{s,13}$, we have

$$\begin{aligned}\eta_{12} &: -\theta^{\rm isi}_{13}N^{ro}_{s,13}, \\ \eta_{21} &: \theta^{\rm isi}_{13}\mathcal{D}_{21}N^{ro}_{s,13}, \\ \eta_{31} &: \theta^{\rm isi}_{13}\mathcal{D}_{31}N^{ro}_{s,13}\end{aligned}$$

Substituting in X_2 given by equation (3.13), we get

$$\begin{aligned}X_2 &= [1 - \mathcal{D}_{121} - \mathcal{D}_{12131} + \mathcal{D}_{1312121} + (\mathcal{D}_{13121} - \mathcal{D}_{12131}) \\ &\quad + (\mathcal{D}_{131212131} - \mathcal{D}_{121313121})]\,\theta^{\rm isi}_{13}N^{ro}_{s,13}.\end{aligned} \tag{4.39}$$

Assuming that delay operators commute, the terms in parentheses disappear and we are back to the results without locking.

One can checked that we obtain the same results as for the case without locking, for all terms of readout noises and optical path noises. Finally, we find that the results are the same with and without locking for all unsuppressed noises.

4.2.4 Correlated acceleration noise

Finally, we consider the correlation scenario (2.29) for test-mass acceleration noise. The correlation relation is

$$\delta_{ij} = \gamma\ \delta_{ik}, \tag{4.40}$$

for $(i,j,k) =$ circular permutation of $(1,2,3)$, with γ the correlation factor and with $j \neq k$. We substitute this in the beam model and then form the IFO measurements. Since the correlated noises are in the same S/C, the IFO measurements remain symmetric (as in the uncorrelated noise case). In S/C 1, we keep only the test-mass acceleration noise from MOSA 12,

$$\begin{cases} \mathrm{isi}_{12} &= 0 \\ \mathrm{rfi}_{12} &= 0 \\ \mathrm{tmi}_{12} &= 2\,\mathcal{F}\,\theta_{12}^{\mathrm{rfi}}\,\delta_{12} \end{cases} \qquad \begin{cases} \mathrm{isi}_{13} &= 0 \\ \mathrm{rfi}_{13} &= 0 \\ \mathrm{tmi}_{13} &= 2\,\mathcal{F}\,\theta_{13}^{\mathrm{rfi}}\,\gamma\delta_{12} \end{cases} \tag{4.41}$$

Then, the TDI intermediary variables η for S/C 1 are

$$\eta_{12} = -\mathcal{F}\left(\gamma\mathcal{D}_{12}\delta_{23} + \delta_{12}\right), \tag{4.42}$$

$$\eta_{13} = -\mathcal{F}\left(\mathcal{D}_{13}\delta_{31} + \gamma\delta_{12}\right) \tag{4.43}$$

Applying the same procedure as for the uncorrelated case, we get the following expression for the PSD:

$$\begin{aligned} \mathrm{S}_{\mathrm{XX}}^{\mathrm{corr\ acc\ tm}}(\omega) &= 32\left[3\gamma^2 + 2\gamma + 3 + (1+\gamma)^2\cos(2\omega L)\right] \\ &\quad \times \sin^2(2\omega L)\sin^2(\omega L)\,S_{\mathcal{F}}(\omega)S_{\delta}(\omega), \end{aligned} \tag{4.44}$$

and, for the CSD,

$$\begin{aligned} \mathrm{S}_{\mathrm{XY}}^{\mathrm{corr\ acc\ tm}}(\omega) &= -64\left[(1+\gamma)^2\cos(2\omega L) - \gamma\right] \\ &\quad \times \sin^2(2\omega L)\sin^2(\omega L)\,S_{\mathcal{F}}(\omega)S_{\delta}(\omega) \end{aligned} \tag{4.45}$$

This example is a good illustration of the importance of correlation. Indeed, at low frequency, $\cos(2\omega L) \sim 1$, and the fully correlated case ($\gamma = 1$) is 1.5 times higher than the uncorrelated case. On the other hand, the fully anticorrelated case ($\gamma = -1$) case is 2 times lower than the uncorrelated case. We note that $\gamma = 0$ does not mean the noises are uncorrelated according to the expression (4.40). Therefore, equations (4.44) and (4.45) do not reduce to equations (4.19) and (4.22) in case $\gamma = 0$.

4.3 Result of analytical transfer function

To summarize all analytical results, we list the noises with the specific correlation and the TDI transfer function for X in table 4.2. The results are the same for Y and Z, even with

laser locking. For all these results, the equal armlengths and equal noise level approximations are used. We do not distinguish between the case with or without laser locking the results are identical for the unsuppressed noises. For the sake of brevity, we introduce two common factors in the summary table:

$$C_{XX}(\omega) = 16\sin^2(\omega L)\sin^2(2\omega L), \tag{4.46}$$

$$C_{XY}(\omega) = -16\sin(\omega L)\sin^3(2\omega L). \tag{4.47}$$

Noise type	Correlation	PSD	CSD
Test-mass acceleration	None	$4C_{XX}(\omega)\,[3+\cos(2\omega L)]$	$4C_{XY}(\omega)$
	Fully-correlated at the same S/C	$8C_{XX}(\omega)$	$-4C_{XX}(\omega)$
	Anti-correlated at the same S/C	$8C_{XX}(\omega)\,[2+\cos(2\omega L)]$	$4C_{XX}(\omega)\,[1-4\cos(\omega L)]$
Readout (TMI) and Optical Path-length (TMI)	None	$C_{XX}(\omega)\,[3+\cos(2\omega L)]$	$C_{XY}(\omega)$
	Correlated adjacent TMI noise	$2C_{XX}(\omega)$	$-C_{XX}(\omega)$
	Anti-correlated adjacent TMI noise	$2C_{XX}(\omega)\,[2+\cos(2\omega L)]$	$C_{XX}(\omega)\,[1-4\cos(\omega L)]$
Backlink (TMI)	None	$C_{XX}(\omega)\,[3+\cos(2\omega L)]$	$C_{XY}(\omega)$
Readout (ISI and RFI) and Optical Path-length (ISI and RFI)	None	$4C_{XX}(\omega)$	$C_{XY}(\omega)$
	Correlated adjacent IFO noise	$2C_{XX}(\omega)$	$-C_{XX}(\omega)$
	Anti-correlated adjacent IFO noise	$6C_{XX}(\omega)$	$C_{XX}(\omega)\,[1-4\cos(\omega L)]$
	Fully correlated at the same telescope	$4C_{XX}(\omega)\,[3+\cos(2\omega L)]$	$4C_{XY}(\omega)$
Backlink (RFI)	None	$4C_{XX}(\omega)$	$C_{XY}(\omega)$

Table 4.2: Summary table of analytical TDI X,Y,Z transfer functions for unsuppressed noises. All results have been simplified using approximations (refer to subsection 4.1.2).

Several types of noises share the same transfer function. For some of them, it is simply because the noises enter identically in the measurement (e.g., readout ISI and optical path ISI).

There is another set of TDI variables, called A,E,T, constructed from X,Y,Z [126, 35]:

$$A = \frac{Z-X}{\sqrt{2}},\ E = \frac{X-2Y+Z}{\sqrt{6}}, T = \frac{X+Y+Z}{\sqrt{3}}. \tag{4.48}$$

A,E,T are useful for data analysis since they have vanishing CSDs under the approximations of equal armlengths and equal noise level for the same type noises. The PSDs for A,E,T are

given in table 4.3. They combine the PSDs and CSDs of X,Y,Z as

$$S_{AA} = \frac{S_{ZZ} + S_{XX} - 2\mathrm{Re}[S_{ZX}]}{2} \tag{4.49}$$

$$S_{EE} = \frac{S_{XX} + 4S_{YY} + S_{ZZ} - 2\mathrm{Re}[2S_{XY} - S_{XZ} + 2S_{YZ}]}{6} \tag{4.50}$$

$$S_{TT} = \frac{S_{XX} + S_{YY} + S_{ZZ} + 2\mathrm{Re}[S_{XY} + S_{XZ} + S_{YZ}]}{3} \tag{4.51}$$

and are therefore slightly more complex. We remark that while the equal arm models derived here are accurate enough to describe the GW sensitive channels X,Y,Z, as well as for the quasi-orthogonal channels A and E, it was demonstrated that this assumption is insufficient for accurately describing the behaviour of the null-channel T, in particular at low frequencies [112, 8].

4.3.1 About the propagation of suppressed noises

Although the unsuppressed noises is our main focus, for the sake of completeness, we will summarize the status of transfer functions for the suppressed noises, i.e., noises suppressed by TDI, as well as the additional noises induced by this suppression.

Laser frequency noise has to be suppressed by several order of magnitude by TDI, in order to be below the required noise level [103, 65, 35] defined by the unsuppressed noises (acceleration, readout and OP). It has been the main focus of TDI noise reduction studies during many years, one of the most recent studies on the topic being [43]. Because of the high level of reduction required, the residual level is sensitive to all limiting effects from the application of TDI: flexing filtering (non commutation between anti-aliasing filters and delays) [43], ranging bias, stochastic ranging (imprecision in the knowledge of delays), interpolation, aliasing and fundamental armlength mismatch (limitation due to the flexing with TDI 2.0). There are ongoing active studies on all these effects and preliminary transfer functions are already available enabling to establish the expected level of the residual laser noise. Moreover, the residual laser noise depends on the laser locking configuration. Only preliminary checks based on simulation have been done and preliminary models have been developed [76], and more detailed studies are necessary.

In principle, most effects leading to residual laser noise will also cause residuals in other noise sources which are perfectly cancelled in an idealized situation. However, since these other suppressed noises are several orders of magnitude smaller than laser noise, their residuals can usually be neglected.

Noise type	Correlation	S_{AA} & S_{EE}	S_{TT}
Test-mass acceleration	None	$4C_{XX}(\omega)\left[3+2\cos(\omega L)+\cos(2\omega L)\right]$	$32C_{XX}(\omega)\sin^4(\frac{\omega L}{2})$
	Fully-correlated noises at the same S/C	$4C_{XX}(\omega)\left[1+2\cos(\omega L)\right]^2$	$64C_{XX}(\omega)\sin^4(\frac{\omega L}{2})$
	Anti-correlated at the same S/C	$12C_{XX}(\omega)$	0
Readout (TMI) and Optical Path-length (TMI)	None	$C_{XX}(\omega)\left[3+2\cos(\omega L)+\cos(2\omega L)\right]$	$8C_{XX}(\omega)\sin^4(\frac{\omega L}{2})$
	Correlated adjacent TMI noise	$3C_{XX}(\omega)$	0
	Anti-correlated adjacent TMI noise	$C_{XX}(\omega)\left[1+2\cos(\omega L)\right]^2$	$16C_{XX}(\omega)\sin^4\left(\frac{\omega L}{2}\right)$
Backlink (TMI)	None	$C_{XX}(\omega)\left[3+2\cos(\omega L)+\cos(2\omega L)\right]$	$8C_{XX}(\omega)\sin^4(\frac{\omega L}{2})$
Readout (ISI and RFI) and Optical Path-length (ISI and RFI)	None	$2C_{XX}(\omega)\left[2+\cos(\omega L)\right]$	$4C_{XX}(\omega)\left[1-\cos(\omega L)\right]$
	Correlated adjacent IFO noise	$3C_{XX}(\omega)$	0
	Anti-correlated adjacent IFO noise	$C_{XX}(\omega)\left[5+4\cos(\omega L)\right]$	$8C_{XX}(\omega)\left[1-\cos(\omega L)\right]$
	Fully correlated at the same telescope	$4C_{XX}(\omega)\left[3+2\cos(\omega L)+\cos(2\omega L)\right]$	$32C_{XX}(\omega)\sin^4(\frac{\omega L}{2})$
Backlink (RFI)	None	$2C_{XX}(\omega)\left[2+\cos(\omega L)\right]$	$4C_{XX}(\omega)\left[1-\cos(\omega L)\right]$

Table 4.3: Summary table of analytical TDI A,E,T transfer functions for unsuppressed noises. All results have been simplified using approximations (refer to subsection 4.1.2).

Clock noise is also reduced by TDI. While its initial level is lower than that of laser noise, it is still a few orders of magnitude higher than the required noise level. In order to suppress clock noise, the laser beams carry sideband modulation with a clock-derived signal, creating so-called clock-sidebands. Interferometric measurements of these sidebands are then used in the TDI algorithm to reduce clock noise [77].

S/C jitter noises $\vec{\Delta}_{ij}$ are in theory perfectly cancelled by TDI when forming the ξ_{ij} (see (3.9) and (3.10)). In reality, this cancellation will not be perfect and some residual noise is expected.

Finally, since the application of TDI is a numerical procedure, some numerical limitations are expected.

The estimated residuals of all suppressed noises are currently below the required level, but some contributions are not negligible and need to be carefully studied. The laser locking will impact will impact some of these suppressed noises and is the topic of further studies currently

underway.

4.4 Validation with simulation

In this section, we review the procedure for the model validation, i.e. to compare the analytical model for the noise propagation through TDI with that power spectra estimated from `LISANode` simulated data[3]. In the final, we give the validation result for some configurations set up for `LISANode` simulator.

4.4.1 Procedure for model validation

The procedure to validate the transfer function of a particular type of noise (for example acceleration noise or readout noise) is the following:

1. We configure the simulation for the noise to be studied, with all other noises configured to produce zeros as output.

2. From the simulated time domain data (TDI variables), we compute the PSD and the CSD.

3. We plot together the simulated and analytical PSDs or CSDs. In addition, we add for the analytical curve, the 99.73% confidence interval which is computed statistically by χ^2-distribution for the PSD/CSD estimations. We will discuss the estimation method and the statistical confident interval more detail in the next subsection.

4. The simulated points outside the confidence interval are detected as the "alert" point. The level of agreement between analytical formulation and simulated data is estimated based on the plot and the number of "alert" point.

4.4.2 Estimation of power spectral density

In the following we describe the procedure of estimating the power spectral density for a stochastic time series $x(t)$ of finite length T. In particular, we use `Scipy` implementation of Welch's Method [153, 59]. The Welch's method is summarized in the following steps. First, the data is divided into M segments of length L and a window function $w(t)$ is applied for every segment. A Fourier transform is then performed for each windowed segment, giving M independent estimates of the power spectral density as defined in (4.52). Finally, the average,

[3]The version of `LISANode` we used in this study is the version 1.2, which still contains graph for computing TDI variables. In the current version of `LISANode`, this graph has been removed and we need to use `PyTDI` [138] to construct TDI variables.

expressed in equation (4.53), over the M segments is taken to reduce the variance.

$$\hat{S}^{(m)}(f_k) = \frac{|\tilde{x}_w^{(m)}(f_k)|^2}{L} \tag{4.52}$$

$$\bar{S}(f_k) = \frac{1}{M}\sum_{m=0}^{M-1} \hat{S}^{(m)}(f_k) \tag{4.53}$$

This procedure yields estimates of $\bar{S}(f_k)$ at frequencies $f_k = \Delta f k$ with k running from zero to $K = Lf_s$. The spectral resolution is given by $\Delta f = \frac{1}{L}$. In principle, one could choose to average over many segments to yield a very precise estimate of the PSD. However, in practice, we are faced with limited amount of data and have to trade off between low variance and high spectral resolution.

In our studies, we aim to validate the analytical PSD models with simulated data. In order to check whether the PSD estimates $\bar{S}(f_k)$ are consistent with the model (null hypothesis), we conduct an hypothesis test. We define the confidence level γ that represents the probability that all PSD estimates are inside a given confidence interval.

$$\gamma = \prod_{k}^{K-1} \mathrm{P}\left(\bar{S}_-(f_k) \leq \bar{S}(f_k) \leq \bar{S}_+(f_k)\right) \tag{4.54}$$

We reject the null hypothesis if a single estimate $\bar{S}(f_k)$ resides outside the confidence interval.

The confidence intervals $[S_-(f_k), S_+(f_k)]$ can be derived from the statistics of the PSD estimates $\bar{S}(f_k)$. It is easy to show that $\bar{S}(f_k)$ has an expectation value of

$$\mathrm{E}\{\bar{S}(f_k)\} = \frac{(|\tilde{w}|^2 * S)(f_k)}{L} \tag{4.55}$$

Moreover, it has been demonstrated in [91] that $\frac{\nu\bar{S}(f_k)}{\mathrm{E}\{\bar{S}(f_k)\}}$ is χ^2_ν distributed with $\nu = 2M$ degrees of freedom. By attributing "equal confidence" to each of the K frequency bins we can write:

$$\mathrm{P}\left(\bar{S}_-(f_k) \leq \bar{S}(f_k) \leq \bar{S}_+(f_k)\right) = \gamma^{\frac{1}{K}} = 1 - \alpha \tag{4.56}$$

where α is the probability that the estimate resides outside the confidence interval. The limits $\bar{S}_-(f_k)$ and $\bar{S}_+(f_k)$ are constructed symmetrically such that

$$\mathrm{P}\left(\bar{S}(f_k) < \bar{S}_-(f_k)\right) = \mathrm{P}\left(\bar{S}(f_k) > \bar{S}_+(f_k)\right) = \frac{\alpha}{2} \tag{4.57}$$

They can be calculated by using the χ^2_ν distributional property.

4.4.3 Result

For the frequency range 10^{-4} to 1 Hz, the simulated and analytical PSD/CSD for TDI X have been plotted (see figures 4.1, 4.2, 4.3 and 4.4). Red lines show the analytical formulation

expressions. The blue dashed lines represent the instrument response to the simulated single noises for a duration about 3×10^5 s (i.e, the test-mass acceleration noise in the following example). The green envelope highlights the 99.73% confidence interval with respect to the analytical formulation. The probability that a single point is outside of the confidence interval is around 4.5×10^{-7} in case of a perfect agreement between analytical formulation and simulation.

Figures 4.1, 4.2 and 4.3 show a great agreement for the test-mass acceleration noise PSD in all uncorrelated, correlated and anti-correlated cases.

The CSD computation shows a slight disagreement (3 % of the simulated data are not in the 99.73% confidence interval of the analytical formulation) with the simulated data from `LISANode`. It is mainly around the zeros (corresponding to sub-multiples of the link frequency c/L). In these particular frequency regions, the computation of the CSD is more sensitive to numerical errors and deviations from the equal armlength approximation[4].

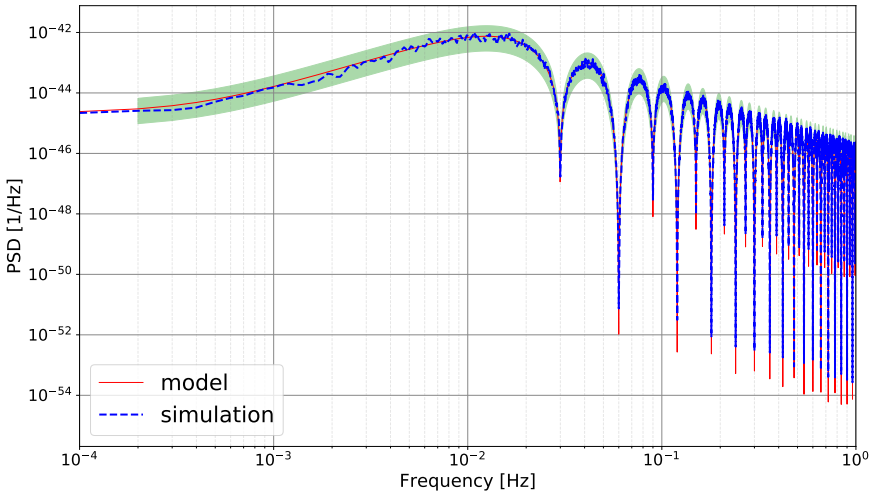

Figure 4.1: Uncorrelated test-mass acceleration noise cross-comparison. The simulated data (red line) at 99.73% confidence interval (green area) are in great agreement with the analytical formulation (blue dashed line).

[4]The confidence interval from the CSD estimation is more complicated so we might not use the the χ^2-distribution as in the case of PSD estimation. From personal communication with Martin Staab, October 2022.

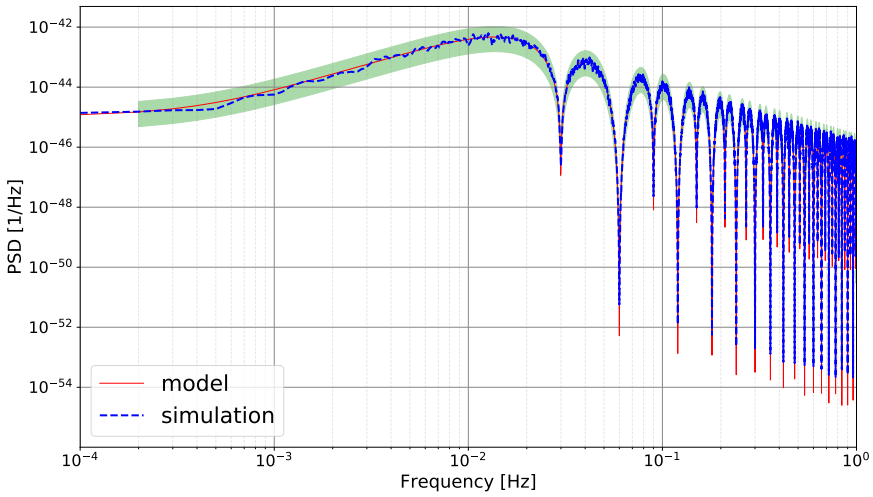

Figure 4.2: Correlated test-mass acceleration noise cross-comparison. The simulated data (red line) at 99.73% confidence interval (green area) are in great agreement with the analytical formulation (blue dashed line).

4.5 Conclusion

The modeling of the noises and their propagation from the measurements to the TDI variables are crucial for the LISA mission. Indeed, the TDI algorithm will reduce some noise sources while leaving others largely untouched. The impact of correlations between links can either improve or deteriorate the performance of the mission at the TDI level. We have seen this in the particular case of test mass acceleration noise, but it is also true for tilt-to-length [120] or thermo-mechanical noises. In addition, many noises related to the application of the algorithm itself, such as interpolation, clock noise residual or sideband modulation noise [77] can only be expressed at TDI level. Whether it is to establish the noise budget of the mission or to improve our understanding and knowledge of the noise for the needs of data analysis, the use of these TDI models is necessary.

The TDI variables are the main data used to extract GW signals. Therefore it is important to have a good modeling of the noise PSD and CSD for the various TDI variables in order to search for GW sources, estimate their parameters and distinguish them from the instrumental noises. This last point is particularly important for the search for stochastic backgrounds which can easily be confused with the noises.

A method for computing analytically the PSD and the CSD of unsuppressed noises by TDI has been presented, as well as reasonable approximations to be used. It has been applied to

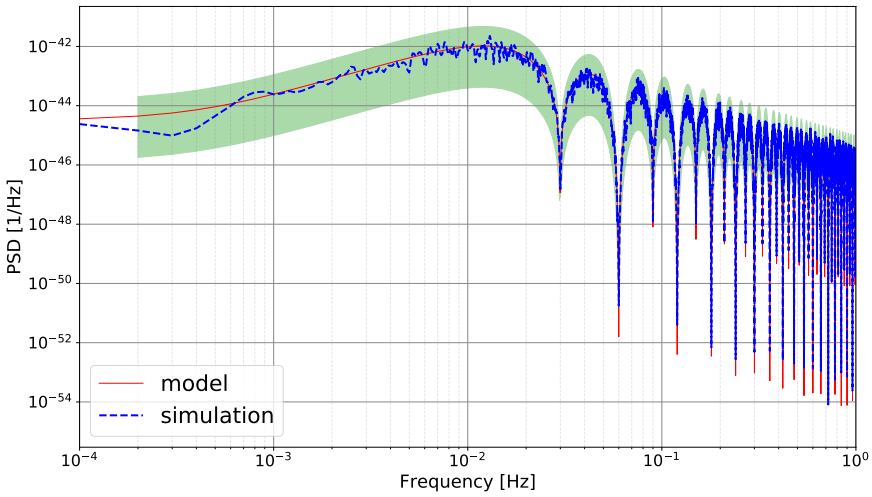

Figure 4.3: Anti-correlated test-mass acceleration noise cross-comparison. The simulated data (red line) at 99.73% confidence interval (green area) are in great agreement with the analytical formulation (blue dashed line).

the main noise sources considering all uncorrelated cases, and standard cases of correlation. The analytical expressions have been provided in tables 4.2 and 4.3 for the TDI variables X,Y,Z, A, E and T. They have been validated against simulations for X,Y,Z. This method can be applied to any unsuppressed noises and to any TDI variables.

The transfer functions for the unsuppressed noises with laser locking are the same as the ones without laser locking. It is not necessarily the case for suppressed noises, but we leave this for future works. Actually the propagation of suppressed noises is usually more complicated. Several studies are underway and should soon in publications.

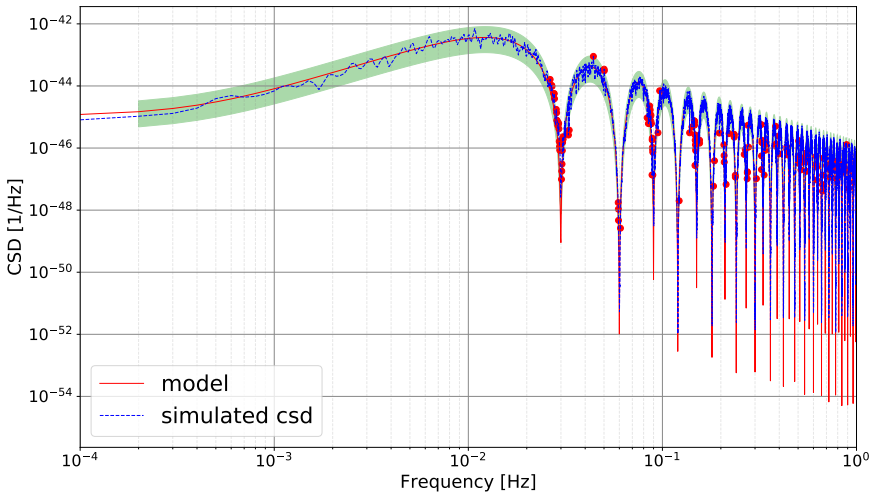

Figure 4.4: CSD uncorrelated TM acceleration noise. The simulated data (red line) at 99.73% confidence interval (green area) are in slight disagreement with the analytical formulation (blue dashed line) around the zeros.

Chapter 5

LISA Dynamics

One of the key technologies for the success of LISA is the control of the different bodies in the system while keeping the reference bodies unperturbed along the sensitive axes of the LISA constellation. As described in section 2.2, each spacecraft in the LISA constellation contains two test-masses, which are used as the reference points for measuring the proper distance changes among spacecraft. The test-masses are shielded by a housing included in the GRS, which can monitor the position of test-masses and apply the electrostatic forces on them in specific directions.

We must keep the test-masses inside spacecraft on their own geodesics, more precisely in a free-falling state along the sensitive axes (axes of LISA laser links) to measure the spacetime deformation. In the meantime, the MOSAs, the spacecraft and the test-masses on other degrees of freedom than the sensitive axis should be controlled and set at their working points by a system called DFACS[31] introduced in section 2.2.

In this chapter, we review the concept and convention of reference frames, which is helpful for the LISA Dynamics simulation. Then, we derive the equations of motion for LISA objectives. After that, a simplified DFACS model for `LISANode` simulation is presented with the extended version to account for the motions of MOSAs, which is the main work in this thesis. Finally, we discuss some preliminary results of LISA Dynamics implementation in `LISANode`. This work is conducted in collaboration with H.Inchauspé.

5.1 Reference frames

First, we introduce the reference frames, in which we derive the equations of motion for the dynamical objects in the next section. This section is mainly based on the technical notes of the reference frames and notations for LISA Dynamics [87] and the to-be-published article of H.Inchauspé et al. [89]

The baseline for all reference frames is the Galilean frame, which we denote as $\mathcal{J}$. This frame is assumed to be inertial, fixed w.r.t. distant stars, and the axes defined by the J2000 convention, or the international coordinate reference frame [134].

The spacecraft body frame, denoted as $\mathcal{B}$-frame, is the reference frame to define the actual attitudes of the spacecraft, w.r.t $\mathcal{J}$-frame. In the following, we give the detailed axes and origin of this frame:

- x-axis $\hat{\mathbf{e}}_{x/\mathcal{B}_i}$ is the unit vector associated with the bisector to the angle between two MOSAs axes of spacecraft i.
- z-axis $\hat{\mathbf{e}}_{z/\mathcal{B}_i}$ is the unit vector normal to the solar panel plane of spacecraft i.
- y-axis $\hat{\mathbf{e}}_{y/\mathcal{B}_i}$ is deduced from the two unit vectors above, by $\hat{\mathbf{e}}_{y/\mathcal{B}_i} = \hat{\mathbf{e}}_{z/\mathcal{B}_i} \times \hat{\mathbf{e}}_{x/\mathcal{B}_i}$.
- The origin of this frame, called B_i, is the center of mass of the whole spacecraft i (platform and MOSAs). Since the MOSAs could move inside the spacecraft, the center of mass B point is not static. For convenience to study the equation of motion in the next section, we define the center of mass S of the spacecraft platform, i.e. spacecraft excluding MOSAs, which is static.

The MOSA body frame, denoted as $\mathcal{H}$-frame, is the reference frame to define the actual attitudes of a single MOSA, w.r.t $\mathcal{B}$-frame. In the following, we give the detailed axes and origin of this frame:

- x-axis $\hat{\mathbf{e}}_{x/\mathcal{H}_i}$ is the unit vector along which the local OMS measurement of the spacecraft to the TM is performed. This unit vector is also along the *drag-free axis*. We can retrieve this unit vector from $\mathcal{B}$-frame axes by rotating $\hat{\mathbf{e}}_{x/\mathcal{B}_i}$ around $\hat{\mathbf{e}}_{z/\mathcal{B}_i}$ by half of the actual opening angle of two MOSAs. In the case of fixed MOSAs, this actual opening angle of two MOSAs is 60^o.
- z-axis $\hat{\mathbf{e}}_{z/\mathcal{H}_i}$ is the unit vector normal to the solar panel plane of spacecraft i, the same as $\hat{\mathbf{e}}_{z/\mathcal{B}_i}$.
- y-axis $\hat{\mathbf{e}}_{y/\mathcal{H}_i}$ is deduced from the two unit vectors above, by $\hat{\mathbf{e}}_{y/\mathcal{H}_i} = \hat{\mathbf{e}}_{z/\mathcal{H}_i} \times \hat{\mathbf{e}}_{x/\mathcal{H}_i}$.
- The origin H_i of the frame $\mathcal{H}_i$ is identified as the geometrical center of the housing belonging to MOSA i. We also denote pivot point P_i for the rotation of MOSAs. On the other hand, the center of mass of MOSA i is denoted as Q_i.

The test-mass body frame, denoted as $\mathcal{T}_i$-frame, is the reference frame to define the actual attitudes of a single test-mass i, w.r.t $\mathcal{H}_i$-frame. The axes and origin are:

- x-axis $\hat{\mathbf{e}}_{x/\mathcal{T}_i}$ is the unit vector normal to the x-face of the test-mass. This axis is aligned with $\hat{\mathbf{e}}_{x/\mathcal{H}_i}$ when the test-mass is nominally oriented with the containing MOSA.
- z-axis $\hat{\mathbf{e}}_{z/\mathcal{H}_i}$ is the unit vector normal to the z-face of the test-mass, and aligned with $\hat{\mathbf{e}}_{z/\mathcal{H}_i}$ when the test-mass is nominally oriented with the containing MOSA.
- y-axis $\hat{\mathbf{e}}_{y/\mathcal{H}_i}$ is deduced from the two unit vectors above, by $\hat{\mathbf{e}}_{y/\mathcal{H}_i} = \hat{\mathbf{e}}_{z/\mathcal{H}_i} \times \hat{\mathbf{e}}_{x/\mathcal{H}_i}$.
- The origin of this frame is identified as the center of mass of the test-mass i, which we denoted as T_i.

In addition to these above coordinates, we define two target body frames for the MOSAs and spacecraft. These target frames will be useful for linearizing equations of motion in section 5.3.2.

The spacecraft target body frame, denoted as $\mathcal{O}$-frame (or $\mathcal{B}^*$-frame in some contexts), helps to define the target attitudes of the spacecraft w.r.t. $\mathcal{J}$-frame. This frame has been built as the following:

- x-axis $\hat{\mathbf{e}}_{x/\mathcal{O}}$ is the unit vector along the bisector of the constellation angle at the local spacecraft.
- z-axis $\hat{\mathbf{e}}_{z/\mathcal{O}}$ is the unit vector normal to LISA constellation plane.
- y-axis $\hat{\mathbf{e}}_{y/\mathcal{O}}$ is deduced from the two unit vectors above, by $\hat{\mathbf{e}}_{y/\mathcal{O}} = \hat{\mathbf{e}}_{z/\mathcal{O}} \times \hat{\mathbf{e}}_{x/\mathcal{O}}$.
- The origin of this frame O is the center of mass of the spacecraft following its ideal orbit. In other words, this coordinate system moves in spacecraft geodesics without spurious forces.

The MOSA target body frame, denoted as $\mathcal{H}^*$-frame, helps to define the target attitudes of the MOSA w.r.t. $\mathcal{J}$-frame. We construct the axes of this frame and define its origin as:

- x-axis $\hat{\mathbf{e}}_{x/\mathcal{H}_i^*}$ is the unit vector aligned to the axis normal to the incoming wavefront. In other words, it is parallel to the wave vector of the distant beam reaching the MOSA i. This vector could also be deduced by rotating the $\hat{\mathbf{e}}_{x/\mathcal{O}_i}$ around $\hat{\mathbf{e}}_{z/\mathcal{O}_i}$ by half of the constellation angle at local spacecraft. In the fixed MOSAs case, we assume that the constellation forms a perfect equilateral triangle, so the constellation angle at every spacecraft is 60^o.
- z-axis $\hat{\mathbf{e}}_{z/\mathcal{H}_i^*}$ is the unit vector normal to the LISA constellation plane, the same as $\hat{\mathbf{e}}_{z/\mathcal{O}_i}$.
- y-axis $\hat{\mathbf{e}}_{y/\mathcal{H}_i^*}$ is deduced from the two unit vectors above, by $\hat{\mathbf{e}}_{y/\mathcal{H}_i^*} = \hat{\mathbf{e}}_{z/\mathcal{H}_i^*} \times \hat{\mathbf{e}}_{x/\mathcal{H}_i^*}$.

- The origin of this frame is the same as the origin of $\mathcal{H}_i$-frame, which is the geometrical center of the housing, H_i.

5.2 Equation of motions

Given the reference frames presented in the previous section, we can derive the equations of motion for the LISA dynamical objects: the test-masses, the MOSAs and the spacecraft. We treat the dynamics of the three LISA spacecraft independently since they are well-separated from each other as 2.5 million kilometers away. In addition, the potential interaction from the distant spacecraft, such as the wavefront defects to the local one, is negligible compared to the local contributors like the micro-propulsion noise [89]. The equations of motion of the second test-mass inside one spacecraft can be deduced from the first ones by symmetry. Hence, in the following equations of this section, there is no index notation for LISA dynamics objects as indicated in figure 2.5.

Each object has two kinds of motion: longitudinal and angular displacements. Fortunately, the longitudinal motions of spacecraft (and of MOSA as well because it is attached to the spacecraft) can be ignored since they do not contribute to the closed-loop dynamics [89]. Therefore, we will have only four types of equations of motion for LISA Dynamics. Among them, the longitudinal motion of TMs is the most important one, and we will go through its derivation carefully in the following subsection. The other three equations of motion, related to the angular motions of the spacecraft, the MOSAs and the test-masses, will be worked out in the later subsections.

These equations of motion were derived in the PhD thesis of H.Inchauspé [90] and extended in recent technical notes and a to-be-published article [89]. Since these equations are essential for the LISA Dynamics implementation, we review them in detail in this section. In addition, most of the equations of motion presented following are cross-checked and validated with a Mathematica notebook which we have developed. We expect the notebook could help derive the equations of motion in more complex configurations of LISA Dynamics in the future.

5.2.1 Test-mass longitudinal motion

The test-masses are shielded by the GRS so that we can reduce the external forces applied to them as much as possible. Although some residual forces could change the motion of test-mass, such as the gravitational gradient forces of the spacecraft [19, 32], the actuation forces from the GRS. We collect all terms of these contributions in Newton's equation for the longitudinal motion of the test-mass in the following expression:

$$\left.\frac{d^2}{dt^2}\right|_{\mathcal{J}} \left[\vec{\mathbf{r}}_{T/\mathcal{J}}\right] = \sum \frac{\vec{\mathbf{f}}_T}{m_{\text{tm}}}, \tag{5.1}$$

where the TM position $\vec{\mathbf{r}}_{T/\mathcal{J}}$ is expressed in Galilean frame $\mathcal{J}$, with the associated mass m_{tm}. The total forces in the Galilean frame acted on the TM are summed in the right-hand side, $\sum \vec{\mathbf{f}}_T$. In order to examine the observable/dynamical quantities in the correct frames, we will expand the equation (5.1) by decomposing the position of the test-mass in $\mathcal{J}$-frame as

$$\vec{\mathbf{r}}_{T/\mathcal{J}} = \vec{\mathbf{r}}_{T/\mathcal{H}} + \vec{\mathbf{r}}_{H/\mathcal{B}} + \vec{\mathbf{r}}_{B/\mathcal{J}}, \tag{5.2}$$

where $\vec{\mathbf{r}}_{T/\mathcal{H}}$ is related to the position of the test-mass w.r.t the GRS (or MOSA in general) in $\mathcal{H}$-frame, driven by the GRS actuation forces; $\vec{\mathbf{r}}_{H/\mathcal{B}}$ denotes the position of the MOSA w.r.t the spacecraft in $\mathcal{B}$-frame, which could be identified as the telescope rotation; the final term is the position of the spacecraft $\vec{\mathbf{r}}_{B/\mathcal{J}}$ in the Galilean frame, which depends on the micro-propulsion forces and other external forces applied on the spacecraft. The final term of the double time derivative of $\vec{\mathbf{r}}_{B/\mathcal{J}}$ in the expansion of equation (5.1) is nothing but the left-hand side of Newton's equation for the spacecraft translational motion::

$$\left.\frac{d^2}{dt^2}\right|_{\mathcal{J}} \left[\vec{\mathbf{r}}_{B/\mathcal{J}}\right] = \sum \frac{\vec{\mathbf{f}}_B}{m_{\text{sc}}}, \tag{5.3}$$

where $\sum \vec{\mathbf{f}}_B$ is the total force applied on the spacecraft.

For the other terms, the equation of dynamical quantity should be expressed in associated reference frame rather than the Galilean one $\mathcal{J}$. We use the transport theorem to transform the time derivative in any $\mathcal{J}$-frame into the one in $\mathcal{O}$-frame as follows[1]:

$$\left.\frac{d}{dt}\right|_{\mathcal{J}} \left[\vec{\mathbf{r}}_{P/\mathcal{O}}\right] = \left.\frac{d}{dt}\right|_{\mathcal{O}} \left[\vec{\mathbf{r}}_{P/\mathcal{O}}\right] + \vec{\omega}_{\mathcal{O}/\mathcal{J}} \times \vec{\mathbf{r}}_{P/\mathcal{O}}, \tag{5.4}$$

where $\vec{\omega}_{\mathcal{O}/\mathcal{J}}$ is the angular velocity vector of the $\mathcal{O}$-frame w.r.t $\mathcal{J}$-frame, $\times$ notates the cross product of two vectors. From now on, we use notation $\vec{\omega}_{\mathcal{A}/\mathcal{B}}$ for the angular velocity vector of A-frame w.r.t. B-frame, in general. Apply this theorem for the double time derivative of $\vec{\mathbf{r}}_{H/\mathcal{B}}$ gives:

$$\begin{aligned}
\left.\frac{d^2}{dt^2}\right|_{\mathcal{J}} \left[\vec{\mathbf{r}}_{H/\mathcal{B}}\right] &= \left(\left.\frac{d}{dt}\right|_{\mathcal{B}} + \vec{\omega}_{\mathcal{B}/\mathcal{J}}\times\right)\left(\left.\frac{d}{dt}\right|_{\mathcal{B}} + \vec{\omega}_{\mathcal{B}/\mathcal{J}}\times\right)\left[\vec{\mathbf{r}}_{H/\mathcal{B}}\right] \\
&= \left.\frac{\mathrm{d}^2}{\mathrm{d}t^2}\right|_{\mathcal{B}} \left[\vec{\mathbf{r}}_{H/\mathcal{B}}\right] + 2\vec{\omega}_{\mathcal{B}/\mathcal{J}} \times \left(\left.\frac{\mathrm{d}}{\mathrm{d}t}\right|_{\mathcal{B}} \left[\vec{\mathbf{r}}_{H/\mathcal{B}}\right]\right) \\
&\quad + \left.\frac{\mathrm{d}}{\mathrm{d}t}\right|_{\mathcal{J}} \left[\vec{\omega}_{\mathcal{B}/\mathcal{J}}\right] \times \vec{\mathbf{r}}_{H/\mathcal{B}} + \vec{\omega}_{\mathcal{B}/\mathcal{J}} \times \left(\vec{\omega}_{\mathcal{B}/\mathcal{J}} \times \vec{\mathbf{r}}_{H/\mathcal{B}}\right).
\end{aligned} \tag{5.5}$$

Unfortunately, the origin of the $\mathcal{B}$-frame, which is the center of mass of the spacecraft, is not time-invariant since the distribution of mass in the spacecraft would change due to, for

[1] This theorem is the transformation for the time derivative of any vector from a reference frame to another reference frame, possibly rotating w.r.t. the first one [110].

example, MOSA and test-mass motions. Therefore, we should express our equation in some dynamical quantities with the associated time-invariant origin reference frame. Therefore, we decompose the $\vec{\mathbf{r}}_{H/\mathcal{B}}$ in terms of vectorial quantities w.r.t static points such as pivot point P of MOSA rotation and the spacecraft platform center of mass S:

$$\vec{\mathbf{r}}_{H/\mathcal{B}} \equiv \overrightarrow{\mathbf{BH}}_{\mathcal{B}} = \overrightarrow{\mathbf{BS}}_{\mathcal{B}} + \overrightarrow{\mathbf{SP}}_{\mathcal{B}} + \overrightarrow{\mathbf{PH}}_{\mathcal{B}}. \tag{5.6}$$

We work out the time derivative for each term in the following. Since all of the position vectors are in the $\mathcal{B}$-frame, we omit the $\mathcal{B}$ notation for simplicity.

- $\overrightarrow{\mathbf{SP}}$ is fixed in $\mathcal{B}$-frame by construction, so all the $\mathcal{B}$-frame time derivative terms related to this quantity disappear.

- The time derivative of $\overrightarrow{\mathbf{PH}}$ in $\mathcal{B}$-frame is driven by telescope rotation. We apply the transport theorem (5.4) to get:

$$\begin{aligned}
\left.\frac{d}{dt}\right|_{\mathcal{B}} \left[\overrightarrow{\mathbf{PH}}\right] &= \left.\frac{d}{dt}\right|_{\mathcal{H}} \left[\overrightarrow{\mathbf{PH}}\right] + \vec{\omega}_{\mathcal{H}/\mathcal{B}} \times \overrightarrow{\mathbf{PH}} \\
&= 0 + \vec{\omega}_{\mathcal{H}/\mathcal{B}} \times \overrightarrow{\mathbf{PH}} \equiv \vec{\omega}_{\mathcal{H}/\mathcal{B}} \times \vec{\mathbf{r}}_{PH/\mathcal{B}}
\end{aligned} \tag{5.7}$$

$$\begin{aligned}
\left.\frac{d^2}{dt^2}\right|_{\mathcal{B}} \left[\overrightarrow{\mathbf{PH}}\right] &= \left.\frac{d}{dt}\right|_{\mathcal{H}} \left[\vec{\omega}_{\mathcal{H}/\mathcal{B}}\right] \times \overrightarrow{\mathbf{PH}} + \vec{\omega}_{\mathcal{H}/\mathcal{B}} \times \left(\vec{\omega}_{\mathcal{H}/\mathcal{B}} \times \overrightarrow{\mathbf{PH}}\right) \\
&\equiv \left.\frac{d}{dt}\right|_{\mathcal{B}} \left[\vec{\omega}_{\mathcal{H}/\mathcal{B}}\right] \times \vec{\mathbf{r}}_{PH/\mathcal{B}} + \vec{\omega}_{\mathcal{H}/\mathcal{B}} \times \left(\vec{\omega}_{\mathcal{H}/\mathcal{B}} \times \vec{\mathbf{r}}_{PH/\mathcal{B}}\right),
\end{aligned} \tag{5.8}$$

  where we use the identity $\left.\frac{d}{dt}\right|_{\mathcal{B}} \left[\vec{\omega}_{\mathcal{H}/\mathcal{B}}\right] = \left.\frac{d}{dt}\right|_{\mathcal{H}} \left[\vec{\omega}_{\mathcal{H}/\mathcal{B}}\right] + \vec{\omega}_{B/\mathcal{H}} \times \vec{\omega}_{\mathcal{H}/\mathcal{B}} = \left.\frac{d}{dt}\right|_{\mathcal{H}} \left[\vec{\omega}_{\mathcal{H}/\mathcal{B}}\right]$.

- The last component, $\overrightarrow{\mathbf{BS}}$, is more complex. First, we use the equation of the spacecraft center of mass to decompose it into vectors with the time-invariant (static) origins in $\mathcal{B}$-frame.

$$\begin{aligned}
\vec{0} &= m_S \overrightarrow{\mathbf{BS}} + m_{H_1} \overrightarrow{\mathbf{BQ_1}} + m_{H_2} \overrightarrow{\mathbf{BQ_2}} \\
&= m_S \overrightarrow{\mathbf{BS}} + m_{H_1} \left(\overrightarrow{\mathbf{BS}} + \overrightarrow{\mathbf{SP_1}} + \overrightarrow{\mathbf{P_1Q_1}}\right) + m_{H_2} \left(\overrightarrow{\mathbf{BS}} + \overrightarrow{\mathbf{SP_2}} + \overrightarrow{\mathbf{P_2Q_2}}\right) \\
&= \left(m_S + m_{H_1} + m_{H_2}\right) \overrightarrow{\mathbf{BS}} \\
&\quad + m_{H_1} \left(\overrightarrow{\mathbf{P_1Q_1}} + \overrightarrow{\mathbf{SP_1}}\right) + m_{H_2} \left(\overrightarrow{\mathbf{P_2Q_2}} + \overrightarrow{\mathbf{SP_2}}\right)
\end{aligned} \tag{5.9}$$

$$\Rightarrow \overrightarrow{\mathbf{BS}} = -\epsilon_1 \left(\overrightarrow{\mathbf{P_1Q_1}} + \overrightarrow{\mathbf{SP_1}}\right) - \epsilon_2 \left(\overrightarrow{\mathbf{P_2Q_2}} + \overrightarrow{\mathbf{SP_2}}\right), \tag{5.10}$$

  where we denoted ϵ_i is the ratio between the mass of MOSA i with the total mass of the spacecraft. Then we apply the transport theorem (5.4) to convert the time derivative

from $\mathcal{B}$-frame to $\mathcal{H}$-frame. Note that $\overrightarrow{\mathbf{SP_i}}$ for $i = 1, 2$ are fixed in $\mathcal{B}$-frame, we obtain:

$$
\begin{aligned}
-\left.\frac{d}{dt}\right|_{\mathcal{B}}\left[\overrightarrow{\mathbf{BS}}\right] &= \epsilon_1\left(\vec{\omega}_{H_1/\mathcal{B}} \times \overrightarrow{\mathbf{P_1Q_1}}\right) + \epsilon_2\left(\vec{\omega}_{H_2/\mathcal{B}} \times \overrightarrow{\mathbf{P_2Q_2}}\right) && (5.11)\\
-\left.\frac{d^2}{dt^2}\right|_{\mathcal{B}}\left[\overrightarrow{\mathbf{BS}}\right] &= \epsilon_1\left[\left.\frac{d}{dt}\right|_{\mathcal{H}_1}\left[\vec{\omega}_{\mathcal{H}_1/B}\right] \times \overrightarrow{\mathbf{P_1Q_1}} + \vec{\omega}_{\mathcal{H}_1/B} \times \left(\vec{\omega}_{\mathcal{H}_1/B} \times \overrightarrow{\mathbf{P_1Q_1}}\right)\right] \\
&\quad +\epsilon_2\left[\left.\frac{d}{dt}\right|_{\mathcal{H}_2}\left[\vec{\omega}_{\mathcal{H}_2/B}\right] \times \overrightarrow{\mathbf{P_2Q_2}} + \vec{\omega}_{\mathcal{H}_2/B} \times \left(\vec{\omega}_{\mathcal{H}_2/B} \times \overrightarrow{\mathbf{P_2Q_2}}\right)\right]. && (5.12)
\end{aligned}
$$

Then combining all the terms, we get

$$
\begin{aligned}
\left.\frac{d}{dt}\right|_{\mathcal{B}}\left[\vec{\mathbf{r}}_{H/\mathcal{B}}\right] &= \vec{\omega}_{\mathcal{H}/\mathcal{B}} \times \overrightarrow{\mathbf{PH}} \\
&\quad -\epsilon_1\left(\vec{\omega}_{H_1/\mathcal{B}} \times \overrightarrow{\mathbf{P_1Q_1}}\right) - \epsilon_2\left(\vec{\omega}_{H_2/\mathcal{B}} \times \overrightarrow{\mathbf{P_2Q_2}}\right) && (5.13)\\
\left.\frac{d^2}{dt^2}\right|_{\mathcal{B}}\left[\vec{\mathbf{r}}_{H/\mathcal{B}}\right] &= \left.\frac{d}{dt}\right|_{\mathcal{B}}\left[\vec{\omega}_{\mathcal{H}/B}\right] \times \overrightarrow{\mathbf{PH}} + \vec{\omega}_{\mathcal{H}/\mathcal{B}} \times \left(\vec{\omega}_{\mathcal{H}/\mathcal{B}} \times \overrightarrow{\mathbf{PH}}\right) \\
&\quad -\epsilon_1\left[\left.\frac{d}{dt}\right|_{\mathcal{H}_1}\left[\vec{\omega}_{\mathcal{H}_1/B}\right] \times \overrightarrow{\mathbf{P_1Q_1}} + \vec{\omega}_{\mathcal{H}_1/B} \times \left(\vec{\omega}_{\mathcal{H}_1/B} \times \overrightarrow{\mathbf{P_1Q_1}}\right)\right] \\
&\quad -\epsilon_2\left[\left.\frac{d}{dt}\right|_{\mathcal{H}_2}\left[\vec{\omega}_{\mathcal{H}_2/B}\right] \times \overrightarrow{\mathbf{P_2Q_2}} + \vec{\omega}_{\mathcal{H}_2/B} \times \left(\vec{\omega}_{\mathcal{H}_2/B} \times \overrightarrow{\mathbf{P_2Q_2}}\right)\right] && (5.14)
\end{aligned}
$$

Substituting the last two equations into (5.5):

$$
\begin{aligned}
&\left.\frac{d^2}{dt^2}\right|_{\mathcal{J}}\left[\vec{\mathbf{r}}_{H/\mathcal{B}}\right] \\
&= \left.\frac{d}{dt}\right|_{\mathcal{B}}\left[\vec{\omega}_{\mathcal{H}/\mathcal{B}}\right] \times \overrightarrow{\mathbf{PH}} + \vec{\omega}_{\mathcal{H}/\mathcal{B}} \times \left(\vec{\omega}_{\mathcal{H}/\mathcal{B}} \times \overrightarrow{\mathbf{PH}}\right) \\
&\quad - \epsilon_1\left[\left.\frac{d}{dt}\right|_{\mathcal{B}}\left[\vec{\omega}_{\mathcal{H}_1/\mathcal{B}}\right] \times \overrightarrow{\mathbf{P_1Q_1}} + \vec{\omega}_{\mathcal{H}_1/\mathcal{B}} \times \left(\vec{\omega}_{\mathcal{H}_1/\mathcal{B}} \times \overrightarrow{\mathbf{P_1Q_1}}\right)\right] \\
&\quad - \epsilon_2\left[\left.\frac{d}{dt}\right|_{\mathcal{B}}\left[\vec{\omega}_{\mathcal{H}_2/\mathcal{B}}\right] \times \overrightarrow{\mathbf{P_2Q_2}} + \vec{\omega}_{\mathcal{H}_2/\mathcal{B}} \times \left(\vec{\omega}_{\mathcal{H}_2/\mathcal{B}} \times \overrightarrow{\mathbf{P_2Q_2}}\right)\right] \\
&\quad + 2\vec{\omega}_{\mathcal{B}/\mathcal{J}} \times \left[\vec{\omega}_{\mathcal{H}/\mathcal{B}} \times \overrightarrow{\mathbf{PH}} - \epsilon_1\left(\vec{\omega}_{\mathcal{H}_1/\mathcal{B}} \times \overrightarrow{\mathbf{P_1Q_1}}\right) - \epsilon_2\left(\vec{\omega}_{\mathcal{H}_2/\mathcal{B}} \times \overrightarrow{\mathbf{P_2Q_2}}\right)\right] \\
&\quad + \left.\frac{d}{dt}\right|_{\mathcal{J}}\left[\vec{\omega}_{\mathcal{B}/\mathcal{J}}\right] \times \vec{\mathbf{r}}_{\mathcal{H}/\mathcal{B}} + \vec{\omega}_{\mathcal{B}/\mathcal{J}} \times \left(\vec{\omega}_{\mathcal{B}/\mathcal{J}} \times \vec{\mathbf{r}}_{\mathcal{H}/\mathcal{B}}\right) && (5.15)
\end{aligned}
$$

The time derivative of the last component in (5.2), $\vec{\mathbf{r}}_{T/\mathcal{H}}$, is deduced by applying transport theorem (5.4). That gives us:

$$\begin{aligned}\left.\frac{d^2}{dt^2}\right|_{\mathcal{J}}\left[\vec{\mathbf{r}}_{T/\mathcal{H}}\right] &= \left.\frac{\mathrm{d}^2}{\mathrm{d}t^2}\right|_{\mathcal{H}}\left[\vec{\mathbf{r}}_{T/\mathcal{H}}\right] + 2\vec{\omega}_{\mathcal{H}/\mathcal{J}} \times \left(\left.\frac{\mathrm{d}}{\mathrm{d}t}\right|_{\mathcal{H}}\left[\vec{\mathbf{r}}_{T/\mathcal{H}}\right]\right) \\ &\quad + \left.\frac{\mathrm{d}}{\mathrm{d}t}\right|_{\mathcal{J}}\left[\vec{\omega}_{\mathcal{H}/\mathcal{J}}\right] \times \vec{\mathbf{r}}_{T/\mathcal{H}} + \vec{\omega}_{\mathcal{H}/\mathcal{J}} \times \left(\vec{\omega}_{\mathcal{H}/\mathcal{J}} \times \vec{\mathbf{r}}_{T/\mathcal{J}}\right).\end{aligned} \tag{5.16}$$

We can break down the angular velocity vector $\vec{\omega}_{\mathcal{H}/\mathcal{J}} = \vec{\omega}_{\mathcal{H}/\mathcal{B}} + \vec{\omega}_{\mathcal{B}/\mathcal{J}}$ since this quantity is additive [110], and obtain:

$$\begin{aligned}&\left.\frac{d^2}{dt^2}\right|_{\mathcal{J}}\left[\vec{\mathbf{r}}_{T/\mathcal{H}}\right] \\ &= \left.\frac{d^2}{dt^2}\right|_{\mathcal{H}}\left[\vec{\mathbf{r}}_{T/\mathcal{H}}\right] + 2\vec{\omega}_{\mathcal{H}/\mathcal{B}} \times \left.\frac{d}{dt}\right|_{\mathcal{H}}\left[\vec{\mathbf{r}}_{T/\mathcal{H}}\right] + 2\vec{\omega}_{\mathcal{B}/\mathcal{J}} \times \left.\frac{d}{dt}\right|_{\mathcal{H}}\left[\vec{\mathbf{r}}_{T/\mathcal{H}}\right] \\ &+ \left.\frac{d}{dt}\right|_{\mathcal{B}}\left[\vec{\omega}_{\mathcal{H}/\mathcal{B}}\right] \times \vec{\mathbf{r}}_{T/\mathcal{H}} + \left(\vec{\omega}_{\mathcal{B}/\mathcal{J}} \times \vec{\omega}_{\mathcal{H}/\mathcal{B}}\right) \times \vec{\mathbf{r}}_{T/\mathcal{H}} + \left.\frac{d}{dt}\right|_{\mathcal{J}}\left[\vec{\omega}_{\mathcal{B}/\mathcal{J}}\right] \times \vec{\mathbf{r}}_{T/\mathcal{H}} \\ &+ \vec{\omega}_{\mathcal{H}/\mathcal{B}} \times \left(\vec{\omega}_{\mathcal{H}/\mathcal{B}} \times \vec{\mathbf{r}}_{T/\mathcal{H}}\right) + \vec{\omega}_{\mathcal{H}/\mathcal{B}} \times \left(\vec{\omega}_{\mathcal{B}/\mathcal{J}} \times \vec{\mathbf{r}}_{T/\mathcal{H}}\right) \\ &+ \vec{\omega}_{\mathcal{B}/\mathcal{J}} \times \left(\vec{\omega}_{\mathcal{H}/\mathcal{B}} \times \vec{\mathbf{r}}_{T/\mathcal{H}}\right) + \vec{\omega}_{\mathcal{B}/\mathcal{J}} \times \left(\vec{\omega}_{\mathcal{B}/\mathcal{J}} \times \vec{\mathbf{r}}_{T/\mathcal{H}}\right).\end{aligned} \tag{5.17}$$

To simplify the equation, we can use Jacobi identity $\vec{a} \times (\vec{b} \times \vec{c}) + \vec{b} \times (\vec{c} \times \vec{a}) + \vec{c} \times (\vec{a} \times \vec{b}) = \vec{0}$, and cross-product property $\vec{a} \times \vec{b} = -\vec{b} \times \vec{a}$, in practice:

$$\begin{aligned}&\vec{\omega}_{\mathcal{H}/\mathcal{B}} \times \left(\vec{\omega}_{\mathcal{B}/\mathcal{J}} \times \vec{\mathbf{r}}_{T/\mathcal{H}}\right) + \vec{\omega}_{\mathcal{B}/\mathcal{J}} \times \left(\vec{\mathbf{r}}_{T/\mathcal{H}} \times \vec{\omega}_{\mathcal{H}/\mathcal{B}}\right) \\ &\qquad + \vec{\mathbf{r}}_{T/\mathcal{H}} \times \left(\vec{\omega}_{\mathcal{H}/\mathcal{B}} \times \vec{\omega}_{\mathcal{B}/\mathcal{J}}\right) = \vec{0} \\ \Rightarrow\quad &\vec{\omega}_{\mathcal{H}/\mathcal{B}} \times \left(\vec{\omega}_{\mathcal{B}/\mathcal{J}} \times \vec{\mathbf{r}}_{T/\mathcal{H}}\right) + \left(\vec{\omega}_{\mathcal{B}/\mathcal{J}} \times \vec{\omega}_{\mathcal{H}/\mathcal{B}}\right) \times \vec{\mathbf{r}}_{T/\mathcal{H}} \\ &\qquad = \vec{\omega}_{\mathcal{B}/\mathcal{J}} \times \left(\vec{\omega}_{\mathcal{H}/\mathcal{B}} \times \vec{\mathbf{r}}_{T/\mathcal{H}}\right).\end{aligned} \tag{5.18}$$

Hence,

$$\begin{aligned}&\left.\frac{d^2}{dt^2}\right|_{\mathcal{J}}\left[\vec{\mathbf{r}}_{T/\mathcal{H}}\right] \\ &= \left.\frac{d^2}{dt^2}\right|_{\mathcal{H}}\left[\vec{\mathbf{r}}_{T/\mathcal{H}}\right] + 2\vec{\omega}_{\mathcal{H}/\mathcal{B}} \times \left.\frac{d}{dt}\right|_{\mathcal{H}}\left[\vec{\mathbf{r}}_{T/\mathcal{H}}\right] + 2\vec{\omega}_{\mathcal{B}/\mathcal{J}} \times \left.\frac{d}{dt}\right|_{\mathcal{H}}\left[\vec{\mathbf{r}}_{T/\mathcal{H}}\right] \\ &+ \left.\frac{d}{dt}\right|_{\mathcal{B}}\left[\vec{\omega}_{\mathcal{H}/\mathcal{B}}\right] \times \vec{\mathbf{r}}_{T/\mathcal{H}} + \left.\frac{d}{dt}\right|_{\mathcal{J}}\left[\vec{\omega}_{\mathcal{B}/\mathcal{J}}\right] \times \vec{\mathbf{r}}_{T/\mathcal{H}} \\ &+ \vec{\omega}_{\mathcal{H}/\mathcal{B}} \times \left(\vec{\omega}_{\mathcal{H}/\mathcal{B}} \times \vec{\mathbf{r}}_{T/\mathcal{H}}\right) + \vec{\omega}_{\mathcal{B}/\mathcal{J}} \times \left(\vec{\omega}_{\mathcal{B}/\mathcal{J}} \times \vec{\mathbf{r}}_{T/\mathcal{H}}\right) \\ &+ 2\vec{\omega}_{\mathcal{B}/\mathcal{J}} \times \left(\vec{\omega}_{\mathcal{H}/\mathcal{B}} \times \vec{\mathbf{r}}_{T/\mathcal{H}}\right).\end{aligned} \tag{5.19}$$

Collecting all time derivatives of components in (5.2), which are derived in (5.3), (5.5), (5.19), the equation of longitudinal motion of the test-mass (5.1) is expanded into following

detailed form:

$$
\begin{aligned}
&\left.\frac{d^2}{dt^2}\right|_{\mathcal{H}}\left[\vec{\mathbf{r}}_{T/\mathcal{H}}\right]+2\vec{\omega}_{\mathcal{H}/\mathcal{B}}\times\left.\frac{d}{dt}\right|_{\mathcal{H}}\left[\vec{\mathbf{r}}_{T/\mathcal{H}}\right]+2\vec{\omega}_{\mathcal{B}/\mathcal{J}}\times\left.\frac{d}{dt}\right|_{\mathcal{H}}\left[\vec{\mathbf{r}}_{T/\mathcal{H}}\right]\\
&+\left.\frac{d}{dt}\right|_{\mathcal{B}}\left[\vec{\omega}_{\mathcal{H}/\mathcal{B}}\right]\times\vec{\mathbf{r}}_{T/\mathcal{H}}+\left.\frac{d}{dt}\right|_{\mathcal{J}}\left[\vec{\omega}_{\mathcal{B}/\mathcal{J}}\right]\times\vec{\mathbf{r}}_{T/\mathcal{H}}\\
&+\vec{\omega}_{\mathcal{H}/\mathcal{B}}\times\left(\vec{\omega}_{\mathcal{H}/\mathcal{B}}\times\vec{\mathbf{r}}_{T/\mathcal{H}}\right)+\vec{\omega}_{\mathcal{B}/\mathcal{J}}\times\left(\vec{\omega}_{\mathcal{B}/\mathcal{J}}\times\vec{\mathbf{r}}_{T/\mathcal{H}}\right)\\
&+2\vec{\omega}_{\mathcal{B}/\mathcal{J}}\times\left(\vec{\omega}_{\mathcal{H}/\mathcal{B}}\times\vec{\mathbf{r}}_{T/\mathcal{H}}\right)\\
&+\left.\frac{d}{dt}\right|_{\mathcal{B}}\left[\vec{\omega}_{\mathcal{H}/\mathcal{B}}\right]\times\overrightarrow{\mathbf{PH}}+\vec{\omega}_{\mathcal{H}/\mathcal{B}}\times\left(\vec{\omega}_{\mathcal{H}/\mathcal{B}}\times\overrightarrow{\mathbf{PH}}\right)\\
&-\epsilon_1\left[\left.\frac{d}{dt}\right|_{\mathcal{B}}\left[\vec{\omega}_{\mathcal{H}_1/\mathcal{B}}\right]\times\overrightarrow{\mathbf{P_1Q_1}}+\vec{\omega}_{\mathcal{H}_1/\mathcal{B}}\times\left(\vec{\omega}_{\mathcal{H}_1/\mathcal{B}}\times\overrightarrow{\mathbf{P_1Q_1}}\right)\right]\\
&-\epsilon_2\left[\left.\frac{d}{dt}\right|_{\mathcal{B}}\left[\vec{\omega}_{\mathcal{H}_2/\mathcal{B}}\right]\times\overrightarrow{\mathbf{P_2Q_2}}+\vec{\omega}_{\mathcal{H}_2/\mathcal{B}}\times\left(\vec{\omega}_{\mathcal{H}_2/\mathcal{B}}\times\overrightarrow{\mathbf{P_2Q_2}}\right)\right]\\
&+2\vec{\omega}_{\mathcal{B}/\mathcal{J}}\times\left[\vec{\omega}_{\mathcal{H}/\mathcal{B}}\times\overrightarrow{\mathbf{PH}}-\epsilon_1\left(\vec{\omega}_{\mathcal{H}_1/\mathcal{B}}\times\overrightarrow{\mathbf{P_1Q_1}}\right)-\epsilon_2\left(\vec{\omega}_{\mathcal{H}_2/\mathcal{B}}\times\overrightarrow{\mathbf{P_2Q_2}}\right)\right]\\
&+\left.\frac{d}{dt}\right|_{\mathcal{J}}\left[\vec{\omega}_{\mathcal{B}/\mathcal{J}}\right]\times\vec{\mathbf{r}}_{\mathcal{H}/\mathcal{B}}+\vec{\omega}_{\mathcal{B}/\mathcal{J}}\times\left(\vec{\omega}_{\mathcal{B}/\mathcal{J}}\times\vec{\mathbf{r}}_{\mathcal{H}/\mathcal{B}}\right)\\
&=\sum\frac{\vec{\mathbf{f}}_T}{m_{\text{tm}}}-\sum\frac{\vec{\mathbf{f}}_B}{m_{\text{sc}}}
\end{aligned}
\tag{5.20}
$$

Clearly, this equation describes the longitudinal position of a test-mass in a spacecraft given some construction parameters such as the masses of test-masses, MOSAs and spacecraft, housing centers, pivot points, center of mass of the platform, Etc. The inputs of the equation are the forces applied on the test-mass (for example the actuation forces) and the spacecraft (such as the micro-propulsion forces). The angular velocity vectors are also the inputs of the above equation. However, they play a role as variables for other equations of motion, as in the following subsections. Therefore, we will consider them as variables in equations.

5.2.2 Test-mass angular motion

Here, we derive the equation of the angular motion of the test-mass. Starting with the Euler equation,

$$
\left.\frac{d}{dt}\right|_{\mathcal{J}}\left[\mathbf{I}_{\text{tm}/T}\ \vec{\omega}_{\mathcal{T}/\mathcal{J}}\right]=\sum\vec{\mathbf{t}}_T,
\tag{5.21}
$$

where $\mathbf{I}_{\text{tm}/T}$ is the inertia tensor of the test-mass w.r.t. its center of mass T, $\vec{\omega}_{\mathcal{T}/\mathcal{J}}$ is the angular velocity of the test-mass body frame w.r.t. $\mathcal{J}$-frame, $\sum\vec{\mathbf{t}}_T$ is the total torque applied on the test-mass. We can apply transport theorem (5.4) and note that the inertia tensor of

the test-mass is constant in $\mathcal{T}$-frame, so $\frac{d}{dt}\big|_{\mathcal{T}}\left[\mathbf{I}_{\mathrm{tm}/T}\right]=0$, to obtain

$$\begin{aligned}\mathbf{I}_{\mathrm{tm}/T}\,\frac{d}{dt}\Big|_{\mathcal{H}}\left[\vec{\omega}_{\mathcal{T}/\mathcal{J}}\right]+\mathbf{I}_{\mathrm{tm}/T}\left(\vec{\omega}_{\mathcal{H}/\mathcal{J}}\times\vec{\omega}_{\mathcal{T}/\mathcal{J}}\right)\\ +\vec{\omega}_{\mathcal{T}/\mathcal{J}}\times\left(\mathbf{I}_{\mathrm{tm}/T}\;\vec{\omega}_{\mathcal{T}/\mathcal{J}}\right)=\sum\vec{\mathbf{t}}_{T}.\end{aligned}\tag{5.22}$$

We decompose the angular velocity vector $\vec{\omega}_{\mathcal{T}/\mathcal{J}}=\vec{\omega}_{\mathcal{T}/\mathcal{H}}+\vec{\omega}_{\mathcal{H}/\mathcal{B}}+\vec{\omega}_{\mathcal{B}/\mathcal{J}}$, and again apply transport theorem to have:

$$\begin{aligned}&\mathbf{I}_{\mathrm{tm}/T}\,\frac{d}{dt}\Big|_{\mathcal{H}}\left[\vec{\omega}_{\mathcal{T}/\mathcal{H}}\right]+\mathbf{I}_{\mathrm{tm}/T}\,\frac{d}{dt}\Big|_{\mathcal{B}}\left[\vec{\omega}_{\mathcal{H}/\mathcal{B}}\right]+\mathbf{I}_{\mathrm{tm}/T}\,\frac{d}{dt}\Big|_{\mathcal{J}}\left[\vec{\omega}_{\mathcal{B}/\mathcal{J}}\right]\\ &+\left(\vec{\omega}_{\mathcal{T}/\mathcal{H}}+\vec{\omega}_{\mathcal{H}/\mathcal{B}}+\vec{\omega}_{\mathcal{B}/\mathcal{J}}\right)\times\left[\mathbf{I}_{\mathrm{tm}/T}\left(\vec{\omega}_{\mathcal{T}/\mathcal{H}}+\vec{\omega}_{\mathcal{H}/\mathcal{B}}+\vec{\omega}_{\mathcal{B}/\mathcal{J}}\right)\right]\\ &+\mathbf{I}_{\mathrm{tm}/T}\left[\left(\vec{\omega}_{\mathcal{H}/\mathcal{B}}+\vec{\omega}_{\mathcal{B}/\mathcal{J}}\right)\times\vec{\omega}_{\mathcal{T}/\mathcal{H}}\right]=\sum\vec{\mathbf{t}}_{T}.\end{aligned}\tag{5.23}$$

5.2.3 MOSA angular motion

In this subsection, we examine the equation that governs the motion of MOSA. This motion is the rotation of the telescope attached in MOSA. This rotation is mainly due to the pointing mechanism when we need to adjust the telescopes in all spacecraft to align with distant ones and the jittering of the angular motion of the MOSAs. In detail, when the spacecraft rotates by the thrust system of DFACS to follow the test-mass geodesics, the telescopes have to follow the spacecraft rigidly in its rotation w.r.t. $\mathcal{J}$-frame by a structure torque. We define this torque applied on the telescope or precisely on the MOSA as:

$$\vec{\mathbf{t}}^{\,\mathrm{struct}}_{\mathcal{H}}\;=\;\frac{d}{dt}\Big|_{\mathcal{J}}\left[\mathbf{I}_{\mathrm{mo}/Q}\;\vec{\omega}_{\mathcal{B}/\mathcal{J}}\right]\tag{5.24}$$

which is simply the Euler equation for the MOSA following the spacecraft rotation in $\mathcal{J}$-frame. We denoted $\mathbf{I}_{\mathrm{mo}/Q}$ as the inertia tensor of MOSA w.r.t. its center of mass Q.

On the other hand, there would be the relative angular motion between MOSA and spacecraft in $\mathcal{H}$-frame, denoted as $\sum\vec{\mathbf{t}}^{\,\mathrm{rel}}_{\mathcal{H}}$. These torques (with the structure torque we described above) are the inputs of the following Euler equation for MOSA angular motion:

$$\begin{aligned}\frac{d}{dt}\Big|_{\mathcal{J}}\left[\mathbf{I}_{\mathrm{mo}/Q}\;\vec{\omega}_{\mathcal{H}/\mathcal{J}}\right]&=\sum\vec{\mathbf{t}}_{\mathcal{H}}\\ \Leftrightarrow\;\frac{d}{dt}\Big|_{\mathcal{J}}\left[\mathbf{I}_{\mathrm{mo}/Q}\;\vec{\omega}_{\mathcal{H}/\mathcal{B}}\right]+\frac{d}{dt}\Big|_{\mathcal{J}}\left[\mathbf{I}_{\mathrm{mo}/Q}\;\vec{\omega}_{\mathcal{B}/\mathcal{J}}\right]&=\sum\vec{\mathbf{t}}^{\,\mathrm{rel}}_{\mathcal{H}}+\vec{\mathbf{t}}^{\,\mathrm{struct}}_{\mathcal{H}}\\ \Rightarrow\;\frac{d}{dt}\Big|_{\mathcal{H}}\left[\mathbf{I}_{\mathrm{mo}/Q}\;\vec{\omega}_{\mathcal{H}/\mathcal{B}}\right]+\vec{\omega}_{\mathcal{H}/\mathcal{J}}\times\left(\mathbf{I}_{\mathrm{mo}/Q}\;\vec{\omega}_{\mathcal{H}/\mathcal{B}}\right)&=\sum\vec{\mathbf{t}}^{\,\mathrm{rel}}_{\mathcal{H}},\end{aligned}\tag{5.25}$$

where we decompose the angular velocity vector $\vec{\omega}_{\mathcal{H}/\mathcal{J}}=\vec{\omega}_{\mathcal{H}/\mathcal{B}}+\vec{\omega}_{\mathcal{B}/\mathcal{J}}$ and the total torque applied on MOSA to get the second line, note that we have already defined the structure

torque in (5.24); the final line is derived by using the transport theorem (5.4) from $\mathcal{J}$-frame to $\mathcal{H}$-frame.

The MOSA inertia tensor is constant in $\mathcal{H}$-frame so its time derivative in that frame will disappear. Again decomposing $\vec{\omega}_{\mathcal{H}/\mathcal{J}} = \vec{\omega}_{\mathcal{H}/\mathcal{B}} + \vec{\omega}_{\mathcal{B}/\mathcal{J}}$, we get

$$\mathbf{I}_{\mathrm{mo}/Q} \left.\frac{d}{dt}\right|_{\mathcal{H}} \left[\vec{\omega}_{\mathcal{H}/\mathcal{B}}\right] + \left(\vec{\omega}_{\mathcal{H}/\mathcal{B}} + \vec{\omega}_{\mathcal{B}/\mathcal{J}}\right) \times \left(\mathbf{I}_{\mathrm{mo}/Q} \vec{\omega}_{\mathcal{H}/\mathcal{B}}\right) \quad = \quad \sum \vec{\mathbf{t}}^{\mathrm{rel}}_{\mathcal{H}} \tag{5.26}$$

5.2.4 Spacecraft angular motion

We use a similar procedure in the case of MOSA and test-mass angular motion. We derive the equation of motion for the spacecraft rotation by starting with the Euler equation in $\mathcal{J}$-frame:

$$\left.\frac{d}{dt}\right|_{\mathcal{J}} \left[\mathbf{I}_{\mathrm{sc}/B}\ \vec{\omega}_{\mathcal{B}/\mathcal{J}}\right] = \sum \vec{\mathbf{t}}_{\mathcal{B}}. \tag{5.27}$$

We want to express this equation in the spacecraft body frame $\mathcal{B}$-frame like we have done for the case of the test-mass in $\mathcal{T}$-frame and the MOSA in $\mathcal{H}$-frame. Unfortunately, in this spacecraft case, the difficulty comes from the fact that the inertia tensor of the whole spacecraft could change even in the $\mathcal{B}$-frame due to the motions of the telescopes and test-masses. The complete equations of motion for the spacecraft angular motion were worked out in [90]. Due to its complexity and the limitation of the scope of our study, we will take the following assumption:

Dynamics assumption 1

The motions of the telescopes and the test-masses inside the spacecraft do not change the inertia tensor of the whole spacecraft significantly in the short time scale.

Hence, we can neglect the $\mathcal{B}$-frame time derivative of the spacecraft inertia tensor in our equations. We again use the transport theorem (5.4)to obtain:

$$\mathbf{I}_{\mathrm{sc}/B} \left.\frac{d}{dt}\right|_{\mathcal{B}} \left[\vec{\omega}_{\mathcal{B}/\mathcal{J}}\right] + \vec{\omega}_{\mathcal{B}/\mathcal{J}} \times \left(\mathbf{I}_{\mathrm{sc}/B}\ \vec{\omega}_{\mathcal{B}/\mathcal{J}}\right) = \sum \vec{\mathbf{t}}_{\mathcal{B}}. \tag{5.28}$$

The equations (5.20), (5.23), (5.26), and (5.28) are the main objective of the LISA Dynamics. The solution of those equations gives us the information of all LISA objects and will be a part of the DFACS control loops which are essential for LISA operations. Unfortunately, these equations are non-linear. For instance, the dynamical quantity $\vec{\omega}_{\mathcal{B}/\mathcal{J}}$, which is the variable to solve in (5.28), exists in (5.20) including quadratic terms like $\vec{\omega}_{\mathcal{B}/\mathcal{J}} \times \left(\vec{\omega}_{\mathcal{B}/\mathcal{J}} \times \vec{\mathbf{r}}_{T/\mathcal{H}}\right)$. We could try to solve these equations with general solvers using, for example, the Runge-Kutta method, but this is out of the scope of this thesis. In the next section, we will introduce a way

to solve these equations with our implementation in the `LISANode` simulator. In particular, we expand the equations of motion in the linearized form and write them in the state space vector representation before implementation.

5.3 Simulation model

5.3.1 Linearisation of the equation of motion

In order to linearize the equations of motion, we use the target body frames introduced in section 5.1 to break down the spacecraft and MOSA motions into two parts:

1. The first one is the displacement of the working point in the target frame w.r.t. $\mathcal{J}$-frame, which varies with the large margin but gradually over a long time (in years or months) so that its effect is at very low frequencies and out of LISA frequency band.

2. The second part is related to the small fluctuation of LISA objects around their working points, which is in LISA frequency band.

For instance, we decompose the angular velocities:

$$\vec{\omega}_{\mathcal{B}/\mathcal{J}} = \vec{\omega}_{\mathcal{B}/\mathcal{O}} + \vec{\omega}_{\mathcal{O}/\mathcal{J}}, \tag{5.29}$$

$$\vec{\omega}_{\mathcal{H}/\mathcal{B}} = \vec{\omega}_{\mathcal{H}/\mathcal{H}^*} + \vec{\omega}_{\mathcal{H}^*/\mathcal{O}} + \vec{\omega}_{\mathcal{O}/\mathcal{B}}. \tag{5.30}$$

In the above equations, $\vec{\omega}_{\mathcal{O}/\mathcal{J}}$ varies slowly in years so that we can use the annual average for this quantity in the equations of motion. While $\vec{\omega}_{\mathcal{B}/\mathcal{O}}, \vec{\omega}_{\mathcal{H}/\mathcal{H}^*}$ are the LISA in-band jitter motions of spacecraft and MOSA around their working point in target frame O and H^*, respectively, they are treated by perturbation approach so we keep only their linear terms in the equations of motion. The last term $\vec{\omega}_{\mathcal{H}^*/\mathcal{O}}$ is defined by the rate change of the constellation angle, which is also varying slowly over a long time so that we can use the annual average of this term in the equations of motion.

In our study, to simplify the problem we use following assumption:

Dynamics assumption 2

We neglect the MOSA angular velocity, $\vec{\omega}_{\mathcal{H}/\mathcal{B}} = \vec{0}$, in our derived equation of motion.

Hence, we do not consider the MOSA rotation as a dynamic variable in the first stage. In particular, we neglect non-inertial forces and torques arising from the slow (out-of-band) MOSA rotation. Hence, the equation of MOSA angular motion (5.26) no longer plays any role. In addition, the equations of test-mass longitudinal motion (5.20) are simplified a lot in

our limited study case. This assumption is temporary and physically unacceptable, but it is still helpful in the first analysis stage before we advance with a complete study. Eventually, we still consider some dominant terms due to the displacement in MOSA angular position in other equations of motion to account for the effect of MOSAs motions. We will see that in the subsection 5.3.3.

For convenience, especially in state space representation in the next subsection, we want to express the vectorial quantities into specific reference frame as follows rules:

- Longitudinal displacements of test-masses are expressed in MOSA frames, i.e. $\mathcal{H}_i$-frame.
- Test-mass angular velocities are expressed in their respective body frames, $\mathcal{T}_i$.
- MOSA angular jitter are expressed in their respective body frames, $\mathcal{H}_i$.
- Spacecraft angular velocities w.r.t. $\mathcal{O}$-frame are expressed in its body frame $\mathcal{B}$. While the angular velocity of spacecraft target body frame w.r.t. Galilean frame is expressed in $\mathcal{O}$-frame.
- The force and torque vectors applied on test-masses are expressed in the MOSA target body frame, $\mathcal{H}_i^*$-frame, or eventually MOSA body frame $\mathcal{H}_i$-frame as explained in the discussion following the dynamics assumption 1. For the forces and torques applied on the spacecraft, we express them in the spacecraft target body O-frame.

As a result, we need to rotate some vectors which are represented in a preferable reference frame, different from the one of equations of motion. We introduce some rotation matrices for that purpose. For example, to rotate the spacecraft angular velocities, which are preferably expressed in $\mathcal{B}$-frame or $\mathcal{J}$-frame, in (5.28) to be in $\mathcal{H}$-frame, we express:

$$\vec{\omega}_{\mathcal{B}/\mathcal{O}} \overset{\mathcal{H}}{=} \vec{\omega}^{\,\mathcal{H}}_{\mathcal{B}/\mathcal{O}} = T^{\mathcal{H}}_{\mathcal{B}} \vec{\omega}^{\,\mathcal{B}}_{\mathcal{B}/\mathcal{O}} \tag{5.31}$$

$$\vec{\omega}_{\mathcal{O}/\mathcal{J}} \overset{\mathcal{H}}{=} \vec{\omega}^{\,\mathcal{H}}_{\mathcal{O}/\mathcal{J}} = T^{\mathcal{H}}_{\mathcal{B}}\, T^{\mathcal{B}}_{\mathcal{O}}\, T^{\mathcal{O}}_{\mathcal{J}}\, \vec{\omega}^{\,\mathcal{J}}_{\mathcal{O}/\mathcal{J}}, \tag{5.32}$$

where the rotation matrices are functions of the relative orientation of reference frames. For instance, $T^{\mathcal{B}}_{\mathcal{O}} = T^{\mathcal{B}}_{\mathcal{O}}\left(\vec{\alpha}_{\mathcal{B}/\mathcal{O}}\right)$ is the rotation matrix from the spacecraft target body $\mathcal{O}$-frame to the spacecraft body $\mathcal{B}$-frame, where $\vec{\alpha}_{\mathcal{B}/\mathcal{O}}$ is the Euler angles or attitude vector of the actual spacecraft in the target spacecraft body $\mathcal{O}$-frame. Its transpose matrix is $T^{\mathcal{O}}_{\mathcal{B}} = \left(T^{\mathcal{B}}_{\mathcal{O}}\right)^{\mathrm{T}}$. Using the short notation for sine (s_x) and cosine (c_x) functions and ZYX Cardan sequence convention

[61], we define the rotation matrix function as follows:

$$T(\vec{\alpha}) = T(\phi,\eta,\theta) = \begin{bmatrix} 1 & 0 & 0 \\ 0 & c_\theta & s_\theta \\ 0 & -s_\theta & c_\theta \end{bmatrix} \begin{bmatrix} c_\eta & 1 & -s_\eta \\ 0 & 1 & 0 \\ s_\eta & 0 & c_\eta \end{bmatrix} \begin{bmatrix} c_\phi & s_\phi & 0 \\ -s_\phi & c_\phi & 0 \\ 0 & 0 & 1 \end{bmatrix} \tag{5.33}$$

$$= \begin{bmatrix} c_\eta c_\phi & c_\eta s_\phi & -s_\eta \\ s_\theta s_\eta c_\phi - c_\theta s_\phi & s_\theta s_\eta c_\phi + c_\theta s_\phi & c_\eta s_\theta \\ c_\theta s_\eta c_\phi + s_\theta s_\phi & c_\theta s_\eta c_\phi - s_\theta c_\phi & c_\eta c_\theta \end{bmatrix}. \tag{5.34}$$

We can also express any cross-product as a matrix product between a skew-symmetric matrix $\left[\vec{\mathbf{a}}^{\mathcal{H}}\right]^\times$ made out of vector $\vec{\mathbf{a}}$ and target vector $\vec{\mathbf{b}}$ as:

$$\vec{\mathbf{a}} \times \vec{\mathbf{b}} \overset{H}{=} \left[\vec{\mathbf{a}}^{\mathcal{H}}\right]^\times \vec{\mathbf{b}}^{\mathcal{H}} = \begin{bmatrix} 0 & -a_z^{\mathcal{H}} & a_y^{\mathcal{H}} \\ a_z^{\mathcal{H}} & 0 & -a_x^{\mathcal{H}} \\ -a_y^{\mathcal{H}} & a_x^{\mathcal{H}} & 0 \end{bmatrix} \begin{bmatrix} b_x^{\mathcal{H}} \\ b_y^{\mathcal{H}} \\ b_z^{\mathcal{H}} \end{bmatrix} \tag{5.35}$$

With all the required material introduced above, we are ready to linearize our equations of motion. First, let us consider the test-mass longitudinal motion, (5.20). We decompose angular velocity as (5.29), ignore the angular velocity $\vec{\omega}_{\mathcal{H}/\mathcal{B}}$ between $\mathcal{H}$ and $\mathcal{B}$ frames, and apply the transport theorem for time derivative frame transformation to have:

$$\begin{aligned} &\left.\frac{d^2}{dt^2}\right|_{\mathcal{H}} \left[\vec{\mathbf{r}}_{T/\mathcal{H}}\right] + 2\left(\vec{\omega}_{\mathcal{B}/\mathcal{O}} + \vec{\omega}_{\mathcal{O}/\mathcal{J}}\right) \times \left.\frac{d}{dt}\right|_{\mathcal{H}} \left[\vec{\mathbf{r}}_{T/\mathcal{H}}\right] \\ &+ \left(\left.\frac{d}{dt}\right|_{\mathcal{O}} \left[\vec{\omega}_{\mathcal{B}/\mathcal{O}}\right] + \vec{\omega}_{\mathcal{O}/\mathcal{J}} \times \vec{\omega}_{\mathcal{B}/\mathcal{O}} + \left.\frac{d}{dt}\right|_{\mathcal{J}} \left[\vec{\omega}_{\mathcal{O}/\mathcal{J}}\right] \right) \times \left(\vec{\mathbf{r}}_{T/\mathcal{H}} + \vec{\mathbf{r}}_{\mathcal{H}/\mathcal{B}}\right) \\ &+ \left(\vec{\omega}_{\mathcal{B}/\mathcal{O}} + \vec{\omega}_{\mathcal{O}/\mathcal{J}}\right) \times \left[\left(\vec{\omega}_{\mathcal{B}/\mathcal{O}} + \vec{\omega}_{\mathcal{O}/\mathcal{J}}\right) \times \left(\vec{\mathbf{r}}_{T/\mathcal{H}} + \vec{\mathbf{r}}_{\mathcal{H}/\mathcal{B}}\right)\right] \\ &= \sum \frac{\vec{\mathbf{f}}_T}{m_{\text{tm}}} - \sum \frac{\vec{\mathbf{f}}_B}{m_{\text{sc}}}. \end{aligned} \tag{5.36}$$

We use the dot notation to express the time derivative of vectorial quantities in the exact frame in which the vectors are coordinated, for instance, $\left.\frac{d}{dt}\right|_{\mathcal{H}} \left[\vec{\mathbf{r}}_{\mathcal{T}/\mathcal{H}}\right] = \dot{\vec{\mathbf{r}}}_{\mathcal{T}/\mathcal{H}}$ and rewrite the equation in term of matrix representation to have::

$$\begin{aligned} &\ddot{\vec{\mathbf{r}}}^{\,\mathcal{H}}_{T/\mathcal{H}} + 2\left[\vec{\omega}^{\,\mathcal{H}}_{\mathcal{B}/\mathcal{O}} + \vec{\omega}^{\,\mathcal{H}}_{\mathcal{O}/\mathcal{J}}\right]^\times \dot{\vec{\mathbf{r}}}^{\,\mathcal{H}}_{\mathcal{T}/\mathcal{H}} + \left[\dot{\vec{\omega}}^{\,\mathcal{H}}_{\mathcal{B}/\mathcal{O}} + \dot{\vec{\omega}}^{\,\mathcal{H}}_{\mathcal{O}/\mathcal{J}}\right]^\times \left(\vec{\mathbf{r}}^{\,\mathcal{H}}_{T/\mathcal{H}} + \vec{\mathbf{r}}^{\,\mathcal{H}}_{H/\mathcal{B}}\right) \\ &+ \left[\vec{\omega}^{\,\mathcal{H}}_{\mathcal{B}/\mathcal{O}}\right]^\times \left[\vec{\omega}^{\,\mathcal{H}}_{\mathcal{B}/\mathcal{O}}\right]^\times \left(\vec{\mathbf{r}}^{\,\mathcal{H}}_{T/\mathcal{H}} + \vec{\mathbf{r}}^{\,\mathcal{H}}_{H/\mathcal{B}}\right) + \left[\vec{\omega}^{\,\mathcal{H}}_{\mathcal{O}/\mathcal{J}}\right]^\times \left[\vec{\omega}^{\,\mathcal{H}}_{\mathcal{O}/\mathcal{J}}\right]^\times \left(\vec{\mathbf{r}}^{\,\mathcal{H}}_{T/\mathcal{H}} + \vec{\mathbf{r}}^{\,\mathcal{H}}_{H/\mathcal{B}}\right) \\ &+ 2\left[\vec{\omega}^{\,\mathcal{H}}_{\mathcal{O}/\mathcal{J}}\right]^\times \left[\vec{\omega}^{\,\mathcal{H}}_{\mathcal{B}/\mathcal{O}}\right]^\times \left(\vec{\mathbf{r}}^{\,\mathcal{H}}_{T/\mathcal{H}} + \vec{\mathbf{r}}^{\,\mathcal{H}}_{H/\mathcal{B}}\right) = \sum \frac{\vec{\mathbf{f}}^{\mathcal{H}}_T}{m_{\text{tm}}} - \sum \frac{\vec{\mathbf{f}}^{\mathcal{H}}_B}{m_{\text{sc}}}. \end{aligned} \tag{5.37}$$

We want to express all the vectorial quantities in the related body reference frame we have discussed previously, by using rotation matrices. Hence, the final form for the equation of

longitudinal motion of test-mass is rewritten as:

$$
\begin{aligned}
&m_{\text{tm}}\ddot{\vec{\mathbf{r}}}^{\,\mathcal{H}}_{T/\mathcal{H}} + 2m_{\text{tm}}\left[T^{\mathcal{H}}_{\mathcal{B}}\vec{\omega}^{\,\mathcal{B}}_{\mathcal{B}/\mathcal{O}} + T^{\mathcal{H}}_{\mathcal{B}}T^{\mathcal{B}}_{\mathcal{O}}\vec{\omega}^{\,\mathcal{O}}_{\mathcal{O}/\mathcal{J}}\right]^{\times}\dot{\vec{\mathbf{r}}}^{\,\mathcal{H}}_{T/\mathcal{H}} \\
&+ m_{\text{tm}}\left[T^{\mathcal{H}}_{\mathcal{B}}\dot{\vec{\omega}}^{\,\mathcal{B}}_{\mathcal{B}/\mathcal{O}} + T^{\mathcal{H}}_{\mathcal{B}}T^{\mathcal{B}}_{\mathcal{O}}\dot{\vec{\omega}}^{\,\mathcal{O}}_{\mathcal{O}/\mathcal{J}}\right]^{\times}\left(\vec{\mathbf{r}}^{\,\mathcal{H}}_{T/\mathcal{H}} + \vec{\mathbf{r}}^{\,\mathcal{H}}_{H/\mathcal{B}}\right) \\
&+ m_{\text{tm}}\left[T^{\mathcal{H}}_{\mathcal{B}}\vec{\omega}^{\,\mathcal{B}}_{\mathcal{B}/\mathcal{O}}\right]^{\times}\left[T^{\mathcal{H}}_{\mathcal{B}}\vec{\omega}^{\,\mathcal{B}}_{\mathcal{B}/\mathcal{O}}\right]^{\times}\left(\vec{\mathbf{r}}^{\,\mathcal{H}}_{T/\mathcal{H}} + \vec{\mathbf{r}}^{\,\mathcal{H}}_{H/\mathcal{B}}\right) \\
&+ m_{\text{tm}}\left[T^{\mathcal{H}}_{\mathcal{B}}T^{\mathcal{B}}_{\mathcal{O}}\vec{\omega}^{\,\mathcal{O}}_{O/\mathcal{J}}\right]^{\times}\left[T^{\mathcal{H}}_{\mathcal{B}}T^{\mathcal{B}}_{\mathcal{O}}\vec{\omega}^{\,\mathcal{O}}_{O/\mathcal{J}}\right]^{\times}\left(\vec{\mathbf{r}}^{\,\mathcal{H}}_{T/\mathcal{H}} + \vec{\mathbf{r}}^{\,\mathcal{H}}_{H/\mathcal{B}}\right) \\
&+ 2m_{\text{tm}}\left[T^{\mathcal{H}}_{\mathcal{B}}T^{\mathcal{B}}_{\mathcal{O}}\vec{\omega}^{\,\mathcal{O}}_{O/\mathcal{J}}\right]^{\times}\left[T^{\mathcal{H}}_{\mathcal{B}}\vec{\omega}^{\,\mathcal{B}}_{\mathcal{B}/\mathcal{O}}\right]^{\times}\left(\vec{\mathbf{r}}^{\,\mathcal{H}}_{T/\mathcal{H}} + \vec{\mathbf{r}}^{\,\mathcal{H}}_{H/\mathcal{B}}\right) \\
&= \sum T^{\mathcal{H}}_{\mathcal{T}}\vec{\mathbf{f}}^{\mathcal{T}}_{T} - \frac{m_{\text{tm}}}{m_{\text{sc}}}\sum T^{\mathcal{H}}_{\mathcal{O}}\vec{\mathbf{f}}^{\mathcal{O}}_{B}.
\end{aligned}
\tag{5.38}
$$

The same procedure is applied to other equations of motion. The test-mass angular motion equation (5.23) is rewritten as follows

$$
\begin{aligned}
&\mathbf{I}^{\mathcal{T}}_{\text{tm}/T}\dot{\vec{\omega}}^{\,\mathcal{T}}_{\mathcal{T}/\mathcal{H}} + \mathbf{I}^{\mathcal{T}}_{\text{tm}/T}T^{\mathcal{T}}_{\mathcal{B}}\dot{\vec{\omega}}^{\,\mathcal{B}}_{\mathcal{B}/\mathcal{O}} + \mathbf{I}^{\mathcal{T}}_{\text{tm}/T}\left[T^{\mathcal{T}}_{\mathcal{O}}\vec{\omega}^{\,\mathcal{O}}_{O/\mathcal{J}}\right]^{\times}T^{\mathcal{T}}_{\mathcal{B}}\vec{\omega}^{\,\mathcal{B}}_{\mathcal{B}/\mathcal{O}} \\
&+ \left(\left[\vec{\omega}^{\,\mathcal{T}}_{T/\mathcal{H}}\right]^{\times} + \left[T^{\mathcal{T}}_{\mathcal{B}}\vec{\omega}^{\,\mathcal{B}}_{\mathcal{B}/\mathcal{O}}\right]^{\times} + \left[T^{\mathcal{T}}_{\mathcal{O}}\vec{\omega}^{\,\mathcal{O}}_{O/\mathcal{J}}\right]^{\times}\right)\mathbf{I}^{\mathcal{T}}_{\text{tm}/T}\left(\vec{\omega}^{\,\mathcal{T}}_{\mathcal{T}/\mathcal{H}} + T^{\mathcal{T}}_{\mathcal{B}}\vec{\omega}^{\,\mathcal{B}}_{\mathcal{B}/\mathcal{O}} + T^{\mathcal{T}}_{\mathcal{O}}\vec{\omega}^{\,\mathcal{O}}_{\mathcal{O}/\mathcal{J}}\right) \\
&+ \mathbf{I}^{\mathcal{T}}_{\text{tm}/T}\left(\left[T^{\mathcal{T}}_{\mathcal{B}}\vec{\omega}^{\,\mathcal{B}}_{\mathcal{B}/\mathcal{O}}\right]^{\times} + \left[T^{\mathcal{T}}_{\mathcal{O}}\vec{\omega}^{\,\mathcal{O}}_{O/\mathcal{J}}\right]^{\times}\right)\vec{\omega}^{\,\mathcal{T}}_{T/\mathcal{H}} = \sum\vec{\mathbf{t}}^{\mathcal{T}}_{T}.
\end{aligned}
\tag{5.39}
$$

The spacecraft angular motion equation (5.28), worked out similarly, reads

$$
\begin{aligned}
&\mathbf{I}^{\mathcal{B}}_{\text{sc}/B}\dot{\vec{\omega}}^{\,\mathcal{B}}_{\mathcal{B}/\mathcal{O}} + \mathbf{I}^{\mathcal{B}}_{\text{sc}/B}T^{\mathcal{B}}_{\mathcal{O}}\dot{\vec{\omega}}^{\,\mathcal{O}}_{\mathcal{O}/\mathcal{J}} + \mathbf{I}^{\mathcal{B}}_{\text{sc}/B}\left[T^{\mathcal{B}}_{\mathcal{O}}\dot{\vec{\omega}}^{\,\mathcal{O}}_{\mathcal{O}/\mathcal{J}}\right]^{\times}\vec{\omega}^{\,\mathcal{B}}_{\mathcal{B}/\mathcal{O}} \\
&+ \left(\left[\vec{\omega}^{\,\mathcal{B}}_{\mathcal{B}/\mathcal{O}}\right]^{\times} + \left[T^{\mathcal{B}}_{\mathcal{O}}\vec{\omega}^{\,\mathcal{O}}_{O/\mathcal{J}}\right]^{\times}\right)\mathbf{I}^{\mathcal{B}}_{\text{sc}/B}\left(\vec{\omega}^{\,\mathcal{B}}_{\mathcal{B}/\mathcal{O}} + T^{\mathcal{B}}_{\mathcal{O}}\vec{\omega}^{\,\mathcal{O}}_{O/\mathcal{J}}\right) = \sum T^{\mathcal{B}}_{\mathcal{O}}\vec{\mathbf{t}}^{\mathcal{O}}_{\mathcal{B}}.
\end{aligned}
\tag{5.40}
$$

Finally, the spacecraft translational motion equation (5.3) has been rewritten in the same way we did for the equation (5.38), from its simple form into:

$$
\begin{aligned}
&m_{\text{sc}}\ddot{\vec{\mathbf{r}}}^{\,\mathcal{O}}_{B/\mathcal{O}} + m_{\text{sc}}\left[\dot{\vec{\omega}}^{\,\mathcal{O}}_{O/\mathcal{J}}\right]^{\times}\vec{\mathbf{r}}^{\,\mathcal{O}}_{B/\mathcal{O}} \\
&+ m_{\text{sc}}\left[\vec{\omega}^{\,\mathcal{O}}_{O/\mathcal{J}}\right]^{\times}\left[\vec{\omega}^{\,\mathcal{O}}_{O/\mathcal{J}}\right]^{\times}\vec{\mathbf{r}}^{\,\mathcal{O}}_{B/\mathcal{O}} + 2m_{\text{sc}}\left[\vec{\omega}^{\,\mathcal{O}}_{O/\mathcal{J}}\right]^{\times}\dot{\vec{\mathbf{r}}}^{\,\mathcal{O}}_{B/\mathcal{O}} = \sum\vec{\mathbf{f}}^{\,\mathcal{O}}_{B} - m_{\text{sc}}T^{\mathcal{T}}_{\mathcal{O}}\ddot{\vec{\mathbf{r}}}^{\,\mathcal{O}}_{O/\mathcal{J}}
\end{aligned}
\tag{5.41}
$$

5.3.2 State-space representation

In order to have a compact representation of our dynamical system described by the previous equations of motion, we use the state-space model [121]. Accordingly, the system is constructed by four matrices: the system matrix $\mathbf{A}$, the input matrix $\mathbf{B}$, the output matrix $\mathbf{C}$, and the feedforward matrix $\mathbf{D}$, as well as two vectors: the state vector $\vec{\mathbf{x}}(t)$, and the input vector $\vec{\mathbf{u}}(t)$. Depending on the matrices $\mathbf{A}, \mathbf{B}$ and the initial state, we can have various system categories, such as linear and non-linear systems, time-invariant and time-varying systems, Etc.

The core of a state-space model is a set of the state-space equations, or shortly state equations [122], which have the following form:

$$\dot{\vec{\mathbf{x}}}(t) = \mathbf{A}\vec{\mathbf{x}}(t) + \mathbf{B}\vec{\mathbf{u}}(t), \tag{5.42}$$

$$\vec{\mathbf{y}}(t) = \mathbf{C}\vec{\mathbf{x}}(t) + \mathbf{D}\vec{\mathbf{u}}(t). \tag{5.43}$$

With this formalism, the state of the system, which is expressed as state vector $\vec{\mathbf{x}}(t)$, consists of a finite number of state variables. Given the initial values of the state vector at t_0, the input vector for $t > t_0$, and the mathematical model for the relation between the input, state and system itself, or matrices $\mathbf{A}, \mathbf{B}$ in (5.42), the state variables could be well-determined at any future moment $t > t_0$. The first equation (5.42) describes the dynamical system, while the equation (5.43) is called the observation equation. To understand better the meaning of the two above equations, let us consider an example: the one-dimensional driven and damped harmonic oscillation is described by the following equation of motion [110]:

$$\ddot{\vec{x}} = -\frac{k}{m}\vec{x} - \frac{b}{m}\dot{\vec{x}} + \frac{C_0}{m}e^{i\omega_0 t}. \tag{5.44}$$

This system can be represented in state-space model with the state vector $\vec{\mathbf{x}} = \begin{pmatrix} \vec{x} \\ \dot{\vec{x}} \end{pmatrix}$, the input $\vec{\mathbf{u}}(t) = C_0 e^{i\omega_0 t}$, and the state equation (5.42) reads

$$\dot{\vec{\mathbf{x}}} = \mathbf{A}\vec{\mathbf{x}} + \mathbf{B}\vec{\mathbf{u}} = \begin{pmatrix} 0 & 1 \\ \frac{-k}{m} & \frac{-b}{m} \end{pmatrix} \vec{\mathbf{x}} + \begin{pmatrix} 0 \\ \frac{1}{m} \end{pmatrix} \vec{\mathbf{u}}. \tag{5.45}$$

The $\mathbf{A}$ matrix contains the dynamics of the system while the $\mathbf{B}$ gives the influence of the external forces or noises on the system, in this case, the driven force applied on the oscillation. Because not all state variables are measurable or in our interest, we need to construct the output vector $\vec{\mathbf{y}}(t)$ from the input and state vectors. Accordingly, the $\mathbf{C}$ matrix determines the measurement of the dynamical system, which gives the direct relation between the dynamical variables and the observable ones. For instance, the C matrix should include the scaling factor of the measurement devices (such as ruler, thermometer, ammeter, sensor, Etc.) if they scale the measured values themselves. On the other hand, the $\mathbf{D}$ matrix gives information on the interaction of the measurement system with the input. In the simulation, we use separated models for the in-loop measurements so that the noise, i.e. sensing noises, will be added via these blocks later, see figure 5.1.

From the above example, we see that the state vector helps to transform a differential equation of order 2 into two differential equations of order 1. Indeed, the state vector is constructed such that the dynamical differential equation of n order governing the system could then be written as n differential equation of order 1. Hence, they are easier to program in a simulator [122].

Back to our LISA dynamics equations, we can construct a state vector from dynamical variables as follows:

$$\vec{\mathbf{x}}(t) = \begin{bmatrix} \vec{\mathbf{r}}_{B/\mathcal{O}}^{\,\mathcal{O}} \\ \vec{\alpha}_{\mathcal{B}/\mathcal{O}} \\ \dot{\vec{\mathbf{r}}}_{B/\mathcal{O}}^{\,\mathcal{O}} \\ \vec{\omega}_{\mathcal{B}/\mathcal{O}}^{\,\mathcal{B}} \end{bmatrix} \oplus \begin{bmatrix} \vec{\mathbf{r}}_{T_1/\mathcal{H}_1}^{\,\mathcal{H}_1} \\ \vec{\alpha}_{\mathcal{T}_1/\mathcal{H}_1} \\ \vec{\mathbf{r}}_{T_2/\mathcal{H}_2}^{\,\mathcal{H}_2} \\ \vec{\alpha}_{\mathcal{T}_2/\mathcal{H}_2} \end{bmatrix} \oplus \begin{bmatrix} \dot{\vec{\mathbf{r}}}_{T_1/\mathcal{H}_1}^{\,\mathcal{H}_1} \\ \vec{\omega}_{T_1/\mathcal{H}_1}^{\,\mathcal{T}_1} \\ \dot{\vec{\mathbf{r}}}_{T_2/\mathcal{H}_2}^{\,\mathcal{H}_2} \\ \vec{\omega}_{T_2/\mathcal{H}_2}^{\,\mathcal{T}_2}, \end{bmatrix} \tag{5.46}$$

where we have used operator $\oplus$ for appending column matrices to have final matrix of 36x1 dimension. We define the dynamical variables contained in the state vector as follows

- $\vec{\mathbf{r}}_{X/\mathcal{A}}^{\,\mathcal{B}}$: longitudinal position vector of object X in the preferable reference frame $\mathcal{A}$, expressed in reference frame $\mathcal{B}$ in the equation of motion.

- $\vec{\alpha}_{\mathcal{A}/\mathcal{B}} \equiv \alpha_{\mathcal{A}/\mathcal{B}}^{\mathcal{B}}$: angular position or attitude vector of the object A attached in its body reference frame $\mathcal{A}$ w.r.t. reference frame $\mathcal{B}$, always expressed in preferable reference frame $\mathcal{B}$, so we omitted the upper index.

- $\dot{\vec{\mathbf{r}}}_{X/\mathcal{A}}^{\,\mathcal{B}}$: longitudinal velocity vector of object X in the preferable reference frame $\mathcal{A}$, expressed in reference frame $\mathcal{B}$ in the equation of motion.

- $\vec{\omega}_{\mathcal{A}/\mathcal{B}}^{\,\mathcal{C}}$: angular velocity vector of the object A attached in its body reference frame $\mathcal{A}$ w.r.t reference frame $\mathcal{B}$, expressed in reference frame $\mathcal{C}$. According to our notation of the attitude vector $\vec{\alpha}_{\mathcal{A}/\mathcal{B}}$ above, one can deduce a useful expression:

  $$\vec{\omega}_{\mathcal{A}/\mathcal{B}}^{\,\mathcal{B}} = \dot{\vec{\alpha}}_{\mathcal{A}/\mathcal{B}}, \tag{5.47}$$

  which is valid only for small $\vec{\alpha}_{\mathcal{A}/\mathcal{B}}$ angles. The attitudes attributed to the state vector correspond to the small jitter rotation motion around working points, so this assumption is well established.

Hence, our state vector has 12 vectorial variables or 36 dynamical variables. Meanwhile, the input vector is defined as

$$\vec{\mathbf{u}}(t) = \begin{bmatrix} \vec{\mathbf{f}}_B^{\,\mathcal{O}} \\ \vec{\mathbf{t}}_B^{\,\mathcal{O}} \end{bmatrix} \oplus \begin{bmatrix} \vec{\mathbf{f}}_{T_1}^{\,\mathcal{H}_1} \\ \vec{\mathbf{t}}_{T_1}^{\,\mathcal{H}_1} \\ \vec{\mathbf{f}}_{T_2}^{\,\mathcal{H}_2} \\ \vec{\mathbf{t}}_{T_2}^{\,\mathcal{H}_2} \end{bmatrix} \oplus \begin{bmatrix} \vec{\mathbf{fr}}_{T_1}^{\,\mathcal{H}_1} \\ \vec{\mathbf{tr}}_{T_1}^{\,\mathcal{H}_1} \\ \vec{\mathbf{fr}}_{T_2}^{\,\mathcal{H}_2} \\ \vec{\mathbf{tr}}_{T_2}^{\,\mathcal{H}_2} \end{bmatrix}, \tag{5.48}$$

where the force and torque acting on the spacecraft are respectively $\vec{\mathbf{f}}_B^{\,\mathcal{O}}$, $\vec{\mathbf{t}}_B^{\,\mathcal{O}}$. It is similar to the ones acting on each test-mass inside the spacecraft, which corresponds to the second matrix term. The last matrix term contains the recoil forces $\vec{\mathbf{fr}}_T^{\,\mathcal{H}}$ and recoil torques $\vec{\mathbf{tr}}_T^{\,\mathcal{H}}$ of

the spacecraft acting on the test-masses, which is considered as the non-inertial forces when we examine the equation of motion in the test-mass frames (non-inertial).

In our study, we modify the state equations, (5.42), (5.43) to be:

$$\mathbf{M}\left(t,\vec{\mathbf{x}}\right)\dot{\vec{\mathbf{x}}}(t) = \mathbf{A}\left(t,\vec{\mathbf{x}}\right)\vec{\mathbf{x}}(t)+\mathbf{B}\left(t,\vec{\mathbf{x}}\right)\vec{\mathbf{u}}(t) \tag{5.49}$$

$$\vec{\mathbf{y}}(t) = \mathbf{C}\left(t,\vec{\mathbf{x}}\right)\vec{\mathbf{x}}(t)+\mathbf{D}\left(t,\vec{\mathbf{x}}\right)\vec{\mathbf{u}}(t), \tag{5.50}$$

where we add the $\mathbf{M}$ matrix due to the complexity of our equations of motion. These equations could return to the original state equations as:

$$\dot{\vec{\mathbf{x}}}(t) = \mathbf{M^{-1}}\left(t,\vec{\mathbf{x}}\right)\mathbf{A}\left(t,\vec{\mathbf{x}}\right)\vec{\mathbf{x}}(t)+\mathbf{M^{-1}}\left(t,\vec{\mathbf{x}}\right)\mathbf{B}\left(t,\vec{\mathbf{x}}\right)\mathbf{M}\left(t,\vec{\mathbf{x}}\right)\vec{\mathbf{u}}(t) \tag{5.51}$$

$$\vec{\mathbf{y}}(t) = \mathbf{C}\left(t,\vec{\mathbf{x}}\right)\vec{\mathbf{x}}(t)+\mathbf{D}\left(t,\vec{\mathbf{x}}\right)\vec{\mathbf{u}}(t). \tag{5.52}$$

Interestingly, we also add the arguments time and state vector for the matrices $\mathbf{M},\mathbf{A},\mathbf{B},\mathbf{C},\mathbf{D}$, so that we can even describe a non-linear and time-varying dynamical system.

Then the equations (5.38), (5.39), (5.40), (5.41) are compactly expressed by following matrix equation:

$$\mathbf{M}\left(t,\vec{\mathbf{x}}\right)\begin{bmatrix}\dot{\vec{\mathbf{r}}}^{\,\mathcal{O}}_{\mathcal{B}/\mathcal{O}}\\ \vec{\omega}^{\,\mathcal{O}}_{B/\mathcal{O}}\\ \ddot{\vec{\mathbf{r}}}^{\,\mathcal{O}}_{\mathcal{B}/\mathcal{O}}\\ \dot{\vec{\omega}}^{\,\mathcal{B}}_{B/\mathcal{O}}\\ \dot{\vec{\mathbf{r}}}^{\,\mathcal{H}_1}_{T_1/\mathcal{H}_1}\\ \vec{\omega}^{\,\mathcal{H}_1}_{T_1/\mathcal{H}_1}\\ \dot{\vec{\mathbf{r}}}^{\,\mathcal{H}_2}_{T_2/\mathcal{H}_2}\\ \vec{\omega}^{\,\mathcal{H}_2}_{T_2/\mathcal{H}_2}\\ \ddot{\vec{\mathbf{r}}}^{\,\mathcal{H}_1}_{T_1/\mathcal{H}_1}\\ \dot{\vec{\omega}}^{\,\mathcal{T}_1}_{T_1/\mathcal{H}_1}\\ \ddot{\vec{\mathbf{r}}}^{\,\mathcal{H}_2}_{T_2/\mathcal{H}_2}\\ \dot{\vec{\omega}}^{\,\mathcal{T}_2}_{T_2/\mathcal{H}_2}\end{bmatrix} = \mathbf{A}\left(t,\vec{\mathbf{x}}\right)\begin{bmatrix}\vec{\mathbf{r}}^{\,\mathcal{O}}_{\mathcal{B}/\mathcal{O}}\\ \vec{\alpha}^{\,\mathcal{O}}_{\mathcal{B}/\mathcal{O}}\\ \dot{\vec{\mathbf{r}}}^{\,\mathcal{O}}_{\mathcal{B}/\mathcal{O}}\\ \vec{\omega}^{\,\mathcal{B}}_{\mathcal{B}/\mathcal{O}}\\ \vec{\mathbf{r}}^{\,\mathcal{H}_1}_{T_1/\mathcal{H}_1}\\ \vec{\alpha}^{\,\mathcal{H}_1}_{T_1/\mathcal{H}_1}\\ \vec{\mathbf{r}}^{\,\mathcal{H}_2}_{T_2/\mathcal{H}_2}\\ \vec{\alpha}^{\,\mathcal{H}_2}_{T_2/\mathcal{H}_2}\\ \dot{\vec{\mathbf{r}}}^{\,\mathcal{H}_1}_{T_1/\mathcal{H}_1}\\ \vec{\omega}^{\,\mathcal{T}_1}_{T_1/\mathcal{H}_1}\\ \dot{\vec{\mathbf{r}}}^{\,\mathcal{H}_2}_{T_2/\mathcal{H}_2}\\ \vec{\omega}^{\,\mathcal{T}_2}_{T_2/\mathcal{H}_2}\end{bmatrix} + \mathbf{B}\left(t,\vec{\mathbf{x}}\right)\begin{bmatrix}\vec{\mathbf{f}}^{\,\mathcal{O}}_{B}\\ \vec{\mathbf{t}}^{\,\mathcal{O}}_{B}\\ \vec{\mathbf{f}}^{\,\mathcal{H}_1}_{T_1}\\ \vec{\mathbf{t}}^{\,\mathcal{H}_1}_{T_1}\\ \vec{\mathbf{f}}^{\,\mathcal{H}_2}_{T_2}\\ \vec{\mathbf{t}}^{\,\mathcal{H}_2}_{T_2}\\ \vec{\mathbf{fr}}^{\,\mathcal{H}_1}_{T_1}\\ \vec{\mathbf{tr}}^{\,\mathcal{H}_1}_{T_1}\\ \vec{\mathbf{fr}}^{\,\mathcal{H}_2}_{T_2}\\ \vec{\mathbf{tr}}^{\,\mathcal{H}_2}_{T_2}\end{bmatrix}. \tag{5.53}$$

The $\mathbf{M}\left(t,\vec{\mathbf{x}}\right),\mathbf{A}\left(t,\vec{\mathbf{x}}\right),\mathbf{B}\left(t,\vec{\mathbf{x}}\right)$ are lengthy, so we use some short notations for zero-matrix and identity matrix, respectively,

$$O_3 = \begin{pmatrix}0&0&0\\0&0&0\\0&0&0\end{pmatrix}, \qquad I_3 = \begin{pmatrix}1&0&0\\0&1&0\\0&0&1\end{pmatrix}, \tag{5.54}$$

and also write non-zero components implicitly as follows:

$$\mathbf{A}\left(t,\vec{\mathbf{x}}\right)=\begin{pmatrix} O_3 & O_3 & A_{1,3} & O_3 & O_3 & O_3 & O_3 & O_3 & O_3 & O_3 & O_3 & O_3 \\ O_3 & O_3 & O_3 & O_3 & A_{2,4} & O_3 & O_3 & O_3 & O_3 & O_3 & O_3 & O_3 \\ A_{3,1} & O_3 & O_3 & O_3 & O_3 & O_3 & O_3 & O_3 & O_3 & O_3 & O_3 & O_3 \\ O_3 & O_3 & O_3 & O_3 & O_3 & O_3 & O_3 & O_3 & O_3 & O_3 & O_3 & O_3 \\ O_3 & O_3 & O_3 & O_3 & O_3 & O_3 & O_3 & O_3 & A_{5,9} & O_3 & O_3 & O_3 \\ O_3 & O_3 & O_3 & O_3 & O_3 & O_3 & O_3 & O_3 & O_3 & A_{6,10} & O_3 & O_3 \\ O_3 & O_3 & O_3 & O_3 & O_3 & O_3 & O_3 & O_3 & O_3 & O_3 & A_{7,11} & O_3 \\ O_3 & O_3 & O_3 & O_3 & O_3 & O_3 & O_3 & O_3 & O_3 & O_3 & O_3 & A_{8,12} \\ O_3 & O_3 & O_3 & O_3 & A_{9,5} & O_3 & O_3 & O_3 & O_3 & O_3 & O_3 & O_3 \\ O_3 & O_3 & O_3 & O_3 & O_3 & O_3 & O_3 & O_3 & O_3 & O_3 & O_3 & O_3 \\ O_3 & O_3 & O_3 & O_3 & O_3 & O_3 & A_{11,7} & O_3 & O_3 & O_3 & O_3 & O_3 \\ O_3 & O_3 & O_3 & O_3 & O_3 & O_3 & O_3 & O_3 & O_3 & O_3 & O_3 & O_3 \end{pmatrix}, \tag{5.55}$$

where

$$A_{1,3}=A_{2,4}=I_3 \tag{5.56}$$

$$A_{3,1}=-m_{\text{sc}}\left(\left[\dot{\vec{\omega}}_{O/\mathcal{J}}^{\,\mathcal{O}}\right]^{\times}+\left[\vec{\omega}_{O/\mathcal{J}}^{\,\mathcal{O}}\right]^{\times}\left[\vec{\omega}_{O/\mathcal{J}}^{\,\mathcal{O}}\right]^{\times}\right) \tag{5.57}$$

$$A_{5,9}=A_{6,10}=A_{7,11}=A_{8,12}=I_3 \tag{5.58}$$

$$\begin{aligned} A_{9,5}=-m_{\text{tm}_1}\Bigg(&\left[T_{\mathcal{B}}^{\mathcal{H}_1}T_{\mathcal{O}}^{\mathcal{B}}\dot{\vec{\omega}}_{\mathcal{O}/\mathcal{J}}^{\,\mathcal{O}}\right]^{\times}+\left[T_{\mathcal{B}}^{\mathcal{H}_1}\vec{\omega}_{\mathcal{B}/\mathcal{O}}^{\,\mathcal{B}}\right]^{\times}\left[T_{\mathcal{B}}^{\mathcal{H}_1}\vec{\omega}_{\mathcal{B}/\mathcal{O}}^{\,\mathcal{B}}\right]^{\times} \\ &+\left[T_{\mathcal{B}}^{\mathcal{H}_1}T_{\mathcal{O}}^{\mathcal{B}}\vec{\omega}_{O/\mathcal{J}}^{\,\mathcal{O}}\right]^{\times}\left[T_{\mathcal{B}}^{\mathcal{H}_1}T_{\mathcal{O}}^{\mathcal{B}}\vec{\omega}_{O/\mathcal{J}}^{\,\mathcal{O}}\right]^{\times}+2\left[T_{\mathcal{B}}^{\mathcal{H}_1}T_{\mathcal{O}}^{\mathcal{B}}\vec{\omega}_{O/\mathcal{J}}^{\,\mathcal{O}}\right]^{\times}\left[T_{\mathcal{B}}^{\mathcal{H}_1}\vec{\omega}_{\mathcal{B}/\mathcal{O}}^{\,\mathcal{B}}\right]^{\times}\Bigg) \end{aligned} \tag{5.59}$$

$$\begin{aligned} A_{11,7}=-m_{\text{tm}_2}\Bigg(&\left[T_{\mathcal{B}}^{\mathcal{H}_2}T_{\mathcal{O}}^{\mathcal{B}}\dot{\vec{\omega}}_{\mathcal{O}/\mathcal{J}}^{\,\mathcal{O}}\right]^{\times}+\left[T_{\mathcal{B}}^{\mathcal{H}_2}\vec{\omega}_{\mathcal{B}/\mathcal{O}}^{\,\mathcal{B}}\right]^{\times}\left[T_{\mathcal{B}}^{\mathcal{H}_2}\vec{\omega}_{\mathcal{B}/\mathcal{O}}^{\,\mathcal{B}}\right]^{\times} \\ &+\left[T_{\mathcal{B}}^{\mathcal{H}_2}T_{\mathcal{O}}^{\mathcal{B}}\vec{\omega}_{O/\mathcal{J}}^{\,\mathcal{O}}\right]^{\times}\left[T_{\mathcal{B}}^{\mathcal{H}_2}T_{\mathcal{O}}^{\mathcal{B}}\vec{\omega}_{O/\mathcal{J}}^{\,\mathcal{O}}\right]^{\times}+2\left[T_{\mathcal{B}}^{\mathcal{H}_2}T_{\mathcal{O}}^{\mathcal{B}}\vec{\omega}_{O/\mathcal{J}}^{\,\mathcal{O}}\right]^{\times}\left[T_{\mathcal{B}}^{\mathcal{H}_2}\vec{\omega}_{\mathcal{B}/\mathcal{O}}^{\,\mathcal{B}}\right]^{\times}\Bigg). \end{aligned} \tag{5.60}$$

$$\mathbf{M}\left(t,\vec{\mathbf{x}}\right)=\begin{pmatrix} M_{1,1} & O_3 & O_3 & O_3 & O_3 & O_3 & O_3 & O_3 & O_3 & O_3 & O_3 & O_3 \\ O_3 & M_{2,2} & O_3 & O_3 & O_3 & O_3 & O_3 & O_3 & O_3 & O_3 & O_3 & O_3 \\ M_{3,1} & O_3 & M_{3,3} & O_3 & O_3 & O_3 & O_3 & O_3 & O_3 & O_3 & O_3 & O_3 \\ O_3 & M_{4,2} & O_3 & M_{4,4} & O_3 & O_3 & O_3 & O_3 & O_3 & O_3 & O_3 & O_3 \\ O_3 & O_3 & O_3 & O_3 & M_{5,5} & O_3 & O_3 & O_3 & M_{5,9} & O_3 & O_3 & O_3 \\ O_3 & O_3 & O_3 & O_3 & O_3 & M_{6,6} & O_3 & O_3 & O_3 & O_3 & O_3 & O_3 \\ O_3 & O_3 & O_3 & O_3 & O_3 & O_3 & M_{7,7} & O_3 & O_3 & O_3 & M_{7,11} & O_3 \\ O_3 & O_3 & O_3 & O_3 & O_3 & O_3 & O_3 & M_{8,8} & O_3 & O_3 & O_3 & O_3 \\ O_3 & M_{9,2} & O_3 & M_{9,4} & M_{9,5} & O_3 & O_3 & O_3 & M_{9,9} & O_3 & O_3 & O_3 \\ O_3 & M_{10,2} & O_3 & M_{10,4} & O_3 & M_{10,6} & O_3 & O_3 & O_3 & M_{10,10} & O_3 & O_3 \\ O_3 & M_{11,2} & O_3 & M_{11,4} & O_3 & O_3 & M_{11,7} & O_3 & O_3 & O_3 & M_{11,11} & O_3 \\ O_3 & M_{12,2} & O_3 & M_{12,4} & O_3 & O_3 & O_3 & M_{12,8} & O_3 & O_3 & O_3 & M_{12,12} \end{pmatrix}, \tag{5.61}$$

where

$$M_{1,1}=I_3 \tag{5.62}$$

$$M_{2,2}=T_{\mathcal{O}}^{\mathcal{B}} \tag{5.63}$$

$$M_{3,1}=2m_{\text{sc}}\left[\vec{\omega}_{O/\mathcal{J}}^{\,\mathcal{O}}\right]^{\times} \tag{5.64}$$

$$M_{3,3}=m_{\text{sc}}I_3 \tag{5.65}$$

$$M_{4,2}=\left\{\left(\left[\vec{\omega}_{\mathcal{B}/\mathcal{O}}^{\,\mathcal{B}}\right]^{\times}+\left[T_{\mathcal{O}}^{\mathcal{B}}\vec{\omega}_{O/\mathcal{J}}^{\,\mathcal{O}}\right]^{\times}\right)\mathbf{I}_{\text{sc}/B}^{\mathcal{B}}+\mathbf{I}_{\text{sc}/B}^{\mathcal{B}}\left[T_{\mathcal{O}}^{\mathcal{B}}\vec{\omega}_{O/\mathcal{J}}^{\,\mathcal{O}}\right]^{\times}-\left[\mathbf{I}_{\text{sc}/B}^{\mathcal{B}}T_{\mathcal{O}}^{\mathcal{B}}\vec{\omega}_{O/\mathcal{J}}^{\,\mathcal{O}}\right]^{\times}\right\}T_{\mathcal{O}}^{\mathcal{B}} \tag{5.66}$$

$$M_{4,4}=\mathbf{I}_{\text{sc}/B}^{\mathcal{B}} \tag{5.67}$$

$$M_{5,5}=I_3 \tag{5.68}$$

$$M_{6,6}=T_{\mathcal{T}_1}^{\mathcal{H}_1} \tag{5.69}$$

$$M_{7,7}=I_3 \tag{5.70}$$

$$M_{8,8}=T_{\mathcal{T}_2}^{\mathcal{H}_2} \tag{5.71}$$

$$M_{9,2} = -m_{\text{tm}_1}\left(\left[T_{\mathcal{B}}^{\mathcal{H}_1}\vec{\omega}_{\mathcal{B}/\mathcal{O}}^{\ \mathcal{B}}\right]^{\times}\left[T_{\mathcal{B}}^{\mathcal{H}_1}\vec{\mathbf{r}}_{H_1/\mathcal{B}}^{\mathcal{B}}\right]^{\times} + 2\left[T_{\mathcal{B}}^{\mathcal{H}_1}T_{\mathcal{O}}^{\mathcal{B}}\vec{\omega}_{O/\mathcal{J}}^{\ \mathcal{O}}\right]^{\times}\left[T_{\mathcal{B}}^{\mathcal{H}_1}\vec{\mathbf{r}}_{H_1/\mathcal{B}}^{\mathcal{B}}\right]^{\times}\right)T_{\mathcal{B}}^{\mathcal{H}_1}T_{\mathcal{O}}^{\mathcal{B}} \tag{5.72}$$

$$M_{9,4} = -m_{\text{tm}_1}\left[\vec{\mathbf{r}}_{T_1/\mathcal{H}_1}^{\ \mathcal{H}_1} + T_{\mathcal{B}}^{\mathcal{H}_1}\vec{\mathbf{r}}_{H_1/\mathcal{B}}^{\mathcal{B}}\right]^{\times}T_{\mathcal{B}}^{\mathcal{H}_1} \tag{5.73}$$

$$M_{9,5} = 2m_{\text{tm}_1}\left[T_{\mathcal{B}}^{\mathcal{H}_1}\vec{\omega}_{\mathcal{B}/\mathcal{O}}^{\ \mathcal{B}} + T_{\mathcal{B}}^{\mathcal{H}_1}T_{\mathcal{O}}^{\mathcal{B}}\vec{\omega}_{O/\mathcal{J}}^{\ \mathcal{O}}\right]^{\times} \tag{5.74}$$

$$M_{9,9} = m_{\text{tm}_1}I_3 \tag{5.75}$$

$$\begin{aligned}M_{10,2} = &\left\{\mathbf{I}_{\text{tm}_1/T_1}^{\mathcal{T}_1}\left[T_{\mathcal{H}_1}^{\mathcal{T}_1}T_{\mathcal{B}}^{\mathcal{H}_1}T_{\mathcal{O}}^{\mathcal{B}}\vec{\omega}_{O/\mathcal{J}}^{\ \mathcal{O}}\right]^{\times}\right.\\ &\left.+\left(\left[\vec{\omega}_{T_1/\mathcal{H}_1}^{\ \mathcal{T}_1}\right]^{\times} + \left[T_{\mathcal{H}_1}^{\mathcal{T}_1}T_{\mathcal{B}}^{\mathcal{H}_1}\vec{\omega}_{\mathcal{B}/\mathcal{O}}^{\ \mathcal{B}}\right]^{\times} + \left[T_{\mathcal{H}_1}^{\mathcal{T}_1}T_{\mathcal{B}}^{\mathcal{H}_1}T_{\mathcal{O}}^{\mathcal{B}}\vec{\omega}_{O/\mathcal{J}}^{\ \mathcal{O}}\right]^{\times}\right)\mathbf{I}_{\text{tm}_1/T_1}^{\mathcal{T}_1}\right\}T_{\mathcal{H}_1}^{\mathcal{T}_1}T_{\mathcal{B}}^{\mathcal{H}_1}T_{\mathcal{O}}^{\mathcal{B}}\end{aligned} \tag{5.76}$$

$$M_{10,4} = \mathbf{I}_{\text{tm}_1/T_1}^{\mathcal{T}_1} \tag{5.77}$$

$$\begin{aligned}M_{10,6} = &\left\{\left(\left[\vec{\omega}_{T_1/\mathcal{H}_1}^{\ \mathcal{T}_1}\right]^{\times} + \left[T_{\mathcal{H}_1}^{\mathcal{T}_1}T_{\mathcal{B}}^{\mathcal{H}_1}\vec{\omega}_{\mathcal{B}/\mathcal{O}}^{\ \mathcal{B}}\right]^{\times}\right)\mathbf{I}_{\text{tm}_1/T_1}^{\mathcal{T}_1}\right.\\ &\left.+\mathbf{I}_{\text{tm}_1/T_1}^{\mathcal{T}_1}\left(\left[T_{\mathcal{H}_1}^{\mathcal{T}_1}T_{\mathcal{B}}^{\mathcal{H}_1}\vec{\omega}_{\mathcal{B}/\mathcal{O}}^{\ \mathcal{B}}\right]^{\times} + \left[T_{\mathcal{H}_1}^{\mathcal{T}_1}T_{\mathcal{B}}^{\mathcal{H}_1}T_{\mathcal{O}}^{\mathcal{B}}\vec{\omega}_{O/\mathcal{J}}^{\ \mathcal{O}}\right]^{\times}\right)\right\}T_{\mathcal{H}_1}^{\mathcal{T}_1}\end{aligned} \tag{5.78}$$

$$M_{10,10} = \mathbf{I}_{\text{tm}_1/T_1}^{\mathcal{T}_1} \tag{5.79}$$

$$M_{11,2} = -m_{\text{tm}_2}\left(\left[T_{\mathcal{B}}^{\mathcal{H}_2}\vec{\omega}_{\mathcal{B}/\mathcal{O}}^{\ \mathcal{B}}\right]^{\times}\left[\vec{\mathbf{r}}_{\mathcal{H}_2/\mathcal{B}}^{\mathcal{H}_2}\right]^{\times} + 2\left[T_{\mathcal{B}}^{\mathcal{H}_2}T_{\mathcal{O}}^{\mathcal{B}}\vec{\omega}_{O/\mathcal{J}}^{\ \mathcal{O}}\right]^{\times}\left[T_{\mathcal{B}}^{\mathcal{H}_2}\vec{\mathbf{r}}_{H_2/\mathcal{B}}^{\mathcal{B}}\right]^{\times}\right)T_{\mathcal{B}}^{\mathcal{H}_2}T_{\mathcal{O}}^{\mathcal{B}} \tag{5.80}$$

$$M_{11,4} = -m_{\text{tm}_2}\left[\vec{\mathbf{r}}_{T_2/\mathcal{H}_2}^{\ \mathcal{H}_2} + \vec{\mathbf{r}}_{\mathcal{H}_2/\mathcal{B}}^{\mathcal{H}_2}\right]^{\times}T_{\mathcal{B}}^{\mathcal{H}_2} \tag{5.81}$$

$$M_{11,7} = 2m_{\text{tm}_2}\left[T_{\mathcal{B}}^{\mathcal{H}_2}\vec{\omega}_{\mathcal{B}/\mathcal{O}}^{\ \mathcal{B}} + T_{\mathcal{B}}^{\mathcal{H}_2}T_{\mathcal{O}}^{\mathcal{B}}\vec{\omega}_{O/\mathcal{J}}^{\ \mathcal{O}}\right]^{\times} \tag{5.82}$$

$$M_{11,11} = m_{\text{tm}_2}I_3 \tag{5.83}$$

$$\begin{aligned}M_{12,2} = &\left\{\mathbf{I}_{\text{tm}_2/T_2}^{\mathcal{T}_2}\left[T_{\mathcal{H}_2}^{\mathcal{T}_2}T_{\mathcal{B}}^{\mathcal{H}_2}T_{\mathcal{O}}^{\mathcal{B}}\vec{\omega}_{O/\mathcal{J}}^{\ \mathcal{O}}\right]^{\times}\right.\\ &\left.+\left(\left[\vec{\omega}_{T_2/\mathcal{H}_2}^{\ \mathcal{T}_2}\right]^{\times} + \left[T_{\mathcal{H}_2}^{\mathcal{T}_2}T_{\mathcal{B}}^{\mathcal{H}_2}\vec{\omega}_{\mathcal{B}/\mathcal{O}}^{\ \mathcal{B}}\right]^{\times} + \left[T_{\mathcal{H}_2}^{\mathcal{T}_2}T_{\mathcal{B}}^{\mathcal{H}_2}T_{\mathcal{O}}^{\mathcal{B}}\vec{\omega}_{O/\mathcal{J}}^{\ \mathcal{O}}\right]^{\times}\right)\mathbf{I}_{\text{tm}_2/T_2}^{\mathcal{T}_2}\right\}T_{\mathcal{H}_2}^{\mathcal{T}_2}T_{\mathcal{B}}^{\mathcal{H}_2}T_{\mathcal{O}}^{\mathcal{B}}\end{aligned} \tag{5.84}$$

$$M_{12,4} = \mathbf{I}_{\text{tm}_2/T_2}^{\mathcal{T}_2} \tag{5.85}$$

$$\begin{aligned}M_{12,8} = &\left\{\left(\left[\vec{\omega}_{T_2/\mathcal{H}_2}^{\ \mathcal{T}_2}\right]^{\times} + \left[T_{\mathcal{H}_2}^{\mathcal{T}_2}T_{\mathcal{B}}^{\mathcal{H}_2}\vec{\omega}_{\mathcal{B}/\mathcal{O}}^{\ \mathcal{B}}\right]^{\times}\right)\mathbf{I}_{\text{tm}_2/T_2}^{\mathcal{T}_2}\right.\\ &\left.+\mathbf{I}_{\text{tm}_2/T_2}^{\mathcal{T}_2}\left(\left[T_{\mathcal{H}_2}^{\mathcal{T}_2}T_{\mathcal{B}}^{\mathcal{H}_2}\vec{\omega}_{\mathcal{B}/\mathcal{O}}^{\ \mathcal{B}}\right]^{\times} + \left[T_{\mathcal{H}_2}^{\mathcal{T}_2}T_{\mathcal{B}}^{\mathcal{H}_2}T_{\mathcal{O}}^{\mathcal{B}}\vec{\omega}_{O/\mathcal{J}}^{\ \mathcal{O}}\right]^{\times}\right)\right\}T_{\mathcal{H}_2}^{\mathcal{T}_2}\end{aligned} \tag{5.86}$$

$$M_{12,12} = \mathbf{I}_{\text{tm}_2/T_2}^{\mathcal{T}_2}. \tag{5.87}$$

$$\mathbf{B}\left(t,\vec{\mathbf{x}}\right)=\begin{pmatrix} O_3 & O_3 & O_3 & O_3 & O_3 & O_3 & O_3 & O_3 & O_3 & O_3 \\ O_3 & O_3 & O_3 & O_3 & O_3 & O_3 & O_3 & O_3 & O_3 & O_3 \\ B_{3,1} & O_3 & O_3 & O_3 & O_3 & O_3 & B_{3,7} & O_3 & B_{3,9} & O_3 \\ O_3 & B_{4,2} & O_3 & O_3 & O_3 & O_3 & B_{4,7} & B_{4,8} & B_{4,9} & B_{4,10} \\ O_3 & O_3 & O_3 & O_3 & O_3 & O_3 & O_3 & O_3 & O_3 & O_3 \\ O_3 & O_3 & O_3 & O_3 & O_3 & O_3 & O_3 & O_3 & O_3 & O_3 \\ O_3 & O_3 & O_3 & O_3 & O_3 & O_3 & O_3 & O_3 & O_3 & O_3 \\ O_3 & O_3 & O_3 & O_3 & O_3 & O_3 & O_3 & O_3 & O_3 & O_3 \\ B_{9,1} & O_3 & B_{9,3} & O_3 & O_3 & O_3 & B_{9,7} & O_3 & O_3 & O_3 \\ O_3 & O_3 & O_3 & B_{10,4} & O_3 & O_3 & O_3 & B_{10,8} & O_3 & O_3 \\ B_{11,1} & O_3 & O_3 & O_3 & B_{11,5} & O_3 & O_3 & O_3 & B_{11,9} & O_3 \\ O_3 & O_3 & O_3 & O_3 & O_3 & B_{12,6} & O_3 & O_3 & O_3 & B_{12,10} \end{pmatrix}, \quad (5.88)$$

where

$$\begin{array}{llll} B_{3,1}=I_3 & B_{4,2}=T^{\mathcal{B}}_{\mathcal{O}} & B_{9,1}=-\dfrac{m_{\mathrm{tm}_1}}{m_{\mathrm{sc}}}T^{\mathcal{H}_1}_{\mathcal{B}}T^{\mathcal{B}}_{\mathcal{O}} & B_{11,1}=-\dfrac{m_{\mathrm{tm}_2}}{m_{\mathrm{sc}}}T^{\mathcal{H}_2}_{\mathcal{B}}T^{\mathcal{B}}_{\mathcal{O}} \\ B_{3,7}=-T^{\mathcal{O}}_{\mathcal{B}}T^{\mathcal{B}}_{\mathcal{H}_1}, & B_{4,7}=-\left[\vec{\mathbf{r}}^{\mathcal{B}}_{H_1/\mathcal{B}}\right]^{\times}T^{\mathcal{B}}_{\mathcal{H}_1} & B_{9,3}=I_3 & B_{11,5}=I_3 \\ B_{3,9}=-T^{\mathcal{O}}_{\mathcal{B}}T^{\mathcal{B}}_{\mathcal{H}_2} & B_{4,8}=-T^{\mathcal{B}}_{\mathcal{H}_1} & B_{9,7}=I_3 & B_{11,9}=I_3 \\ & B_{4,9}=-\left[\vec{\mathbf{r}}^{\mathcal{B}}_{\mathcal{H}_2/\mathcal{B}}\right]^{\times}T^{\mathcal{B}}_{\mathcal{H}_2} & B_{10,4}=T^{\mathcal{T}_1}_{\mathcal{H}_1} & B_{12,6}=T^{\mathcal{T}_2}_{\mathcal{H}_2} \\ & B_{4,10}=-T^{\mathcal{B}}_{\mathcal{H}_2} & B_{10,8}=T^{\mathcal{T}_1}_{\mathcal{H}_1} & B_{12,10}=T^{\mathcal{T}_2}_{\mathcal{H}_2} \end{array}. \quad (5.89)$$

The dimensions of the matrices presented above are 36x36 for $\mathbf{A},\mathbf{M}$ matrices, and 36x30 for $\mathbf{B}$ matrix. We see that some elements of the matrix $\mathbf{A},\mathbf{B},\mathbf{M}$ involve some dynamical variables of the state vector, which are colored in red, so they attribute to non-linear terms in the equations of motion. We note that the rotation matrices $T^{\mathcal{B}}_{\mathcal{O}}=T^{\mathcal{B}}_{\mathcal{O}}(\vec{\alpha}_{\mathcal{B}/\mathcal{O}})$, $T^{\mathcal{T}_i}_{\mathcal{H}_i}=T^{\mathcal{T}_i}_{\mathcal{H}_i}\left(\vec{\alpha}_{\mathcal{T}_i/\mathcal{H}_i}\right)$, and their transpose are also dynamical-variable dependent. On the other hand, the leftover rotation matrix $T^{\mathcal{H}_i}_{\mathcal{B}}=T^{\mathcal{H}_i}_{\mathcal{B}}(\vec{\alpha}_{\mathcal{H}_i/\mathcal{B}})$ and its transpose depending on the breathing angle of the MOSA i in the $\mathcal{B}$-frame will be the objectives to adapt in the simulation for studying the effect of rotating MOSAs. We will revisit this point later on in the implementation section 5.3.4. Therefore, to linearize the equations, we will use the target values of all dynamic variables in the factor in front of any components of the state vector, which are null values. In other words, dynamical variables are the perturbations around their working points or target values. We can keep only the first order of dynamical variable terms in the equations of motion. The rotation matrices in $\mathbf{A},\mathbf{B},\mathbf{M}$ are identity in this approximation, i.e. $T^{\mathcal{B}}_{\mathcal{O}}=T^{\mathcal{H}_i}_{\mathcal{B}}=I_3$.

Dynamics assumption 3

We keep only the linear terms of the dynamical variables in the equation of motion, assuming they stay very close to their dynamical target values, which is guaranteed by the control-loop of DFACS.

Consequently, we have a new set of equations of motion that describes the linear system. In particular, we evaluate the state matrices M, A, B at the target points $\vec{\mathbf{x}}^{\text{target}}$. In addition, the time-dependent terms in these matrices are computed as the average over the simulation time, which is a good approximation for the simulation time much less than 1 year. The equation (5.49) becomes:

$$\mathbf{M}^{\text{target}}\left(t, \vec{\mathbf{x}}^{\text{target}}\right) \dot{\vec{\mathbf{x}}}(t) = \mathbf{A}^{\text{target}}\left(t, \vec{\mathbf{x}}^{\text{target}}\right) \vec{\mathbf{x}}(t) + \mathbf{B}^{\text{target}}\left(t, \vec{\mathbf{x}}^{\text{target}}\right) \vec{\mathbf{u}}(t). \tag{5.90}$$

For the observation equation (5.50), the matrices are defined as follows:

$$\mathbf{C}\left(t, \vec{\mathbf{x}}\right) = \begin{pmatrix} O_3 & C_{1,2} & O_3 & O_3 & O_3 & O_3 & O_3 & O_3 & O_3 & O_3 & O_3 & O_3 \\ O_3 & O_3 & O_3 & O_3 & C_{2,5} & O_3 & O_3 & O_3 & O_3 & O_3 & O_3 & O_3 \\ O_3 & O_3 & O_3 & O_3 & O_3 & C_{3,6} & O_3 & O_3 & O_3 & O_3 & O_3 & O_3 \\ O_3 & O_3 & O_3 & O_3 & O_3 & O_3 & C_{4,7} & O_3 & O_3 & O_3 & O_3 & O_3 \\ O_3 & O_3 & O_3 & O_3 & O_3 & O_3 & O_3 & C_{5,8} & O_3 & O_3 & O_3 & O_3 \end{pmatrix}, \tag{5.91}$$

$$\mathbf{D}\left(t, \vec{\mathbf{x}}\right) = 0, \tag{5.92}$$

where

$$C_{1,2} = C_{2,5} = C_{3,6} = C_{4,7} = C_{5,8} = I_3. \tag{5.93}$$

Hence, the observation state vector $\vec{\mathbf{y}} = \left(\vec{\alpha}_{\mathcal{B}/\mathcal{O}}, \vec{\mathbf{r}}^{\,\mathcal{H}_1}_{T_1/\mathcal{H}_1}, \vec{\alpha}_{\mathcal{T}_1/\mathcal{H}_1}, \vec{\mathbf{r}}^{\,\mathcal{H}_2}_{T_2/\mathcal{H}_2}, \vec{\alpha}_{\mathcal{T}_2/\mathcal{H}_2}\right)$, which are the quantities observed by the sensors. The sensing noises of the measurement system, which are usually embedded in $\mathbf{D}\left(t, \vec{\mathbf{x}}\right)$, will be modelled separately, so we set it null here.

5.3.3 Implementation

So far, we derive all necessary equations of motion for LISA dynamics and write them in the linearization form in the target reference frames. In this section, we present the implementation of the LISA Dynamics in the `LISANode` simulator.

The idea is to simulate the dynamics of one spacecraft included in the LISA to first check the implementation before connecting it to the full LISA simulation graph *LISA* in `LISANode` (see section 2.8). The first implementation of LISA Dynamics for one spacecraft has been done by H.Inchauspé, O.Sauter, P.Wass and J.B.Bayle [89]. Based on that implementation, we apply some modifications to account for the motion of MOSAs, which we called rotating MOSAs case. The top-level graph of the LISA dynamics implementation in `LISANode` is *ScDynamics*,

which is constructed by $\boxed{LISADyn}$ graph. $\boxed{LISADyn}$ is the instance of the closed-loop system, which is implemented in $\boxed{ClosedLoopSystem}$ graph, with out-of-loop sources such as sensing noise, direct forces and torques, guidances. Some input parameters of this graph are provided from LPF. In addition, the test-mass acceleration noise model built from LPF data attributes to the direct forces applied on the test-mass in the closed-loop system. This noise plays a role of a spurious force which influences the test-mass in LPF mission. We will see in section 5.4 that the relative motion between test-mass and spacecraft is about this noise level if the DFACS works perfectly. The outputs are the in-loop measurements (DWS, IFO sensing, GRS sensing) and the commanded forces and torques of DFACS. $\boxed{ClosedLoopSystem}$ is the assemble of DFACS features, including DWS, GRS and IFO sensing measurements, the Micro-Propulsion System (MPS) and GRS actuation systems. Importantly, the core of this closed-loop system, the equations of motions, has been implemented in the $\boxed{EomMovingMosas}$ or $\boxed{EomFixedMosas}$ graph depending on the considered MOSAs configuration, i.e. fixed or moving. This graph is connected to the total forces and torques blocks, as the inputs $\vec{\mathbf{u}}$ for (5.90), and also to the measurement blocks for feeding the current state-space vector to the DFACS features. The state-space matrices are created outside the graph and used as the fixed parameters. We illustrate the connection of $\boxed{ClosedLoopSystem}$ graph in figure 5.1.

The $\boxed{DFACS}$ graph is built from a Matlab controller developed by H.Inchauspé et al. [90], which is also based on the state space representation for dynamics demonstration.

Since the main work of this thesis focuses on implementing the rotating MOSAs configuration, we would like to analyze the graph of the equation of motion carefully. First, we need to evaluate the matrices $\mathbf{M}^{\text{target}}, \mathbf{A}^{\text{target}}, \mathbf{B}^{\text{target}}, \mathbf{C}, \mathbf{D}$ in the linearized equations of motion (5.90) and (5.50). In our study, the components of these matrices are built time-independently. To promote any term to be time-dependent, one can extract the corresponding contribution from $\boxed{EoM}$ graph, build a suitable node/sub-graph to make it as an external, time-varying term, and then connect that node/sub-graph to the $\boxed{EoM}$ graph. This trick allows us to introduce MOSA rotation while keeping a generally linear, time-invariant framework for the simulation model. The matrix $\mathbf{A}^{\text{target}}$ has the same zero components as the $\mathbf{A}\left(t, \vec{\mathbf{x}}\right)$ in (5.55), with other components showed in the following:

$$A_{1,3} = A_{2,4} = I_3 \tag{5.94}$$

$$A_{3,1} = -m_{\text{sc}} \left(\left[\dot{\vec{\omega}}^{\,\mathcal{O}}_{O/\mathcal{J}} \right]^{\times} + \left[\vec{\omega}^{\,\mathcal{O}}_{O/\mathcal{J}} \right]^{\times} \left[\vec{\omega}^{\,\mathcal{O}}_{O/\mathcal{J}} \right]^{\times} \right) \tag{5.95}$$

$$A_{5,9} = A_{6,10} = A_{7,11} = A_{8,12} = I_3 \tag{5.96}$$

$$A_{9,5} = -m_{\text{tm}_1} \left(\left[T^{\mathcal{H}_1}_{\mathcal{B}} \dot{\vec{\omega}}^{\,\mathcal{O}}_{O/\mathcal{J}} \right]^{\times} + \left[T^{\mathcal{H}_1}_{\mathcal{B}} \vec{\omega}^{\,\mathcal{O}}_{O/\mathcal{J}} \right]^{\times} \left[T^{\mathcal{H}_1}_{\mathcal{B}} \vec{\omega}^{\,\mathcal{O}}_{O/\mathcal{J}} \right]^{\times} \right) \tag{5.97}$$

$$A_{11,7} = -m_{\text{tm}_2} \left(\left[T^{\mathcal{H}_2}_{\mathcal{B}} \dot{\vec{\omega}}^{\,\mathcal{O}}_{O/\mathcal{J}} \right]^{\times} + \left[T^{\mathcal{H}_2}_{\mathcal{B}} \vec{\omega}^{\,\mathcal{O}}_{O/\mathcal{J}} \right]^{\times} \left[T^{\mathcal{H}_2}_{\mathcal{B}} \vec{\omega}^{\,\mathcal{O}}_{O/\mathcal{J}} \right]^{\times} \right). \tag{5.98}$$

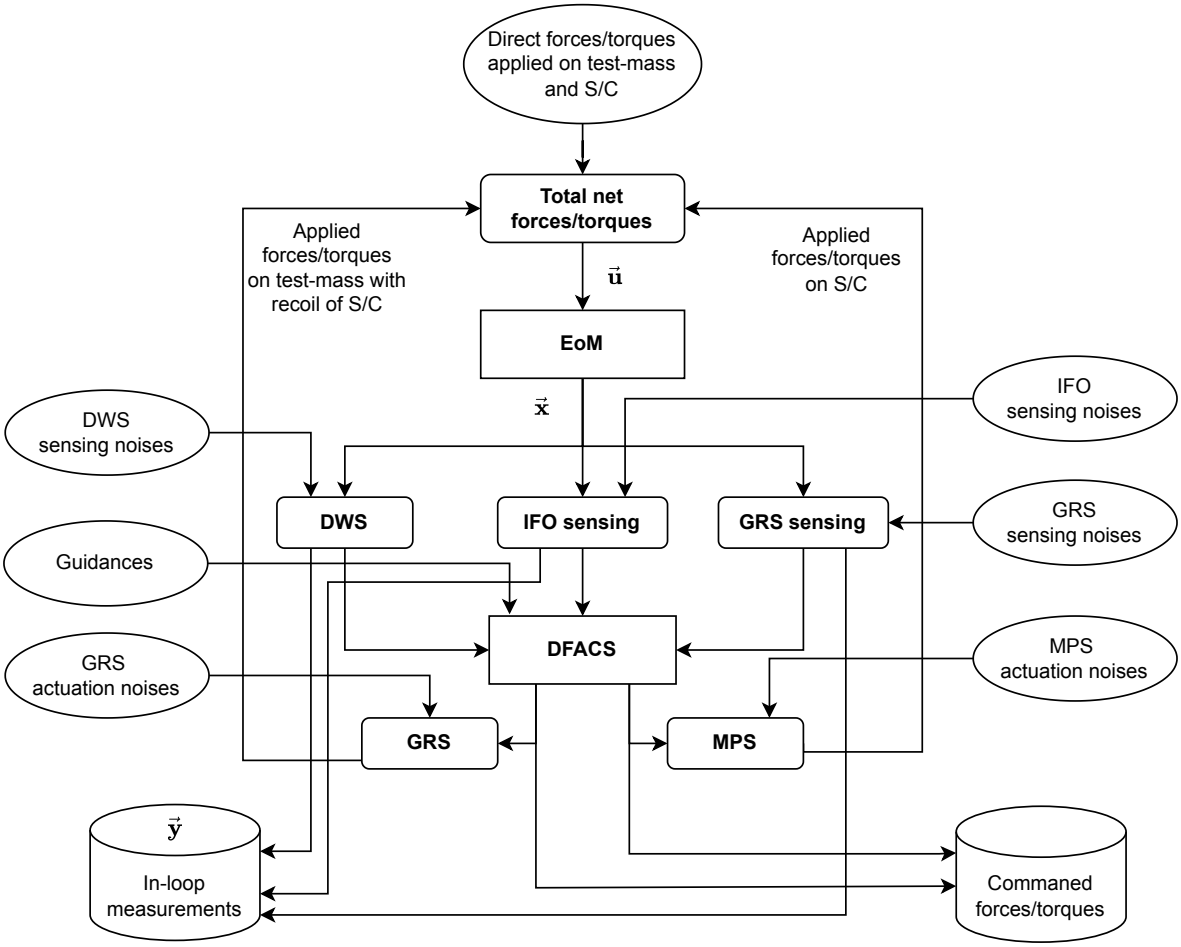

Figure 5.1: Schematic of $\boxed{ClosedLoopSystem}$ graph. The central block is $\boxed{EoM}$ graph, which needs the total net forces/torques in the input vector $\vec{\mathbf{u}}$. The outputs of $\boxed{EoM}$ are the dynamical state vector $\vec{\mathbf{x}}$, which is used to monitor the in-loop measurements such as differential wavefront sensing (DWS), Interferometer (IFO) sensing and Gravitational Reference Sensor (GRS) sensing. These in-loop measurements are, in fact, the components of the observational state vector $\vec{\mathbf{y}}$. The model for the measurements in $\boxed{DWS}$, $\boxed{IFOsensing}$ and $\boxed{GRSsensing}$ graphs is simply the sum of the components of $\vec{\mathbf{x}}$ and the associated sensing noise. These sensing noises are the input of the whole $\boxed{ClosedLoopSystem}$ graph. The outputs of in-loop measurements are then fed to the $\boxed{DFACS}$ graph to provide the demanded forces and torques to the Gravitational Reference Sensor (GRS) system and Micro-Propulsion System (MPS) in order to apply the forces/torques on test-mass and spacecraft, respectively. The applied forces/torques from GRS and MPR systems are the sum of demanded ones with the actuation noises. Finally, the applied forces/torques are combined with the direct forces/torques, which are the inputs of the $\boxed{ClosedLoopSystem}$ graph, to get the total net forces/torques, as the input vector $\vec{\mathbf{u}}$ of the $\boxed{EoM}$ graph. That completes the control loops.

Similarly, we work out for the $\mathbf{M}^{\text{target}}$ in (5.61). The non-zero components are:

$$M_{1,1} = M_{2,2} = I_3 \tag{5.99}$$

$$M_{3,1} = 2m_{\text{sc}} \left[\vec{\omega}_{O/\mathcal{J}}^{\,\mathcal{O}}\right]^{\times} \tag{5.100}$$

$$M_{3,3} = m_{\text{sc}} I_3 \tag{5.101}$$

$$M_{4,2} = \left\{ \left[\vec{\omega}_{O/\mathcal{J}}^{\,\mathcal{O}}\right]^{\times} \mathbf{I}^{\mathcal{B}}_{\text{sc}/B} + \mathbf{I}^{\mathcal{B}}_{\text{sc}/B} \left[\vec{\omega}_{O/\mathcal{J}}^{\,\mathcal{O}}\right]^{\times} - \left[\mathbf{I}^{\mathcal{B}}_{\text{sc}/B} \vec{\omega}_{O/\mathcal{J}}^{\,\mathcal{O}}\right]^{\times} \right\} \tag{5.102}$$

$$M_{4,4} = \mathbf{I}^{\mathcal{B}}_{\text{sc}/B} \tag{5.103}$$

$$M_{5,5} = M_{6,6} = M_{7,7} = M_{8,8} = I_3 \tag{5.104}$$

$$M_{9,2} = -2m_{\text{tm}_1} \left[T^{\mathcal{H}_1}_{\mathcal{B}} \vec{\omega}_{O/\mathcal{J}}^{\,\mathcal{O}}\right]^{\times} \left[T^{\mathcal{H}_1}_{\mathcal{B}} \vec{\mathbf{r}}^{\mathcal{B}}_{H_1/\mathcal{B}}\right]^{\times} T^{\mathcal{H}_1}_{\mathcal{B}} \tag{5.105}$$

$$M_{9,4} = -m_{\text{tm}_1} \left[T^{\mathcal{H}_1}_{\mathcal{B}} \vec{\mathbf{r}}^{\mathcal{B}}_{H_1/\mathcal{B}}\right]^{\times} T^{\mathcal{H}_1}_{\mathcal{B}} \tag{5.106}$$

$$M_{9,5} = 2m_{\text{tm}_1} \left[T^{\mathcal{H}_1}_{\mathcal{B}} \vec{\omega}_{O/\mathcal{J}}^{\,\mathcal{O}}\right]^{\times} \tag{5.107}$$

$$M_{9,9} = m_{\text{tm}_1} I_3 \tag{5.108}$$

$$M_{10,2} = \left\{ \mathbf{I}^{\mathcal{T}_1}_{\text{tm}_1/T_1} \left[T^{\mathcal{H}_1}_{\mathcal{B}} \vec{\omega}_{O/\mathcal{J}}^{\,\mathcal{O}}\right]^{\times} + \left[T^{\mathcal{H}_1}_{\mathcal{B}} \vec{\omega}_{O/\mathcal{J}}^{\,\mathcal{O}}\right]^{\times} \mathbf{I}^{\mathcal{T}_1}_{\text{tm}_1/T_1} \right\} T^{\mathcal{H}_1}_{\mathcal{B}} \tag{5.109}$$

$$M_{10,4} = \mathbf{I}^{\mathcal{T}_1}_{\text{tm}_1/T_1} \tag{5.110}$$

$$M_{10,6} = \mathbf{I}^{\mathcal{T}_1}_{\text{tm}_1/T_1} \left[T^{\mathcal{H}_1}_{\mathcal{B}} \vec{\omega}_{O/\mathcal{J}}^{\,\mathcal{O}}\right]^{\times} \tag{5.111}$$

$$M_{10,10} = \mathbf{I}^{\mathcal{T}_1}_{\text{tm}_1/T_1} \tag{5.112}$$

$$M_{11,2} = -2m_{\text{tm}_2} \left[T^{\mathcal{H}_2}_{\mathcal{B}} \vec{\omega}_{O/\mathcal{J}}^{\,\mathcal{O}}\right]^{\times} \left[T^{\mathcal{H}_2}_{\mathcal{B}} \vec{\mathbf{r}}^{\mathcal{B}}_{H_2/\mathcal{B}}\right]^{\times} T^{\mathcal{H}_2}_{\mathcal{B}} \tag{5.113}$$

$$M_{11,4} = -m_{\text{tm}_2} \left[\vec{\mathbf{r}}^{\mathcal{H}_2}_{\mathcal{H}_2/\mathcal{B}}\right]^{\times} T^{\mathcal{H}_2}_{\mathcal{B}} \tag{5.114}$$

$$M_{11,7} = 2m_{\text{tm}_2} \left[T^{\mathcal{H}_2}_{\mathcal{B}} \vec{\omega}_{O/\mathcal{J}}^{\,\mathcal{O}}\right]^{\times} \tag{5.115}$$

$$M_{11,11} = m_{\text{tm}_2} I_3 \tag{5.116}$$

$$M_{12,2} = \left\{ \mathbf{I}^{\mathcal{T}_2}_{\text{tm}_2/T_2} \left[T^{\mathcal{H}_2}_{\mathcal{B}} \vec{\omega}_{O/\mathcal{J}}^{\,\mathcal{O}}\right]^{\times} + \left[T^{\mathcal{H}_2}_{\mathcal{B}} \vec{\omega}_{O/\mathcal{J}}^{\,\mathcal{O}}\right]^{\times} \mathbf{I}^{\mathcal{T}_2}_{\text{tm}_2/T_2} \right\} T^{\mathcal{H}_2}_{\mathcal{B}} \tag{5.117}$$

$$M_{12,4} = \mathbf{I}^{\mathcal{T}_2}_{\text{tm}_2/T_2} \tag{5.118}$$

$$M_{12,8} = \mathbf{I}^{\mathcal{T}_2}_{\text{tm}_2/T_2} \left[T^{\mathcal{H}_2}_{\mathcal{B}} \vec{\omega}_{O/\mathcal{J}}^{\,\mathcal{O}}\right]^{\times} \tag{5.119}$$

$$M_{12,12} = \mathbf{I}^{\mathcal{T}_2}_{\text{tm}_2/T_2} \tag{5.120}$$

Finally, the non-zero components of $\mathbf{B}^{\text{target}}$ in (5.88) are reduced to

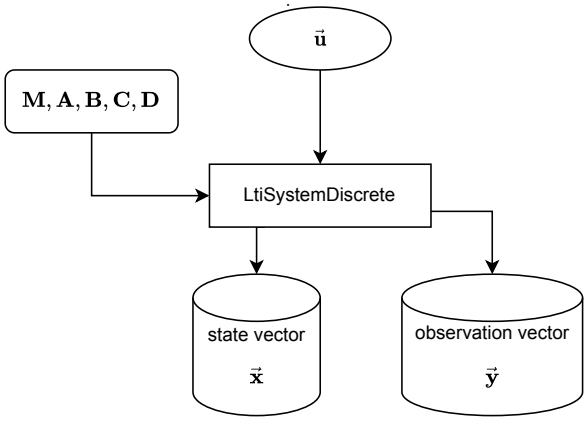

Figure 5.2: Schematic of general (fixed MOSAs) $\boxed{EoM}$ graph for discrete linear time-invariant system.

$$
\begin{aligned}
&B_{3,1} = I_3 \\
&B_{3,7} = -T^{\mathcal{B}}_{\mathcal{H}_1}, \\
&B_{3,9} = -T^{\mathcal{B}}_{\mathcal{H}_2}
\end{aligned}
\quad
\begin{aligned}
&B_{4,2} = I_3 \\
&B_{4,7} = -\left[\vec{\mathbf{r}}^{\mathcal{B}}_{H_1/\mathcal{B}}\right]^{\times} T^{\mathcal{B}}_{\mathcal{H}_1} \\
&B_{4,8} = -T^{\mathcal{B}}_{\mathcal{H}_1} \\
&B_{4,9} = -\left[\vec{\mathbf{r}}^{\mathcal{B}}_{\mathcal{H}_2/\mathcal{B}}\right]^{\times} T^{\mathcal{B}}_{\mathcal{H}_2} \\
&B_{4,10} = -T^{\mathcal{B}}_{\mathcal{H}_2}
\end{aligned}
\quad , \quad
\begin{aligned}
&B_{9,1} = -\frac{m_{\mathrm{tm}_1}}{m_{\mathrm{sc}}} T^{\mathcal{H}_1}_{\mathcal{B}} \\
&B_{9,3} = I_3 \\
&B_{9,7} = I_3 \\
&B_{10,4} = I_3 \\
&B_{10,8} = I_3
\end{aligned}
\quad , \quad
\begin{aligned}
&B_{11,1} = -\frac{m_{\mathrm{tm}_2}}{m_{\mathrm{sc}}} T^{\mathcal{H}_2}_{\mathcal{B}} \\
&B_{11,5} = I_3 \\
&B_{11,9} = I_3 \\
&B_{12,6} = I_3 \\
&B_{12,10} = I_3
\end{aligned}
\quad . \tag{5.121}
$$

Then all matrices are the arguments of a linear time-invariant system graph, either discrete or continuous, contained in $\boxed{EoM}$ graph. The input of this graph is the input vector $\vec{\mathbf{u}}$. The output is the state vector $\vec{\mathbf{x}}$ and the observation vector $\vec{\mathbf{y}}$. In this study, we use the discrete linear time-invariant system for constructing our $\boxed{EoM}$ graph, illustrated in figure 5.2.

In the case of fixed MOSAs, we assume the angle between x-axis of the MOSA body $\mathcal{H}$-frame and x-axis of the spacecraft body $\mathcal{B}$-frame are constantly $\pm 30^o$. Hence, the opening angle between the two MOSAs is fixed at 60^o.

5.3.4 Application with MOSA motion

In practice, the MOSAs have their rotation motions so that the opening angle evolves, or in other words, is breathing, during LISA operation. We address the MOSA motion in the LISA Dynamics implementation by the following assumption:

Dynamics assumption 4

MOSAs in each spacecraft have the right direction toward the distant spacecraft, assuming the re-pointing antenna process has been done perfectly and continuously during LISA operation.

Consequently, the wave vector of the distant beam reaching the MOSA is along the drag-free axis. Therefore, *the drag-free axis and sensitive axis are identical*, according to the notation and definition of reference frames presented in section 5.1. On the other hand, the opening angle between two MOSAs is defined from distant spacecraft locations since the MOSAs point ideally to the distant spacecraft. Hence, one can compute the breathing angle $\vec{\alpha}_{\mathcal{H}_i/\mathcal{B}}$ from the LISA orbits[2].

In a first approximation, we identify the leading order effect of the MOSA rotation on the test-mass longitudinal dynamics. The breathing angle $\vec{\alpha}_{\mathcal{H}_i/\mathcal{B}}$ appears in the rotation matrix $T^{\mathcal{T}}_{\mathcal{H}}$ and contributes to the projection of the spacecraft's noisy motion along rotating MOSA axis, c.f. to the second term of the right-hand side of equation (5.38). Therefore, it induces an apparent motion of the test-mass in a rotating MOSA. In order to account for this effect, our approach is to modify the $\mathbf{B}^{\text{target}}$ with the time-dependent matrix $T^{\mathcal{H}_1}_{\mathcal{B}}$ and its transpose.

For simplified implementation, we want to keep the matrix $\mathbf{B}^{\text{target}}$ in the $\boxed{EoM}$ graph time-invariant. The breathing angle computed from the LISA orbits is used to rotate the force applied on the spacecraft in the input vector $\vec{\mathbf{u}}$ from $\mathcal{O}$-frame to $\mathcal{H}$-frame. Hence, the force applied on the spacecraft is now projected on the MOSA axis in $\mathcal{H}$-frame instead of the spacecraft axis in $\mathcal{B}$-frame. Then, we connect the rotated spacecraft force to the linear time-invariant block in the $\boxed{EoM}$ graph, see the figure 5.3.

Meanwhile, we still keep the original applied forces and torques in their default reference frame as the components in the vector $\vec{\mathbf{u}}$ to be used in other equations of motion. Hence, in the case of rotating MOSA, $\vec{\mathbf{u}}$ is extended by two more components to account for the force applied on the spacecraft, which is projected on the **rotating** MOSA axis. We note that the introduction of two extra inputs is a modeling trick to simplify the implementation, and it is not fundamentally necessary. We read the extended input vector $\vec{\mathbf{u}}$ and matrix $\mathbf{B}^{\text{target}}$:

$$\vec{\mathbf{u}}(t) = \begin{bmatrix} \vec{\mathbf{f}}^{\,\mathcal{O}}_{B} \\ \vec{\mathbf{t}}^{\,\mathcal{O}}_{B} \end{bmatrix} \oplus \begin{bmatrix} \vec{\mathbf{f}}^{\,\mathcal{H}_1}_{T_1} \\ \vec{\mathbf{t}}^{\,\mathcal{H}_1}_{T_1} \\ \vec{\mathbf{f}}^{\,\mathcal{H}_2}_{T_2} \\ \vec{\mathbf{t}}^{\,\mathcal{H}_2}_{T_2} \end{bmatrix} \oplus \begin{bmatrix} \vec{\mathbf{fr}}^{\,\mathcal{H}_1}_{T_1} \\ \vec{\mathbf{tr}}^{\,\mathcal{H}_1}_{T_1} \\ \vec{\mathbf{fr}}^{\,\mathcal{H}_2}_{T_2} \\ \vec{\mathbf{tr}}^{\,\mathcal{H}_2}_{T_2} \end{bmatrix} \oplus \begin{bmatrix} \vec{\mathbf{f}}^{\,\mathcal{H}_1}_{B} \\ \vec{\mathbf{f}}^{\,\mathcal{H}_2}_{B} \end{bmatrix}, \tag{5.122}$$

[2]This is certainly not the case for the LISA mission in practice, but here we assume that we can calculate the opening angle from LISA orbits.

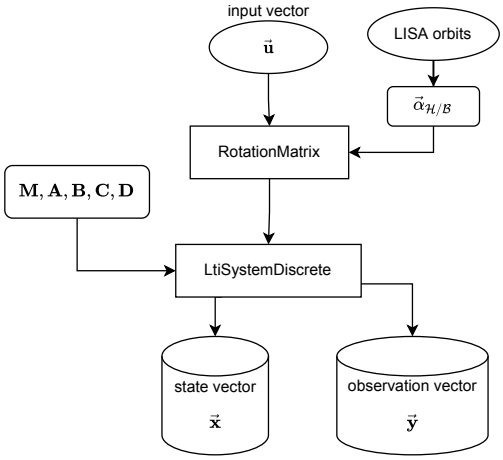

Figure 5.3: Schematic of $\boxed{EomMovingMosas}$ graph for discrete linear time-invariant system.

where $\vec{\mathbf{f}}_B^{\,\mathcal{H}_i} = T_{\mathcal{B}}^{\mathcal{H}_i}\left(\vec{\alpha}_{\mathcal{H}_i/\mathcal{B}}\right) T_{\mathcal{O}}^{\mathcal{B}}\left(\vec{\alpha}_{\mathcal{B}/\mathcal{O}}\right) \vec{\mathbf{f}}_B^{\,\mathcal{O}} = T_{\mathcal{B}}^{\mathcal{H}_i}\left(\vec{\alpha}_{\mathcal{H}_i/\mathcal{B}}\right) \vec{\mathbf{f}}_B^{\,\mathcal{O}}$ since $T_{\mathcal{O}}^{\mathcal{B}}\left(\vec{\alpha}_{\mathcal{B}/\mathcal{O}}\right) = I_3$ in the target frame for linear equations of motion.

$$\mathbf{B}\left(t, \vec{\mathbf{x}}\right) = \begin{pmatrix} O_3 & O_3 & O_3 & O_3 & O_3 & O_3 & O_3 & O_3 & O_3 & O_3 & O_3 & O_3 \\ O_3 & O_3 & O_3 & O_3 & O_3 & O_3 & O_3 & O_3 & O_3 & O_3 & O_3 & O_3 \\ B_{3,1} & O_3 & O_3 & O_3 & O_3 & O_3 & B_{3,7} & O_3 & B_{3,9} & O_3 & O_3 & O_3 \\ O_3 & B_{4,2} & O_3 & O_3 & O_3 & O_3 & B_{4,7} & B_{4,8} & B_{4,9} & B_{4,10} & O_3 & O_3 \\ O_3 & O_3 & O_3 & O_3 & O_3 & O_3 & O_3 & O_3 & O_3 & O_3 & O_3 & O_3 \\ O_3 & O_3 & O_3 & O_3 & O_3 & O_3 & O_3 & O_3 & O_3 & O_3 & O_3 & O_3 \\ O_3 & O_3 & O_3 & O_3 & O_3 & O_3 & O_3 & O_3 & O_3 & O_3 & O_3 & O_3 \\ O_3 & O_3 & O_3 & O_3 & O_3 & O_3 & O_3 & O_3 & O_3 & O_3 & O_3 & O_3 \\ O_3 & O_3 & B_{9,3} & O_3 & O_3 & O_3 & B_{9,7} & O_3 & O_3 & O_3 & B_{9,11} & O_3 \\ O_3 & O_3 & O_3 & B_{10,4} & O_3 & O_3 & O_3 & B_{10,8} & O_3 & O_3 & O_3 & O_3 \\ O_3 & O_3 & O_3 & O_3 & B_{11,5} & O_3 & O_3 & O_3 & B_{11,9} & O_3 & O_3 & B_{11,12} \\ O_3 & O_3 & O_3 & O_3 & O_3 & B_{12,6} & O_3 & O_3 & O_3 & B_{12,10} & O_3 & O_3 \end{pmatrix}, \tag{5.123}$$

where

$$\begin{array}{llll} & B_{4,2} = I_3 & B_{9,3} = I_3 & B_{11,5} = I_3 \\ B_{3,1} = I_3 & B_{4,7} = -\left[\vec{\mathbf{r}}_{H_1/\mathcal{B}}^{\,\mathcal{B}}\right]^{\times} T_{\mathcal{H}_1}^{\mathcal{B}} & B_{9,7} = I_3 & B_{11,9} = I_3 \\ B_{3,7} = -T_{\mathcal{H}_1}^{\mathcal{B}}, & B_{4,8} = -T_{\mathcal{H}_1}^{\mathcal{B}} \quad , & B_{9,11} = -\dfrac{m_{\mathrm{tm}_1}}{m_{\mathrm{sc}}} I_3, & B_{11,12} = -\dfrac{m_{\mathrm{tm}_2}}{m_{\mathrm{sc}}} I_3. \\ B_{3,9} = -T_{\mathcal{H}_2}^{\mathcal{B}} & B_{4,9} = -\left[\vec{\mathbf{r}}_{\mathcal{H}_2/\mathcal{B}}^{\,\mathcal{B}}\right]^{\times} T_{\mathcal{H}_2}^{\mathcal{B}} & B_{10,4} = I_3 & B_{12,6} = I_3 \\ & B_{4,10} = -T_{\mathcal{H}_2}^{\mathcal{B}} & B_{10,8} = I_3 & B_{12,10} = I_3 \end{array} \tag{5.124}$$

In this case, the dimesion of $\mathbf{B}$ is 36x36 instead of 36x30 in equation (5.88). In the next section, we show some preliminary results of `LISANode` simulation with the dynamics implementation and discuss about the performance of DFACS with fixed and rotating MOSAs cases.

5.4 Result

The output of the $\boxed{ScDynamics}$ graph is the state vector which includes the attitudes and positions of the test-mass. To see the performance of DFACS, we use the following evaluation quantities:

- Velocity of the spacecraft, computed from the integration of the force applied on the S/C (quantity known by the simulator), this quantity can be projected in either sensitive axis or drag-free axis;
- Velocity of the test-mass 1[3], which is $\dot{\vec{\mathbf{r}}}^{\mathcal{H}_1}_{T_1/\mathcal{H}_1}$ of state vector (5.46), hence this quantity is always projected on the drag-free axis;
- Relative velocity between the test-mass and the spacecraft, by combining two above quantities.

We remind here that the sensitive axis is along the laser link between two spacecraft. In the convention of reference frame presented in section 5.1, this axis is associated with x-axis of the $\mathcal{H}^*$-frame. On the other hand, the drag-free axis is the x-axis of $\mathcal{H}$-frame. These two axes are identical in the fixed opening angle between two MOSAs. In the case of rotating MOSAs, the two axes are also the same due to Dynamics assumption 4. All the quantities are computed in ASD and converted into the unit of fractional frequency deviation.

We consider three cases of LISA Dynamics implementation and compute the evaluation quantities:

1. $\boxed{ScDynamics}$ graph with fixed MOSAs implementation in $\boxed{EoM}$ graph, all quantities are projected on drag-free axis, i.e. x-axis of $\mathcal{H}$-frame. This is the baseline case of the study.
2. $\boxed{ScDynamics}$ graph with fixed MOSAs implementation in $\boxed{EoM}$ graph. The test-mass velocity is projected on drag-free axis as enforced in the equations of motion. However, we project the spacecraft velocity on the sensitive axis, i.e. x-axis of $\mathcal{H}^*$-frame. This projection requires the breathing (varying opening) angle as the input. In this case, we

[3]Due to the symmetry, we can examine one test-mass inside the spacecraft.

note that the Equations of Motion (EoM) graph remains using the fixed opening angle between the two MOSAs. In other words, the test-mass motion is projected onto a fixed drag-free axis while the spacecraft motion is projected on a movable sensitive axis, which is different from the drag-free in this case.

3. $\boxed{ScDynamics}$ graph with rotating MOSAs implementation in the equation of motion to account for the effect of breathing angle. We use Dynamics assumption 4 to compute the breathing angle. The evaluation quantities are projected on sensitive axis, i.e. x-axis of $\mathcal{H}^*$-frame, which is identical to the drag-free axis. However, this drag-free axis is not fixed as in the first case.

For case 1, with a fixed opening angle between two MOSAs, i.e. 60^o, the DFACS works well so that the relative motion between test-mass and spacecraft is small. As we see in figure 5.4, the motion of the test-mass and the spacecraft are well controlled by the DFACS. In subfigure 5.4b, the test-mass motion w.t.t. the containing spacecraft has a peak at around 0.1 Hz in the spectral density due to the limitation of the drag-free bandwidth. At lower frequencies, DFACS performs well so the test-mass and spacecraft move as a rigid body. At higher frequencies than the peak frequency, the drag-free control is more effective since the jittering of the spacecraft is insignificant (the large inertia of the spacecraft avoids its fast oscillating). The residual motion of the test-mass is small, with ASD around 10^{-22} to 10^{-24} in fractional frequency deviation unit, in the frequency band from 10^{-2} to 1 Hz. The residual motion of the test-mass is compatible with the test-mass acceleration noise, which is about the LISA requirement level [103], as we see in the combined plot 5.5. According to this result, we see that the DFACS can suppress the jitter motion between test-mass and the spacecraft in the fixed MOSAs configuration, which is similar to the capacity of TDI to suppress the spacecraft jitter motion by combining the ISI and TMI measurements, as described in section 3.2.2.

Then, we consider case 2, in which the opening angle between two MOSA is breathing, or called rotating MOSAs. Since the velocity for the test-mass and spacecraft motions do not contain much information in this case, we only show the relative motion between them in figure 5.5 (orange curve). From that figure, we see that the performance of DFACS worsens compared to the first cases: there is a considerable residual from 10^{-2} Hz. The reason can be that we projected test-mass and spacecraft motion on different directions: the spacecraft motion is projected on the sensitive axis, but the projection of test-mass motion is done on drag-free axis. Therefore, we have to modify equations of motion, accounting for the breathing angle, in order to have the same projections of two motions.

Finally, we examine case 3, with the breathing angle impact in the equations of motion for LISA Dynamics, particularly in the rotation matrix for the input force applied on the spacecraft as described at the end of section 5.3.3. The motions of test-mass and spacecraft

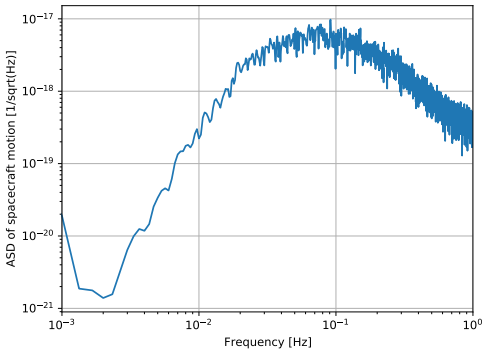

(a) Spacecraft motion w.r.t inertial frame

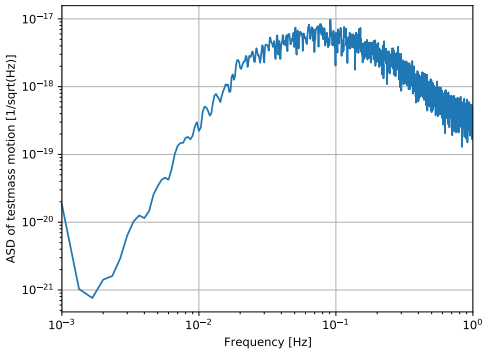

(b) Test-mass motion w.r.t. spacecraft

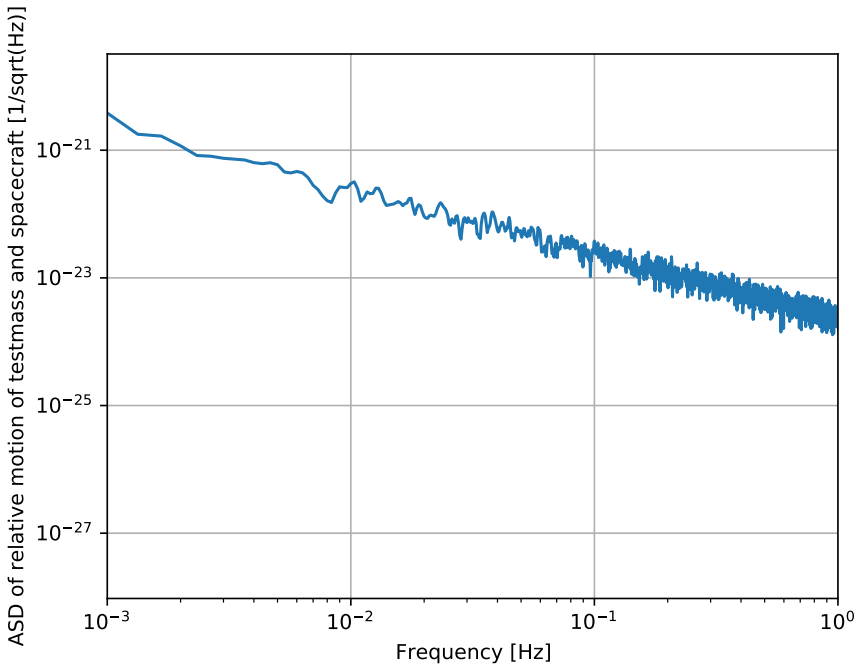

(c) Residual motion of test-mass

Figure 5.4: Results for fixed MOSAs case with the drag-free axis projection. The data are generated from `LISANode` simulator, duration of 10^4 seconds, with LISA Dynamics implementation for one spacecraft with a fixed angle between two MOSAs. All quantities are computed in ASD and expressed in fractional frequency deviation units. Two top plots present the motions of the spacecraft w.r.t. inertial Galilean frame (a) and of the test-mass 1 w.r.t. to the containing spacecraft (b). The bottom plot (c) shows the residual relative motion of the test-mass by subtracting the test-mass-to-spacecraft motion to the spacecraft-to-inertial motion.

are projected on sensitive axis before computing the relative motion between them. The result of the relative motion between the test-mass and spacecraft is shown in figure 5.5 (green curve). We have a lower residual than the previous case, so the correction added in the new implementation of LISA Dynamics works. With our first naive model for breathing angle impact on the implementation on `LISANode`, we have 90% less residual relative motion between test-mass and spacecraft compared to case 2. The DFACS works well at low frequencies, so there is no residual relative motion in all three cases. However, to obtain the result as in the baseline case, i.e. the fixed MOSAs, we still need to investigate more correction terms in the equation of motion that could contribute significantly to the motion of spacecraft and test-mass. This potential work is proposed in future tasks for developing the LISA dynamics simulation.

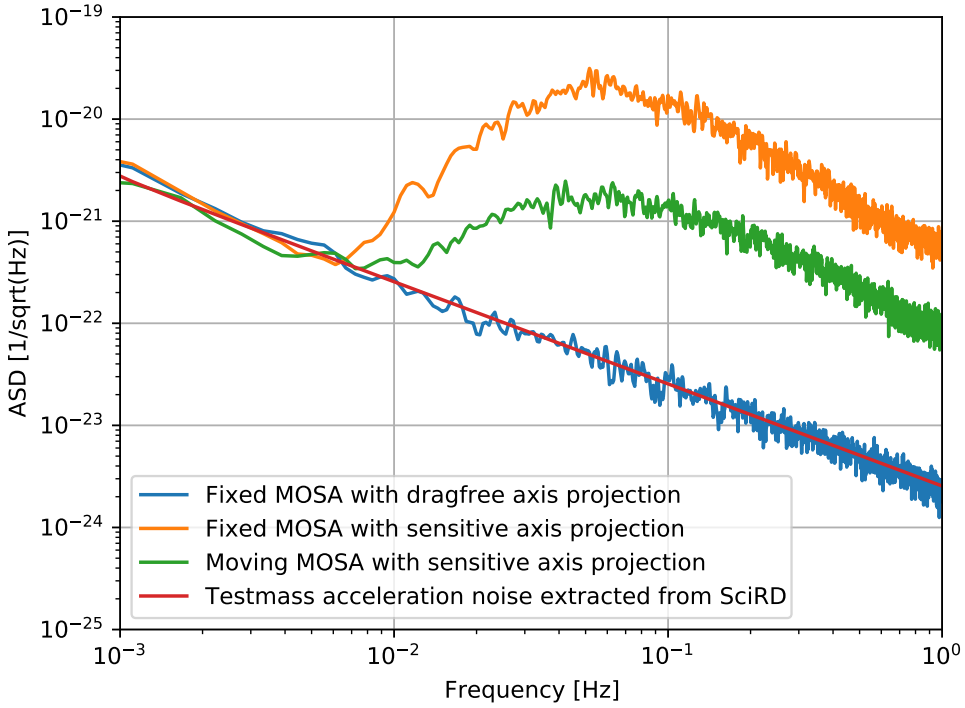

Figure 5.5: Comparison between three cases of LISA Dynamics implementation. The blue curve is the relative motion between test-mass and spacecraft in the fixed MOSAs case with sensitive axis projection, so there is no impact of breathing angle. The orange curve is for the case of fixed MOSAs, and the motions of test-mass and spacecraft are projected on sensitive axis, depending on the breathing angle. The green curve is in the case of rotating MOSAs with sensitive axis projection. For reference, the red line is the test-mass acceleration noise shape which is taken from the LISA SciRD, or expressed in (2.5), with the multiply factor of 2 to take into account that the bouncing off on the test-mass gives twice times the noise level in the measurement. All quantities are computed in ASD and expressed in fractional frequency deviation units.

Chapter 6

SGWB data analysis with LISA

This work is conducted in collaboration with Mauro Pieroni, Germano Nardini, Chiara Caprini and Antoine Petiteau.

6.1 Introduction

The search for a SGWB of cosmological origin is particularly challenging for two main reasons: first, if present, the signal is stochastic and therefore very similar to the instrumental noise; second, there is no clear expectation about the effective presence of the signal, and no definitive prediction about its spectral characteristics.

This study aims at examine how uncertainties in the shape of the noise spectral density can alter the signal reconstruction in the data analysis. In order to perform the SGWB search in the simulated data, we use the `SGWBinner` tool, which allows for a blind reconstruction of the SGWB spectral shape by parameterizing it with a sequence of power laws in adapted frequency bins. This code has been designed to perform the science performance characterisations and preliminary data analysis the data analysis without imposing a template for the SGWB spectral shape in the signal search.

The `SGWBinner` tool is accompanied by a data generation package, `SGWB_data`. As discussed in the next section, we can generate the data either by the `SGWB_data` package or by the `LISANode` simulator (presented in section 2.8). We also present two noise models, one characterized by two parameters and another by three, and some signal templates we can use in data generation and data analysis pipelines. Then, we review the `SGWBinner` code and the associated data analysis techniques to search SGWB in section 6.3. Finally, we demonstrate that if we perform the parameter estimation on the noise-only generated data with the wrong noise model, the reconstruction of the noise parameters is biased, and a fake signal is detected. The other analysis runs performed by `SGWBinner` with other data, including different SGWB

signal templates and the galactic foreground, are also presented in this chapter.

6.2 Data generation pipeline

In this study, we consider two different generation pipelines for simulated data, either in the frequency or time domains. In the following, we discuss the two pipelines in detail.

6.2.1 In the frequency domain

The first data generation pipeline which we adopt is `SGWB_data` [54]. This pipeline directly generates data (TDI variables) in frequency domain. The data set includes the instrumental noise, possibly a galactic background and/or SGWB signals. The pipeline for the data generation is illustrated in figure 6.1.

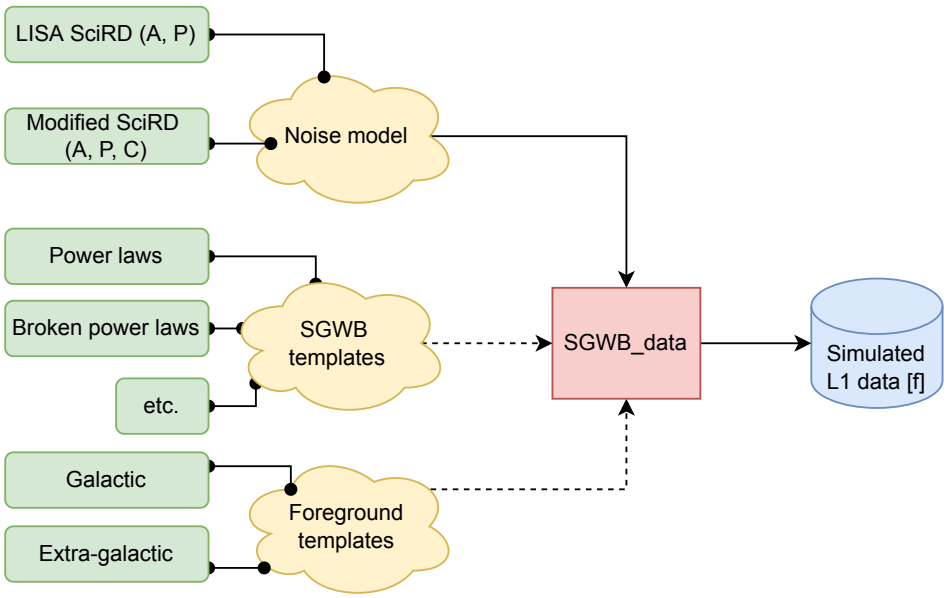

Figure 6.1: Schematic of the data generation pipeline using the `SGWB_data` code. The TDI data are generated in frequency domain. A, P, and C are the noise amplitudes, which will be discussed in section 6.2.3. See section 6.2.1 for the detailed description.

For the generation of the instrumental noise, we can choose either the SciRD noise model [103], characterized by two noise parameters, or a noise model derived from SciRD, characterized by one more parameter. We will discuss these noise models in section 6.2.3. However, we use only **3-parameters noise model to generate all simulated data** for conducting the result presented in this chapter. In addition, we assume that the noises are Gaussian, stationary and uncorrelated.

The generation pipeline directly generates the XYZ or AET TDI variables in frequency domain from the analytical noise spectrum of the TDI variables, either in 1.0 or 2.0 generation. In this chapter, we focus on the combination AET 2.0 generation.

In order to generate long duration data acquisitions, `SGWB_data` generates simulated data in frequency domain by generating several short data chunks. Because the noises are assumed to be uncorrelated, we can generate data in chunks in parallel. Then, one takes the average of the data from all of chunks for each frequency point.

At the time of the start of this study, LISA was expected to be in operation for at least 4 years with gaps due to the antenna re-pointing and other maintenance operations [16]. We assumed that the data acquisition proceeds with continuous measurements for about 11.5 days, which is the expected average time between the antenna re-pointing. We also assume that the total duration of effective data is about 75% (duty cycle) of the whole mission duration, so a total of 3 years over 4 years of mission duration[1]. This corresponds to 95 data chunks of about 11.5 days. The frequency resolution is about 10^{-6} Hz for each data chunk. The current planned duration is 4.5 years for the nominal mission and 4 years for the duration of the usable (i.e. effective) data, corresponding to a duty cycle of 89%.

Similar to the noise generation, `SGWB_data` generates the SGWB signals and the foreground in frequency domain under the assumptions of Gaussian, stationary and uncorrelated signals. The models for the strain sensitivity of the foreground and SGWBs are presented in section 6.2.4. Since the noise and the signal are generated in the same way, it is possible to unify the notation in a combined result. The relation between the strain sensitivity and the power spectral density is defined as

$$S_{ij}^{strain}(f) = \frac{S_{ij}^{psd}(f)}{\mathcal{R}_{ij}(f)}, \tag{6.1}$$

where $i, j \in \{A, E, T\}$ and $R_{ij}(f)$ is the LISA response function, defined as follows:

$$\mathcal{R}_{ij} = 64 \sin^2\left(\frac{2\pi f L}{c}\right) \sin^2\left(\frac{4\pi f L}{c}\right) \left(\frac{4\pi f L}{c}\right)^2 \tilde{\mathcal{R}}_{ij}(f). \tag{6.2}$$

$\tilde{\mathcal{R}}_{ij}(f)$ denotes the geometrical factor of the LISA detector, depending on the TDI channels[2]. Here, we use its numerical form to compute the strain sensitivity (see appendix A.3 in [69] for a detailed derivation).

[1] This duty cycle of 75% were based on the study of performance of LPF. One can find its up-to-date value and the new recommended LISA mission duration in [14]

[2] One can find out that the response function in (6.2) is different from the approximated one in [69] (c.f. equation 2.22 in [69]) by a factor of $4\sin^2\left(\frac{4\pi f L}{c}\right)$. This is because in our study we use the TDI variables in 2.0 generation. In [69], the authors used the TDI variables in 1.0 (or 1.5) generation.

The combined data is written in terms of the total strain sensitivity as (we omit the TDI channel indices ij at the moment):

$$S_{tot}^{strain}(f) = \frac{S_n^{psd}(f)}{\mathcal{R}(f)} + S_{fg}^{strain}(f) + S_{sgwb}^{strain}(f), \tag{6.3}$$

or equivalently in power spectral density,

$$S_{tot}^{psd}(f) = S_n^{psd}(f) + \left[S_{fg}^{strain}(f) + S_{sgwb}^{strain}(f)\right] \mathcal{R}(f), \tag{6.4}$$

where $S_n^{psd}(f)$ is PSD of the instrumental noises, $S_{fg}^{strain}(f)$ is the strain PSD of the foreground signal, $S_{sgwb}^{strain}(f)$ is the strain PSD of the SGWB signal.

In practice, `SGWBinner` generates the combined data via equation (6.4). Then, one needs to divide the input data by LISA response function to obtain the strain sensitivity before the data analysis process.

SGWB are typically expressed in terms of energy density per logarithmic frequency, i.e. $\Omega_{\rm gw}(f)$. The strain sensitivity can therefore be rewritten using equation (1.42) as

$$S_{tot}^{strain,\Omega}(f)h^2 = \frac{4\pi^2 f^3}{3(H_0/h)^2} S_{tot}^{strain}(f). \tag{6.5}$$

6.2.2 In time domain

The second data generation pipeline is more realistic as far as LISA data processing is considered, as described in section 3.1. In particular, we start from the raw LISA data or L0 data generation in time domain, before going through the TDI algorithm to get the TDI variables data. Then, we estimate the spectral density from the time-series TDI data to obtain the power spectra in frequency domain. The pipeline for the data generation is shown in figure 6.2.

The raw (or L0) data are generated using `LISANode`, described in section 2.8. The instrumental noise is generated from a specific analytical noise spectrum, characterized by the noise spectral shape and its amplitude.

The foreground and SGWB signal could be added in the data generation pipeline using an external software, such as `GWResponse` [44]. This step remains to be included as a possible extension of this study.

The L0 data then go through the TDI algorithm to produce the TDI variables, or L1 data, in time domain. For this purpose, we use the python package `PyTDI` [138]. Then we estimate the spectral density for the TDI data by the Welch methods [153], with a specific window, for example, Kaiser type. Due to insufficient memory storage capacity, we can not handle very long time-series data using `PyTDI`. Hence, our strategy is to split the L0 data, which span

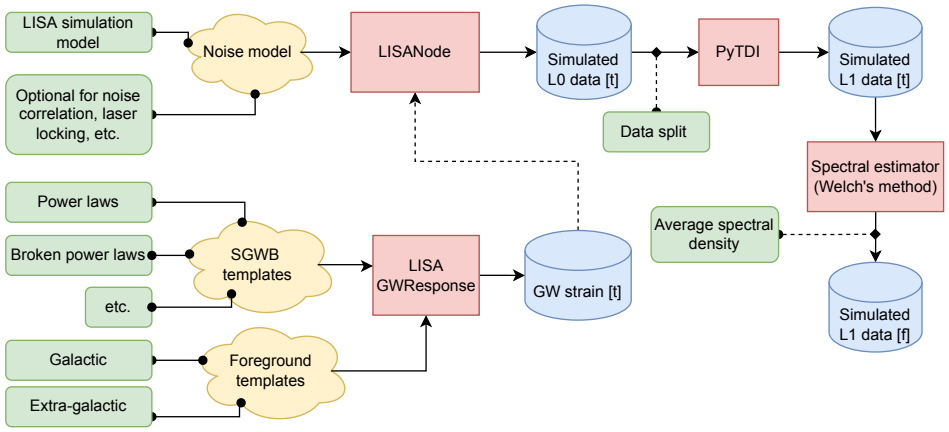

Figure 6.2: Schematic of the data generation pipeline using the `LISANode` simulator: the raw measurement data are simulated in time domain. A detailed description is presented in section 6.2.1.

1 year of observation, into shorten data chunks. We fix the duration of each data chunk to about 11.5 days, similarly to the data generation pipeline presented in section 6.2.1. For each data chunk, we compute the TDI variables and use the Welch method to estimate the power spectral density in frequency domain. Finally, we compute the average value of the spectral densities from all the data chunks.

Similarly to the data generation pipeline using `SGWB_data`, the average spectra estimated from the simulated data (including noise and signal) should be converted into strain sensitivity, and then in terms of Ω_{gw}. We first divide the spectral densities by the LISA response function, shown in equation (6.1), to get the strain sensitivity power spectra. However, we encounter an issue of singularities, shown in the figure 6.3a. This occurs at frequencies where the PSD $S_n^{psd}(f)$ (as we will see in section 6.2.3) and $\mathcal{R}_{ij}$ are both zero, so that the expression (6.1) becomes the undetermined form 0/0. Therefore, the strain sensitivity is unreliable at around these frequencies and should be excluded for the data analysis. In practice, we keep the full data for feeding the data analysis pipeline, but we include a weight factor which is 0 at the singularities. Hence, the 0-weighted data do not contribute to the analysis. The rest of the data, with the weight factor of 1, is shown in figure 6.3b.

Finally, we multiply the strain sensitivity with the conversion factor of equation (6.5) to get the result in terms of energy density per logarithmic frequency.

6.2.3 Noise characterization

This subsection reviews the instrumental noise models, used for the data generation. These models can also be used for the data analysis, as described in section 6.3.2.

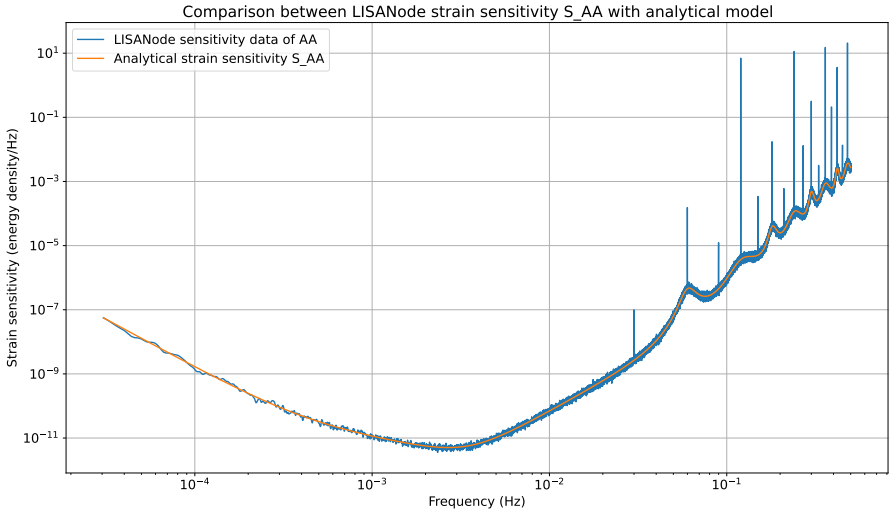

(a) Without mask

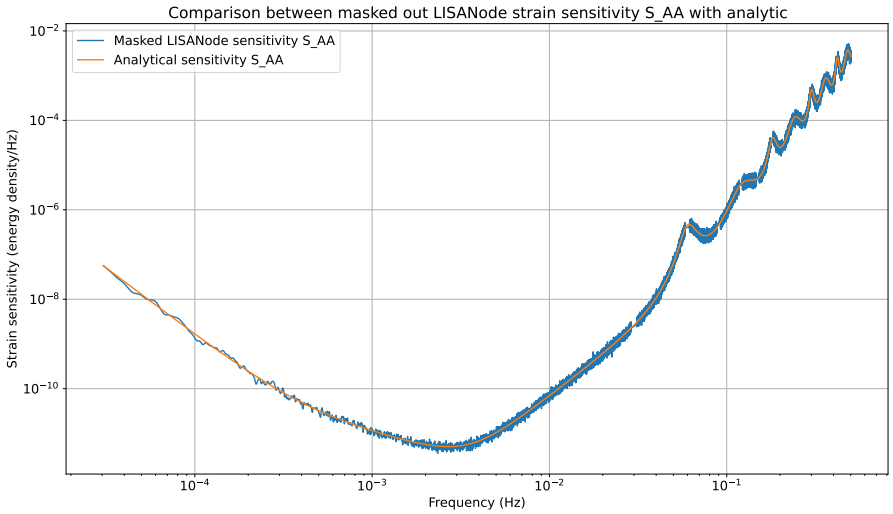

(b) With mask

Figure 6.3: Comparison between the strain sensitivity of the AA channel estimated from `LISANode` simulated data (blue) and the analytical model (orange). In (a), we show all the data generated with `LISANode`. In (b), we mask the singular data by cutting out 1% logarithmic intervals around the frequencies which lead to numerical singularities.

The instrumental noise model typically used by LISA data analysis is the SciRD noise model, which has 2 parameters: the test-mass acceleration and the OMS noises [103, 35]. From the study of the noise propagation presented in chapter 4, it turns out that the noise propagation through TDI of the OMS noises (such as readout and optical path-length noises) in different IFO measurements are not the same, so they cannot be considered as a single term as done in the SciRD noise model. Therefore, we propose a new instrumental noise model, which has one additional noise term, and it is characterized by 3 parameters. This model, called *3-parameters noise model* from now on, captures better the propagation of the instrumental noises through the LISA instrument and TDI algorithm.

In detail, the test-mass acceleration noise is the same for both noise models. On the other hand, the OMS noise contribution gets split into two terms, based on the way they propagate through the interferometric measurements and through the subsequent TDI algorithm. The Inter-Spacecraft Interferometer (ISI) and Reference Interferometer (RFI) OMS noises propagate through TDI in the same way, while the Test Mass Interferometer (TMI) one propagates differently, see tables 4.2. Hence, we combine the ISI and RFI OMS noises into a single term. Finally, we have three parameters characterizing the LISA instrumental noise: the test-mass acceleration noise amplitude, the OMS noise amplitude from the combined ISI and RFI measurements, and the OMS noise amplitude from the TMI measurement. Their noise shapes and levels are given in terms of the power spectral density as

$$S_{\rm acc}(f,A) = A^2 \frac{\rm fm^2}{s^4 \rm Hz}\left[1+\left(\frac{0.4\rm mHz}{f}\right)^4\right]\left(\frac{1}{2\pi f}\right)^4\left(\frac{2\pi f}{c}\right)^2, \tag{6.6}$$

$$S_{\rm OMS,\ isi/rfi}(f,P) = P^2\left[1+\left(\frac{2\rm mHz}{f}\right)^4\right]\frac{\rm pm^2}{\rm Hz}\left(\frac{2\pi f}{c}\right)^2, \tag{6.7}$$

$$S_{\rm OMS,\ tmi}(f,P) = C^2\left[1+\left(\frac{2\rm mHz}{f}\right)^4\right]\frac{\rm pm^2}{\rm Hz}\left(\frac{2\pi f}{c}\right)^2. \tag{6.8}$$

Some approximations are applied to simplify the noise model, as discussed partially in section 4.1.2. First, we assume that the armlengths of the LISA constellation are equal and with constant length L. The second approximation is that noises of the same types have the same spectral shape and amplitude across in different MOSAs or spacecraft. Finally, we assume that all noises are uncorrelated. With these approximations, the total power spectral densities

of TDI Michelson XYZ variables in the second generation are written as (see table 4.2):

$$
\begin{aligned}
S^{\rm tot}_{aa}(f,A,P,C) &= 64\sin^2\left(\frac{2\pi fL}{c}\right)\sin^2\left(\frac{4\pi fL}{c}\right) \\
&\quad \left\{\left[3+\cos\left(\frac{4\pi fL}{c}\right)\right]S_{\rm acc}(f,A)+S_{\rm OMS,\ isi/rfi}(f,P)\right. \\
&\quad \left.+\frac{1}{4}\left[3+\cos\left(\frac{4\pi fL}{c}\right)\right]S_{\rm OMS,\ tmi}(f,C)\right\} \qquad (6.9)\\
S^{\rm tot}_{ab}(f,A,P,C) &= -16\sin\left(\frac{2\pi fL}{c}\right)\sin^3\left(\frac{4\pi fL}{c}\right) \\
&\quad \left[4S_{\rm acc}(f,A)+S_{\rm OMS,\ isi/rfi}(f,P)+S_{\rm OMS,\ tmi}(f,C)\right], \qquad (6.10)
\end{aligned}
$$

where $a,b\in\{X,Y,Z\}$.

The power spectral densities for TDI variables AET in the second generation read, see table 4.3,

$$
\begin{aligned}
S^{\rm tot}_{AA}(f,A,P,C) &= S^{\rm tot}_{EE}(f,A,P,C) \\
&= 32\sin^2\left(\frac{2\pi fL}{c}\right)\sin^2\left(\frac{4\pi fL}{c}\right) \\
&\quad \left\{4\left[1+\cos\left(\frac{2\pi fL}{c}\right)+\cos^2\left(\frac{2\pi fL}{c}\right)\right]S_{\rm acc}(f,A)\right. \\
&\quad +\left[2+\cos\left(\frac{2\pi fL}{c}\right)\right]S_{\rm OMS,\ isi/rfi}(f,P) \\
&\quad \left.+\left[1+\cos\left(\frac{2\pi fL}{c}\right)+\cos^2\left(\frac{2\pi fL}{c}\right)\right]S_{\rm OMS,\ tmi}(f,C)\right\}, \qquad (6.11)\\
S^{\rm tot}_{TT}(f,A,P,C) &= 32\sin^2\left(\frac{2\pi fL}{c}\right)\sin^2\left(\frac{4\pi fL}{c}\right) \\
&\quad \left\{4\left[1-\cos\left(\frac{2\pi fL}{c}\right)\right]^2 S_{\rm acc}(f,A)\right. \\
&\quad +2\left[1-\cos\left(\frac{2\pi fL}{c}\right)\right]S_{\rm OMS,\ isi/rfi}(f,P) \\
&\quad \left.+\left[1-\cos\left(\frac{2\pi fL}{c}\right)\right]^2 S_{\rm OMS,\ tmi}(f,C)\right\}. \qquad (6.12)
\end{aligned}
$$

There is no cross-power spectral density for the AET variables since they are quasi-orthogonal [126]. The comparison of the power spectral densities in the AET variables between the two noise models (SciRD and the 3 parameters noise models) is shown in figure 6.4 and figure 6.5. We see that the differences between the two noise models are primarily at high frequencies, where the OMS noises dominate over the test-mass acceleration one. In addition, the maximum difference relatively between the two noise models is about 25%.

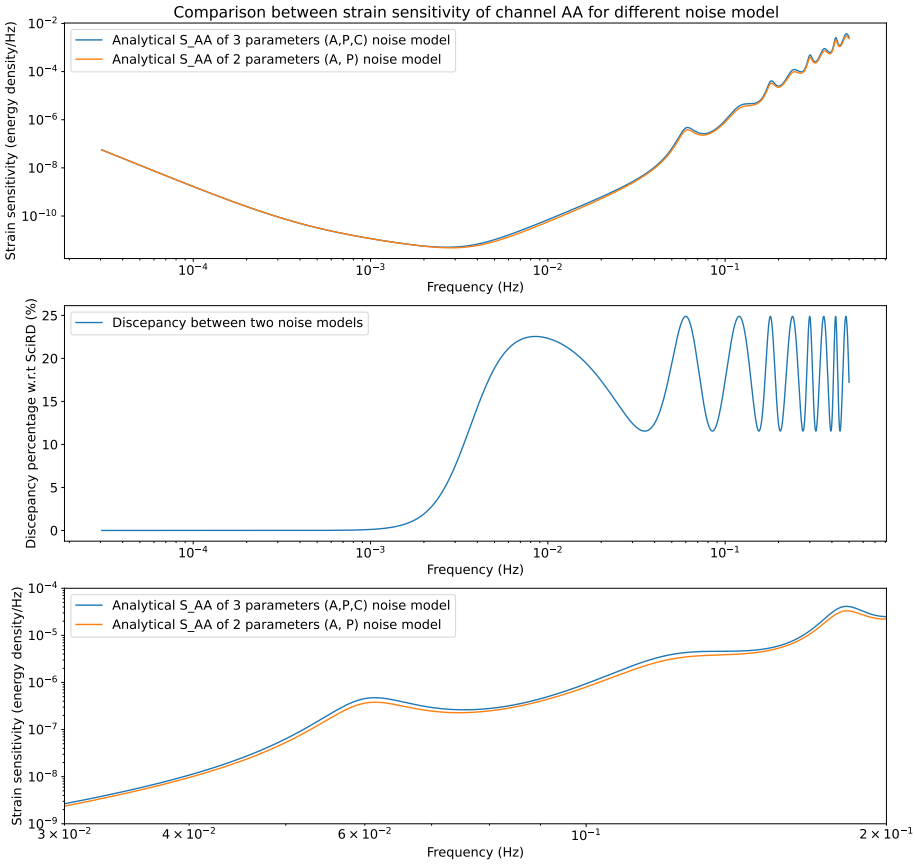

Figure 6.4: Comparison of the strain sensitivities S_{AA} between the analytical 2- and 3-parameters noise models, the values of noise parameters are taken from table 6.1. The top panel shows the whole LISA frequency band. The middle panel is the percentage discrepancy of the 3-parameters noise model w.r.t 2-parameters noise model. The bottom one is zoomed in a narrower frequency band.

The values of A, P, C used for the first data generation pipeline, c.f. section 6.2.1, are given in the table 6.1. These values represent the best fit estimation for the `LISANode` data, as shown figure 6.6 and figure 6.7, because these values are computed from the input parameters of `LISANode`. We collect all the noise terms simulated by `LISANode` with the same propagation through the IFO measurements and the TDI algorithm, so that there are finally 3 different noise terms remaining to characterize the instrumental noise, corresponding to the three parameters A, P, C. In addition, we note that the spectral shape of the OMS noises implemented in `LISANode` at the moment have no relaxation of the factor $\left[1 + (2\text{mHz}/f)^4\right]$, contrary to the

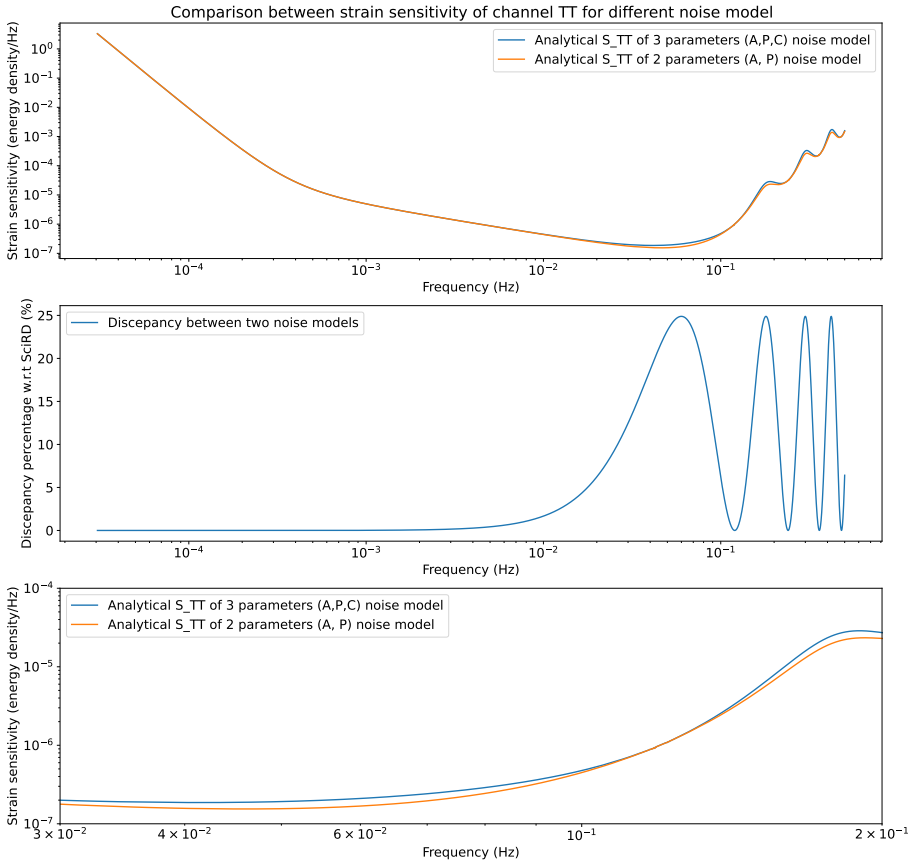

Figure 6.5: Comparison of the strain sensitivities S_{TT} between analytical 2- and 3-parameters noise models, the values of noise parameters are taken from table 6.1. The top panel shows the whole LISA frequency band. The middle panel is the percentage discrepancy of the 3-parameters noise model w.r.t 2-parameters noise model. The bottom one is zoomed the first plot in a narrower frequency band.

analytical expressions in equations (6.7) and (6.8). Therefore, the model used in the data analysis for fitting the `LISANode` data needs to be modified by removing this factor. This has been done also in figures 6.8 and 6.9. On the other hand, the data generation pipeline in frequency domain using `SGWB_data` incorporates the relaxation factor. The comparisons between the strain sensitivity from the two data generation pipelines is illustrated in figure 6.8 for the AA channel and figure 6.9 for the TT channel. The OMS noises in ISI and RFI contributing to the strain sensitivity S_{TT} in (6.12) are dominant at the low frequencies compared to the test-mass acceleration noise ($a^2 \ll a$ with $a = [1 - \cos(2\pi f L/c)] < 1$ for

$f \to 0^+$). Therefore, the impact of the relaxation factor in the two different noise model is more apparent in the TT channel.

We also use the SciRD noise model in this work, to study the impact of inaccurate noise knowledge (i.e. using different noise models for data generation and data analysis pipeline) in the search for SGWBs. The SciRD noise model is similar to the 3-parameters noise model, expressed in equations (6.11), (6.12), (6.9), (6.10), but with $C = 0$ in all equations since in the SciRD the OMS noise in TMI measurement are assumed to be propagated through TDI as the same as ones in ISI and RFI measurements. Therefore, it is unnecessary to rewrite the analytical expressions of SciRD noise model here.

Parameter	A	P	C
True (injected) value	2.4	8.96	4.47
Units	$\frac{\text{fm}}{\text{s}^2\sqrt{\text{Hz}}}$	$\frac{\text{pm}}{\sqrt{\text{Hz}}}$	$\frac{\text{pm}}{\sqrt{\text{Hz}}}$

Table 6.1: The true (injected) values of the noise parameters and their units, used in `SGWB_data` generator.

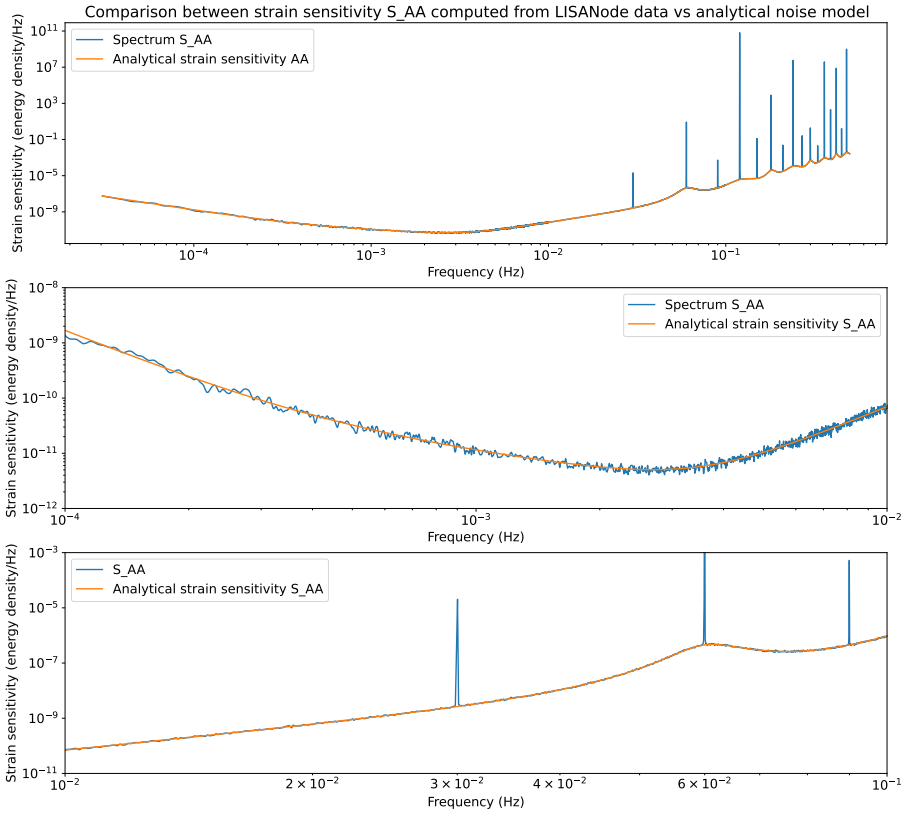

Figure 6.6: Comparison of strain sensitivities S_{AA} computed from the `LISANode` data with the analytical 3-parameters noise model, the values of noise parameters are taken from table 6.1. The top panel shows the whole LISA frequency band. The two bottom ones are zoomed in smaller frequency regions. A part from the singularity spikes of the strain sensitivity (6.1), the strain sensitivity S_{AA} (S_{EE} is the same as S_{AA}) computed from `LISANode` data matches with the analytical noise model (6.11).

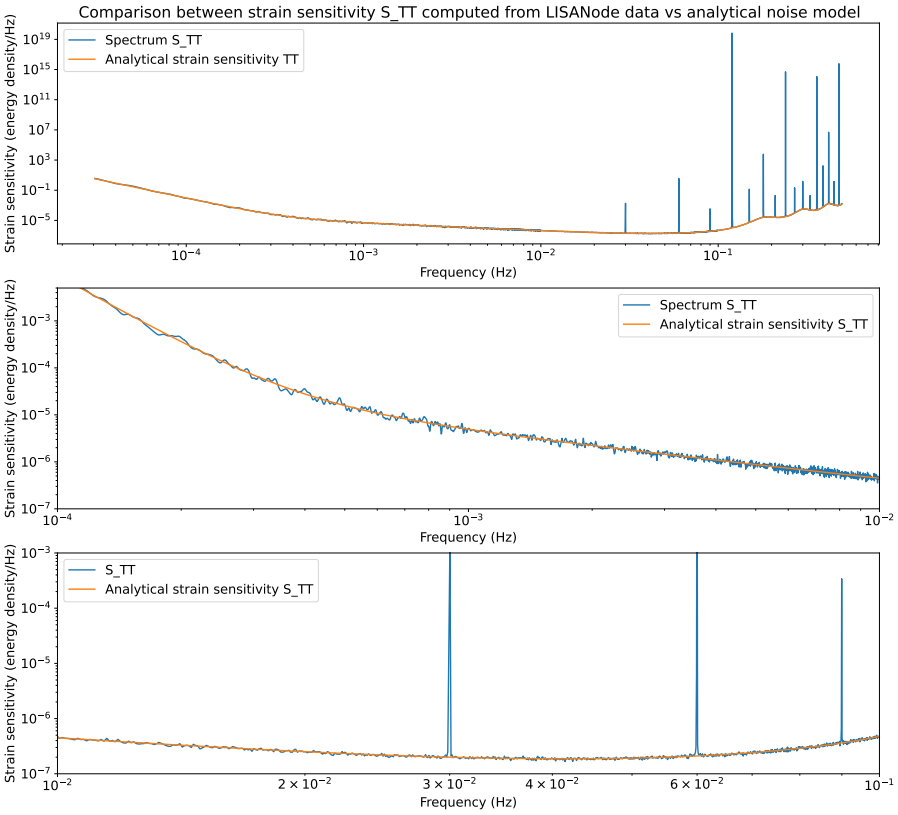

Figure 6.7: Comparison of strain sensitivities S_{TT} computed from the `LISANode` data with the analytical 3-parameters noise model, the values of noise parameters are taken from table 6.1. C.f. figure 6.6 for a detailed description.

6.2.4 Stochastic Gravitational Wave Background signal models

In this section, we describe some SGWB templates used in the frequency data generation pipeline, described in section 6.2.1. We remind here that we did not include a SGWB signal in the data generated with `LISANode`, which contains therefore only the instrumental noise. Time-series data containing SGWBs could be generated with `LISANode` by a python package `GWResponse` [44]. The templates presented in this section can, in principle, be used as the input for this code.

The following templates are designed to have high SNR, so that they can be detected by LISA.

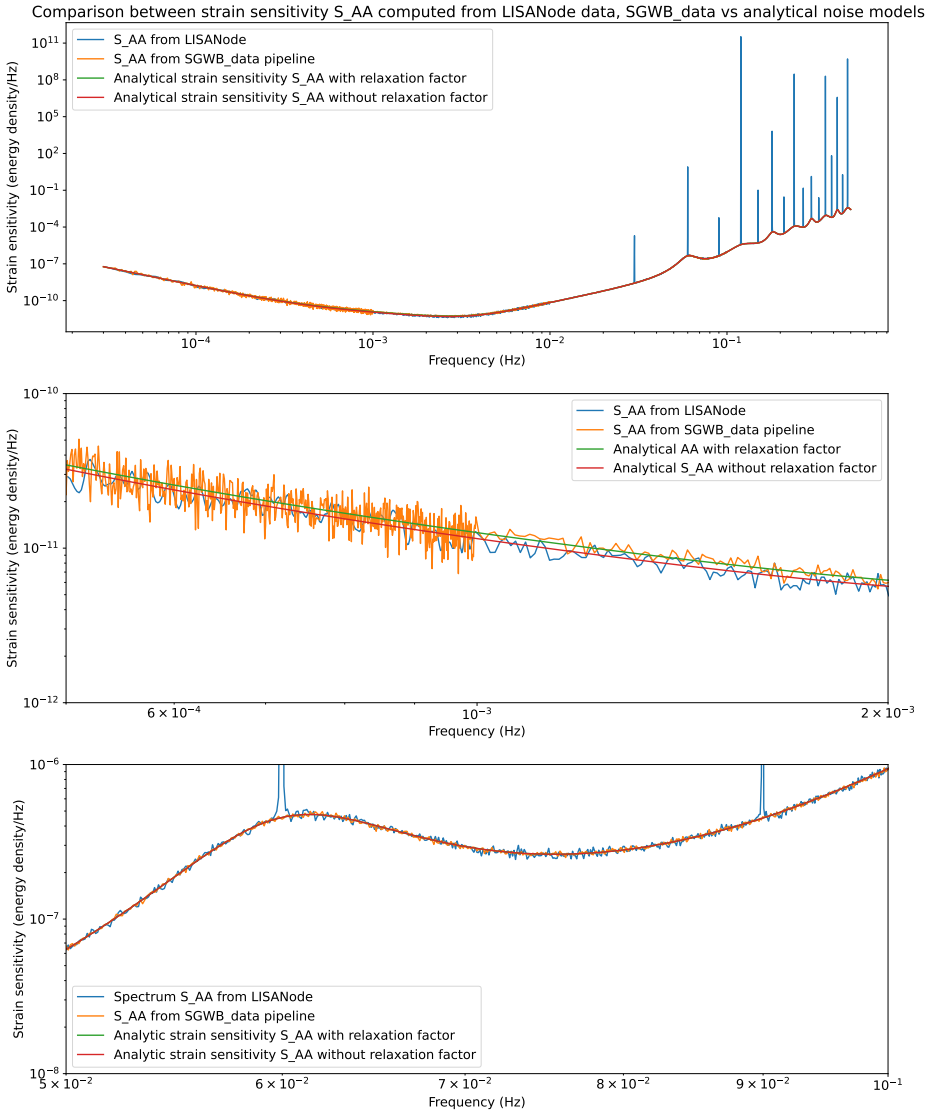

Figure 6.8: Comparison of the strain sensitivity S_{AA} computed from data generated using `LISANode` and the `SGWB_data`, with the analytical 3-parameters noise model. The values of noise parameters are taken from table 6.1. The noises from `LISANode` do not contain the relaxation factor in the OMS noises. The top figure is in the full LISA frequency band. The two bottom ones are zoomed in smaller frequency regions.

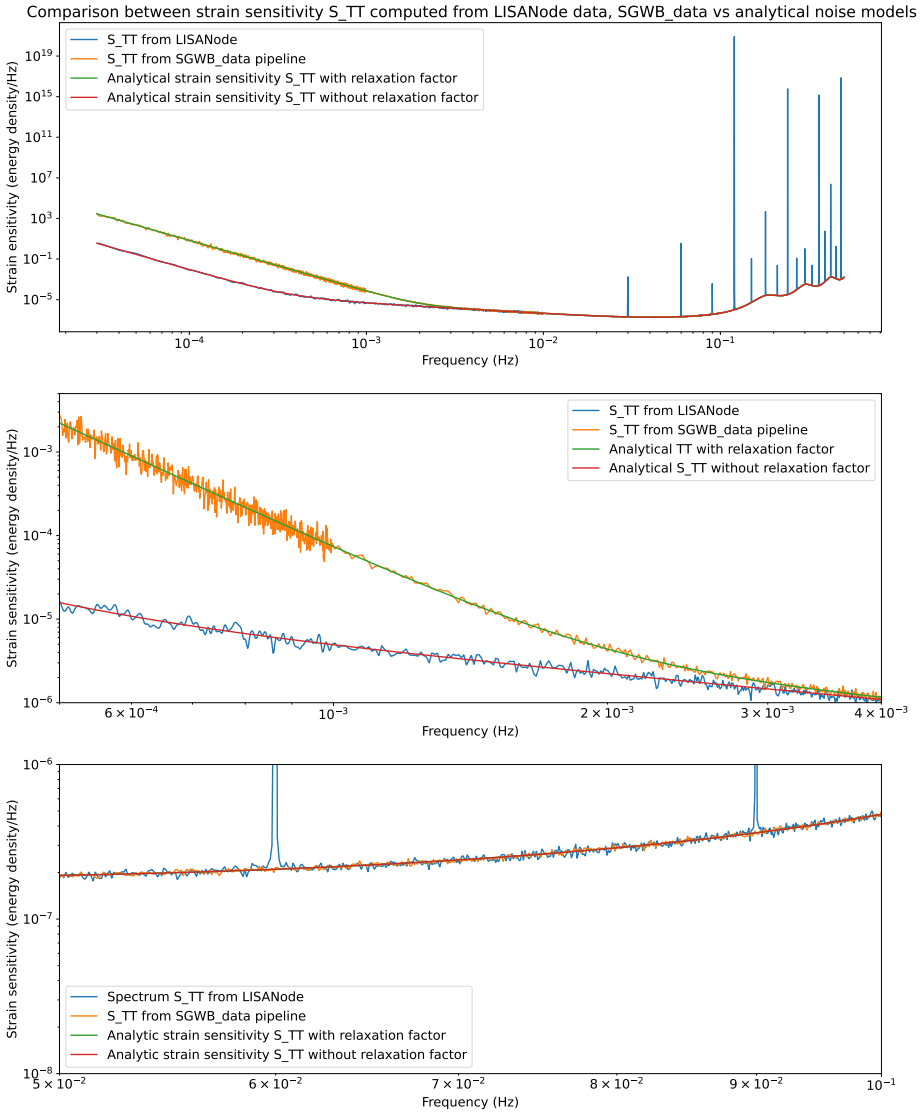

Figure 6.9: Comparison of the strain sensitivity S_{TT} computed from data generated using `LISANode` and the `SGWB_data`, with analytical 3-parameters noise model The values of noise parameters are taken from table 6.1. The noises from `LISANode` do not contain the relaxation factor in the OMS noises. The top figure is in the full LISA frequency band. The two bottom ones are zoomed in smaller frequency regions.

1. Power law SGWB signal, the shape of which is given by

$$h^2\Omega_{\rm gw}(f) = 10^A \left(\frac{f}{f_p}\right)^n . \tag{6.13}$$

We set $A = -12.45, n = 0.67 \approx 2/3$, and $f_p = \sqrt{f_{\rm min} f_{\rm max}}$ is the pivot frequency, typically defined as the geometrical mean of the LISA frequency band $[f_{\rm min}, f_{\rm max}]$. This single power-law template represents the foreground due to SOBHs [52], which potentially emit in the LISA band. As discussed in section 1.3.6, the energy spectral density of the stochastic signal generated during the inspiral phase by many binary systems is proportional to $f^{2/3}$. The amplitude A is computed from the population model of SOBH binaries derived by the LIGO/Virgo observations and has SNR of about 16.

2. "Double" power law SGWB signal, the shape of which is given by

$$h^2\Omega_{\rm gw}(f) = 10^{A_1} \left(\frac{f}{f_p}\right)^{n_1} + 10^{A_2} \left(\frac{f}{f_p}\right)^{n_2} . \tag{6.14}$$

We set $A_1 = -15.5, n_1 = -4, A_2 = -13, n_2 = 3$ and $f_p = 3.2 \times 10^{-3}$. This template is inspired the SGWB generated with first-order phase transitions in the early Universe (see, for example in section 8 and 8.5 in [52]). Searching for this background is one of science objectives of LISA. The shape of the SGWB from first-order phase transitions, expected to be similar to a bell, as illustrated in figure 1.4, peaked at a frequency which can be within LISA frequency bands.

However, we use the reverse shape of the expected signal model in our study. If we can detect the reverse shape of this signal, which is close to the shape of the LISA instrumental noise, in our simulated data, then original shape can be certainly detected as well. The choice of analyzing the reverse shape is therefore motivated by maximizing the potential of detectability of SGWBs from first-order phase transitions by LISA.

We also used a modified version of the broken power law in equation (6.14) to run some tests for the data generation and data analysis pipelines, namely:

$$h^2\Omega_{\rm gw}(f) \quad = \quad 10^A \left(\frac{f}{f_p}\right)^{n_1} \left[\frac{1}{2}\left(1 + \frac{f}{f_p}\right)\right]^{n_2 - n_1} , \tag{6.15}$$

where:

- A is the logarithm of the signal amplitude,
- f_p is the pivot frequency, which we usually choose as the geometric mean of the LISA observation frequency band,
- n_1, n_2 ($n_2 < 0$ and $n_1 > 0$) are the spectral indexes of the power law shape of the SGWB at low and high frequencies, respectively.

- In the the test case, we set $A = -9, f_p = 10^{-2}, n_1 = 6, n_2 = -5$. Note that this parameter choice is not motivated by any theoretical SGWB model.

We also implement the galactic foreground model [128]:

$$S_{\text{galactic\_fg}}(f, A_{\text{fg}}) = 10^{A_{\text{fg}}} f^{2/3} \exp\left[-f^{\alpha} - \beta f \sin(\kappa f)\right] \{1 + \tanh\left[\gamma(f_k - f]\right\}, \quad (6.16)$$

where $f_k, \alpha, \beta, \kappa, \gamma$ are the galactic foreground parameters, given by table 1 in [128]. We use this model with only one free parameter, the log amplitude A_{fg}. The other parameters are set to be fixed at the values corresponding to four years of observation, although we generated data for only 1 year.[3]

6.3 Methodology for data analysis

This section reviews the data analysis algorithm we use to search for the SGWB signal in the simulated data. First, we present the coarse graining of the data, a necessary step in the data processing to reduce the computational work. The coarse graining procedure has been put forward in [54]. Then, we give a brief introduction of the `SGWBinner` software and its data analysis algorithm.

6.3.1 Coarse graining of the data

The outputs of the data generation pipeline (using either `SGWB_data` or `LISANode` codes) are the spectral densities of TDI combinations (L1 data) in frequency domain, as illustrated in figure 6.1 and figure 6.2. The spectral densities are computed by averaging several data chunks, each about 11.5 days long. Hence, the frequency resolution of the output data is about 10^{-6}, which implies a large number of data points at high frequencies in the LISA frequency band. This would increase the computational time, while not providing a significant change in the result at frequencies greater than the resolution. One reasonable solution to reduce computational cost is to coarse-grain the simulated data with an increasing graining factor at higher frequencies. In particular, the values of the data points in the low frequency band (from 3×10^{-5} Hz to 10^{-3}) are not changed, while we split the data at high frequencies (from 10^{-3} to 0.5 Hz) into 1000 intervals of equal log-spacing, and compute the averaged value:

$$\bar{D}_i = \frac{\sum_{j=1}^{N_i} w_j \frac{1}{\sigma_j^2} D_j}{\sum_{j=1}^{N_i} \frac{1}{\sigma_j^2}}, \quad (6.17)$$

[3] It is a convenient choice since we initially want to generate data for 4 years. Unfortunately, the data file size is quite big to handle on our laptop. We will consider alternative ways to work with longer data sequences in subsequent analyses.

where N_i is the number of data points in the interval i, D_j is the value of spectral density data j in the interval, with their weight factor w_j[4], and σ_j^2 is the variance of the data D_j computed in the data generation. Therefore, $\bar{D}_i$ is the representative data for the interval i with error/variance given by $\left(\sum_j 1/\sigma_j^2\right)^{-1/2}$ and weight factor N_i (or $\sum_j w_i$)[5].

6.3.2 `SGWBinner`

The `SGWBinner` is a `Python3` code developed by Mauro Pieroni et al. [54, 69]. It aims at reconstructing the SGWB signal and instrumental noise, including the foreground, for any arbitrary spectral shape for the SGWB signal. It is based on the assumption that the SGWB spectral shape is expected to be sufficiently smooth.

The idea for the reconstruction of an arbitrary shape signal is to divide the LISA frequency band in frequency bins, in which the SGWB is assumed to be a **power law**. One then performs the data analysis in each frequency bin to find the best fit values for the two parameters of the power law SGWB signal, i.e. its amplitude and spectral index. This method is similar to approximating a complex curve by collecting several straight lines.

We assume that the total measurement data provided by the LISA instrument is the uncorrelated sum of the GW signal $\Omega_{\rm gw}$ and the noise $\Omega_{\rm n}$,

$$h^2\Omega_{\rm tot} = h^2\Omega_{\rm gw} + h^2\Omega_{\rm n}. \tag{6.18}$$

The noise models used in the data generation, discussed in section 6.2.3, are the reference for the noise model in the data analysis. Accordingly, we have 2 or 3 parameters to be accounted for in the estimation, based on the noise model used in the data analysis. We treat the foreground as noise and it is due to the galactic binaries, expressed by (6.16): this indicates one extra parameter to be estimated. On the other hand, the signal model for the data analysis is a piece-wise suite of power laws on a set of frequency bins, obtained by dividing the LISA frequency band into $N_{\rm bins}$ equally log-spaced frequency intervals:

$$h^2\Omega_{\rm gw} = \sum_{i=1}^{N_{\rm bins}} 10^{\alpha_i} \left(\frac{f}{\sqrt{f_{{\rm min},i} f_{{\rm max},i}}}\right)^{n_{t,i}} \Theta(f - f_{{\rm min},i})\Theta(f_{{\rm max},i} - f), \tag{6.19}$$

where $\alpha_i, n_{t,i}$ are the two parameters, i.e. logarithmic amplitude and spectral index (tilt), characterizing the power law SGWB signal in the bin i; Θ is the Heaviside step function; $f_{{\rm min},i}, f_{{\rm max},i}$ are the bounds of the frequency bin i. Hence, the total number of parameters to estimate is proportional to $N_{\rm bins}$. In particular, it is $N_n + N_{\rm fg} + 2N_{\rm bins}$, accounting for 2 or 3

[4] We remind that $w_j = 1$ for all j, except the case of `LISANode` data when we need to mask the data to avoid the singularity spikes in the strain sensitivity. The weight factors for the data points in the vicinity of the spike are set to be 0.

[5] In principle, $N_i = \sum_j w_j$ except for the case of `LISANode` data.

parameters of the noise model, 1 parameter for the galactic foreground (in included), and two parameters of the power law in each frequency bins.

6.3.3 Bayesian data analysis

The `SGWBinner` uses a data analysis technique based on the Bayesian theorem to estimate the parameters. In the Bayesian approach, the posterior probability for the model parameters is given by [104, 69]

$$P(\vec{\theta},\vec{n}|D) = \frac{\pi_S(\vec{\theta})\pi_N(\vec{n})\mathcal{L}\left(D|\vec{\theta},\vec{n}\right)}{p(D)}, \tag{6.20}$$

where $\mathcal{L}(D|\vec{\theta},\vec{n})$ is the likelihood of the experimental (or simulated) data D given by the model consisting of a set of signal parameters $\vec{\theta}$ and noise parameters $\vec{n}$; $\pi_N(\vec{n}), \pi_S(\vec{\theta})$ are the prior distribution for the noise and signal parameters, respectively; $p(D)$ is the model evidence, which is generally a constant normalized factor. We are not interested in the model evidence in this study, so from now on, we will work with the unnormalized posterior, which is the numerator of equation (6.20). In addition, we omit the D in the notations from now on for simplicity. We usually use the log posterior function for convenience:

$$\ln P(\vec{\theta},\vec{n}) = \ln \pi_S(\vec{\theta}) + \ln \pi_N(\vec{n}) + \ln \mathcal{L}(\vec{\theta},\vec{n}). \tag{6.21}$$

The priors of the noise and foreground (if included)[6] parameters are assumed to be Gaussian distributed, so that

$$\pi_N(\vec{n}) \sim \mathcal{N}(\vec{\mu},\Sigma), \tag{6.22}$$

where $\mathcal{N}$ is a Gaussian distribution, the mean $\vec{\mu}$ is the set of true (injected) values of the noise parameters $\vec{n}$ in the simulation, and Σ is the covariance matrix for the distribution. We set $\Sigma = \mathrm{diag}(0.2\vec{\mu})^2$, where diag stands for a diagonal matrix, assuming the noises are uncorrelated and their individual standard deviations are 20 percent the true values. Hence, the contribution of noise prior in the log posterior, equation (6.21), is:

$$\ln \pi_N(\vec{n}) = -\sum_i \frac{1}{2}\left[\ln(2\pi\sigma_i^2) + \left(\frac{n_i-\mu_i}{\sigma_i}\right)^2\right], \tag{6.23}$$

where i is the noise parameter index; n_i, μ_i are the ith-components of the noise parameter vector $\vec{n}$ and of true-value vector $\vec{\mu}$, respectively; σ_i is the standard deviation of the Gaussian distribution for the noise i.

The priors for the signal parameters are generally model-dependent. In `SGWBinner`, we fit parameters for a power law SGWB signal in each bin. To adapt an arbitrary overall SGWB, we

[6] From now on, we consider the foreground as an extra noise component. The foreground parameters are included in the noise parameter vector.

use uniform distributions for the priors of the log amplitude and the spectral index parameters to estimate them in every frequency bins. The range of the uniform distributions for the log amplitude parameter is from -30 to -5 with the initial guess value is -30. While the range for the spectral index is from -50 to 50 with the initial guess value is 0. The minimum log amplitude and null spectral index are chosen for the initial guess values for a prediction of no significant SGWB signal at the beginning. Therefore, the signal prior attributes to the total log posterior as a constant:

$$\ln \pi_S(\vec{\theta}) = \sum_i 1/(\max_i - \min_i), \tag{6.24}$$

where i is the signal parameter index; $\max_i, \min_i$ are, respectively, the maximum and minimum values for the prior of signal parameter i. Since a constant plays no role in maximizing the posterior, we can choose the log prior of signal parameters equal to 0.

The likelihood function is built by combining a Gaussian likelihood and a log-normal one [69]:

$$\ln \mathcal{L} = \frac{1}{3} \ln \mathcal{L}_G + \frac{2}{3} \ln \mathcal{L}_{LN}, \tag{6.25}$$

where the Gaussian likelihood is defined as:

$$\ln \mathcal{L}_G \left(D|\vec{\theta}, \vec{n} \right) = -\frac{N_c}{2} \sum_{i,j} \sum_k n_{ij}^{(k)} \left[\frac{\mathcal{D}_{ij}^{theory}(f_{ij}^k, \vec{\theta}, \vec{n}) - \mathcal{D}_{ij}^{(k)}}{\mathcal{D}_{ij}^{theory}(f_{ij}^k, \vec{\theta}, \vec{n})} \right]^2, \tag{6.26}$$

and the log-normal likelihood is expressed by

$$\ln \mathcal{L}_{LN} \left(D|\vec{\theta}, \vec{n} \right) = -\frac{N_c}{2} \sum_{i,j} \sum_k n_{ij}^{(k)} \ln^2 \left[\frac{\mathcal{D}_{ij}^{theory}(f_{ij}^k, \vec{\theta}, \vec{n})}{\mathcal{D}_{ij}^{(k)}} \right]. \tag{6.27}$$

In the above equations, i, j are TDI channels ({A,E,T} in our case); k is the bin index; $n_{ij}^{(k)}$ is the number of considered data points (in other words, the data point with non-zero weight factor) within the bin k; $\mathcal{D}_{ij}^{theory}(f_{ij}^k, \vec{\theta}, \vec{n})$ is the model for the data within the bin k, including the noise and the signal (if any) models presented in sections 6.2.3, and 6.2.4; $\mathcal{D}_{ij}^{(k)}$ are the simulated data in the bin k, depending on the true (injected) values of noise and signal parameters in the simulator.

For the parameter estimation, we use the conditions of Maximum A Posteriori (MAP) values, defined as

$$\partial_j \ln P(\vec{\theta}, \vec{n})\Big|_{\vec{\theta}_b, \vec{n}_b} = 0, \tag{6.28}$$

where $\vec{\theta}_b, \vec{n}_b$ are the vectors of the best fit values of the signal and the noise (including foreground if any) parameters, respectively, and j is the index running over the total number of

parameters (noises, signal, foreground). One can recognize that these conditions are the differential equations for finding the local maxima of a function depending on a set of parameters. In addition, a useful quantity is the Fisher information matrix, defined as

$$\mathcal{I}_{ij} \equiv -\,\partial_i \partial_j \ln P(\vec{\theta}, \vec{n})\Big|_{\vec{\theta}_b, \vec{n}_b}\,, \tag{6.29}$$

where again i, j are indices run over the total number of parameters, including noises, foreground (if any) and SGWB signal (if any). The Fisher information matrix is used to compute the covariance matrix of the estimated parameters, assuming they are Gaussian distributed, and then the contours for the parameter estimation. The covariance matrix is the inverse of the Fisher matrix,

$$C_{ij} = \mathcal{I}_{ij}^{-1}. \tag{6.30}$$

If the noise components are uncorrelated, we have

$$C_{ab} \approx \mathrm{diag}(\vec{\sigma^2}), \tag{6.31}$$

where a, b are the indices run over the number of the **noise** parameters, and $\vec{\sigma^2}$ is a set of variances of the noise parameters. These variances can be used to construct the reference priors (Jeffrey's prior, for example, see in pages 314, 315 in [48]) for the noise parameters. This is the way how we redefine the noise prior for the AA, EE channels based on the parameter estimation in TT channel, as described later in section 6.3.4.

6.3.4 Algorithm for the binned reconstruction by `SGWBinner`

The algorithm of the `SGWBinner` code is first introduced in [54] and modified for an improved version in [69]. In this work, we use the improved algorithm, which is summarized from [69], in the following procedure:

1. We first use the TT-channel data to redefine the prior for the noise parameters since any GW signal is significantly suppressed at low frequencies in this TDI combination. As shown in [126], the SNR of a GW signal in the TT channel is much smaller than in the AA and EE channels. Hence, we expect to constrain the better noise prior from TT-channel data before applying it in the signal reconstruction for the data of AA and EE channels.

   In practice, the `SGWBinner` computes the log posterior in the TT channel of a power law signal and a given noise, e.g. the 3-parameters noise model expressed in (6.12). From maximizing that log posterior in equation (6.28), the code estimates the best fit values for the signal and noise parameters. The noise prior using in this parameter estimation is described in previous section 6.20: Gaussian distribution for noise parameters and

normal distribution for signal parameters. Then, we compute the Fisher information matrix (6.29). The noise block in this Fisher information matrix is used to redefine the priors for noise parameters. These new noise priors is applied for computing the log posterior in AA and EE channels.

2. The next step is to bin the data (AA and EE channels) in frequency in an arbitrary number of initial bins, N_b. At the end of this step, the total frequency interval is split into N_b equally log-spaced frequency bins.

3. Then, we estimate the parameters of the noise, the foreground (if any) and a power law signal independently in each bin, by maximizing the log posterior function, expressed in equation (6.21). In other words, we find the best fit values of the parameters, fulfilling the condition (6.28). This comprises two signal parameters, two or three noise parameters depending on the adopted noise model, and one parameter for the foreground model (we use the galactic foreground model with one free parameter (6.16)). The noise and signal models are introduced in sections 6.2.3 and 6.2.4. Since the data in AA and EE channels are almost similar, we only show the reconstruction and parameter estimation results for data in AA channel in this thesis.

4. By dividing the frequency interval into bins, we can improve the signal reconstruction for an arbitrary SGWB with complicated spectral shape. However, having too many bins would lead to unnecessary fitting parameters in the data analysis process, and possibly degrade the result. Therefore, we apply an iterative process to merge two nearby bins if appropriate. This makes use of the Akaike Information Criterion (AIC) quantity [9], defined as

$$\mathrm{AIC} \equiv \chi^2_{\text{best fit}} + 2k, \tag{6.32}$$

where $\chi^2_{\text{best fit}} = -2\ln\mathcal{L}|_{\vec{\theta}_b,\vec{n}_b}$; k is the number of parameters to estimate (which is, in our case, proportional to the number of bins). It is statistically favored to merge one or more nearby bins if the AIC of the parameter estimation performed in the merged bins is smaller than the one performed in the original bin configuration. If so, the `SGWBinner` code redefines the bin configuration (i.e. it merges the two initial bins into a single one) and repeats the previous step of the parameter estimation by maximizing the likelihood in the merged bins. This process is done iteratively until having a bin configuration with the smallest AIC value.

5. When the number of bins has converged, the code computes the error of the signal and noise reconstructions with the Fisher information matrix (6.29). The `SGWBinner` decides whether a power law GW signal is detected in a bin based on the information of its amplitude (if the best fit value of the log amplitude is above the threshold -20, which

is the expected amplitude level for a signal detectable by LISA), and of the statistic of the estimation.

6. It is possible to include an optional step in the algorithm consisting in a MCMC sampler on the total posterior of all bins and all channel combinations. In particular, once the optimal number of bins has been obtained after the merging process, a MCMC algorithm estimates the parameters of a power law signal in every merged bin, and the parameters of the noise model common to the whole frequency band. The parameters of the foreground are also estimated globally, as the noise parameters. The MCMC sampler code used in this study is `PolyChord` [74, 75] via its interface with `Cobaya` [146]. The data analysis results are conducted using `GetDist` [101]. This process provides a more accurate estimation of the parameters and improves the components reconstruction with less uncertainty. However, the authors in [69] found that there is little difference between the results provided by the `SGWBinner` including MCMC option and excluding it. In our study, we try to run the `SGWBinner` with the MCMC option wherever possible.

We illustrate the `SGWBinner` data analysis pipeline in figure 6.10.

6.4 Results

This section presents some preliminary results using `SGWBinner`. We first examine noise-only data, without any SGWB signal. In this the case, we have generated the data using either `LISANode` or `SGWB_data`. We then proceed to analyze the data including SGWB signals, generated according to the templates presented in section 6.2.4. In addition, in some cases we also include the galactic foreground in the data.

6.4.1 Noise-only data

In order to demonstrate that the noise reconstruction works well in the simplest case, we first run the `SGWBinner` on the noise-only one-year data generated with `SGWB_data`. In this run, the parameter estimation is performed with the MCMC global fit, i.e. in one single bin. We adopt **the same 3 parameters** noise model in both the data generation and the data analysis pipelines. The result is shown in figure 6.11. It appears from the triangle plot in figure 6.11b that the estimated amplitude of the signal has a probability distribution compatible with zero, so that there is no signal detection. Furthermore, the noise has been reconstructed well, since the 1σ regions of the reconstructed noise parameters include the true (injected) values $A = 2.4, P = 8.96, C = 5.38$[7]. Hence, no SGWB signal is detected in this case as, it should be

[7] The C value here is different from the one presented in table 6.1 since this data set is generated with an old version of `SGWB_data`.

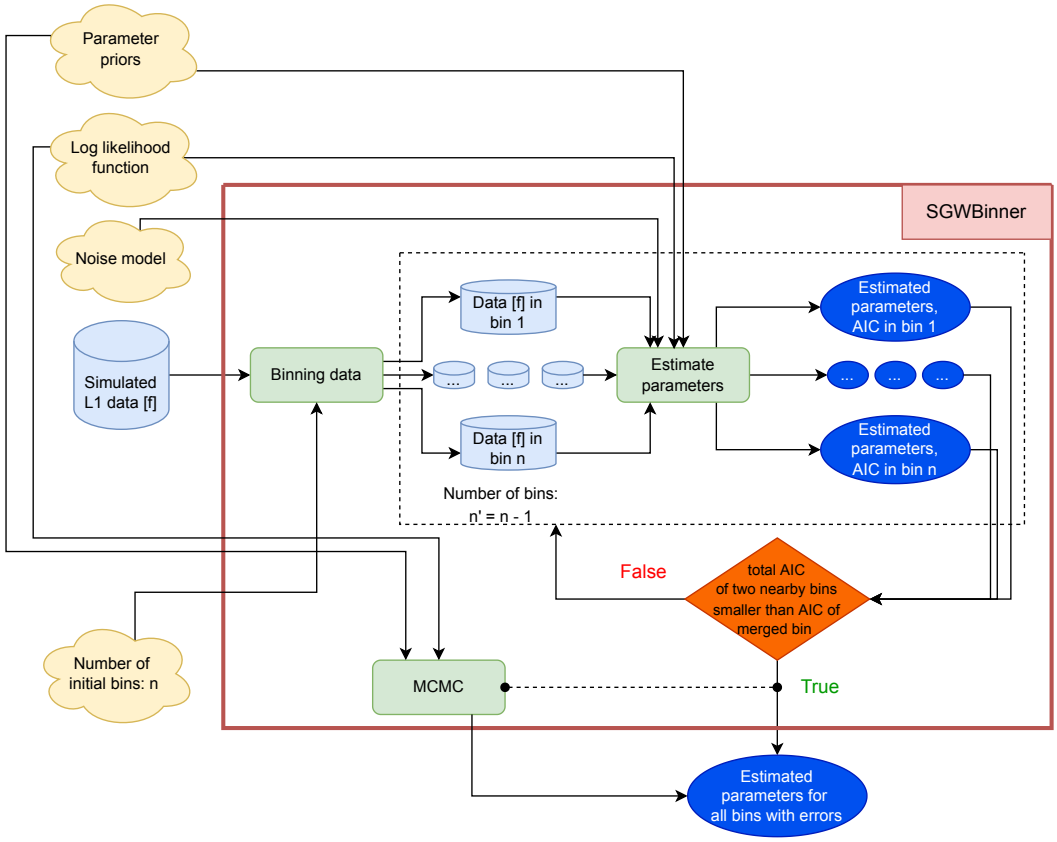

Figure 6.10: Schematic of the data analysis pipeline using the `SGWBinner`. See sections 6.3.2 and 6.3.4 for detailed description.

since we have a good prior knowledge of the noise model used in the data generation, and we fit this exact model to the data. The contour plot for P and C parameters, it indicates a strong anti-correlation between the two parameters. However, there is no physical process explaining that anti-correlation between OMS noise amplitudes in TMI and ISI/RFI measurements.The anti-correlated behavior of P and C parameters is due to fact that we assume they have the same noise shape as expressed in equations (6.7) and (6.8). After propagating through the TDI algorithm, they still share some common terms, although the two total transfer functions are different. As shown in equation (6.11), the common term is associated with $1 + \cos(2\pi f L/c)$. Therefore, in the parameter estimation, the larger value of P will constrain the smaller value of C and vice versa.

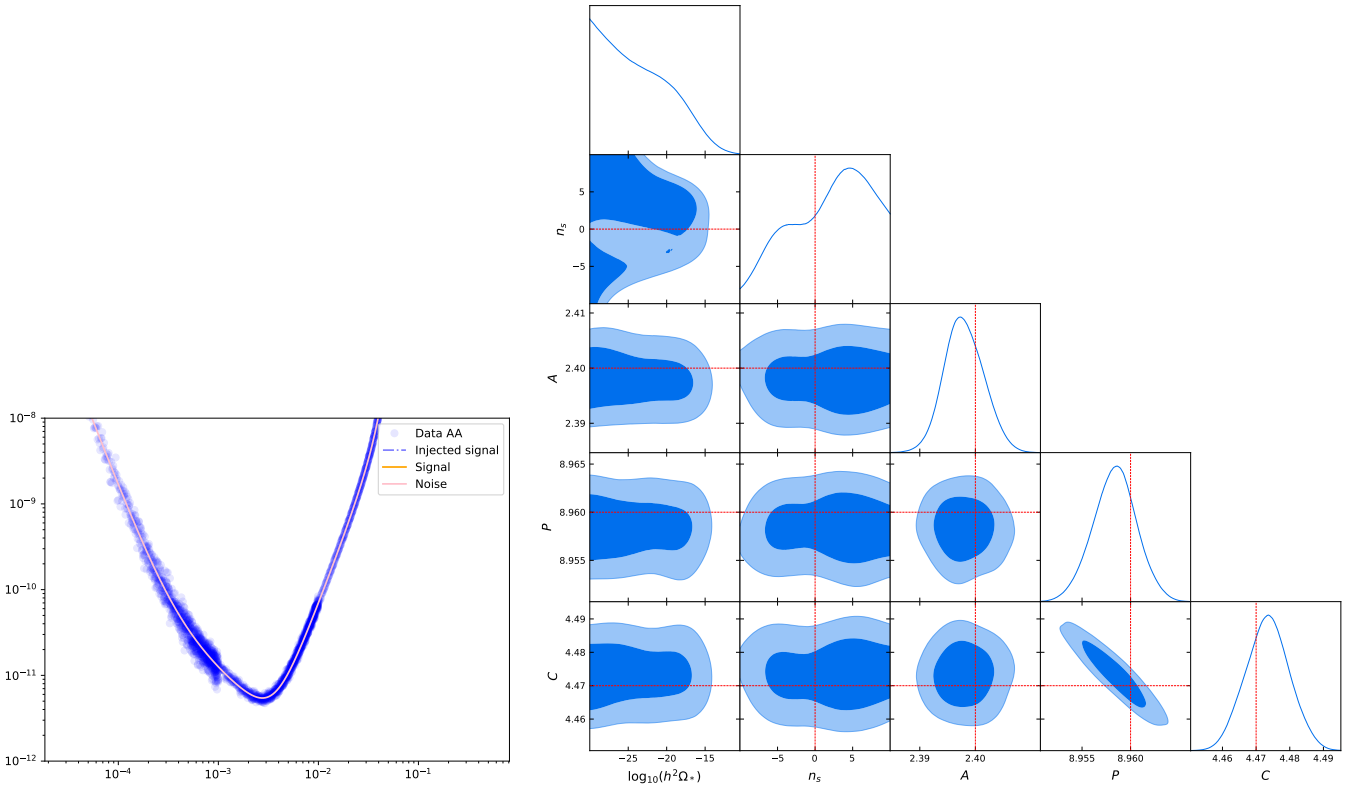

(a) Reconstruction plot

(b) Triangle plot from parameter estimation

Figure 6.11: Reconstruction plot and probability distributions of the estimated parameters. The data analysis is performed using `SGWBinner` with the MCMC global fit, on the **noise-only data** generated with `SGWB_data`, using the **same 3 parameters noise model** in both the data generation and the data analysis pipelines. Subfigure (a) is the reconstruction plot showing no signal detection, in agreement with the fact that there is no injected signal in the data. Subfigure (b) is the triangle plot showing the cross correlation of all parameters (noise and signal). The top plot in each column is the probability density distribution of each parameter, and the bottom ones are the correlations of that parameter with the others. The true (injected) values used in the data generation pipeline are indicated by the red dashed lines. There are no injected signal so that its true amplitude and spectral index (tilt) are zeros. The bold blue colored area shows the 1σ confidence interval region, while the faint blue one represents the 2σ confidence interval region.

In addition, we perform an analysis using the `SGWBinner` with 10 initial bins, and with Fisher parameter estimation only to check if we miss any SGWB signal due to the fact that we do a global fit in the previous case[8]. The reconstruction plot presented in figure 6.12 confirms our conclusion that no SGWB signal is detected when one adopts the same noise model in both the data analysis and the data generation pipelines. In the figure, we also show the power law sensitivity curve (PLS) with the SNR of 10, in 4 years mission duration, and duty cycle 75%, as a reference for the amplitude of the SGWB signal which could be detected by LISA. We will show this curve in all the reconstruction plots in the rest of this chapter.

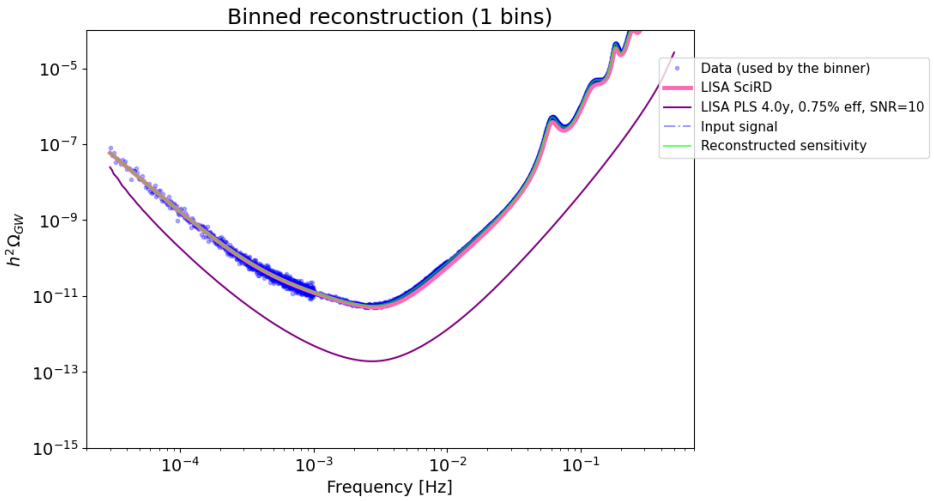

Figure 6.12: Reconstruction plot obtained by running the `SGWBinner` without MCMC option, starting from 10 initial bins, on **noise-only data** generated with `SGWB_data` in one year. The **same noise model**, characterized by **3 parameters** (A, P, C), is used in both the data generation and the data analysis pipelines.

We also analyze the noise-only data generated using `LISANode`. This data set is more complicated to analyze, since one needs to mask the data points around the singularity spikes as discussed in section 6.2.2. From figure 6.13, it can be appreciated that a SGWB signal is erroneously detected in the data. In addition, the estimation of the noise parameters, shown in figure 6.13b, indicates that the reconstruction of the noise model is biased. The probability distributions of the amplitude of the test-mass acceleration noise, A, and the one of the OMS noise in ISI/RFI measurements, P, do not contain the injected values. We need to investigate more in depth this problem arising with data generated in time-series before any further analysis with `LISANode` simulated data. We defer this to future analyses.

[8]The `SGWBinner` has a problem when running with the MCMC option and several initial bins (no global fit) on the noise-only data with the same noise model in both the data generation and the data analysis pipelines. Since we used the exact noise model, the SGWBinner gives zero-compatible distribution for the SGWB signal. The `PolyChord` and `Cobaya` packages, which are used for running MCMC, seems not to be able to run in this case. We will see with the authors of these codes.

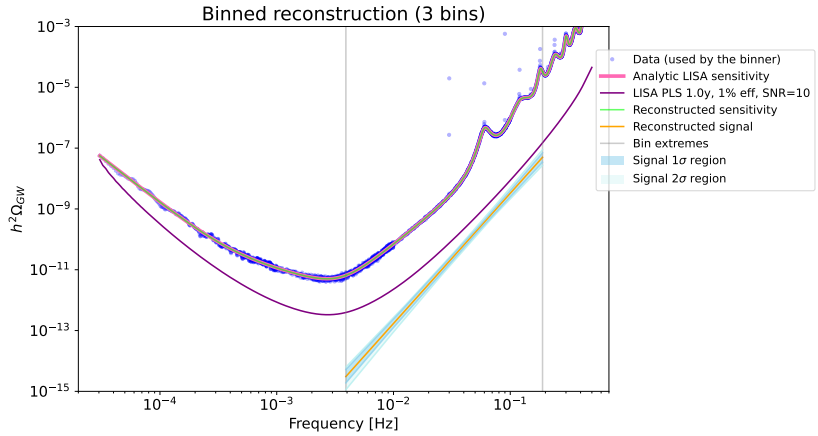

(a) Reconstruction plot

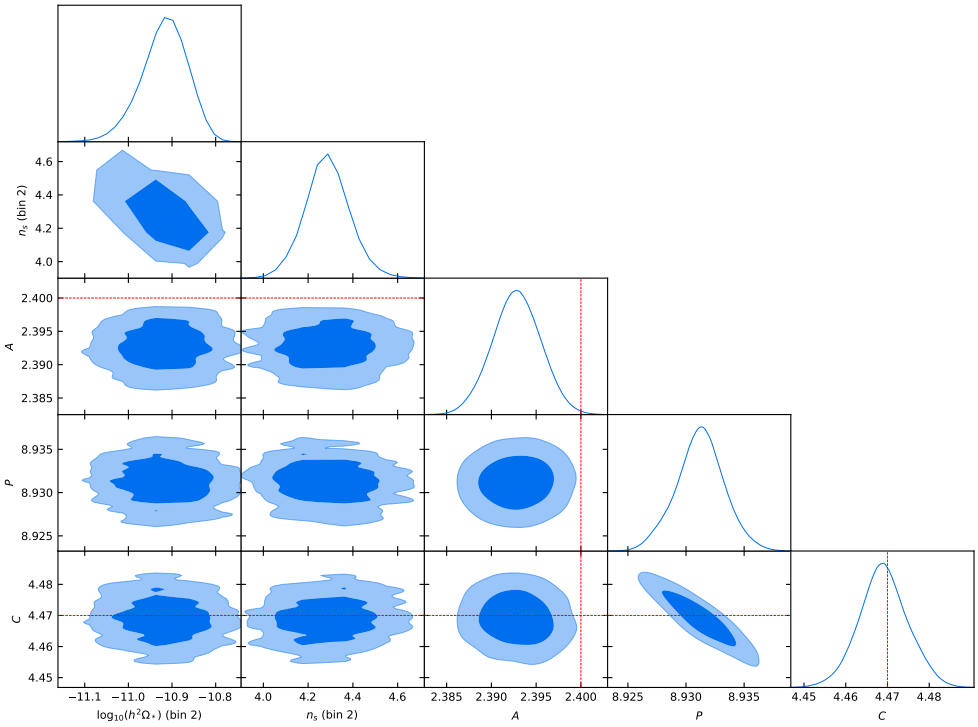

(b) Triangle plot

Figure 6.13: Results obtained by running `SGWBinner` with the MCMC option, starting from 10 initial bins, on the **noise-only data** generated with `LISANode` in one year, AET 2.0, and **1% mask-out** in log frequency around singularity spikes. The **same noise model**, characterized by **3 parameters** (A, P, C), is used in both the data generation and the data analysis pipelines. Subfigure (a) is the reconstruction plot of the data. A power law signal is erroneously detected in the second bin although there is no injected signal in the data. Subfigure (b) is the combined triangle plot of all estimated parameters, including two parameters for the fake signal, and three ones for the noise. The red dashed lines indicate the true (injected) parameter values used in the data generation pipeline. We note that the P-parameter injected value lies outside the figure margins, while there is no references for the true signal parameter values (no injected signal).

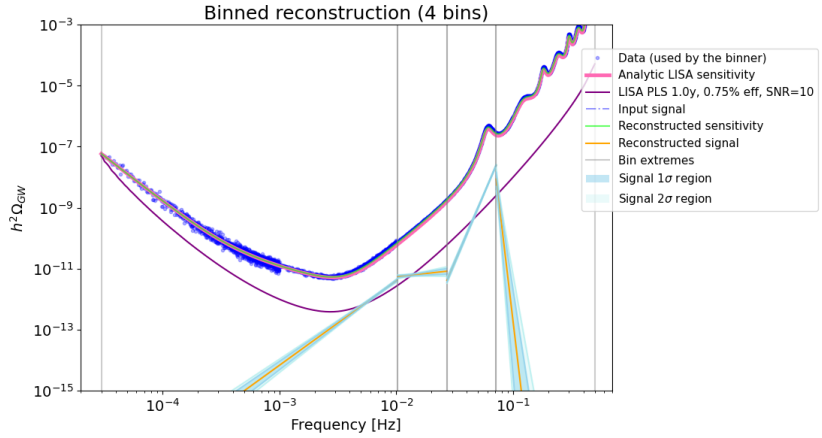

(a) Reconstruction plot

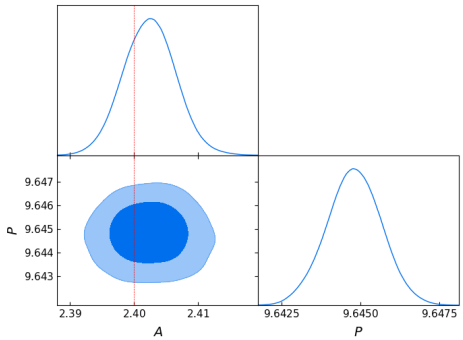

(b) Noise parameter estimation

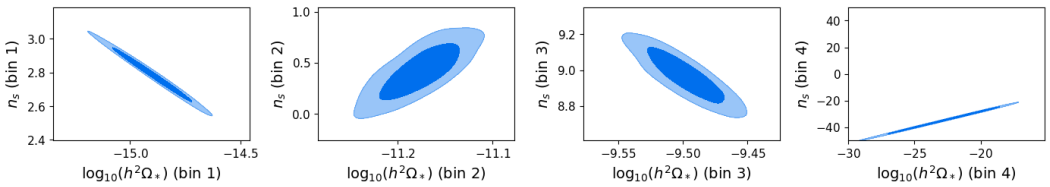

(c) Signal contour plot

Figure 6.14: Results obtained by running the `SGWBinner` with MCMC option, starting from 10 initial bins, on the **noise-only data** generated with `SGWB_data` in one year, AET 2.0. The SciRD noise model, characterized by **2 parameters** (A, P), is adopted for in the data analysis, while we use the **3 parameters** model for the data generation pipeline. Subfigure (a) is the reconstruction plot showing a fake signals detection, although there is no injected signal in the data. Subfigure (b) presents the marginal probability distributions for the 2 noise parameters, A, P, with the red dashed line indicating the true (injected) value used in the data generation pipeline (see table 6.1). We note that the P-parameter value lies outside the figure margins. Subfigure (c) presents the contour plots of the cross correlation between the two parameters of the detected power law signals in every bin. A fake signal is clearly detected in all 4 bins according to these contour plots. We skip the triangle plot for combined parameters (noise and signal).

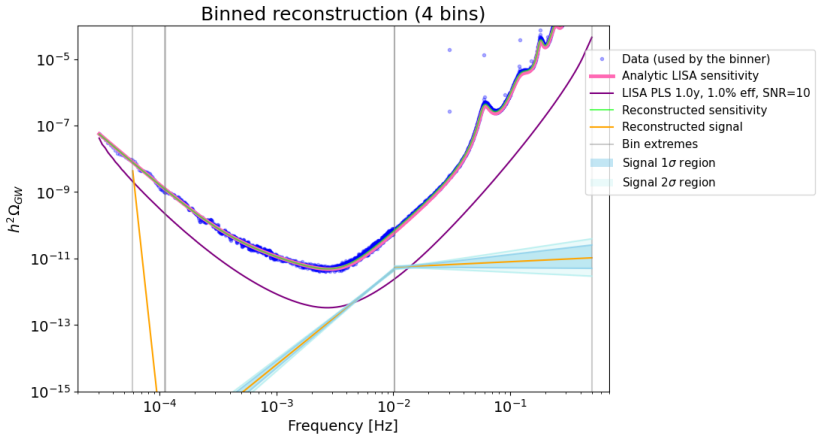

(a) Reconstruction plot

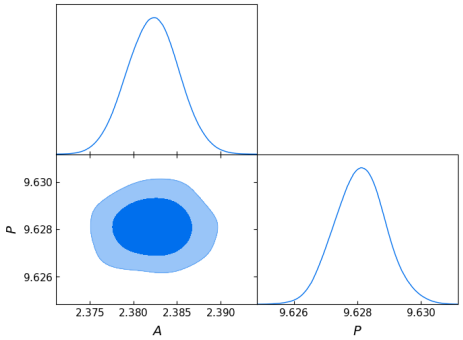

(b) Noise parameter estimation

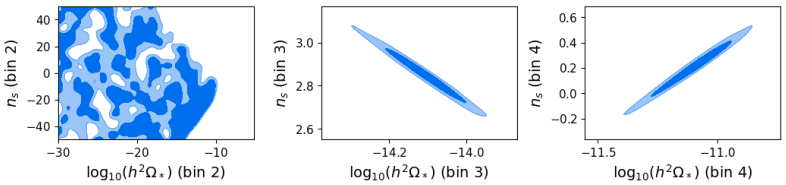

(c) Signal contour plot

Figure 6.15: Results obtained by running `SGWBinner` with MCMC option, starting from 15 initial bins, for **noise-only data** generated with `LISANode` in one year, AET 2.0. The SciRD noise model, characterized by **2 parameters** (A, P), is adopted for the **data analysis**, while we use the **3 parameters** noise model for the **data generation** pipeline. Subfigure (a) is the reconstruction plot showing fake signals detection in 3 bins, although there is no injected signal in the data. Subfigure (b) presents the marginal probability distributions for the 2 noise parameters, A, P. The red dashed lines indicating the true (injected) values used in the data generation pipeline, see table 6.1, are out of the range of the plot's axes. Subfigure (c) presents the contour plots of the cross correlation between the two parameters of the detected power law signals in every bin. These plots indicate that a fake signal is clearly detected in bins 3 and 4.

We also perform a data analysis run adopting a noise model in the data analysis, which is different from the one used in the data generation. In particular, we use the LISA SciRD noise model, characterized by two noise parameters (presented in section 6.2.3) to analyze the data generated with the 3-parameters noise model. This study aims at testing the performance of the `SGWBinner` in searching SGWBs in the data with inaccurate knowledge of the noise that contaminated the signal. In fact, it is possible to know some noise contributions in the LISA mission, but others will not be well-measured/modelled, or might even be unknown. The results of the data analysis using `SGWBinner` with MCMC option are shown in figure 6.14 on the data generated using `SGWB_data`, and in figure 6.15, and ones generated using `LISANode`. In both approaches, some power law signals are erroneously detected in several bins of the noise-only data. It is due to the mismatch between the noise model used for the reconstruction and the one used in the data generation. This result implies that the noise knowledge plays a crucial role in the SGWB data analysis. Although the `SGWBinner` can fit the parameters for the overall noise level, the parameter estimation results are unreliable if the true noise's shape is different from the one attributed to the simulated data (or to the realistic experimental data).

6.4.2 Data including signal and noise

The next data set in our study includes the instrumental noise and a SGWB signal. We examine some shapes of SGWB signal presented in 6.2.4, which are injected using exclusively the data generation pipeline of `SGWB_data`. All data sets using in this subsection are generated in one year, 75% duty cycle, and in TDI combination AET 2.0.

Broken power law

The first model of SGWB used in the data generation is a broken power law signal, given by expression (6.15). The signal parameters in the data generation are set to $A = -9, f_p = 10^{-2}, n_1 = 6$ and $n_2 = -5$. This choice is adopted for test purposes, and is not motivated by any theoretical model of SGWB.

Figure 6.16 shows the result of the data analysis done with the `SGWBinner` on data generated with `SGWB_data`, when we adopt the same noise model in the data analysis as the one implemented in the data generation pipeline. The 10 initial bins have converged to 5 final bins, and in each of them there is a signal detection with a power law shape. This allows us to reconstruct approximately the shape of the injected signal in the data. In the outermost merged bins, the signal parameters are not estimated well and the 1σ regions of the reconstructed signals do not include the injected (input) signal. It can be explained by the fact that the noise is dominant in these frequency regions compared to the signal. Hence, the biases in the noise parameter estimation can lead to bigger biases in the signal parameter estimation.

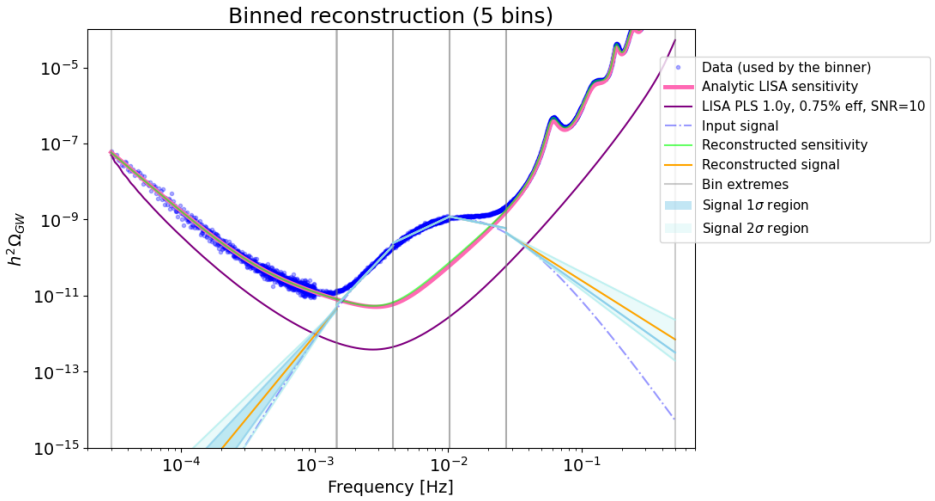

(a) Reconstruction plot

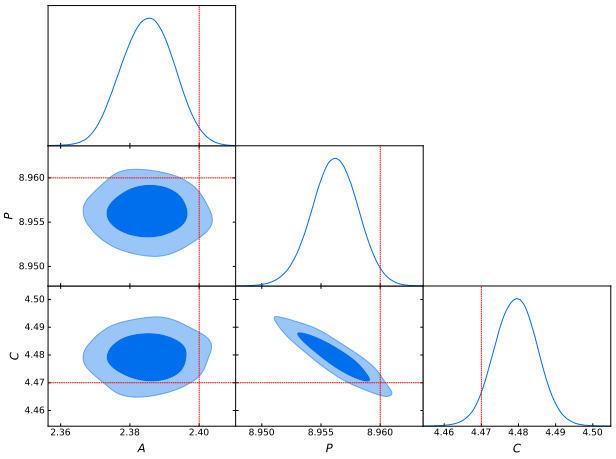

(b) Noise parameter estimation

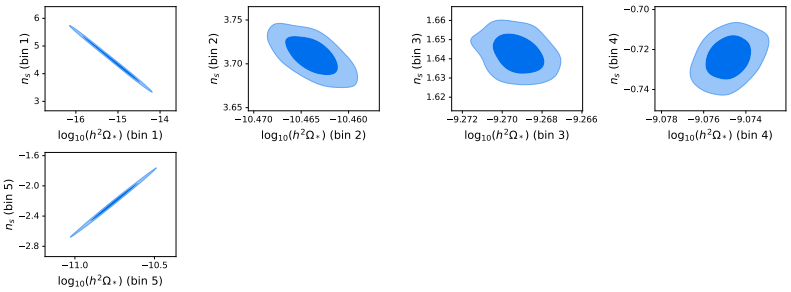

(c) Signal contour plot

Figure 6.16: Results obtained by running `SGWBinner` with the MCMC option, starting from 10 initial bins, on data including **noise and a broken power law SGWB signal**. The **same 3-parameters noise model** is used in both the data generation and the data analysis pipelines. Subfigure (a) is the reconstruction plot showing a signal detection. From the 10 initial bins, the `SGWBinner` converges to 5 final bins and gives the parameter estimation for a power law signal in each merged bin. The collection of these power law shapes gives an approximated broken power law signal. Subfigure (b) presents the marginal probability distributionss of the 3 noise parameters, A, P, C, with the red dashed lines indicating the true (injected) values used in the data generation pipeline (see table 6.1). Subfigure (c) presents the contour plots of the cross correlation between the two parameters of the detected power law signals in every bin.

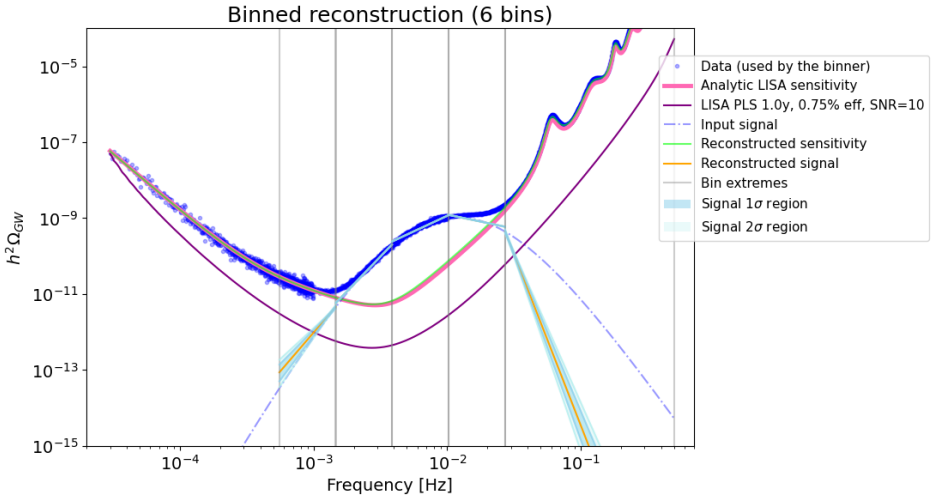

(a) Reconstruction plot

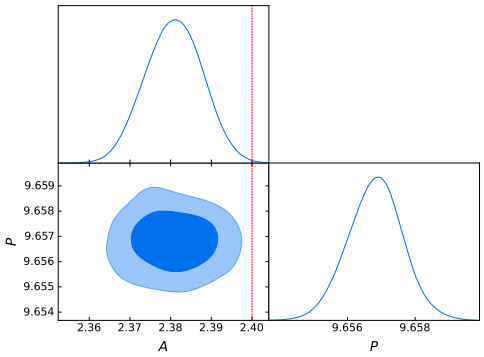

(b) Noise parameter estimation

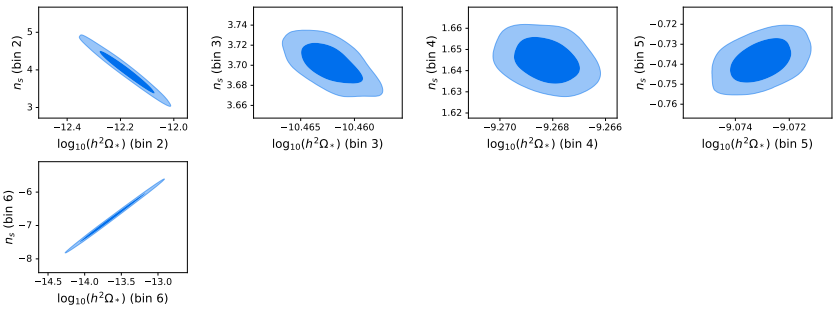

(c) Signal contour plot

Figure 6.17: Results obtained by running `SGWBinner` with the MCMC option, starting from 10 initial bins, for data including **noise and a broken power law** SGWB signal. The SciRD noise model, characterized by **2 parameters** (A, P), is adopted for the data analysis, while we use the **3 parameters** (A, P, C) model for the data generation pipeline. Subfigure (a) is the reconstruction plot showing a signal detection. The `SGWBinner` merges the 10 initial bins into 6 bins. In 5 of the merged bins, the code detects a power law signal for each. For the first bin, the parameter distribution is compatible with the no signal detection. Subfigure (b) presents the marginal probability distributions for the 2 noise parameters, A, P, with the red dashed lines indicating the true values used in the data generation pipeline presented in table 6.1. The red dashed line corresponding to the P parameter is not visible since its true value is out of range of the plot's axes. Subfigure (c) presents the contour plots of the cross correlation between the two parameters of the detected power law signals in every bin.

The result worsens if we use different noise models between the data generation and the data analysis pipelines, as illustrated in figure 6.17. The signal reconstructions for the inner bins, where the SGWB signal has high SNR, are still good. However, the reconstruction results in the outermost bins are not convincing. In addition, we see in figure 6.17b that the noise parameter estimation is biased, especially for the OMS noise parameter P. This bias in the noise parameter estimation is probably the reason for the bad signal reconstruction in the outermost bins, where the noises are dominant over the SGWB signal.

Power law

We also inject in the data a power law SGWB signal given by (6.13). This signal is predicted to be generated by the inspirals of SOBH binaries. The signal parameters chosen for the data generation are $A = -12.45, n = 0.67$.

When one adopts the same noise model in both the data generation and the data analysis pipelines, the `SGWBinner` gives pretty good results for the noise and signal reconstructions, as shown in figure 6.18. From the plot 6.18b, one appreciates that the 2σ regions of the estimated parameters of the signal and the noise contain the true (injected) values.

On the contrary, the result is not convincing when the noise model (SciRD or 2-parameters noise model) used in the data analysis is different from the one (3-parameters noise model) used in the data generation, see figure 6.19. The reconstructed signal does not match with the injected (input) signal in the simulated data. In addition, the estimated noise parameters are biased: the true values of noise parameters are outside of 2σ regions of the estimated ones. We recognize that the reconstructed signal is further away from the injected one at high frequency, where the two noise models are discrepant, see figure 6.4.

"Double" power law

In this case, a "double" power law SGWB signal, expressed in (6.14), is injected in the data. We choose the injected signal parameters as $A_1 = -15.5, n_1 = -4, A_2 = -13, n_2 = 3$.

The result of the `SGWBinner` when we adopt the same noise model (3 parameters) in both pipelines is presented in figure 6.20. There are only two bins left from the merging of the 10 initial bins. The power law signals reconstructed in the two bins combined approximately into the injected double power law shape. The noise estimation from the reconstruction is good, according to the subfigure 6.20b, all the true values of the noise and signal parameters, except the signal amplitudes, lay within 1σ regions of the estimation. One can recover the true (injected) values of the signal parameters from the estimated ones of the two independent power law signals that the `SGWBinner` reconstructs in the two merged bins.

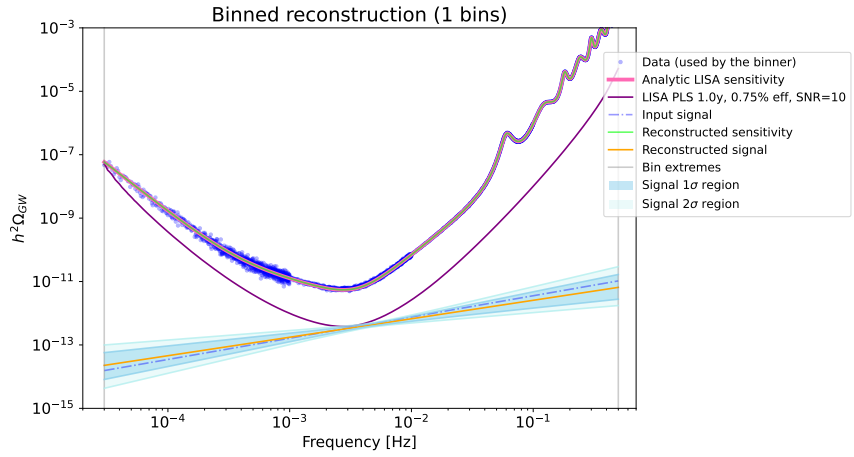

(a) Reconstruction plot

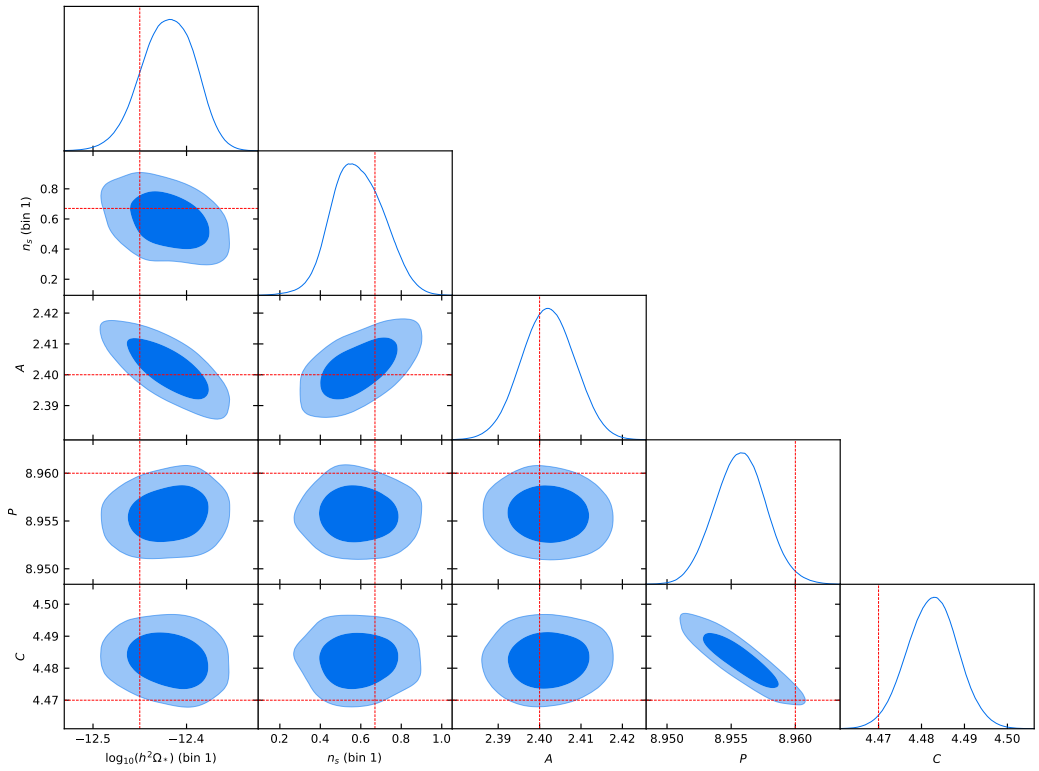

(b) Triangle plot

Figure 6.18: Results obtained by running the `SGWBinner` with the MCMC option, starting from 15 initial bins, on data including **noise and a power law** SGWB signal. The **same 3-parameters noise model** is used in both the data generation and the data analysis pipelines. Subfigure (a) is the reconstruction plot showing a signal detection. From the 15 initial bins, the `SGWBinner` converges to a single bin with the detection of a power law signal. Subfigure (b) is the triangle plot showing the cross correlation among parameters (signal and noise). The top plot of each column is the marginal probability distribution of each estimated parameter. The true values used in the data generation pipeline are indicated by the red dashed lines.

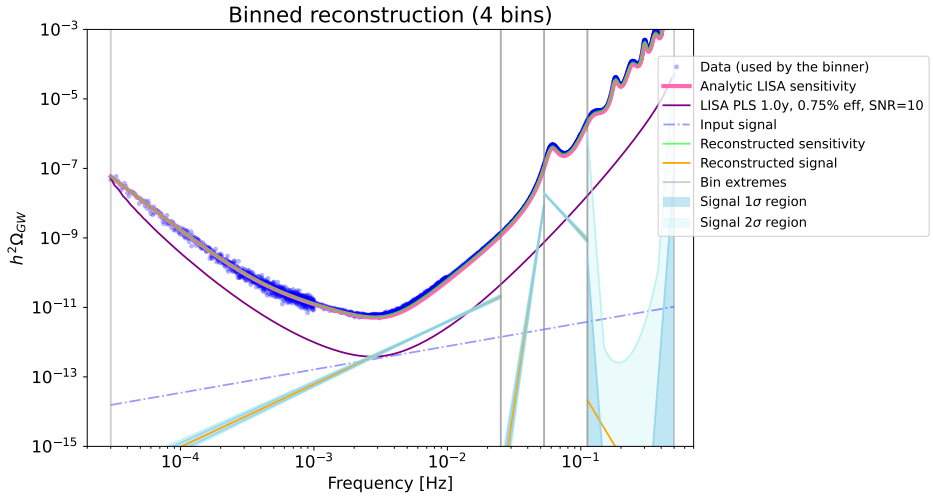

(a) Reconstruction plot

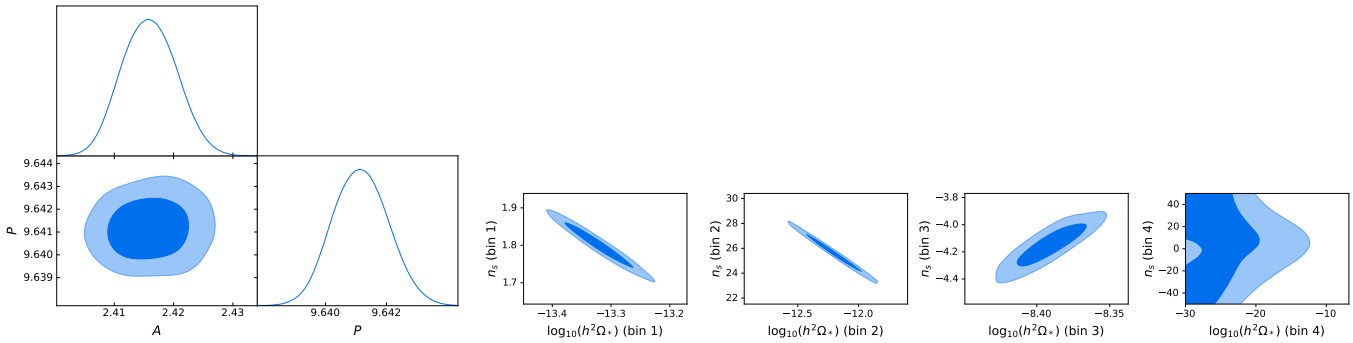

(b) Noise parameter estimation

(c) Signal contour plot

Figure 6.19: Results obtained by running the `SGWBinner` with the MCMC option, starting from 13 initial bins, on data including **noise and a power law** SGWB signal. The SciRD noise model, characterized by **2 parameters** (A, P), are used in the data analysis while we use **3 parameters** noise model in the data generation pipeline. Subfigure (a) is the reconstruction plot showing a signal detection. From the 13 initial bins, `SGWBinner` merges them into 4 bins. In each of them, the code detects a power law signal. Subfigure (b) presents the marginal probability distributions from parameter estimation for 2 noise parameters, A, P. The red dashed lines indicating the true (injected) values used in the data generation pipeline, see table 6.1, are out of range of the plot's axes. Subfigure (c) presents the contour plots of the cross correlation of the two parameters of detected power law signals in every bin. The last contour plot corresponds to the signal reconstruction in bin 6, which is compatible with null signal.

- At low frequencies in the first bin of subfigure 6.20a, the double power law (6.14) is dominated by the power law term with $A_1 = -15.5, n_1 = -4$. The best fit values of the power law signal in the first bin are $A^{1st} = -11.32, n^{1st} = -4.02$, shown in subfigure 6.20b. The value of the spectral index n_1 is within the 1σ region of the best fit value, so it is acceptable. The power law model used in the parameter estimation has a different pivot frequency than the one in (6.14) since this pivot frequency is computed as the geometrical mean of the frequency **within the merged bin**. In particular, the first bin in subfigure 6.20a has frequency range from 3×10^{-5} to approximately 3.87×10^{-3} Hz so the pivot frequency is $f_*^{1st} = 3.41 \times 10^{-4}$ Hz, while the pivot frequency used in (6.14) is the geometrical mean of the full LISA frequency band $(3 \times 10^{-5}, 0.5)$ Hz, i.e. $f_p = 3.87 \times 10^{-3}$ Hz. Hence, the injected value of A_1 is compatible with the estimated log amplitude parameter A^{1st} of the first bin via the relation $A_1 = \log\left[10^{A^{1st}}(f_p/f_*^{1st})^{n^{1st}}\right]$.
- In the second bin of the reconstruction plot 6.20a, where the power law with $A_2 = -13, n_2 = 3$ is dominant, the best estimated parameters are $A^{2nd} = -10.21, n^{2nd} = 3.02$. We can recover the true value of A_2 in similar way done above for A_1. The pivot frequency for the second bin is $f_*^{2nd} = 4.4 \times 10^{-2}$ Hz. One then can verify that the relation $A_2 = \log\left[10^{A^{2nd}}(f_p/f_*^{2nd})^{n^{2nd}}\right]$, where $f_p = 3.87 \times 10^{-3}$ Hz, holds approximately. We illustrate in figure 6.21 the power law shapes in the two bins with the best fit values from the data analysis done by the `SGWBinner`, and the double power law shape expressed in (6.14).

Once again, if we use different noise models between the data generation and the data analysis pipelines, the reconstruction result worsens, as shown in figure 6.22. At low frequency, the reconstruction of the SGWB is still good. However, it goes worsen at high frequency, the reconstructed signal does not match with the injected one. This is due to the differences between two noise models in that frequency band. The bias in the estimation of the OMS noise parameter P, which is dominant at high frequency, leads to the bad signal reconstruction.

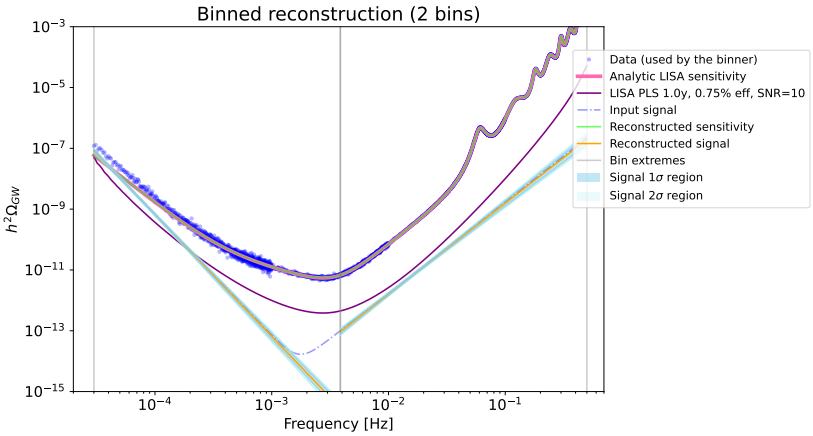

(a) Reconstruction plot

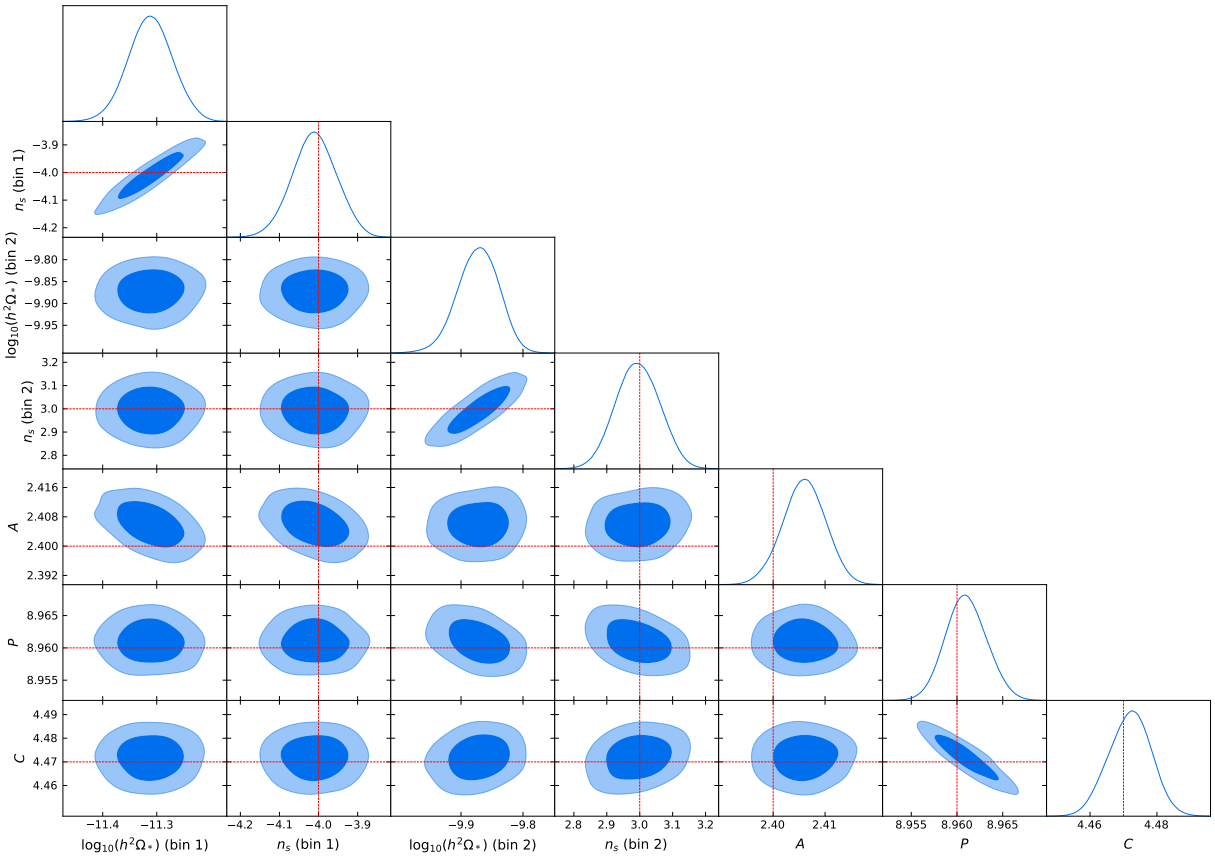

(b) Triangle plot

Figure 6.20: Results obtained by running `SGWBinner` with MCMC option, starting from 10 initial bins, on data including **noise and a double power law** SGWB signal. The **same 3-parameters noise model** is used in both the data generation and the data analysis pipelines. Subfigure (a) is the reconstruction plot showing the signal detection. Subfigure (b) is the triangle plot showing the cross correlation among parameters (signal and noise). The top plot of each column is the marginal probability distribution of each estimated parameter. The true values used in the data generation pipeline are indicated by the red dashed lines. The true values of signal amplitudes are out of range of the plot's axes. They can be recovered from the estimated values, as explained in the double power law subsection of section 6.4.2.

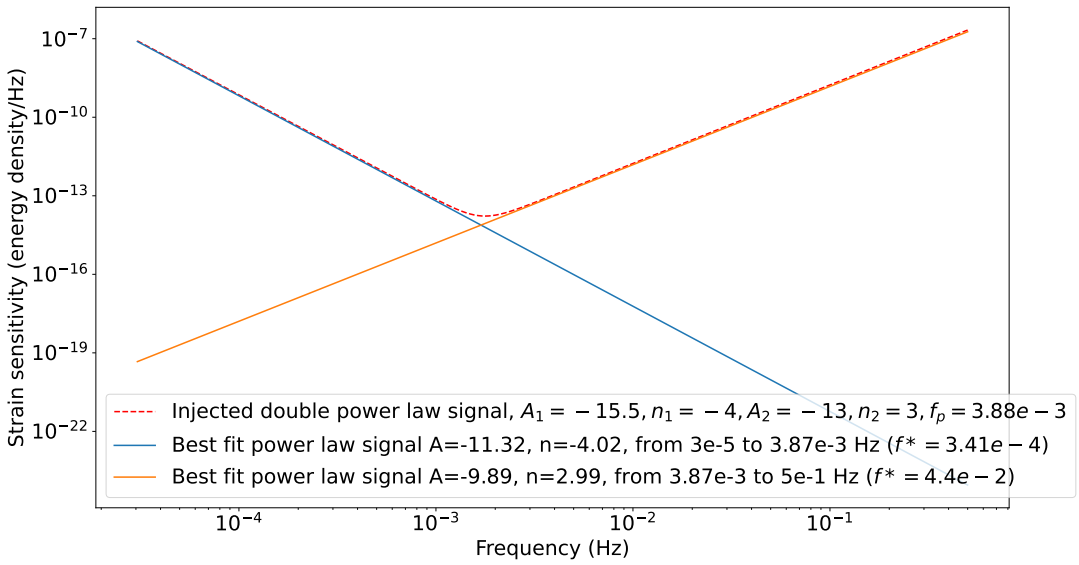

Figure 6.21: Decomposition of the double power law signal into the two power law shapes which are reconstructed by the `SGWBinner` in figure 6.20.

6.4.3 Impact of galactic foreground

We can extend the previous analysis by including the galactic foreground. We adopt the model expressed in (6.16) for injecting the foreground in the data. We always use the **same noise model**, e.g. the 3 parameter noise model, in both the data generation and the data analysis pipelines, since it is not necessary to reconsider the case that leads to a misinterpretation of the SGWB signal in the reconstruction for studying the impact of the galactic foreground. In addition, we assume that we fully understand the galactic foreground characterization, so we can use the same foreground model (6.16) in both the data generation and the analysis pipelines. Note that the `SGWBinner` treats the GW foreground as an additional noise, so the parameters of the foreground model are estimated in the same way as the parameters of the noise model. All the data sets used in the following plots are generated by `SGWBinner`, in one year duration, and 75% duty cycle.

First, for the data containing noise and galactic foreground only, we obtain a good reconstruction of the foreground by running `SGWBinner` with the MCMC global fit option, as shown in figure 6.23. We also run the `SGWBinner` on this data set for 10 initial bins without the MCMC option[9], to confirm the conclusion of no fake signal detection, illustrated in figure 6.24.

[9] As mentioned in section 6.4.1, the MCMC (non-global fit) option does not work on noise-only data with the perfect knowledge of noise (here the galactic foreground plays a role as an extra noise component).

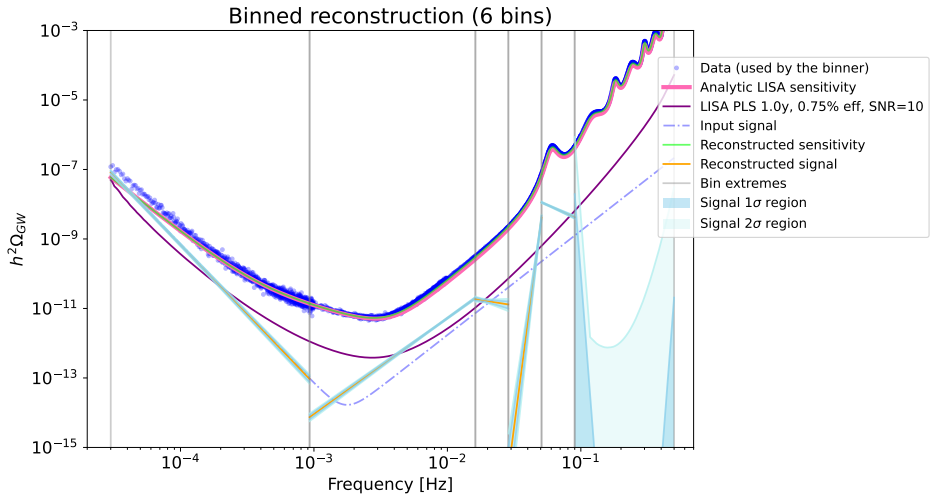

(a) Reconstruction plot

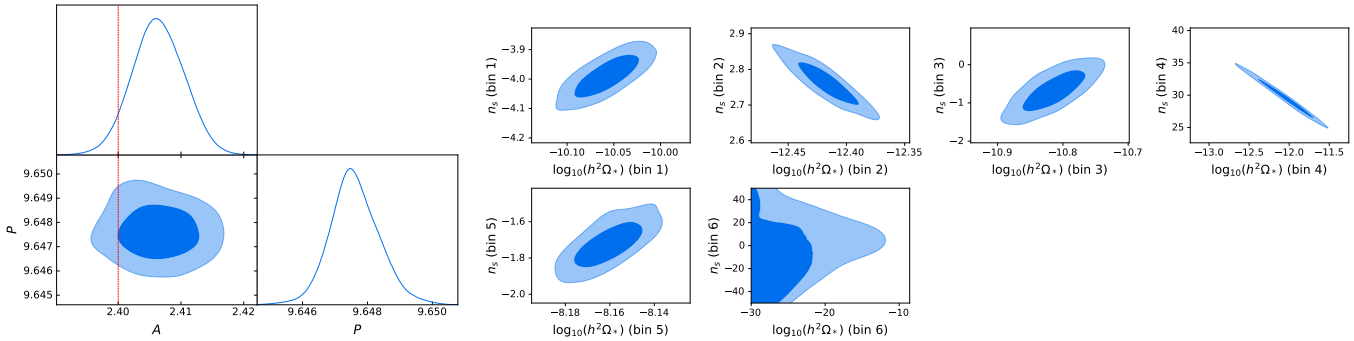

(b) Noise parameter estimation

(c) Signal contour plot

Figure 6.22: Result obtained by running `SGWBinner` with the MCMC option, starting from 17 initial bins, on data including **noise and a double power law** SGWB signal. The SciRD noise model, characterized by **2 parameters** (A, P), is used in the data analysis, while we use **3 parameters** model for the data generation pipeline. Subfigure (a) is the reconstruction plot showing the signal detection. From the 17 initial bins, the `SGWBinner` converges to 6 bins. Subfigure (b) presents the marginal probability distributions for the 2 noise parameters, A, P, with the red dashed lines indicating the true values used in the data generation pipeline presented in table 6.1. The injected value of the P parameter is out of range of the plot's axes. Subfigure (c) presents the contour plots showing the cross correlation between the two parameters of the detected power law signals in every bin. The last contour plot corresponds to the parameter estimation in bin 6, and is compatible with a null signal.

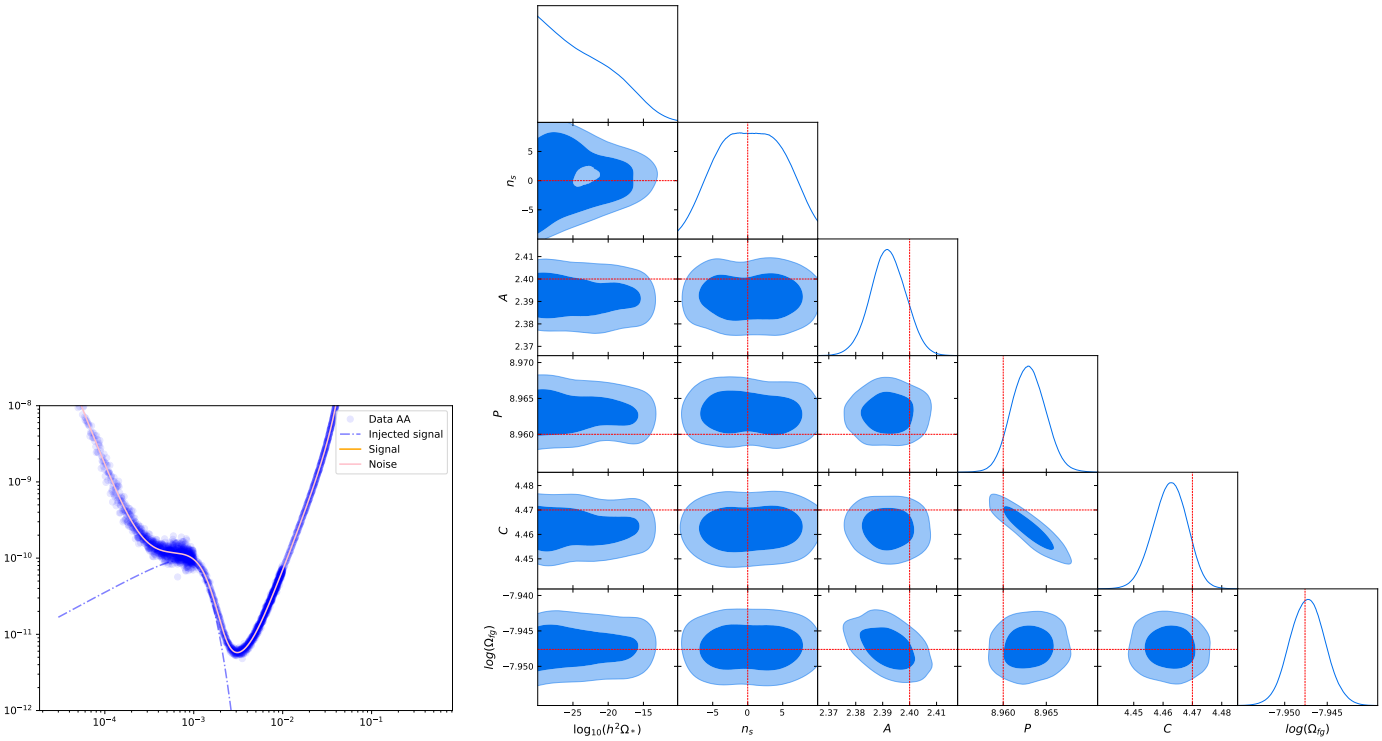

(a) Reconstruction plot

(b) Triangle plot from parameter estimation

Figure 6.23: Reconstruction plot and triangle plot of the estimated parameters by running the `SGWBinner`, with the MCMC global fit option, using **the same noise (3 parameters) and galactic foreground model** in both the data generation and the data analysis pipelines. Subfigure (a) is the reconstruction plot showing the absence of a fake SGWB signal detection, in agreement with the fact that there is no injected signal, except the galactic foreground in the data. Subfigure (b) is the triangle plot showing the cross correlation of all estimated parameters. The true (injected) values used in the data generation pipeline are indicated by the red dashed lines. The first two parameters corresponds to the search of a power law signal. The log amplitude of the putative signal is compatible with zero. The other three ones are related to the noise. The last parameter is the log amplitude of the galactic foreground.

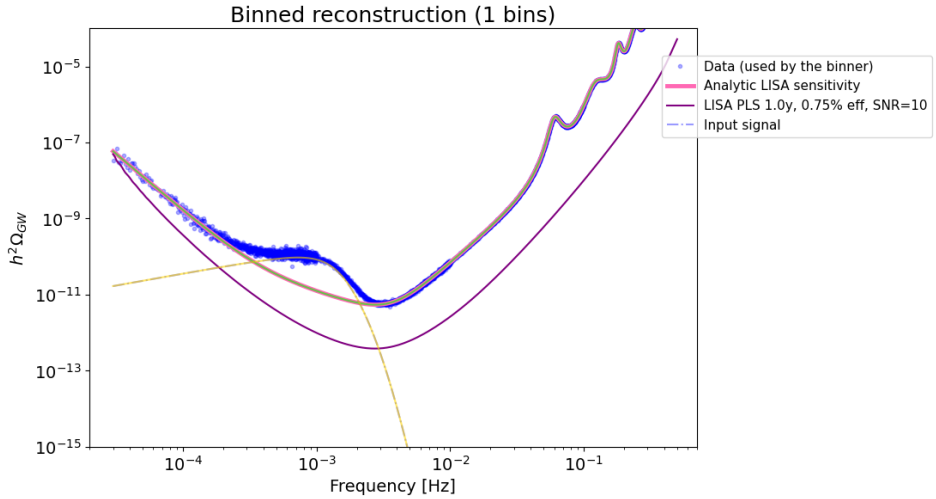

Figure 6.24: Reconstruction plot obtained by running the `SGWBinner` without the MCMC option, for 10 initial bins, on data including **noise and galactic foreground**. The same noise model, characterized by 3 parameters (A, P, C), and galactic foreground model, characterized by 1 parameter $\log \Omega_{\rm fg} \equiv A_{\rm fg}$, is used in both the data generation and the data analysis pipelines.

For the data including noise, galactic foreground and a SGWB signal, the data analysis results of the `SGWBinner` remain good as in the case of data excluding the galactic foreground.

- As shown in figure 6.25, in the case of data including a broken power law signal (6.15), the collection of the power law signals in all merged bins approximates well the broken power law shape, except for the last merged bin where the instrumental noise highly dominates over the signal. The noise and foreground parameters are estimated very well by the `SGWBinner` reconstruction, since the true (injected) values of these parameters are all within the 1σ regions around the best fit values, see subfigure 6.25b.

- We also inject a power law signal (6.13) in the data, and the analysis results from the `SGWBinner` are presented in figure 6.26. We obtain a good reconstruction of the noise, galactic foreground and SGWB signal. All the true values of the parameters lie in at least 2σ the region around the best fit values.

- The final case is the double power law signal, as illustrated in figure 6.27. With this SGWB injection, the signal reconstruction in the first bin (see subfigure 6.27a) does not match to the injected signal. A reasonable explanation for this mismatch is the impact of the galactic foreground. In the first bin, the contribution of the galactic foreground is dominant, both over the instrumental noise and the SGWB signal. Hence, the uncertainty of the parameter estimation for the foreground, probably from the confusion

with instrumental noise, has an effect on the estimation result for the signal parameters. Moreover, we see in subfigure 6.27b that the amplitude of test-mass acceleration noise, A, is biased, since its true value lies outside of the 2σ region. The uncertainty on the test-mass acceleration noise parameter also influences to the signal reconstruction in the first bin. On the other hand, the signal in the second bin in subfigure 6.27a is reconstructed to be compatible with the injected SGWB signal.

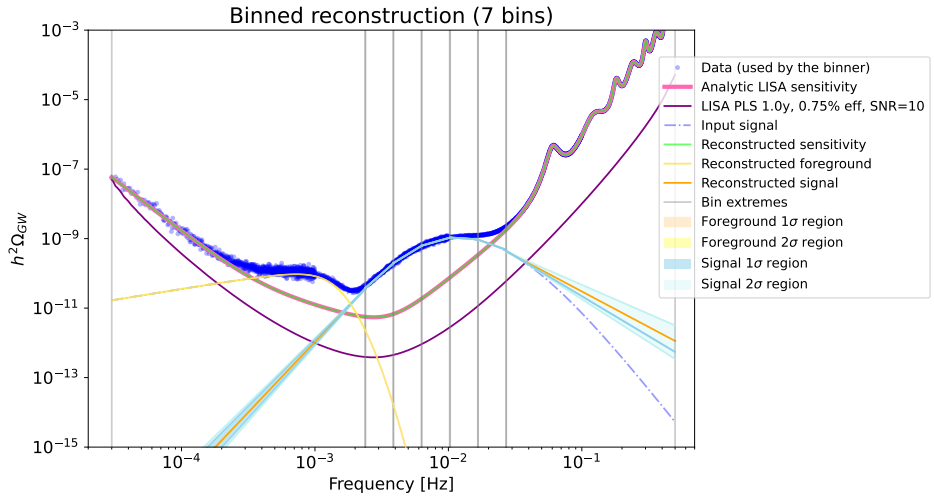

(a) Reconstruction plot

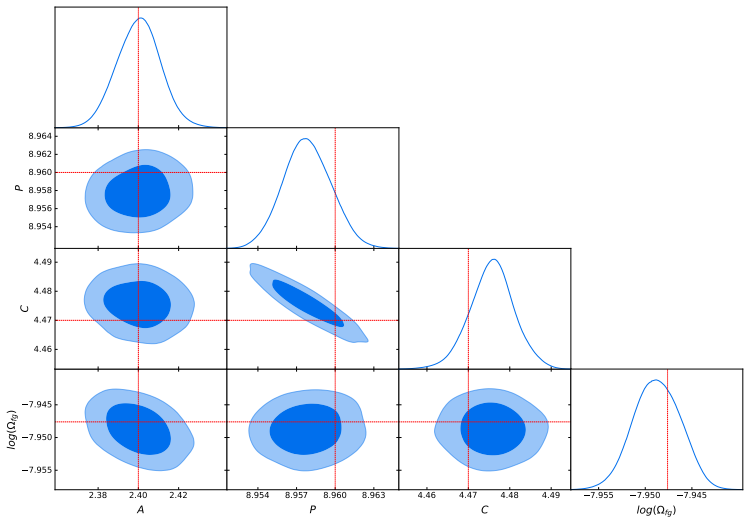

(b) Noise parameter estimation

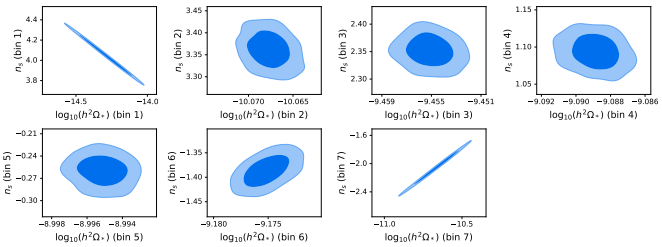

(c) Contour plots for signal parameter estimation

Figure 6.25: Results obtained by running the `SGWBinner` with the MCMC option, starting from 20 initial bins, on data including **noise, galactic foreground and a broken power law** SGWB signal. The **same 3-parameters noise model and 1-parameter galactic foreground model** are used in the data generation and data analysis pipeline. Subfigure (a) is the reconstruction plot showing the signal detection. From the 20 initial bins, the `SGWBinner` converges to 7 bins, for each of which a signal is detected as a power law. Subfigure (b) presents the marginal probability distributions from the parameter estimation for the 3 noise parameters, A, P, C, and for the galactic foreground amplitude, $\log \Omega_{fg} \equiv A_{\rm fg}$. The red dashed lines indicate the true (injected) values used in the data generation pipeline (the injected galactic foreground log amplitude is $A_{\rm fg} \approx -7.95$, while the noise parameters are given in table 6.1). Subfigure (c) presents the contour plots of the cross correlation between the two parameters of a detected power law signal in every bin.

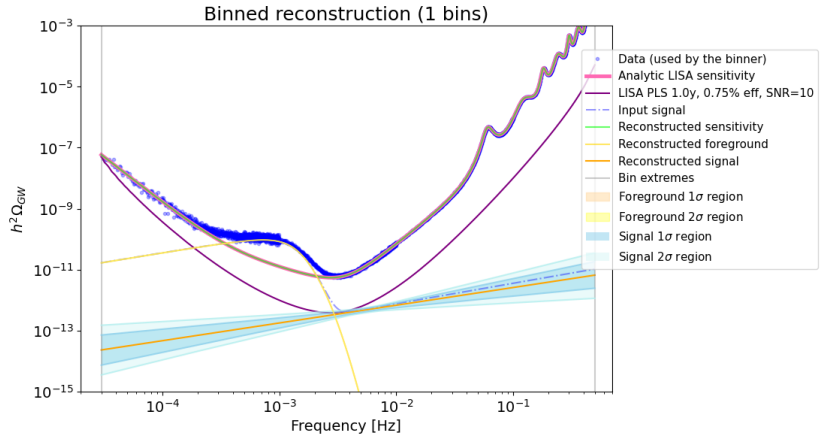

(a) Reconstruction plot

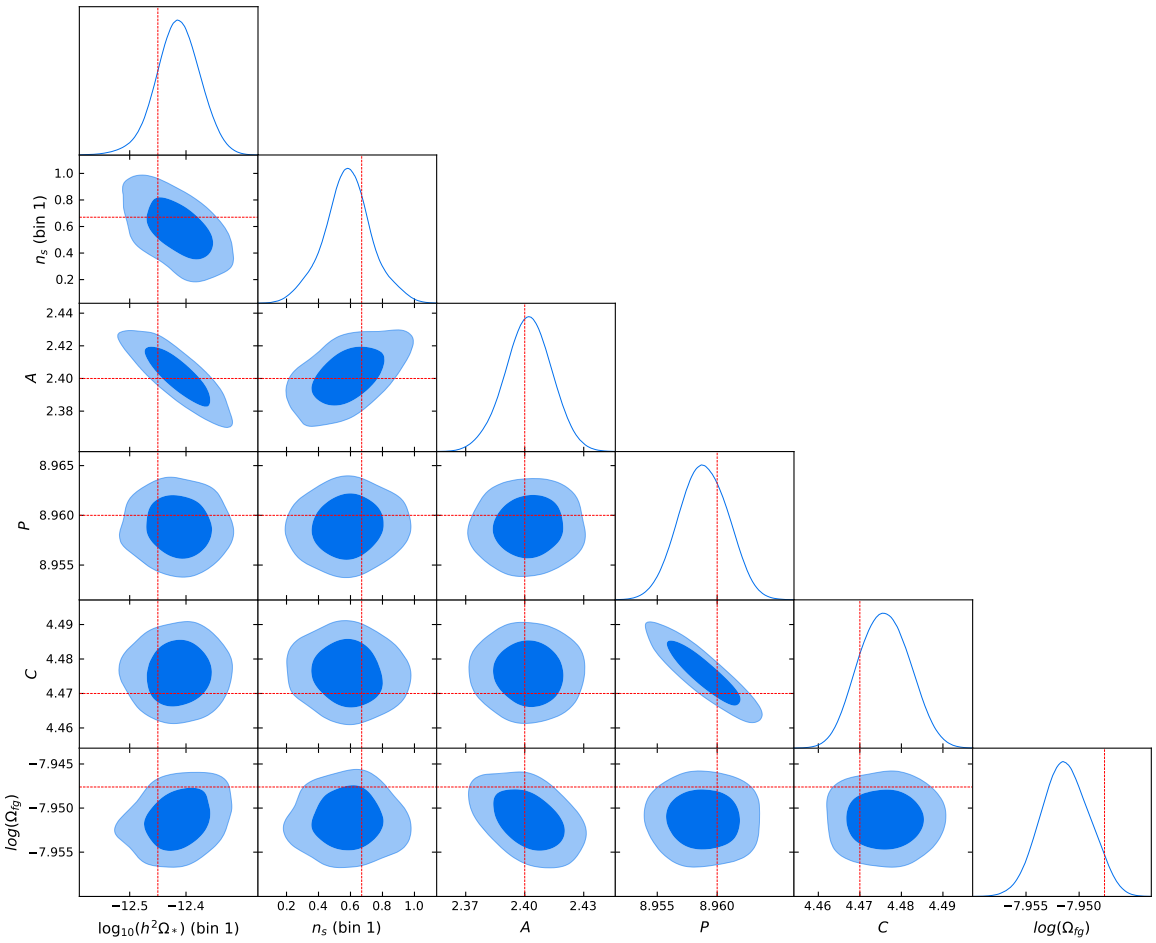

(b) Triangle plot for parameter estimation

Figure 6.26: Results obtained by running the `SGWBinner` with the MCMC option, starting from 16 initial bins, on data including **noise, galactic foreground and a power law** SGWB signal. The **same 3-parameters noise model and 1-parameter galactic foreground model** are used in both the data generation and the data analysis pipelines. Subfigure (a) is the reconstruction plot showing the signal detection. From the 16 initial bins, the `SGWBinner` converges to a single bin where a power law signal is detected. Subfigure (b) is the triangle plot showing the cross correlation of all parameters (signal and noise).

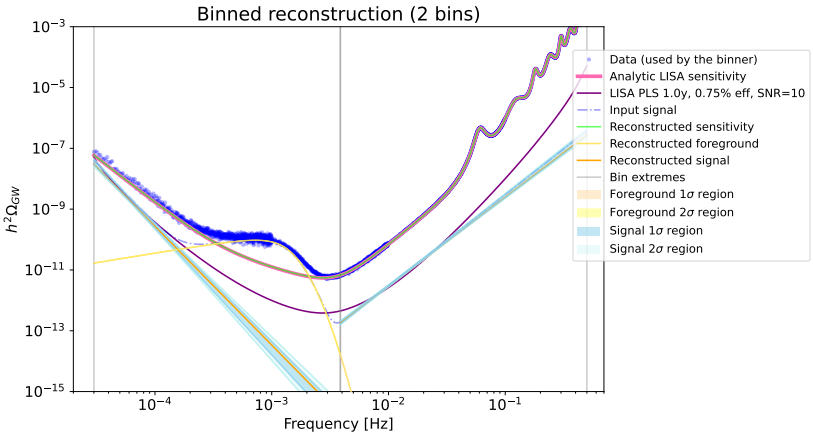

(a) Reconstruction plot

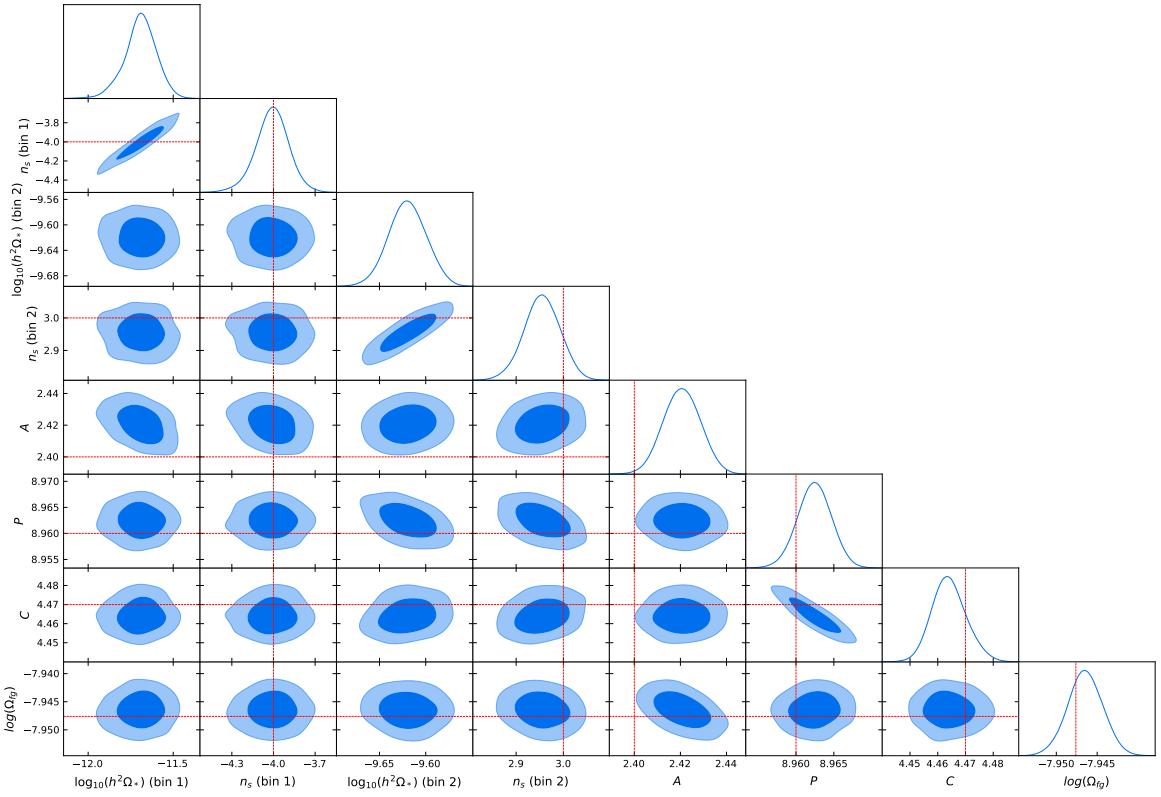

(b) Triangle plot

Figure 6.27: Result obtained by running the `SGWBinner` with the MCMC option, starting from 12 initial bins, for data including **noise, galactic foreground, and a double power law** SGWB signal. The **same 3-parameters noise model and 1-parameter galactic foreground model** are used in both the data generation and the data analysis pipelines. Subfigure (a) is the reconstruction plot showing the signal detection. From the 12 initial bins, the `SGWBinner` converges to two bins, in each of which a power law signal is detected. Subfigure (b) is the triangle plot showing the cross correlation among parameters (signal and noise). The top plot of each column is the marginal probability distribution of each estimated parameter. The true values used in the data generation pipeline are indicated by the red dashed lines. The true values of signal amplitudes are out of range of the plot's axes.

Chapter 7

Conclusion and Outlook

In this thesis, we first briefly reviewed Gravitational Waves (GWs) from the theoretical and the experimental points of view. In addition, some GW sources have been presented, especially the Stochastic Gravitational Wave Backgrounds (SGWBs). Some current and future GW detectors and their detectable sources are also discussed. With several ground-based GW detectors, scientists have discovered many astrophysical events in the recent years. We expect to observe more interesting objects in the next decades, both of astrophysical and cosmological origin. Therefore, the gravitational wave astronomy opens a new window to explore the Universe, its cosmic history and fundamental physics.

Our study then focuses on the future space-based GW detector, Laser Interferometer Space Antenna (LISA). This observatory is one of the most complex space missions, consisting of three spacecraft, separated by 2.5 million kilometers, to observe GW sources in the milli-hertz band. LISA uses laser interferometry to measure the tiny variations (about picometers) of the proper distance between inertial test-masses hosted in the spacecraft when the GWs pass through spacetime. The test-masses are kept in free-falling on their geodesics, while the spacecraft follow them in drag-free motion. The laser beams are exchanged among the spacecraft, going through a complex optical metrology system before their interferences are recorded. Some critical subsystems in this complex measurement chain have been presented in chapter 5. In addition, several dominant noises, which can influence LISA interferometric measurements, are discussed.

The simulator `LISANode` has been developed to generate realistic LISA data to study the instrument, the data measurement and processing chains and to provide the data, on which to develop the data analysis pipelines. In this thesis, we introduced some implementations contributing to the `LISANode` development, especially the model for correlated and nonstationary noises. We also applied this implementation of the correlated noises for data generation, which is used in the model validation of test-mass acceleration noise propagation, presented

in section 4.4. In the future, we would like to study the impact of the nonstationary noise in the data processing chain and data analysis results.

The raw measurement data in LISA are contaminated by instrumental noises, some of which are much higher than the level of the detectable GW signal. Hence, a data processing pipeline called Initial Noise-Reduction Pipeline (INREP) has been developed to suppress the dominant noise sources and to provide variables for the data analysis steps. One of the crucial blocks included in INREP is the Time Delay Interferometry (TDI) algorithm. The main goal of this algorithm is to suppress the laser frequency noise, which is about 8 orders of magnitude higher than the brightest GW signal which will hopefully be detected by LISA. We reviewed the principle of TDI and some of its combinations in chapter 3. In addition, this technique was applied to data generated with an electronic simulator, LISA-On-Table (LOT), to study the laser frequency noise suppression. We analyzed the noise propagation in LOT and TDI variables. The preliminary results show that we can reduce the laser frequency noise in the LOT simulation data for some configurations. Further analyses are necessary to study the effect of the electronic devices in the measurement chain, for a better understanding of LOT and, therefore, of the design of LISA.

One of the main works performed in the thesis is to study the propagation of noise through the LISA instrument, measurement chain and TDI algorithm, addressed in chapter 4. In particular, we computed the analytical transfer functions in TDI Michelson combinations. In addition, we examine some realistic LISA configurations such as laser locking schemes and possible correlation scenarios in the noise propagation study. These analytical results are validated with the `LISANode` simulator. Nevertheless, the statistical test of the validation process needs to be improved, especially for the cross-spectral density. Furthermore, we want to validate the noise propagation in other TDI combinations, for example AET, with simulated data and to consider more blocks in INREP to study the propagation of noises.

The study of noise propagation contributed to the development of the LISA Performance Model and noise budget, which are crucial to understand the impact of changes in the instrument design on the measurement data and hence the on science objectives of the LISA mission. This study provides the basis for constructing a new noise model, which we can use to analyze the data searching for a SGWB signal, as presented in chapter 6.

Besides, a study of LISA dynamics in the `LISANode` simulator has also been conducted in this thesis. In particular, we modified the implementation of LISA Dynamics in the `LISANode`, which accounts for the motion of the MOSAs. We also studied its impact on the performance of the Drag-Free Attitude Control System (DFACS) to control the attitudes and positions of the test-masses and spacecraft. The results presented in chapter 5, reveals the improvement of the simulated result when we account for the breathing angle in the moving MOSAs case to

have the same projections on sensitive axis for test-mass and spacecraft motions. However, the residual relative motion between the test-mass and the spacecraft does not match the injected test-mass acceleration noise, which implies that the implementation of LISA Dynamics needs to be improved. In the future, we would like to add more correction terms in the equations of motion and investigate other methods for solving the equation of motion of LISA dynamics to address this problem.

In the chapter 6, we applied the result of the noise propagation study to develop a new noise model to be adopted when searching for SGWBs. The data have been generated by simulation tools, such as `LISANode` (in the time domain, however we did not inject any SGWB signal in the data with this pipeline) and `SGWB_data` (in the frequency domain). We then used the `SGWBinner` code to reconstruct the noise and the SGWB signal from the simulated data. The data analysis method implemented in the `SGWBinner` is model-independent as far as the signal is concerned, so we can apply it to the data containing arbitrary SGWB signals. However, we found that the noise model used in data analysis needs to accurately represent the one used for the data generation. The lack of noise knowledge, particularly of its spectral shape or of the TDI transfer functions, can lead either to a fake detection of SGWB signals, or to considerable uncertainties in the signal parameter estimation. In the future, we must improve the data generation with `LISANode` in the time domain by including the SGWB signal, since this is the more realistic data generation pipeline. In addition, we would like to develop a more flexible data analysis tools to reconstruct both the SGWB signal and the noise being agnostic on both their spectral shapes because, in practice, the LISA noises will not be fully characterized.

Acronyms

ADC Analog-to-Digital Converter

AIC Akaike Information Criterion

AOM acousto-optic modulator

ASD amplitude spectral density

BSM Beyond Standard Model

CIC Cascaded Integrator–Comb

CMB Cosmic Microwave Background

CSD Cross Spectral Density

DAC Digital-to-Analog Converter

DDS Direct Digital Synthesizer

DECIGO DECi-hertz Interferometer Gravitational wave Observatory

DFACS Drag-Free Attitude Control System

DLL delay-locked loop

DPLL digital phase locked loop

DWS differential wavefront sensing

EM electromagnetic

EMRIs extreme mass-ratio inspiral

EoM Equations of Motion

EOM Electro-Optical Modulator

ESA European Space Agency

FDS Frequency Distribution System

GBs Galactic Binaries

GRS Gravitational Reference Sensor

GW Gravitational Wave

IFO Interferometer

INDIGO Indian Initiative in Gravitational-wave Observations

INREP Initial Noise-Reduction Pipeline

IPTA International Pulsar Timing Array

ISI Inter-Spacecraft Interferometer

KAGRA Kamioka Gravitational Wave Detector

LIGO Laser Interferemeter Gravitational Wave Observatory

LISA Laser Interferometer Space Antenna

LPF LISA Pathfinder

LOT LISA-On-Table

LSST Large Synoptic Survey Telescope

LUT look-up table

MCMC Markov-chain Monte Carlo

MOSA Moving Optical Sub-Assembly

MPR Measured Pseudo-Range

MPS Micro-Propulsion System

NCO numerically controlled oscillator

OB Optical Bench

OMS Optical Metrology System

OP optical path

PA phase accumulator

PIR phase-increment register

PRN pseudo-random noise

PSD Power Spectral Density

QPD Quadrant photodiode

RF radio frequency

RFI Reference Interferometer

RIN Relative Intensity Noise

S/C spacecraft

SciRD Science Requirement Document

SGWB Stochastic Gravitational Wave Background

SGWBs Stochastic Gravitational Wave Backgrounds

SMBH supermassive black hole

SNR Signal-to-Noise Ratio

SOBH Stellar Origin Black Hole

TCB Barycentric Coordinate Time

TDI Time Delay Interferometry

TDIR Time Delay Interferometry Ranging

TM test mass, *often proof mass*

TMI Test Mass Interferometer

TT *transverse-traceless*

TTL Tilt-To-Length

USO ultra-stable oscillator

Virgo Virgo

Bibliography

[1] Benjamin P Abbott et al. "Binary black hole mergers in the first advanced LIGO observing run". In: *Physical Review X* 6.4 (2016), p. 041015.

[2] Benjamin P Abbott et al. "Gravitational waves and gamma-rays from a binary neutron star merger: GW170817 and GRB 170817A". In: *The Astrophysical Journal Letters* 848.2 (2017), p. L13.

[3] Benjamin P Abbott et al. "GW170817: implications for the stochastic gravitational-wave background from compact binary coalescences". In: *Physical review letters* 120.9 (2018), p. 091101.

[4] Benjamin P Abbott et al. "Observation of gravitational waves from a binary black hole merger". In: *Physical review letters* 116.6 (2016), p. 061102.

[5] Benjamin P Abbott et al. "Upper limits on the rates of binary neutron star and neutron star–black hole mergers from advanced LIGO's first observing run". In: *The Astrophysical journal letters* 832.2 (2016), p. L21.

[6] R. Abbott et al. "Constraints on the cosmic expansion history from GWTC-3". In: (Nov. 2021). arXiv: 2111.03604 [astro-ph.CO].

[7] Roberto Abuter et al. "Detection of the gravitational redshift in the orbit of the star S2 near the Galactic centre massive black hole". In: *Astronomy & Astrophysics* 615 (2018), p. L15.

[8] Matthew R. Adams and Neil J. Cornish. "Discriminating between a Stochastic Gravitational Wave Background and Instrument Noise". In: *Phys. Rev. D* 82 (2010), p. 022002. DOI: 10.1103/PhysRevD.82.022002. arXiv: 1002.1291 [gr-qc].

[9] Hirotugu Akaike. "A new look at the statistical model identification". In: *IEEE transactions on automatic control* 19.6 (1974), pp. 716–723.

[10] Kazunori Akiyama et al. "First M87 event horizon telescope results. VI. The shadow and mass of the central black hole". In: *The Astrophysical Journal Letters* 875.1 (2019), p. L6.

[11] Kazunori Akiyama et al. "First Sagittarius A* Event Horizon Telescope Results. I. The Shadow of the Supermassive Black Hole in the Center of the Milky Way". In: *The Astrophysical Journal Letters* 930.2 (2022), p. L12.

[12] Hewitson et al. "Payload Definition Document". In: (2017).

[13] Bruce Allen and Joseph D Romano. "Detecting a stochastic background of gravitational radiation: Signal processing strategies and sensitivities". In: *Physical Review D* 59.10 (1999), p. 102001.

[14] Pau Amaro Seoane et al. "The effect of mission duration on LISA science objectives". In: *General Relativity and Gravitation* 54.1 (2022), pp. 1–47.

[15] Pau Amaro-Seoane et al. "Intermediate and extreme mass-ratio inspirals—astrophysics, science applications and detection using LISA". In: *Classical and Quantum Gravity* 24.17 (2007), R113.

[16] Pau Amaro-Seoane et al. "Laser interferometer space antenna". In: *arXiv preprint arXiv:1702.00786* (2017).

[17] J. Antoniadis et al. "The International Pulsar Timing Array second data release: Search for an isotropic Gravitational Wave Background". In: *"Mon. Not. Roy. Astron. Soc."* (Jan. 2022). DOI: 10.1093/mnras/stab3418. arXiv: 2201.03980 [astro-ph.HE].

[18] M Armano et al. "Temperature stability in the sub-milliHertz band with LISA Pathfinder". In: *Mon. Not. Roy. Astron. Soc.* 486.3 (2019), pp. 3368–3379. DOI: 10.1093/mnras/stz1017. arXiv: 1905.09060 [astro-ph.IM].

[19] M Armano et al. "Constraints on LISA Pathfinder's self-gravity: design requirements, estimates and testing procedures". In: *Classical and quantum gravity* 33.23 (2016), p. 235015.

[20] M. Armano et al. "Calibrating the system dynamics of LISA Pathfinder". In: *Phys. Rev. D* D97.12 (2018), p. 122002. DOI: 10.1103/PhysRevD.97.122002. arXiv: 1806.08581 [astro-ph.IM].

[21] M. Armano et al. "Characteristics and Energy Dependence of Recurrent Galactic Cosmic-Ray Flux Depressions and of a Forbush Decrease with LISA Pathfinder". In: *Astrophys. J.* 854.2 (2018), p. 113. DOI: 10.3847/1538-4357/aaa774. arXiv: 1802.09374 [physics.space-ph].

[22] M. Armano et al. "LISA Pathfinder micronewton cold gas thrusters: In-flight characterization". In: *Phys. Rev. D* D99.12 (2019), p. 122003. DOI: 10.1103/PhysRevD.99.122003.

[23] M. Armano et al. "LISA Pathfinder Performance Confirmed in an Open-Loop Configuration: Results from the Free-Fall Actuation Mode". In: *Phys. Rev. Lett.* 123.11 (2019), p. 111101. DOI: 10.1103/PhysRevLett.123.111101. arXiv: 1908.11584 [physics.space-ph].

[24] M. Armano et al. "Measuring the Galactic Cosmic Ray Flux with the LISA Pathfinder Radiation Monitor". In: *Astropart. Phys.* 98 (2018), pp. 28–37. DOI: 10.1016/j.astropartphys.2018.01.006. arXiv: 1711.07427 [astro-ph.IM].

[25] M. Armano et al. "Precision Charge Control for Isolated Free-Falling Test Masses: LISA Pathfinder Results". In: *Phys. Rev. D* D98.6 (2018), p. 062001. DOI: 10.1103/PhysRevD.98.062001. arXiv: 1807.02435 [physics.ins-det].

[26] M. Armano et al. "Beyond the Required LISA Free-Fall Performance: New LISA Pathfinder Results down to 20 μHz". In: *Phys. Rev. Lett.* 120 (6 Feb. 2018), p. 061101. DOI: 10.1103/PhysRevLett.120.061101. URL: https://link.aps.org/doi/10.1103/PhysRevLett.120.061101.

[27] M. Armano et al. "Capacitive sensing of test mass motion with nanometer precision over millimeter-wide sensing gaps for space-borne gravitational reference sensors". In: *Phys. Rev. D* 96 (6 Sept. 2017), p. 062004. DOI: 10.1103/PhysRevD.96.062004. URL: https://link.aps.org/doi/10.1103/PhysRevD.96.062004.

[28] M. Armano et al. "Charge-Induced Force Noise on Free-Falling Test Masses: Results from LISA Pathfinder". In: *Phys. Rev. Lett.* 118 (17 Apr. 2017), p. 171101. DOI: 10.1103/PhysRevLett.118.171101. URL: https://link.aps.org/doi/10.1103/PhysRevLett.118.171101.

[29] M. Armano et al. "Sensor Noise in LISA Pathfinder: In-Flight Performance of the Optical Test Mass Readout". In: *"Phys. Rev. Lett."* 126.13, 131103 (Apr. 2021), p. 131103. DOI: 10.1103/PhysRevLett.126.131103.

[30] M. Armano et al. "Spacecraft and interplanetary contributions to the magnetic environment on-board LISA Pathfinder". In: *Mon. Not. Roy. Astron. Soc.* 494.2 (Apr. 2020), pp. 3014–3027. DOI: 10.1093/mnras/staa830. arXiv: 2005.03423 [astro-ph.IM].

[31] Michele Armano et al. "LISA Pathfinder platform stability and drag-free performance". In: *Physical Review D* 99.8 (2019), p. 082001.

[32] Michele Armano et al. "Sub-femto-g free fall for space-based gravitational wave observatories: LISA pathfinder results". In: *Physical review letters* 116.23 (2016), p. 231101.

[33] Zaven Arzoumanian et al. "The NANOGrav 12.5 yr Data Set: Search for an Isotropic Stochastic Gravitational-wave Background". In: *Astrophys. J. Lett.* 905.2 (2020), p. L34. DOI: 10.3847/2041-8213/abd401. arXiv: 2009.04496 [astro-ph.HE].

[34] S. Babak et al. "Science with the space-based interferometer LISA. V. Extreme mass-ratio inspirals". In: *Phys. Rev. D* 95.10, 103012 (May 2017), p. 103012. DOI: 10.1103/PhysRevD.95.103012. arXiv: 1703.09722 [gr-qc].

[35] Stanislav Babak, Antoine Petiteau, and Martin Hewitson. "LISA Sensitivity and SNR Calculations". In: (Aug. 2021). arXiv: 2108.01167 [astro-ph.IM].

[36] Simon Barke. "Inter-spacecraft frequency distribution for future gravitational wave observatories". PhD thesis. Leibniz U., Hannover, 2015. DOI: 10.15488/8405.

[37] Simon Barke et al. "LISA metrology system-final report". In: (2014).

[38] JB Bayle and O Hartwig. *LISA simulation model*. Tech. rep. 2020.

[39] Jean-Baptiste Bayle. *Power Spectral Density python tool*. https://pypi.org/project/psd/.

[40] Jean-Baptiste Bayle. *Simulation and Data Analysis for LISA*. Université Paris Diderot (Paris 7), 2019.

[41] Jean-Baptiste Bayle, Olaf Hartwig, and Martin Staab. "Adapting time-delay interferometry for LISA data in frequency". In: *Phys. Rev. D* 104.2 (2021), p. 023006. DOI: 10.1103/PhysRevD.104.023006. arXiv: 2103.06976 [gr-qc].

[42] Jean-Baptiste Bayle, Olaf Hartwig, and Martin Staab. *LISA Instrument*. Version 1.1.1. Aug. 2022. DOI: 10.5281/zenodo.7071251. URL: https://doi.org/10.5281/zenodo.7071251.

[43] Jean-Baptiste Bayle et al. "Effect of filters on the time-delay interferometry residual laser noise for LISA". In: *Phys. Rev. D* 99.8 (2019), p. 084023. DOI: 10.1103/PhysRevD.99.084023. arXiv: 1811.01575 [astro-ph.IM].

[44] Jean-Baptiste Bayle et al. *LISA GW Response*. Version 1.1. Apr. 2022. DOI: 10.5281/zenodo.6423436. URL: https://doi.org/10.5281/zenodo.6423436.

[45] Jean-Baptiste Bayle et al. *LISANode*. Version 1.4. Sept. 2022. DOI: 10.5281/zenodo.6461078. URL: https://doi.org/10.5281/zenodo.6461078.

[46] Maurice Bellanger. *Traitement numérique du signal*. Ed. Techniques Ingénieur, 1981.

[47] Peter L Bender and Dieter Hils. "Confusion noise level due to galactic and extragalactic binaries". In: *Classical and Quantum Gravity* 14.6 (1997), p. 1439.

[48] José M Bernardo and Adrian FM Smith. *Bayesian theory*. Vol. 405. John Wiley & Sons, 2009.

[49] Pierre Binetruy et al. "Cosmological backgrounds of gravitational waves and eLISA/NGO: phase transitions, cosmic strings and other sources". In: *Journal of Cosmology and Astroparticle Physics* 2012.06 (2012), p. 027.

[50] D. Bortoluzzi et al. "In-flight testing of the injection of the LISA Pathfinder test mass into a geodesic". In: *Advances in Space Research* 67.1 (Jan. 2021), pp. 504–520. DOI: 10.1016/j.asr.2020.09.009.

[51] Chiara Caprini, Ruth Durrer, and Géraldine Servant. "The stochastic gravitational wave background from turbulence and magnetic fields generated by a first-order phase transition". In: *Journal of Cosmology and Astroparticle Physics* 2009.12 (2009), p. 024.

[52] Chiara Caprini and Daniel G Figueroa. "Cosmological backgrounds of gravitational waves". In: *Classical and Quantum Gravity* 35.16 (2018), p. 163001.

[53] Chiara Caprini et al. "Detecting gravitational waves from cosmological phase transitions with LISA: an update". In: *Journal of Cosmology and Astroparticle Physics* 2020.03 (2020), p. 024.

[54] Chiara Caprini et al. "Reconstructing the spectral shape of a stochastic gravitational wave background with LISA". In: *Journal of Cosmology and Astroparticle Physics* 2019.11 (2019), p. 017.

[55] Chiara Caprini et al. "Science with the space-based interferometer eLISA. II: Gravitational waves from cosmological phase transitions". In: *Journal of cosmology and astroparticle physics* 2016.04 (2016), p. 001.

[56] Sean M Carroll. *Spacetime and geometry*. Cambridge University Press, 2014.

[57] S. Chen et al. "Common-red-signal analysis with 24-yr high-precision timing of the European Pulsar Timing Array: inferences in the stochastic gravitational-wave background search". In: *"Mon. Not. Roy. Astron. Soc."* 508.4 (Dec. 2021), pp. 4970–4993. DOI: 10.1093/mnras/stab2833. arXiv: 2110.13184 [astro-ph.HE].

[58] Sidney Coleman and Erick Weinberg. "Radiative corrections as the origin of spontaneous symmetry breaking". In: *Physical Review D* 7.6 (1973), p. 1888.

[59] The SciPy community. *Scipy python package, Welch's funtion in signal processing*. https://docs.scipy.org/doc/scipy/reference/generated/scipy.signal.welch.html.

[60] S. V. Dhurandhar, K. Rajesh Nayak, and J. Y. Vinet. "Algebraic approach to time-delay data analysis for LISA". In: *Phys. Rev. D* 65.10 (2002), p. 102002. DOI: 10.1103/PhysRevD.65.102002. arXiv: gr-qc/0112059.

[61] James Diebel. "Representing attitude: Euler angles, unit quaternions, and rotation vectors". In: *Matrix* 58.15-16 (2006), pp. 1–35.

[62] Albert Einstein. *Erklärung der Perihelbewegung des Merkur aus der allgemeinen Relativitätstheorie*. Gedruckt in der Reichsdruckerei, 1915.

[63] Albert Einstein. "Über gravitationswellen". In: *Albert Einstein: Akademie-Vorträge: Sitzungsberichte der Preußischen Akademie der Wissenschaften 1914–1932* (2005), pp. 135–149.

[64] Albert Einstein. "Zur elektrodynamik bewegter körper". In: *Annalen der physik* 4 (1905).

[65] ESA Study team, (Gehler et al.) *Mission Requirement Document*. Requirement Document ESA-L3-EST-MIS-RS-001-i1.10. ESA, Oct. 2021.

[66] F. B. Estabrook, Massimo Tinto, and J. W. Armstrong. "Time delay analysis of LISA gravitational wave data: Elimination of spacecraft motion effects". In: *Phys. Rev. D* 62 (2000), p. 042002. DOI: 10.1103/PhysRevD.62.042002.

[67] F. B. Estabrook and H. D. Wahlquist. "Response of Doppler spacecraft tracking to gravitational radiation." In: *General Relativity and Gravitation* 6.5 (Oct. 1975), pp. 439–447. DOI: 10.1007/BF00762449.

[68] Eanna E Flanagan and Scott A Hughes. "The basics of gravitational wave theory". In: *New Journal of Physics* 7.1 (2005), p. 204.

[69] Raphael Flauger et al. "Improved reconstruction of a stochastic gravitational wave background with LISA". In: *Journal of Cosmology and Astroparticle Physics* 2021.01 (2021), p. 059.

[70] David J Griffiths. *Introduction to electrodynamics*. American Association of Physics Teachers, 2005.

[71] C. Grimani et al. "Forbush Decreases and <2 Day GCR Flux Non-recurrent Variations Studied with LISA Pathfinder". In: *Astrophys. J.* 874.2 (2019), p. 167. DOI: 10.3847/1538-4357/ab0c99. arXiv: 1904.04694 [physics.space-ph].

[72] LISA Instrument Group. *LISA Payload Definition Document*. Technical report ESA-L3-EST-INST-DD-001, 2018.

[73] Hubert Halloin. "Note on decimation and interpolation filters for LISA simulation". In: *LISA Technical Notes* (2017), p. 57.

[74] WJ Handley, MP Hobson, and AN Lasenby. "PolyChord: nested sampling for cosmology". In: *Monthly Notices of the Royal Astronomical Society: Letters* 450.1 (2015), pp. L61–L65.

[75] WJ Handley, MP Hobson, and AN Lasenby. "POLYCHORD: next-generation nested sampling". In: *Monthly Notices of the Royal Astronomical Society* 453.4 (2015), pp. 4384–4398.

[76] Olaf Hartwig. "Instrumental modelling and noise reduction algorithms for the laser interferometer space antenna". PhD thesis. Hannover: Institutionelles Repositorium der Leibniz Universität Hannover, 2021.

[77] Olaf Hartwig and Jean-Baptiste Bayle. "Clock-jitter reduction in LISA time-delay interferometry combinations". In: *Phys. Rev. D* 103.12 (2021), p. 123027. DOI: 10.1103/PhysRevD.103.123027. arXiv: 2005.02430 [astro-ph.IM].

[78] Olaf Hartwig et al. "Time-delay interferometry without clock synchronization". In: *Phys. Rev. D* 105.12 (2022), p. 122008. DOI: 10.1103/PhysRevD.105.122008. arXiv: 2202.01124 [gr-qc].

[79] Heinzel. *LISA-AEI-INST-TN-002 1.0 LISA Frequency Planning*. Technical Note LISA-AEI-INST-TN-002. AEI, 2018.

[80] Gerhard Heinzel et al. "Tracking length and differential-wavefront-sensing signals from quadrant photodiodes in heterodyne interferometers with digital phase-locked-loop readout". In: *Physical Review Applied* 14.5 (2020), p. 054013.

[81] Fitzsimons Hewitson and Weber. "LISA-LCST-INST-TN-003 - LISA Performance Model and Error Budget". In: (2018).

[82] M Hewitson, E Fitzsimons, and B Weber. *LISA performance model and error budget*. Tech. rep. LISA-LCST-INST-TN-003, 2019.

[83] Mark Hindmarsh et al. "Gravitational waves from the sound of a first order phase transition". In: *Physical Review Letters* 112.4 (2014), p. 041301.

[84] Mark Hindmarsh et al. "Numerical simulations of acoustically generated gravitational waves at a first order phase transition". In: *Physical Review D* 92.12 (2015), p. 123009.

[85] Wen-Rui Hu and Yue-Liang Wu. "Taiji program in space for gravitational wave physics and nature of gravity". In: *National Science Review* (2017).

[86] Stephan J Huber and Thomas Konstandin. "Gravitational wave production by collisions: more bubbles". In: *Journal of Cosmology and Astroparticle Physics* 2008.09 (2008), p. 022.

[87] Henri Inchauspé and Jean-Baptiste Bayle. *Reference frames and system of coordinates conventions for LISA dynamics modeling*. Tech. rep. Technical report, 2022.

[88] Henri Inchauspé, Ioannis Valindras, and Peter Wass. *Derivation of the full non-linear equations of motion for LISA closed-loop dynamics*. Tech. rep. Technical report, 2022.

[89] Henri Inchauspé et al. "LISA spacecraft-test mass system dynamics and suppression of jitters with Time-Delay Interferometry". In: *To be published* ().

[90] Henri-René Inchauspé. "De LISA Pathfinder à LISA: Élaboration d'un simulateur dynamique pour la mission spatiale eLISA". PhD thesis. Université Paris Diderot, 2015.

[91] Gwilym M. Jenkins and Donald G. Watts. *Spectral Analysis and Its Applications*. Holden-Day Series in Time Series Analysis. San Francisco: Holden-Day, 1968. ISBN: 978-0-8162-4464-5.

[92] Nikolaos Karnesis et al. "Characterization of the stochastic signal originating from compact binary populations as measured by LISA". In: *Phys. Rev. D* 104.4 (2021), p. 043019. DOI: 10.1103/PhysRevD.104.043019. arXiv: 2103.14598 [astro-ph.IM].

[93] Seiji Kawamura et al. "The Japanese space gravitational wave antenna: DECIGO". In: *Classical and Quantum Gravity* 28.9 (2011), p. 094011.

[94] Antoine Klein et al. "Science with the space-based interferometer eLISA: Supermassive black hole binaries". In: *Physical Review D* 93.2 (2016), p. 024003.

[95] Valeriya Korol et al. "Prospects for detection of detached double white dwarf binaries with Gaia, LSST and LISA". In: *Mon. Not. Roy. Astron. Soc.* 470.2 (2017), pp. 1894–1910. DOI: 10.1093/mnras/stx1285. arXiv: 1703.02555 [astro-ph.HE].

[96] Andrea Kulier et al. "Understanding black hole mass assembly via accretion and mergers at late times in cosmological simulations". In: *The Astrophysical Journal* 799.2 (2015), p. 178.

[97] T. Kupfer et al. "LISA verification binaries with updated distances from Gaia Data Release 2". In: *Mon. Not. Roy. Astron. Soc.* 480.1 (2018), pp. 302–309. DOI: 10.1093/mnras/sty1545. arXiv: 1805.00482 [astro-ph.SR].

[98] M. Laporte et al. "Status of the LISA On table experiment: a electro-optical simulator for LISA". In: *Journal of Physics: Conference Series*. Vol. 840. 1. IOP Publishing. 2017, p. 012014.

[99] Matthieu Laporte. "Amélioration et exploitation d'un simulateur électro-optique du détecteur spatial d'ondes gravitationnelles LISA". PhD thesis. Sorbonne Paris Cité, 2019.

[100] Shane L. Larson, William A. Hiscock, and Ronald W. Hellings. "Sensitivity curves for spaceborne gravitational wave interferometers". In: *Phys. Rev. D* 62 (2000), p. 062001. DOI: 10.1103/PhysRevD.62.062001. arXiv: gr-qc/9909080.

[101] Antony Lewis. "GetDist: a Python package for analysing Monte Carlo samples". In: *arXiv preprint arXiv:1910.13970* (2019).

[102] LISA Consortium. *Conventions And Nomenclature*. LISA-LCST-MIS-ST-001-i1.0. LISA Consortium, Sept. 2021.

[103] LISA Science Study Team. *LISA Science Requirements Document*. Requirement Document ESA-L3-EST-SCI-RS-001-i1.0. https://www.cosmos.esa.int/web/lisa/lisa-documents/. ESA, May 2018.

[104] Tyson B Littenberg and Neil J Cornish. "Bayesian approach to the detection problem in gravitational wave astronomy". In: *Physical Review D* 80.6 (2009), p. 063007.

[105] Jun Luo et al. "TianQin: a space-borne gravitational wave detector". In: *Classical and Quantum Gravity* 33.3 (2016), p. 035010.

[106] Michele Maggiore. "Gravitational wave experiments and early universe cosmology". In: *Physics Reports* 331.6 (2000), pp. 283–367.

[107] Joseph Martino. *LISA Single Link and Correlations*. Tech. rep. 2019.

[108] Makoto Matsumoto and Takuji Nishimura. "Mersenne twister: a 623-dimensionally equidistributed uniform pseudo-random number generator". In: *ACM Transactions on Modeling and Computer Simulation (TOMACS)* 8.1 (1998), pp. 3–30.

[109] Charles W Misner, Kip S Thorne, and John Archibald Wheeler. *Gravitation*. Macmillan, 1973.

[110] David Morin. *Introduction to classical mechanics: with problems and solutions*. Cambridge University Press, 2008.

[111] Martina Muratore. "Time delay interferometry for LISA science and instrument characterization". PhD thesis. University of Trento, 2021.

[112] Martina Muratore et al. "On the effectiveness of null TDI channels as instrument noise monitors in LISA". In: (July 2022). arXiv: 2207.02138 [gr-qc].

[113] Martina Muratore et al. "Time delay interferometry combinations as instrument noise monitors for LISA". In: *Phys. Rev. D* 105.2 (2022), p. 023009. DOI: 10.1103/PhysRevD.105.023009. arXiv: 2108.02738 [gr-qc].

[114] K. Rajesh Nayak et al. "Reducing the flexing of the arms of LISA". In: (2005). arXiv: gr-qc/0507105 [gr-qc].

[115] Gijs Nelemans, LR Yungelson, and SF Portegies Zwart. "The gravitational wave signal from the Galactic disk population of binaries containing two compact objects". In: *Astronomy & Astrophysics* 375.3 (2001), pp. 890–898.

[116] Isaac Newton. Correspondence letter to Richard Bentley, Cohen's translation(1978), 1692/93.

[117] Isaac Newton. *Philosophiae naturalis principia mathematica*. Vol. 1. G. Brookman, 1833.

[118] Markus Otto. *Time-Delay Interferometry Simulations for the Laser Interferometer Space Antenna*. PhD thesis, University Hannover, 2016.

[119] Fabio Pacucci and Abraham Loeb. "Separating Accretion and Mergers in the Cosmic Growth of Black Holes with X-Ray and Gravitational-wave Observations". In: *The Astrophysical Journal* 895.2 (2020), p. 95.

[120] S. Paczkowski et al. "Postprocessing subtraction of tilt-to-length noise in LISA". In: *Phys. Rev. D* 106.4 (2022), p. 042005. DOI: 10.1103/PhysRevD.106.042005.

[121] Sarah Paczkowski. *Modelling the S/C and TM Motion for LISA*. Master thesis, University Hannover, 2014.

[122] Paraskevas N Paraskevopoulos. *Modern control engineering*. CRC Press, 2017.

[123] A. Petiteau et al. "LISACode: Simulating LISA". In: *AIP Conf. Proc.* 873.1 (2006). Ed. by Stephen M. Merkowitz and Jeffrey C. Livas, pp. 633–639. DOI: 10.1063/1.2405110.

[124] Antoine Petiteau. *PhD thesis : De la simulation de LISA a l'analyse des donnees*. Université Paris Diderot (Paris 7), 2008.

[125] Antoine Petiteau et al. "LISACode: A scientific simulator of LISA". In: *Physical Review D* 77.2 (2008), p. 023002.

[126] Thomas A Prince et al. "LISA optimal sensitivity". In: *Physical Review D* 66.12 (2002), p. 122002.

[127] Dam Quang Nam et al. "TDI noises transfer functions for LISA". In: *arXiv e-prints* (2022), arXiv:2211.02539.

[128] Travis Robson, Neil J. Cornish, and Chang Liu. "The construction and use of LISA sensitivity curves". In: *Class. Quant. Grav.* 36.10 (2019), p. 105011. DOI: 10.1088/1361-6382/ab1101. arXiv: 1803.01944 [astro-ph.HE].

[129] Joseph D Romano. "Searches for stochastic gravitational-wave backgrounds". In: *Lecture notes at Les Houches Summer School July 2018, arXiv preprint arXiv:1909.00269* (2019).

[130] Joseph D Romano, Neil Cornish, et al. "Detection methods for stochastic gravitational-wave backgrounds: a unified treatment". In: *Living reviews in relativity* 20.1 (2017), pp. 1–223.

[131] Louis J Rubbo, Neil J Cornish, and Olivier Poujade. "Forward modeling of space-borne gravitational wave detectors". In: *Physical Review D* 69.8 (2004), p. 082003.

[132] Rainer Schödel et al. "A star in a 15.2-year orbit around the supermassive black hole at the centre of the Milky Way". In: *Nature* 419.6908 (2002), pp. 694–696.

[133] Bernard Schutz. *A first course in general relativity*. Cambridge university press, 2009.

[134] Bob Schutz, Byron Tapley, and George H Born. *Statistical orbit determination*. Elsevier, 2004.

[135] Uros Seljak and Matias Zaldarriaga. "Signature of gravity waves in the polarization of the microwave background". In: *Physical Review Letters* 78.11 (1997), p. 2054.

[136] Alberto Sesana et al. "Low-frequency gravitational radiation from coalescing massive black hole binaries in hierarchical cosmologies". In: *The Astrophysical Journal* 611.2 (2004), p. 623.

[137] Robert S Shankland. "Michelson-morley experiment". In: *American Journal of Physics* 32.1 (1964), pp. 16–35.

[138] Martin Staab, Jean-Baptiste Bayle, and Olaf Hartwig. *PyTDI*. Version 1.2.1. July 2022. DOI: 10.5281/zenodo.6867012. URL: https://doi.org/10.5281/zenodo.6867012.

[139] Julien Sylvestre and Massimo Tinto. "Noise characterization for LISA". In: *Phys. Rev. D* 68 (2003), p. 102002. DOI: 10.1103/PhysRevD.68.102002. arXiv: gr-qc/0308085.

[140] Stephen R Taylor. "The Nanohertz Gravitational Wave Astronomer". In: *arXiv preprint arXiv:2105.13270* (2021).

[141] R Thompson et al. "A flight-like optical reference cavity for GRACE follow-on laser frequency stabilization". In: *2011 Joint conference of the IEEE international frequency control and the European frequency and time forum (FCS) proceedings*. IEEE. 2011, pp. 1–3.

[142] J. I. Thorpe et al. "Micrometeoroid Events in LISA Pathfinder". In: *"Astrophys. J."* 883.1, 53 (Sept. 2019), p. 53. DOI: 10.3847/1538-4357/ab3649. arXiv: 1905.02765 [astro-ph.EP].

[143] Massimo Tinto and Sanjeev V. Dhurandhar. "Time-Delay Interferometry". In: *Living Rev. Rel.* 17.1 (2014), p. 6. DOI: 10.12942/lrr-2014-6.

[144] Massimo Tinto, Michele Vallisneri, and JW Armstrong. "Time-delay interferometric ranging for space-borne gravitational-wave detectors". In: *Physical Review D* 71.4 (2005), p. 041101.

[145] Silvia Toonen, Gijs Nelemans, and S Portegies Zwart. "Supernova Type Ia progenitors from merging double white dwarfs-Using a new population synthesis model". In: *Astronomy & Astrophysics* 546 (2012), A70.

[146] Jesus Torrado and Antony Lewis. "Cobaya: Code for Bayesian Analysis of hierarchical physical models". In: *Journal of Cosmology and Astroparticle Physics* 2021.05 (2021), p. 057.

[147] Michele Vallisneri. "Geometric time delay interferometry". In: *Phys. Rev. D* 72 (2005). [Erratum: Phys.Rev.D 76, 109903 (2007)], p. 042003. DOI: 10.1103/PhysRevD.76.109903. arXiv: gr-qc/0504145.

[148] Michele Vallisneri. "Synthetic LISA: Simulating time delay interferometry in a model LISA". In: *Physical Review D* 71.2 (2005), p. 022001.

[149] Michele Vallisneri et al. "Time-delay interferometry without delays". In: *Phys. Rev. D* 103.8 (2021), p. 082001. DOI: 10.1103/PhysRevD.103.082001. arXiv: 2008.12343 [gr-qc].

[150] Léon Vidal. *Validation expérimentale des performances interférométriques de LISA*. Université Paris Cité, 2022.

[151] Marta Volonteri. "Formation of supermassive black holes". In: *The Astronomy and Astrophysics Review* 18.3 (2010), pp. 279–315.

[152] Yan Wang, Gerhard Heinzel, and Karsten Danzmann. "First stage of LISA data processing II: Alternative filtering dynamic models for LISA". In: *Phys. Rev. D* 92.4 (2015), p. 044037. DOI: 10.1103/PhysRevD.92.044037. arXiv: 1503.08377 [gr-qc].

[153] Peter Welch. "The use of fast Fourier transform for the estimation of power spectra: a method based on time averaging over short, modified periodograms". In: *IEEE Transactions on audio and electroacoustics* 15.2 (1967), pp. 70–73.